Development of Nickel-Titanium Shape Memory Alloys via Laser Power Bed Fusion

Zhu, Jia-Ning

Important note
To cite this publication, please use the final published version (if applicable).
Please check the document version above.

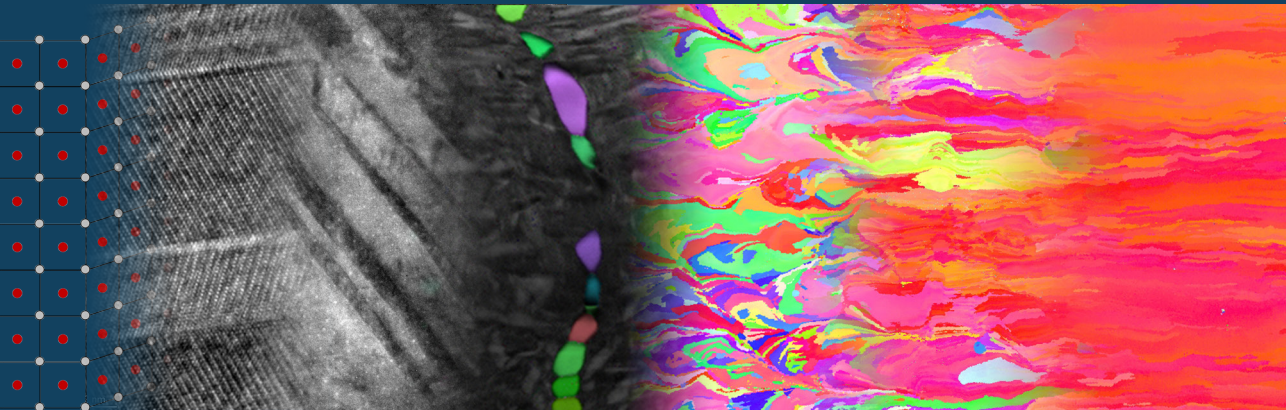# Development of Nickel-Titanium Shape Memory Alloys via Laser Power Bed Fusion

Jianing Zhu

Development of Nickel-Titanium Shape Memory Alloys via Laser Power Bed Fusion

Jianing ZHU

Development of Nickel-Titanium Shape Memory Alloys via Laser Power Bed Fusion

Dissertation

for the purpose of obtaining the degree of doctor
at Delft University of Technology
by the authority of the Rector Magnificus Prof.dr.ir. T.H.J.J. van der Hagen,
chair of the Board for Doctorates,
to be defended publicly on
Thursday 2 November 2023 at 12:30 o'clock

by

Jianing ZHU
Master of Engineering in Material Processing Engineering,
Jilin University, China
born in Nei Mongol, China

This dissertation has been approved by the promotors.

Composition of the doctoral committee:

Rector Magnificus,	chairman
Dr. V. A. Popovich	Delft University of Technology, promotor
Dr. ir. M. J. M. Hermans	Delft University of Technology, promotor

Independent members:

Prof. dr. ir. J. Sietsma	Delft University of Technology
Prof. dr.ir. E. Schlangen	Delft University of Technology
Prof. dr. ir. L. A.I. Kestens	Ghent University, Belgium
Prof. dr. M. Vedani	Politecnico di Milano, Italy
Prof. dr. I. Gibson	University of Twente, The Netherlands

Contents

Summary

Shape memory alloys (SMAs), such as nickel-titanium (NiTi) alloys or Nitinol, possess remarkable properties, including superelasticity and shape memory effects, which are attributed to the reversible martensitic transformation. However, traditional manufacturing of NiTi SMAs is challenging due to its high ductility and reactivity, which limits NiTi applications to simple geometries. In this context, laser powder bed fusion (L-PBF), an additive manufacturing technique, emerges as a promising solution capable of overcoming these limitations and introducing the concept of four-dimensional (4D) printing. This approach enables the creation of morphing shapes that can be activated by external stimuli, such as heat or stress, particularly beneficial for SMAs.

Until now, achieving customized 4D functional responses in NiTi via L-PBF remains a challenging task, due to complexities associated with both the L-PBF process and the NiTi material itself. Furthermore, the intricate interplay between the L-PBF process and materials must be taken into account when designing components, making the situation more complicated. Therefore, aiming to address these challenges and enhance the feasibility of 4D printed NiTi SMAs, this study has undertaken a comprehensive approach that integrates multiple important aspects including L-PBF process, microstructure, functionalities and designs.

Firstly, from the aspect of the L-PBF process, a key objective is to produce highly dense parts that are free from structural defects. However, due to the involvement of multiple processing parameters during L-PBF, optimizations of processing parameters mainly rely on trial-and-error methods and rough estimations based on energy inputs, which is time-consuming and costly. This results in the selection of L-PBF processing parameters only being constrained in a narrow processing space. Therefore, the need arises for a generic model to predict structural defect formation and design L-PBF processing parameters. To address this challenge, a novel approach has been proposed in this study to establish L-PBF NiTi processing maps, combining the prediction of NiTi L-PBF melt pool dimensions with criteria for identifying structural defects (including balling, lack of fusion and keyhole

induced pores). The accuracy of this model has been successfully demonstrated through experimental validation, employing two distinct L-PBF processing conditions: high laser power of 950 W with a 500 μm beam size, and low laser power of 250 W with a small beam size of 80 μm. Based on the guidance of developed processing maps, high-quality L-PBF NiTi parts with relative densities exceeding 99% were achieved under both conditions. This model not only enables to accelerate the optimization of high-quality L-PBF parts but also allows to explore processing parameters across a wide range of processing space, thereby endowing greater flexibility with tailoring microstructure and designing NiTi components.

From the microstructure centric perspective, it becomes essential to consider grain features and crystal defects, as phase transformation behaviour and functional properties can be affected by microstructures. However, the influence of various processing parameters on crystal defects and grain morphologies in L-PBF NiTi remains unclear. The reason is mainly attributed to two aspects. Firstly, the complexity of the L-PBF process makes it challenging to monitor temperature and thermal stress accurately, thereby hindering a comprehensive understanding of microstructure evolution. Secondly, to achieve superelasticity, Ni-rich NiTi alloys are commonly utilized in L-PBF. However, the phase transformation behaviour in Ni-rich NiTi is highly sensitive to the Ni/Ti atomic ratio. The Ni evaporation that occurs during L-PBF introduces changes in the NiTi composition, making it difficult to distinguish whether the change in phase transformation behaviour is influenced by the Ni/Ti ratio or microstructures. To overcome this challenge, slightly Ti-rich (near-equiatomic) NiTi, possessing a less sensitivity of Ni/Ti ratio-phase transformation behaviour, was used as the raw material to exclude the effect of Ni/Ti ratio on phase transformation. Based on the optimized linear energy input by the developed processing maps, the effect of various hatch distances on phase transformation behaviour of NiTi has been investigated by employing DSC, XRD, TEM and FEM. The findings revealed that the phase transformation can be adjusted by modifying the hatch distance. This phenomenon is closely associated with changes in dislocation densities, which results from the combined influence of thermal stress and in-situ reheating. Employing an appropriate hatch distance facilitates the formation of high-density dislocations and equiaxed grains, thereby enhancing the cyclic stability of thermally induced phase transformations. Such strategy is also applicable to investigate the effect of other L-PBF processing parameters on microstructure evolution and designing stable thermally cyclic NiTi.

From the functionality's perspective, the two important functional properties of NiTi, shape memory effect and superelasticity are separately concerned. Regarding the shape memory effect, dense Ti-rich NiTi was fabricated using specific parameters: 250 W laser

power, 1250 mm/s scanning velocity, 120 μm hatch distance, and 30 μm layer thickness, as determined from the developed processing maps. The as-fabricated NiTi shows an intermediate one-way and two-way shape memory effect. To improve shape memory effect, various heat treatments were employed. The solutionized annealing was found to enhance one-way shape memory cyclic stability, which is associated to the reduction of defects and solid solution strengthening. The subsequent aging promotes the formation of nano scaled Ti_2NiO_x intergranular precipitates, leading to the strain partitioning and enclosure of internal stress within individual grains. This results in the enhanced two-way shape memory response. These findings contribute toward the development of tailored shape memory behaviour in L-PBF NiTi.

However, another important functional property, superelasticity, is still difficult to achieve in Ti-rich NiTi. Superelasticity in NiTi is governed by reversible stress-induced martensitic transformation, which requires the critical stress for transformation to be lower than the yield strength. Unfortunately, Ti-rich NiTi, with its higher martensitic transformation temperature, is more prone to plastic deformation instead of superelasticity. Moreover, due to a low solidification nucleation rate and limited solubility of Ti in NiTi, traditional methods like grain refinement, solid solution strengthening, and precipitation strengthening are impractical for improving Ti-rich NiTi's yield strength. Conventional way for introducing superelasticity in NiTi is to increase Ni content or other alloying elements to enhance solid-solution or precipitation strengthening, as well as severe plasticity deformation with subsequent complex heat treatments to introduce grain refinement. However, all above methods lead to the decreased phase transformation temperatures (around room temperature), restricting NiTi's potential for high-temperature applications.

In this context, a novel strategy of fabricating fiber-textured Ti-rich NiTi has been proposed to achieve high-temperature superelasticity. Firstly, molecular dynamics was employed to investigate the superelastic anisotropy along various crystallographic orientations and select optimal orientation for enhancing NiTi superelasticity. Then, utilizing the tailorable solidification rates and temperature gradients offered by L-PBF, high quality Ti-rich NiTi with targeted [001] texture was created with aids of finite element modelling prediction and developed L-PBF processing maps. Finally, superelasticity was, for the first time, demonstrated in as-fabricated L-PBF Ti-rich NiTi. The achieved superelasticity was found to be exceptional, as it exhibited a remarkable superelastic temperature range that is maintained up to 453K. This temperature range is comparable to, yet surpasses, that of rare earth alloyed NiTi alloys, as it offers a wider superelastic temperature span of approximately

110 K. Thus, this framework introduces a new concept on designing high performance functional materials which benefits from functional anisotropy.

Ti-rich NiTi with [001] fiber-textured columnar grains was found to have highly sensitive to hot-cracking. To address this issue, cracks healing by employing the spark plasma sintering technique has been investigated in this work. With applying heat and force provided by the spark plasma sintering, cracks were successfully healed. The healing mechanism can be attributed to the formation of diffusion bonding around crack flanks, utilizing segregated Ti and oxygen to react with NiTi to form Ti_2NiO_x. Importantly, healed NiTi not only preserved [001] texture, allowing to keep superelasticity, but also showed an enhanced mechanical properties and two-way shape memory effect. This approach demonstrates the feasibility of using spark plasma sintering to heal NiTi cracks, allowing for a more sustainable utilization of cracked materials.

Overall, extensive investigations were conducted to develop 4D printing of NiTi shape memory alloys. A comprehensive framework, including L-PBF processing optimization, microstructure control, function design, post treatment, was established. Furthermore, aiming to improve NiTi component design feasibility, functionally graded NiTi parts, including the microstructural gradient achieved via tailoring grain textures and the chemical composition gradient achieved through in-situ alloying, were fabricated. This advancement enables designers to simultaneously obtain both functions of shape memory effect and superelasticity within one NiTi part, which takes a step toward 5D printing.

Therefore, this research significantly contributes to the advancement of 4D printed metallic materials, offering valuable insights into the complex relationship between processing parameters, microstructures, and functional properties of NiTi SMAs. The findings hold the potential to revolutionize the design of superior-performance NiTi-based alloys and expand the application potential of L-PBF NiTi parts, thereby enabling breakthroughs in various industries that rely on shape memory alloys.

Samenvatting

Legeringen met vormgeheugen (Shape Memory Alloys, SMA's), zoals nikkel-titanium (NiTi) legeringen of Nitinol, bezitten opmerkelijke eigenschappen, waaronder superelasticiteit en vormgeheugeneffecten, die worden toegeschreven aan de omkeerbare martensitische transformatie. De traditionele productie van NiTi SMA's is echter een uitdaging vanwege de hoge ductiliteit en reactiviteit, waardoor NiTi toepassingen beperkt blijven tot eenvoudige geometrieën. In deze context komt poederbed gebaseerd lasersmelten (L-PBF), een additive manufacturing-techniek, naar voren als een veelbelovende oplossing die deze beperkingen kan overwinnen en het concept van vierdimensionaal (4D) printen kan introduceren. Deze aanpak maakt het mogelijk om veranderende vormen te creëren die kunnen worden geactiveerd door externe prikkels, zoals hitte of spanning, wat zeker voor SMA's gunstig is.

Het bereiken van op maat gemaakte 4D-functionele responsen in NiTi via L-PBF blijft tot nu toe een uitdagende taak, vanwege de complexiteit van zowel het L-PBF-proces als het NiTi-materiaal zelf. Bovendien moet bij het ontwerpen van componenten rekening worden gehouden met het ingewikkelde samenspel tussen het L-PBF-proces en materialen, wat de situatie ingewikkelder maakt. Om deze uitdagingen aan te gaan en de haalbaarheid van 4D-geprinte NiTi SMA's te vergroten, heeft deze studie daarom een alomvattende aanpak gevolgd die meerdere belangrijke aspecten integreert, waaronder het L-PBF-proces, de microstructuur, functionaliteiten en het ontwerp.

Ten eerste, vanuit het aspect van het L-PBF-proces, is een hoofddoel het produceren van zeer dichte onderdelen die vrij zijn van structurele defecten. Vanwege de betrokkenheid van meerdere verwerkingsparameters tijdens L-PBF, berusten optimalisaties van verwerkingsparameters echter voornamelijk op trial-and-error-methoden en ruwe schattingen op basis van energie-input, wat tijdrovend en kostbaar is. Dit heeft als gevolg dat de selectie van L-PBF-verwerkingsparameters alleen wordt beperkt in een nauwe verwerkingsruimte. Daarom ontstaat de behoefte aan een generiek model om structurele defectvorming te voorspellen en L-PBF-verwerkingsparameters te ontwerpen. Om deze uitdaging aan te gaan,

is in deze studie een nieuwe benadering voorgesteld om L-PBF NiTi-verwerkingskaarten op te stellen, waarbij de voorspelling van NiTi L-PBF smeltbadafmetingen wordt gecombineerd met criteria voor het identificeren van structurele defecten (waaronder kogelvorming, gebrek aan fusie en sleutelgatgeïnduceerde poriën). De nauwkeurigheid van dit model is met succes aangetoond door middel van experimentele validatie, waarbij twee verschillende L-PBF-verwerkingsomstandigheden worden gebruikt: een hoog laservermogen van 950 W met een bundelgrootte van 500 μm en een laag laservermogen van 250 W met een kleine bundelgrootte van 80 μm. Op basis van de richtlijnen van ontwikkelde verwerkingskaarten werden onder beide omstandigheden hoogwaardige L-PBF NiTi-onderdelen met relatieve dichtheden van meer dan 99% bereikt. Dit model maakt het niet alleen mogelijk om de optimalisatie van hoogwaardige L-PBF-onderdelen te versnellen, maar maakt het ook mogelijk om verwerkingsparameters over een breed scala aan verwerkingsruimten te onderzoeken, waardoor meer flexibiliteit wordt geboden bij het aanpassen van de microstructuur en het ontwerpen van NiTi-componenten.

Vanuit het perspectief van de microstructuur wordt het essentieel om rekening te houden met korrelkenmerken en kristaldefecten, aangezien fasetransformatiegedrag en functionele eigenschappen kunnen worden beïnvloed door microstructuren. De invloed van verschillende verwerkingsparameters op kristaldefecten en korrelmorfologieën in L-PBF NiTi blijft echter onduidelijk. De reden wordt voornamelijk toegeschreven aan twee aspecten. Ten eerste maakt de complexiteit van het L-PBF-proces het een uitdaging om de temperatuur en thermische spanning nauwkeurig te bewaken, waardoor een alomvattend begrip van de evolutie van de microstructuur wordt belemmerd. Ten tweede worden Ni-rijke NiTi-legeringen gewoonlijk gebruikt in L-PBF om superelasticiteit te bereiken. Het fasetransformatiegedrag in Ni-rijk NiTi is echter zeer gevoelig voor de atomaire verhouding Ni/Ti. De Ni-verdamping die optreedt tijdens L-PBF introduceert veranderingen in de NiTi-samenstelling, waardoor het moeilijk te onderscheiden is of de verandering in fasetransformatiegedrag wordt beïnvloed door de Ni/Ti-verhouding of microstructuren. Om deze uitdaging te overwinnen, werd enigszins Ti-rijk (bijna-equiatomisch) NiTi, met een mindere gevoeligheid van Ni/Ti-ratio-fasetransformatiegedrag, gebruikt als grondstof om het effect van de Ni/Ti-ratio op fasetransformatie uit te sluiten. Op basis van de geoptimaliseerde lineaire energie-invoer door de ontwikkelde verwerkingskaarten, is het effect van verschillende luikafstanden op het fasetransformatiegedrag van NiTi onderzocht door gebruik te maken van DSC, XRD, TEM en FEM. De bevindingen toonden aan dat de fasetransformatie kan worden aangepast door de luikafstand aan te passen. Dit fenomeen hangt nauw samen met veranderingen in dislocatiedichtheden, die het gevolg zijn van de

gecombineerde invloed van thermische spanning en in-situ opwarming. Het gebruik van een geschikte luikafstand vergemakkelijkt de vorming van dislocaties met hoge dichtheid en gelijkgestelde korrels, waardoor de cyclische stabiliteit van thermisch geïnduceerde fasetransformaties wordt verbeterd. Een dergelijke strategie is ook toepasbaar om het effect van andere L-PBF-verwerkingsparameters op de evolutie van de microstructuur te onderzoeken en voor het ontwerpen van stabiel thermisch cyclisch NiTi.

Vanuit het oogpunt van functionaliteit worden de twee belangrijke functionele eigenschappen van NiTi, vormgeheugeneffect en superelasticiteit, apart behandeld. Wat betreft het vormgeheugeneffect, werd dicht Ti-rijk NiTi vervaardigd met behulp van specifieke parameters: 250 W laservermogen, 1250 mm / s scansnelheid, 120 μm arceringsafstand en 30 μm laagdikte, zoals bepaald op basis van de ontwikkelde verwerkingskaarten. Het als-gefabriceerde NiTi vertoont een tussenliggend eenrichtings- en tweerichtingsvormgeheugeneffect. Om het vormgeheugeneffect te verbeteren, werden verschillende warmtebehandelingen toegepast. Opgelost uitgloeien bleek de cyclische stabiliteit van het vormgeheugen in één richting te verbeteren, wat wordt geassocieerd met de vermindering van defecten en vaste oplossingsversterking. De daaropvolgende veroudering bevordert de vorming van interkristallijne Ti_2NiO_x-precipitaten op nanoschaal, wat leidt tot spanningsverdeling en insluiting van interne spanning binnen individuele korrels. Dit resulteert in de verbeterde tweerichtingsvormgeheugenrespons. Deze bevindingen dragen bij aan de ontwikkeling van op maat gemaakt vormgeheugengedrag in L-PBF NiTi.

Een andere belangrijke functionele eigenschap, superelasticiteit, is echter nog steeds moeilijk te bereiken in Ti-rijk NiTi. Superelasticiteit in NiTi wordt bepaald door omkeerbare door spanning geïnduceerde martensitische transformatie, waarvoor de kritische spanning voor transformatie lager moet zijn dan de vloeigrens. Helaas is Ti-rijk NiTi, met zijn hogere martensitische transformatietemperatuur, meer vatbaar voor plastische vervorming in plaats van superelasticiteit. Bovendien zijn traditionele methoden zoals korrelverfijning, vaste oplossingsversterking en precipitatieversterking, vanwege een lage stollingskiemvormingssnelheid en beperkte oplosbaarheid van Ti in NiTi onpraktisch voor het verbeteren van de vloeigrens van Ti-rijk NiTi. De conventionele manier om superelasticiteit in NiTi te introduceren, is het verhogen van het Ni-gehalte of andere legeringselementen om de vaste oplossingsversterking of precipitatie te verbeteren, evenals ernstige plasticiteitsvervorming met daaropvolgende complexe warmtebehandelingen om korrelverfijning te introduceren. Alle bovenstaande methoden leiden echter tot lagere fasetransformatietemperaturen (rond kamertemperatuur), waardoor het potentieel van NiTi voor toepassingen bij hoge temperaturen wordt beperkt.

In deze context werd een nieuwe strategie voorgesteld voor het vervaardigen van éénkristalachtig Ti-rijk NiTi om superelasticiteit bij hoge temperaturen te bereiken. Ten eerste werd moleculaire dynamica gebruikt om de superelastische anisotropie langs verschillende kristallografische oriëntaties te onderzoeken en om de optimale oriëntatie te selecteren voor het verbeteren van NiTi-superelasticiteit. Vervolgens werd, gebruikmakend van de aanpasbare stollingssnelheden en temperatuurgradiënten aangeboden door L-PBF, Ti-rijk NiTi van hoge kwaliteit met gerichte [001] textuur gecreëerd met behulp van eindige-elementenmodelleringsvoorspelling en de ontwikkelde L-PBF-verwerkingskaarten. Ten slotte werd superelasticiteit voor het eerst aangetoond in als-gefabriceerde L-PBF Ti-rijk NiTi. De bereikte superelasticiteit bleek uitzonderlijk te zijn, aangezien het een opmerkelijk superelastisch temperatuurbereik vertoonde dat tot 453K wordt gehandhaafd. Dit temperatuurbereik is vergelijkbaar met, maar overtreft, dat van met zeldzame aarde gelegeerde NiTi-legeringen, omdat het een breder superelastisch temperatuurbereik biedt van ongeveer 110 K. Dit raamwerk introduceert dus een nieuw concept voor het ontwerpen van hoogwaardige functionele materialen die profiteren van functionele anisotropie.

Ti-rijk NiTi met monokristallijne [001] getextureerde kolomvormige korrels bleek zeer gevoelig te zijn voor warmscheuren. Om dit probleem aan te pakken, is in dit werk onderzoek gedaan naar het genezen van scheuren door gebruik te maken van de vonkplasma-sintertechniek. Met het toepassen van warmte en kracht die werden geleverd door het sinteren met vonkplasma, werden scheuren met succes genezen. Het genezingsmechanisme kan worden toegeschreven aan de vorming van diffusiebinding rond scheurflanken, waarbij gescheiden Ti en zuurstof worden gebruikt om te reageren met NiTi om Ti_2NiO_x te vormen. Belangrijk is dat genezen NiTi niet alleen de textuur [001] behield, waardoor superelasticiteit behouden bleef, maar ook verbeterde mechanische eigenschappen en een tweezijdig vormgeugeneffect vertoonde. Deze benadering toont de haalbaarheid aan van het gebruik van vonkplasma-sinteren om NiTi-scheuren te genezen, waardoor een duurzamer gebruik van gebarsten materialen mogelijk wordt.

Over het algemeen werden uitgebreide onderzoeken uitgevoerd om 4D-printen van NiTi-legeringen met vormgeheugen te ontwikkelen. Er werd een alomvattend raamwerk opgesteld, inclusief L-PBF-verwerkingsoptimalisatie, controle van de microstructuur, functieontwerp en nabehandeling. Om de haalbaarheid van het ontwerp van NiTi-componenten te verbeteren, werden bovendien functioneel gegradeerde NiTi-onderdelen vervaardigd, inclusief de microstructurele gradiënt die wordt bereikt door korrelstructuren op maat te maken en de gradiënt van de chemische samenstelling die wordt bereikt door in-situ legering. Deze vooruitgang stelt ontwerpers in staat om tegelijkertijd beide de functie van

vormgeheugeneffect en superelasticiteit binnen één NiTi-onderdeel te verkrijgen, wat een stap in de richting van 5D-printen is.

Daardoor draagt dit onderzoek aanzienlijk bij aan de vooruitgang van 4D-geprinte metalen, en biedt het waardevolle inzichten in de complexe relatie tussen verwerkingsparameters, microstructuren en functionele eigenschappen van NiTi SMA's. De bevindingen hebben het potentieel om het ontwerp van op NiTi gebaseerde legeringen met superieure prestaties radicaal te veranderen en het toepassingspotentieel van L-PBF NiTi-onderdelen uit te breiden, waardoor doorbraken mogelijk worden in verschillende industrieën die afhankelijk zijn van legeringen met vormgeheugen.

1

Introduction

1

Shape memory materials (SMMs) are characterized by the ability to recover their original shape from a significant deformation when a particular stimulus is applied [1]. These materials can generally be classified into three categories: shape memory alloys (SMAs), shape memory polymers (SMPs), and shape memory ceramics (SMCs) [2]. In comparison to SMPs, SMAs exhibit higher actuation stress, longer cyclic life, and higher actuation energy density [3]. Additionally, SMAs outperform SMCs by enabling larger recoverable strain, reaching up to 8% [2]. Consequently, among all SMMs, SMAs are widely considered as excellent candidates for practical engineering applications.

Reversible martensitic transformation, a diffusionless solid-solid phase transformation [4], gives SMAs unique functionalities. Depending on the initial phase prior to deformation, these functionalities are divided into superelasticity and shape memory effect (SME). Superelasticity (also termed pseudoelasticity), giving SMAs a rubbery feel, allows SMAs recover their deformation after unloading [5]. Unlike traditional metallic materials, superelastic SMAs are able to several percent of strains. SME is a capability of SMAs to regain their original shapes after deformation by heating. Due to such very attractive functionalities [6, 7], SMAs are widely utilized in fields including actuators, sensors, dampers and medical implants.

Due to excellent shape recoverability, durability and corrosion resistance, nickel-titanium (Ni-Ti) alloys (also termed as Nitinol) are most widely used among all shape memory or superelastic alloys [8]. However, it is well known that the fabrication of Nitinol components using conventional production methods is a challenge because of its high ductility, work hardening and reactivity [9, 10]. Therefore, applications of Nitinol alloys are mainly limited to simple geometries including sheets, rods, wires and tubes [11].

Laser powder bed fusion (L-PBF), one of the additive manufacturing (AM) (or 3D printing) techniques, is capable of manufacturing near-net-shaped components, enabling more design feasibility. By combining NiTi's functionalities with its 3D shape design fabricated by L-PBF, a fourth dimension, i.e. morphing shapes activated by external stimulus (including force or heat) over time, is introduced, which is considered as 4D-printing. For L-PBF technique, there are two main characteristics: (1) process-centric aspects, which include part quality dominated by various independent processing parameters, and interplay of these parameters [12]; (2) material-centric aspects, which include non-equilibrium microstructure and chemical non-uniformity present due to high temperature, steep thermal gradient and rapid colling rate during L-PBF process. Hence, establishing accurate processing maps for fabricating high-quality NiTi part and understanding relationship between L-PBF processing

1

parameters, microstructure and functional properties are essential for the development 4D printed NiTi shape memory alloys

1.1. Challenges and Knowledge Gaps

Until now, a number of challenges remain in the L-PBF of NiTi due to the complexity of the L-PBF process and the phase transformations of NiTi. The control of the L-PBF process not only impacts the structural quality but also influences the microstructures and chemical compositions of NiTi. Moreover, the functionality of NiTi, which is governed by its martensitic transformation, relies heavily on microstructures, chemical compositions, crystal defects, and grain orientations. Consequently, it is challenging to simultaneously consider and establish relationships among all these influencing factors. Furthermore, when aiming to achieve specific functionalities through the utilization of L-PBF NiTi in the design process, the complexity increases as the effects of both L-PBF and NiTi itself need to be taken into account. Therefore, the current challenges can be categorized into process-, material- and design-related challenges.

1.1.1. Process-related challenges

Despite a variety of L-PBF processing parameters leading to expanded design freedom, the complex parameters and their interactions make quality control difficult. To roughly estimate the processing windows of NiTi, energy inputs, such as volumetric energy density (J/mm^3) and linear energy density (J/mm), are introduced [13]. However, such metrics lack accuracy and require subsequent laborious trial and error. It is not possible to carry out large adjustments of process parameters to fulfil the demands of smart NiTi design. Therefore, one of the overarching challenges is how to produce defect-free components and establish a reliable model to predict L-PBF processing maps.

In the absence of a precise model for predicting the processing maps of L-PBF NiTi, the selection of processing parameters often becomes arbitrary and varies among different studies. Consequently, a dilemma arises where it becomes difficult to draw a general conclusion regarding the fabrication of high-quality L-PBF NiTi. Furthermore, the rapid heating and cooling, heat overshooting, and complex thermal history during L-PBF can result in non-equilibrium microstructure, chemical segregation, and thermal stress, further complicating the fabrication of NiTi.

1.1.2. Material-related challenges

The functionalities of NiTi, including shape memory effect and superelasticity, arise from reversible martensitic transformation. The transformation characteristics are linked to NiTi chemical compositions, microstructures, crystal defects and grain orientations [14]. Although the flexibility of the L-PBF technique allows for the utilization of these influencing factors to customize the functionalities of NiTi, the complexity also increases when aiming to achieve specific material properties, as multiple factors need to be considered simultaneously.

The phase transformation temperature of NiTi is highly sensitive to the Ni/Ti ratios [15]. However, during L-PBF, challenges arise due to Ni evaporation and local chemical segregation caused by the high temperature and non-equilibrium solidification [16]. These factors introduce uncertainties in the phase transformation after L-PBF fabrication. Quantitatively estimating changes in the chemical compositions of NiTi proves challenging due to the difficulty of monitoring element evaporation and elemental distribution fluctuations during L-PBF. Furthermore, the high reactivity of Ti results in its oxidation, as it reacts with residual oxygen in the protective gas and impurities [17], which makes the design of L-PBF NiTi with targeted phase transformation behavior more complicated.

NiTi alloys can be classified into Ni-rich and Ti-rich compositions, with Ni50Ti50 (at. %) acting as the dividing line. However, Ti-rich and equiatomic NiTi alloys lack strengthening factors due to the limited solid solubility of Ti in NiTi and the absence of solidification nucleation. As a result, plastic deformation occurs instead of superelasticity [18]. Consequently, most research efforts have been directed towards Ni-rich NiTi and its superelastic properties [13]. To date, achieving superelasticity in Ti-rich L-PBF NiTi has not been reported, despite the potential of Ti-rich NiTi with its higher phase transformation temperatures for exhibiting high-temperature superelasticity and shape memory effects.

Furthermore, factors such as grain size, crystal defects, and precipitates also influence the phase transformation behavior and functionalities of NiTi [14]. The mechanisms underlying these influences are detailed in Chapter 2. These microstructural features can be altered by the L-PBF process. For example, grain size and morphology can be changed by varying the thermal gradient and grain growth rate during L-PBF [19]. The rapid heating, cooling, and thermal stress associated with L-PBF can introduce crystal defects in NiTi [19]. Additionally, complex thermal histories, including reheating, can promote the formation of in-situ precipitates. Hence, the complex relationship between L-PBF process, microstructural

features, phase transformation and functionalities of NiTi presents further material-related challenges.

Moreover, the non-equilibrium microstructure introduced by L-PBF can be modified through heat treatment. However, research on post-treatments has predominantly been focused on Ni-rich NiTi, where aging-induced Ni_4Ti_3 phases enhance superelastic and elastocaloric effects [20-22]. There is limited investigation into post-treatment responses in Ti-rich NiTi [23-25], primarily concerning mechanical properties. Understanding the impact of heat-treated microstructures on shape memory effects, both one-way and two-way, is lacking. Additionally, the elimination of structural defects and enhancement of mechanical/functional properties in L-PBF NiTi require further research.

NiTi shows functional anisotropy with different functional behavior along various crystallographic orientations. Sehitoglu et al. [26] employed the energy minimization theory with experimental validation and demonstrated that Ni-rich aged NiTi along [148] orientation, close to [100] orientation, had the best superelasticity. However, this approach is only applicable for predicting superelastic behavior in single crystal NiTi and does not consider interactions between stress-induced martensitic variants and reverse transformation from martensite to austenite during unloading. This limitation arises from the crystallographic complexity of martensitic transformation in polycrystalline NiTi. Therefore, comprehensive understanding of effect of NiTi crystallographic texture on functional properties needs to be investigated. In terms of texture fabricated by deformation in NiTi, only <111> and <110> textures can be fabricated [27, 28]. In contrast, controlling the thermal gradient direction during L-PBF allows for more freedom in promoting preferred grain growth along specific orientations, thereby enabling tailored L-PBF textures. However, comprehensive investigations on the relationship between L-PBF process, texture evolution, and functional responses of NiTi have not yet been reported.

Hence, it is important to consider both process-related and material-related challenges to comprehensively understand the relationships between the L-PBF process, NiTi microstructures and NiTi functionalities. This challenging topic also serves as the research focus of this study.

1.1.3. Design-related challenges

To achieve a realistic application of NiTi, it is necessary to design specific NiTi components for various applications. The emergence of additive manufacturing techniques

has led to recent research focusing on expanding the capabilities of NiTi shape memory alloys (SMAs), which can be summarized in the following three aspects [29]: 1) The design and fabrication of architectured NiTi alloys that combine the advantageous shape memory properties of NiTi with macroscopically engineered structures. 2) Functionally graded (FG) NiTi, which benefits from the combination of the functional properties of NiTi and the characteristics of functionally graded structures. 3) The use of NiTi as the supporting matrix in composites, which enables the enhancement of the properties of other materials. However, there are several challenges associated with achieving the above-mentioned goals.

For the design of architectured NiTi components, it is crucial to consider the microstructural and chemical heterogeneities. Due to different thermal histories, the microstructures and chemical compositions vary between locations near the outer surfaces and inner parts of the components [30]. This difference leads to a difficulty in achieving the anticipated functions of architectured NiTi. Furthermore, NiTi shows an asymmetrical functional response under tension, compression, and torsion [31]. During loading, different struts within architectured NiTi experience either tension, compression, or torsion, depending on their topological geometries and locations [32]. This requires a comprehensive understanding of the local stress states of architectured NiTi and their corresponding functional responses. Therefore, achieving a compatible architectural structure with NiTi functions to realize a desirable design is challenging. Additionally, due to powder adhesion and thermal shrinkage during solidification, ensuring a high surface finish and geometrical accuracy of L-PBF architectured materials is also a matter of concern [33].

In terms of functionally graded NiTi, there are two types of gradients to consider: chemical and microstructural gradients. To adjust the NiTi compositions, in-situ alloying or controlling element evaporation can be employed. However, achieving in-situ alloying remains challenging due to limitations in the L-PBF powder feedstock. Although the directed energy deposition technique allows for in-situ NiTi alloying by controlling material feeding, the low building resolution imposes limitations on the geometry accuracy of the designed components [34]. On the other hand, to achieve chemical gradients, the Ni/Ti ratio can be tuned by employing different energy inputs [35], taking advantage of the differences in evaporation pressure and temperature between Ni and Ti. However, there are limitations to the tunable amplitude, and excessive energy inputs can lead to the instability of the laser bead, resulting in structural defects [36].

The microstructural gradient in L-PBF NiTi has not yet been reported. Due to the low solidification nucleation rate in NiTi, creating pronounced graded microstructures with various grain sizes is challenging. Moreover, the comprehensive understanding of the

relationship between L-PBF processes, grain morphologies, textures, and the functions of NiTi is still lacking. Hence, it is challenging to design multi-functional NiTi components by creating graded crystallographic textures.

When it comes to NiTi-based composites, due to different thermal-physical properties and laser absorptivity of NiTi and other materials, the selection of desirable material combinations remains challenging [37]. In addition, the wettability and interface bonding strength between NiTi and added materials also affect final mechanical and functional properties of NiTi-based composites.

Overall, the application of L-PBF for fabricating NiTi presents numerous challenges as an emerging technique. These challenges consist of various aspects, including the L-PBF process, NiTi materials, and design considerations. It is crucial to not isolate these challenges but rather comprehend the intricate interactions among the process, materials, and performance. Achieving this requires a comprehensive understanding of the relationships among the L-PBF process, the NiTi material itself, and the specific design requirements. By considering these interdependencies, it becomes possible to deal with the challenges effectively and optimize the fabrication of NiTi using L-PBF.

1.2. Research Objectives and Thesis Outline

As the acknowledged challenges and knowledges gaps, it is important to achieve L-PBF processing parameter optimizations, understand how L-PBF process affects NiTi functionalities, and establish a knowledge chain including L-PBF process-NiTi functions-NiTi component design. Hence, a lot of efforts have been taken by researchers to investigate L-PBF investigated NiTi [13, 38-42]. However, these studies do not provide sufficient information and comprehensive understanding allowing to design NiTi in a customized way.

Therefore, the objective of this work is to develop an integrated framework for designing L-PBF NiTi that includes the L-PBF process, microstructure evolution, realization of NiTi functionalities, and post-treatments. To achieve high-quality dense L-PBF NiTi fabrication, a predictive model has been developed. Then, based on established processing maps, the relationship between the L-PBF process and crystal defects, grain morphologies, and crystallographic textures in NiTi has been determined, enabling the creation of tailored microstructures through L-PBF. Furthermore, through simulation and experiments, a comprehensive understanding of the relationship between these tailored microstructures and NiTi's functions has been achieved. Afterwards, to enhance specific functional responses of

1

L-PBF NiTi, effective post treatments has been investigated. Finally, in order to address design-related challenges, functionally graded L-PBF NiTi parts with chemical and microstructural gradients have been successfully fabricated, opening up possibilities for exploring greater design flexibility.

The outline of this dissertation is listed as follows:

1. Research background, including NiTi martensite phase transformation, factors influencing NiTi's functionalities and additively manufactured NiTi is presented in **Chapter 2**; More information about process-material-design specific challenges are introduced in the Chapter 2.

2. In **Chapter 3**, a model for predicting processing maps of L-PBF NiTi SMAs is introduced, which considers complex interactions between L-PBF melt pool physics, structural defect formation criteria and processing parameters. The accuracy of developed model has been demonstrated based on experimental validations, allowing to search appropriate processing parameters in a wider range of space to fabricate dense L-PBF NiTi.

3. Based on the optimized processing parameters from Chapter 3, the role of hatch distance, an underestimated processing parameter, on microstructures and phase transformation behaviour has been comprehensively investigated in **Chapter 4**.

4. The impact of heat-treated microstructures on shape memory effects, including one-way and two-way shape memory effects, is comprehensively characterized and quantified in **Chapter 5**. Then, the mechanisms of tailorable one- and two-way shape memory effects are revealed.

5. Aim to the knowledge gaps of absent superelasticity in Ti-rich NiTi, the potential of Ti-rich NiTi for exhibiting high-temperature superelasticity and shape memory effect has been explored in **Chapter 6.** The processing parameters are optimized based the model introduced in the chapter 3.

6. Considering that the lack of knowledge on post treatments allowing to eliminating structural defects in L-PBF NiTi, spark plasma sintering technique is employed for healing cracks in L-PBF NiTi. Mechanisms for crack formation and crack healing are presented in the **Chapter 7**.

7. Lastly, **Chapter 8** summarises the main findings and contributions of this research to the materials science and mechanical behaviour community and proposes further relevant developments of 4D printed NiTi shape memory alloys.

1

References

[1] W.M. Huang, Z. Ding, C.C. Wang, J. Wei, Y. Zhao, H. Purnawali, Shape memory materials, Mater. Today, 13(7) (2010) 54-61.

[2] K. Otsuka, C.M. Wayman, Shape memory materials, Cambridge university press1999.

[3] P.K. Kumar, D.C. Lagoudas, Introduction to Shape Memory Alloys, Shape Memory Alloys: Modeling and Engineering Applications, Springer US, Boston, MA, 2008, pp. 1-51.

[4] T. Omori, R. Kainuma, Alloys with long memories, Nature 502(7469) (2013) 42-44.

[5] X. Ren, K. Otsuka, Origin of rubber-like behaviour in metal alloys, Nature 389(6651) (1997) 579-582.

[6] D. Dye, Towards practical actuators, Nat. Mater. 14(8) (2015) 760-761.

[7] X. Huang, G.J. Ackland, K.M. Rabe, Crystal structures and shape-memory behaviour of NiTi, Nat. Mater. 2(5) (2003) 307-311.

[8] T. Nakahata, 4 - Industrial processing of titanium–nickel (Ti–Ni) shape memory alloys (SMAs) to achieve key properties, in: K. Yamauchi, I. Ohkata, K. Tsuchiya, S. Miyazaki (Eds.), Shape Memory and Superelastic Alloys, Woodhead Publishing2011, pp. 53-62.

[9] K. Weinert, V. Petzoldt, Machining of NiTi based shape memory alloys, Mater. Sci. Eng. A. 378(1) (2004) 180-184.

[10] G. Peduk, S. Dilibal, O. Harrysson, S. Özbek, Comparison of the production processes of nickeltitanium shape memory alloy through additive manufacturing, Int. Symposium on 3D Printing (Additive Manufacturing), 2017.

[11] N. Shayesteh Moghaddam, S.E. Saghaian, A. Amerinatanzi, H. Ibrahim, P. Li, G.P. Toker, H.E. Karaca, M. Elahinia, Anisotropic tensile and actuation properties of NiTi fabricated with selective laser melting, Mater. Sci. Eng. A. 724 (2018) 220-230.

[12] A.M. Khorasani, I. Gibson, A. Ghasemi, A. Ghaderi, Modelling of laser powder bed fusion process and analysing the effective parameters on surface characteristics of Ti-6Al-4V, Int. J. Mech. Sci. 168 (2020) 105299.

[13] M. Elahinia, N. Shayesteh Moghaddam, M. Taheri Andani, A. Amerinatanzi, B.A. Bimber, R.F. Hamilton, Fabrication of NiTi through additive manufacturing: A review, Prog. Mater Sci. 83 (2016) 630-663.

[14] K. Otsuka, X. Ren, Physical metallurgy of Ti–Ni-based shape memory alloys, Prog. Mater Sci. 50(5) (2005) 511-678.

[15] J. Frenzel, E.P. George, A. Dlouhy, C. Somsen, M.F.X. Wagner, G. Eggeler, Influence of Ni on martensitic phase transformations in NiTi shape memory alloys, Acta Mater. 58(9) (2010) 3444-3458.

[16] J. Ma, B. Franco, G. Tapia, K. Karayagiz, L. Johnson, J. Liu, R. Arroyave, I. Karaman, A. Elwany, Spatial Control of Functional Response in 4D-Printed Active Metallic Structures, Sci. Rep. 7(1) (2017) 46707.

[17] X. Wang, J. Yu, J. Liu, L. Chen, Q. Yang, H. Wei, J. Sun, Z. Wang, Z. Zhang, G. Zhao, J. Van Humbeeck, Effect of process parameters on the phase transformation behavior and tensile properties of NiTi shape memory alloys fabricated by selective laser melting, Addit. Manuf. 36 (2020) 101545.

[18] S. Miyazaki, My Experience with Ti–Ni-Based and Ti-Based Shape Memory Alloys, Shape Mem. Superelasticity 3(4) (2017) 279-314.

[19] J.-N. Zhu, E. Borisov, X. Liang, R. Huizenga, A. Popovich, V. Bliznuk, R. Petrov, M. Hermans, V. Popovich, Controlling microstructure evolution and phase transformation behavior in additive manufacturing of nitinol shape memory alloys by tuning hatch distance, J. Mater. Sci. (2022) 1-19.

[20] S. Saedi, A.S. Turabi, M. Taheri Andani, C. Haberland, H. Karaca, M. Elahinia, The influence of heat treatment on the thermomechanical response of Ni-rich NiTi alloys manufactured by selective laser melting, J. Alloys Compd. 677 (2016) 204-210.

[21] J. Gan, L. Duan, F. Li, Y. Che, Y. Zhou, S. Wen, C. Yan, Effect of laser energy density on the evolution of Ni_4Ti_3 precipitate and property of NiTi shape memory alloys prepared by selective laser melting, J. Alloys Compd. 869 (2021) 159338.

[22] Y. Cao, X. Zhou, D. Cong, H. Zheng, Y. Cao, Z. Nie, Z. Chen, S. Li, N. Xu, Z. Gao, W. Cai, Y. Wang, Large tunable elastocaloric effect in additively manufactured Ni–Ti shape memory alloys, Acta Mater. 194 (2020) 178-189.

[23] J. Fu, Z. Hu, X. Song, W. Zhai, Y. Long, H. Li, M. Fu, Micro selective laser melting of NiTi shape memory alloy: Defects, microstructures and thermal/mechanical properties, Opt. Laser. Technol. 131 (2020) 106374.

1

1

[24] S. Li, H. Hassanin, M.M. Attallah, N.J.E. Adkins, K. Essa, The development of TiNi-based negative Poisson's ratio structure using selective laser melting, Acta Mater. 105 (2016) 75-83.

[25] C. Tan, S. Li, K. Essa, P. Jamshidi, K. Zhou, W. Ma, M.M. Attallah, Laser Powder Bed Fusion of Ti-rich TiNi lattice structures: Process optimisation, geometrical integrity, and phase transformations, Int. J. Mach. Tools Manuf. 141 (2019) 19-29.

[26] H. Sehitoglu, I. Karaman, R. Anderson, X. Zhang, K. Gall, H.J. Maier, Y. Chumlyakov, Compressive response of NiTi single crystals, Acta Mater. 48(13) (2000) 3311-3326.

[27] G. Laplanche, T. Birk, S. Schneider, J. Frenzel, G. Eggeler, Effect of temperature and texture on the reorientation of martensite variants in NiTi shape memory alloys, Acta Mater. 127 (2017) 143-152.

[28] Y. Liu, The superelastic anisotropy in a NiTi shape memory alloy thin sheet, Acta Mater. 95 (2015) 411-427.

[29] B.S. Shariat, Q. Meng, A.S. Mahmud, Z. Wu, R. Bakhtiari, J. Zhang, F. Motazedian, H. Yang, G. Rio, T.-h. Nam, Y. Liu, Functionally graded shape memory alloys: Design, fabrication and experimental evaluation, Mater. Des. 124 (2017) 225-237.

[30] P. Jamshidi, C. Panwisawas, E. Langi, S.C. Cox, J. Feng, L. Zhao, M.M. Attallah, Development, characterisation, and modelling of processability of nitinol stents using laser powder bed fusion, J. Alloys Compd. 909 (2022) 164681.

[31] R. Mehrabi, M. Kadkhodaei, M. Elahinia, Constitutive modeling of tension-torsion coupling and tension-compression asymmetry in NiTi shape memory alloys, Smart Mater. Struct. 23(7) (2014) 075021.

[32] Z. Yan, J.-N. Zhu, E. Borisov, T. Riemslag, S.P. Scott, M. Hermans, J. Jovanova, V. Popovich, Superelastic response and damping behavior of additively manufactured Nitinol architectured materials, Addit. Manuf. 68 (2023) 103505.

[33] L.N. Carter, V.M. Villapún, L. Grover, S.C. Cox, Exploring the duality of powder adhesion and underlying surface roughness in laser powder bed fusion processed Ti-6Al-4V, J. Manuf. Process. 81 (2022) 14-26.

[34] D. Svetlizky, M. Das, B. Zheng, A.L. Vyatskikh, S. Bose, A. Bandyopadhyay, J.M. Schoenung, E.J. Lavernia, N. Eliaz, Directed energy deposition (DED) additive manufacturing: Physical characteristics, defects, challenges and applications, Mater. Today. 49 (2021) 271-295.

1

[35] X. Wang, M. Speirs, S. Kustov, B. Vrancken, X. Li, J.-P. Kruth, J. Van Humbeeck, Selective laser melting produced layer-structured NiTi shape memory alloys with high damping properties and Elinvar effect, Scripta Mater. 146 (2018) 246-250.

[36] J.-N. Zhu, E. Borisov, X. Liang, E. Farber, M.J.M. Hermans, V.A. Popovich, Predictive analytical modelling and experimental validation of processing maps in additive manufacturing of nitinol alloys, Addit. Manuf. 38 (2021) 101802.

[37] S.L. Sing, S. Huang, G.D. Goh, G.L. Goh, C.F. Tey, J.H.K. Tan, W.Y. Yeong, Emerging metallic systems for additive manufacturing: In-situ alloying and multi-metal processing in laser powder bed fusion, Prog. Mater. Sci. 119 (2021) 100795.

[38] S. Saedi, N. Shayesteh Moghaddam, A. Amerinatanzi, M. Elahinia, H.E. Karaca, On the effects of selective laser melting process parameters on microstructure and thermomechanical response of Ni-rich NiTi, Acta Mater. 144 (2018) 552-560.

[39] S. Dadbakhsh, M. Speirs, J.-P. Kruth, J. Schrooten, J. Luyten, J. Van Humbeeck, Effect of SLM Parameters on Transformation Temperatures of Shape Memory Nickel Titanium Parts, Adv. Eng. Mater. 16(9) (2014) 1140-1146.

[40] C. Wang, X.P. Tan, Z. Du, S. Chandra, Z. Sun, C.W.J. Lim, S.B. Tor, C.S. Lim, C.H. Wong, Additive manufacturing of NiTi shape memory alloys using pre-mixed powders, J. Mater. Process. Technol. 271 (2019) 152-161.

[41] Z. Yu, Z. Xu, Y. Guo, R. Xin, R. Liu, C. Jiang, L. Li, Z. Zhang, L. Ren, Study on properties of SLM-NiTi shape memory alloy under the same energy density, J. Mater. Res. Technol. 13 (2021) 241-250.

[42] S. Wei, J. Zhang, L. Zhang, Y. Zhang, B. Song, X. Wang, J. Fan, Q. Liu, Y. Shi, Laser powder bed fusion additive manufacturing of NiTi shape memory alloys: a review, Int. J. Extreme Manuf. 5(3) (2023) 032001.

1

2

NiTi Shape Memory Alloys and its Additive Manufacturing

2.1. NiTi shape memory alloys

2.1.1. Phenomenology of phase transformation in NiTi

The binary phase diagram of Ni–Ti is shown in Figure 2.1, where the purple area represents the region of the intermetallic NiTi phase (or Nitinol). As the composition range of single NiTi phase is very narrow, its mechanical and functional properties are sensitive to variation in chemical composition, especially for Ni-rich NiTi. In the NiTi binary phase diagram, only stable phases are shown and the NiTi phase is the austenite phase rather than the martensite phase.

2
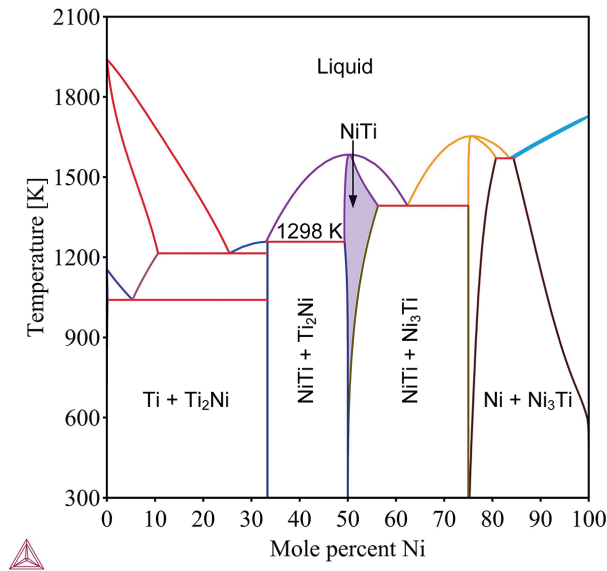
Figure 2.1. The phase diagram of Ni–Ti.

Generally, temperature and stress act as main variables influencing the equilibrium states of phases in NiTi. When temperature is a dominant factor there are two phases: The first one is a high temperature phase called austenite (A, BCC_B2) and is a low temperature phase called martensite (M, B19′). With changing temperatures, austenite and martensite can be transformed into each other through diffusionless phase transformation. In the absence of an applied load, the martensite is called twinned martensite, which exists in the "self-accommodated" state, and this phase transformation is called temperature induced

martensitic phase transformation. The schematic of temperature induced martensitic phase transformation is shown in Figure 2.2. During cooling, the austenite transforms to martensite, which is termed as *the forward transformation.* Austenite begins to transform to martensite at the martensitic start temperature (M_s) and is completely transferred into twinned martensite at the martensitic finish temperature (M_f). Similarly, martensite could transform to austenite during heating, which is termed as *the reverse transformation*. Correspondingly, there is an austenite start temperature (A_s) and austenite finish temperature (A_f) during the reverse transformation. The presence or disappearance of phases during phase transformation introduces phase interface energy and stored elastic energy, which act as barriers, resulting in the occurrence of hysteresis [1]. The hysteresis exhibits a time lag or delay during heating and cooling cycles. It is characterized by a difference in the transformation temperatures between the heating and cooling paths (Figure 2.2).
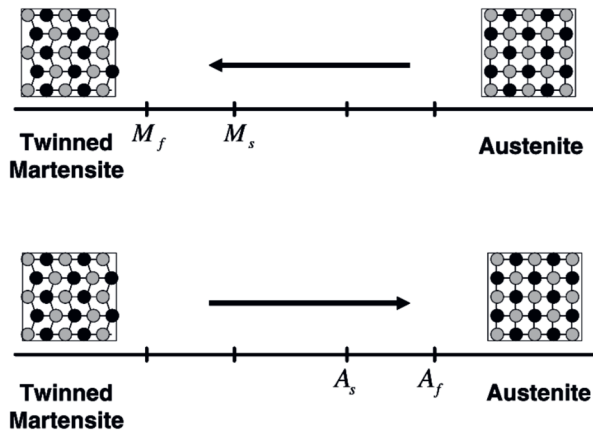
Figure 2.2. Temperature-induced phase transformation of NiTi without stress [2].

When a mechanical load is applied on twinned martensite, twinned martensite variants can be detwinned and reoriented along the loading direction to form *detwinned martensite*. This process could result in a macroscopic shape change, where the deformed configuration is retained when the load is released. Detwinned martensite is metastable phase, and it can be completely transformed to austenite if the temperature is increased above A_f. After the transformation from detwinned martensite to austenite, a complete shape recovery will be obtained. Cooling back to a temperature below M_f (forward transformation) leads to the

formation of twinned martensite again with no associated shape change observed. The process described above is the *one-way shape memory effect* (*OWSME*) and the whole *OWSME* loop is shown in the strain-stress-temperature diagram (Figure 2.3).
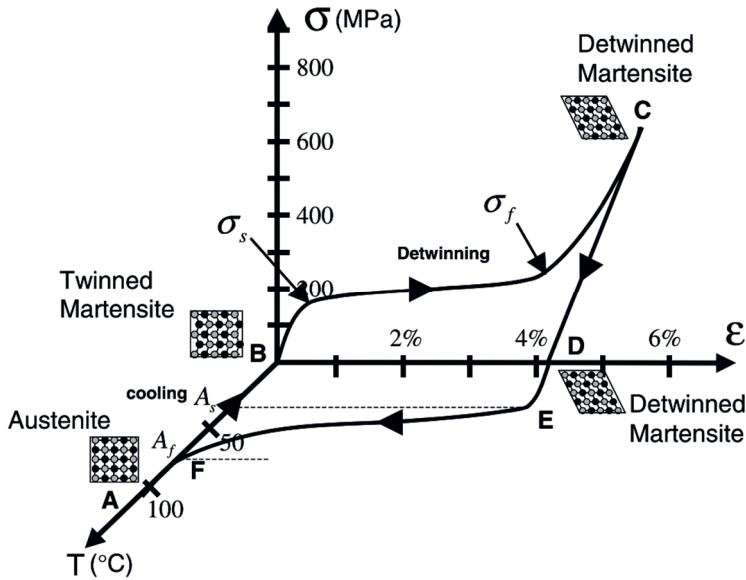
Figure 2.3. Shape memory effects of NiTi in the strain-stress-temperature space [2].

Martensite phase transformation can be also triggered by stress. When a stress, above a critical stress, is applied on austenitic NiTi, austenite can directly transform into detwinned martensite associated with macroscopic deformation. After releasing the stress, stress-induced martensite (detwinned martensite) completely transforms back into austenite and deformation is fully recovered. This behaviour is termed as *superelasticity* (SE) or *pseudoelasticity.* The ideal thermomechanical path of SE and corresponding characteristic stresses are shown in the Figure 2.4.
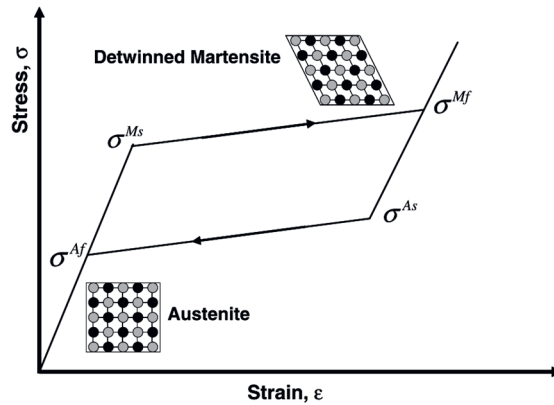
Figure 2.4. Schematic of a superelasticity stress-strain diagram [2].

In certain cases, shape memory alloys (SMAs) can demonstrate repetitive shape changes without any applied mechanical load, but when subjected to a cyclic thermal load (Figure 2.5). This behaviour is known as the two-way shape memory effect (*TWSME*). The *TWSME* can be observed in an SMA material that has undergone repeated thermomechanical cycling along a specific loading path, also referred to as *training*. While the exact underlying mechanism of the TWSME is not yet fully understood, it is widely acknowledged that the formation of oriented dislocation structures during the training process is an essential condition for enabling the reversible shape changes upon thermal cycling [3].
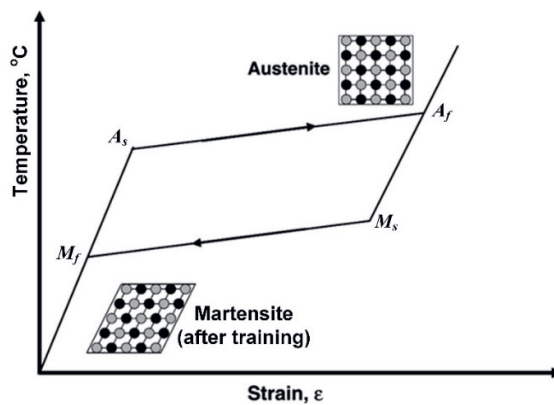
Figure 2.5. Two-way shape memory effect in a temperature-strain diagram [2].

2.1.2. Microstructural features affecting functional properties of NiTi

Depending on specific applications, NiTi shape memory alloys require particular phase transformation temperatures, phase transformation stresses, temperature or stress hysteresis, superelasticity and shape memory effect. These characteristics can be affected by grain sizes, chemical compositions, crystallographic defects and grain orientations. Therefore, to design 4D smart NiTi, it is crucial to understand how theses factors influence NiTi's properties.

2

Grain size

Generally, phase transformation temperatures decrease with decreasing grain sizes since grain boundaries impede the martensitic phase transformation [4]. In addition, grain refinement can effectively improve yield strength of NiTi and inhibits dislocation mobility, which further improves cyclic stability of SE and OWSME [5, 6]. However, due to the lower phase transformation temperatures, applications of NiTi with fine grains are limited below 473 K [7]. It is also worthy to note that the grain size dependent transformation only shows pronounced effect when the grain size is less than 100 nm [4, 6]. As the grain size of NiTi produced by L-PBF is usually in the micrometre ranges [8], the size effect is barely seen in the L-PBF NiTi parts.

Chemical composition

For binary NiTi shape memory alloys, phase transformation temperatures are very sensitive to compositions. With an equiatomic composition (i.e. 50 at. % of Ni and Ti) as the critical point, NiTi shape memory alloys are divided into Ti-rich and Ni-rich alloys. For Ti-rich NiTi, the change of Ni/Ti ratios does not affect the phase transformation temperature. For Ni-rich NiTi, however, phase transformation temperatures decrease with increasing Ni content [9]. In addition, phase transformation hysteresis can be narrower with increasing Ni content for Ni-rich NiTi due to improved crystallographic compatibility [9]. Therefore, the Ni/Ti ratio is an important factor for NiTi shape memory alloys, especially for Ni-rich NiTi.

Local chemical inhomogeneities, including precipitates and impurities also affect the NiTi phase transformation temperatures. For instance, the precipitation of Ni_4Ti_3 results in a decreased Ni/Ti ratio in the NiTi matrix, which increases phase transformation temperatures [10]. Meanwhile, the needle-like Ni_4Ti_3 effectively improve superelasticity in Ni-rich NiTi by increasing its yield strength and inhibiting dislocation movement [10]. However, the

presence of Ti_2Ni (or Ti_2NiO_x) in Ti-rich NiTi does not affect phase transformation temperatures [9]. Impurities, such as oxygen and carbon, mainly take effect by reacting with Ti from NiTi matrix [32]. With the formation of TiO_2 or TiC, the Ni/Ti ratio increase [32]. Hence, decreased phase transformation temperatures are shown in the Ni-rich NiTi.

Depending on specific applications, different elements have been selected for designing NiTi-based shape memory alloys. To obtain the small hysteresis required for actuation applications, Cu is added to replace the Ni site in NiTi to form NiTiCu alloys [11]. Contrary to the small hysteresis in actuators, applications on coupling or fasteners need to have a wide hysteresis, which can be facilitated by Niobium addition can facilitates this characteristic [12]. To meet the demand for high-temperature applications of shape memory alloys, high temperature shape memory alloys (operating temperatures above 473 K) have been developed based on the third element alloying. Additions of Pd, Pt, Hf or Zr increases of phase transformation temperatures in NiTi [13]. However, until now, the high temperature superelasticity has never been reported in binary NiTi alloys. The transformation temperatures for a selection of commercially available and developed shape memory alloys are summarized in the Figure 2.6 [54].
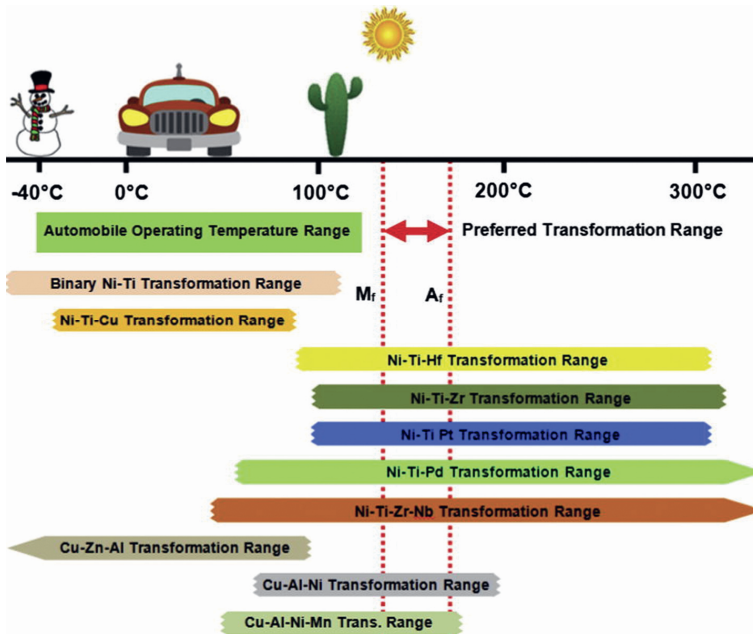
Figure 2.6. The transformation temperatures for a selection of commercially available and developed shape memory alloys [54].

Crystal defects

Crystal defects, such as lattice distortion, dislocations and grain boundaries, can also affect functional properties of NiTi. The intermetallic NiTi B2 phase exhibits some increased solubility for Ni with increasing temperature [14]. In the solid-solution Ni-rich NiTi, the high nickel content in the matrix results in lattice distortion which prevents the martensitic transformation [15]. Dislocations and grain boundaries can act as nucleation sites for the martensitic transformation, affecting the transformation temperatures and stresses [16], thereby affecting the shape memory effect and superelasticity. In addition, due to the accumulation of dislocations induced by cyclic phase transformation, functional degradation occurs in NiTi [17-19].

2

Crystallographic orientation

The crystallographic orientation of NiTi alloys can significantly affect their functional and mechanical properties. The orientation of the martensitic variants can influence the shape memory behaviour. For example, a specific crystallographic orientation may promote the formation of specific variants that contribute to a more pronounced shape memory effect [20, 21]. In terms of superelasticity, the crystallographic orientation can influence the onset of the stress-induced martensitic transformation and the resulting superelastic behaviour [22, 23]. Different orientations may exhibit varying stress-strain responses and transformation temperatures. Furthermore, the crystallographic orientation has an effect on the mechanical properties of NiTi alloys [23], including yield strength, hardness, and fatigue resistance. Depending on the application requirements, specific orientations may be desired to optimize mechanical performance.

2.2. Fabrication of NiTi by conventional methods

The conventional process route of NiTi shape memory alloys consists of several steps. These include melting, hot and cold working, forming and shape memory treatment [24]. For melting NiTi, vacuum induction melting (VIM) and vacuum arc remelting (VAR) are commonly employed methods. VIM utilizes high-frequency induction heating in a vacuum or inert gas, ensuring excellent uniformity of the resulting material. However, impurity contamination from the crucible remains a concern. Since the transformation temperature of NiTi is highly dependent on the nickel concentration, these impurities may locally affect the Ni/Ti ratios. VAR offers the advantage of minimal crucible contamination. By using a water-

cooled copper mould, contact-induced contamination is greatly reduced. However, VAR may result in compositional fluctuations due to partial melting.
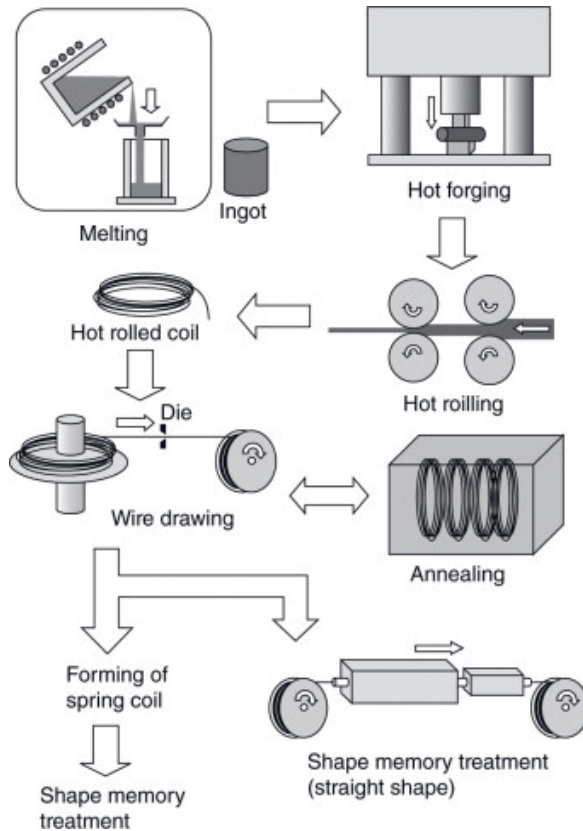
Figure 2.7. Schematic view of the conventional NiTi fabrication process [24].

The as-fabricated NiTi ingots typically exhibit unsatisfactory functional and mechanical properties, which render them unsuitable for direct use in products. Therefore, additional processes such as rolling, drawing, annealing, and aging are necessary [24]. NiTi has poor cold workability, so high-temperature deformation (above 973 K) is commonly employed. However, this poses challenges in fabricating thin wires (<4 mm) due to rapid surface oxidation at such elevated temperatures [25]. Furthermore, inherent segregations and the presence of inclusions in casted NiTi ingots can serve as crack initiation points during processing [26]. While NiTi shape memory alloys can be formed through successive

processes, the range of NiTi products remains largely limited to simple geometries, including sheets, rods, and wires. Additionally, it is important to note that oxidations and contaminations are inherent concerns in each step of conventional NiTi fabrication, further complicating the control of transformation temperatures and functional properties.

2.3. Additively manufactured NiTi

In order to improve design flexibility, reduce material waste and accelerate production cycles, additive manufacturing (AM) of NiTi alloys has attracted researcher's attention in recent years. There are different AM techniques used for NiTi fabrication, such as laser powder bed fusion (L-PBF), electron beam melting [27], directed energy deposition [28], binder jetting [29] and filament extrusion-based additive manufacturing [30]. Among the various additive manufacturing (AM) techniques, Laser Powder Bed Fusion (L-PBF) stands out as particularly appealing for fabricating NiTi due to its ability to produce components with intricated geometrical structures and customizable microstructures on a microscopic scale. Therefore, in this study, the L-PBF technique was selected as the method of choice for developing 4D-printed NiTi.

In LPBF, a laser beam selectively fuses metal powder to the underlying solid material either through full melting (SLM) or partial melting (SLS) as it scans predetermined locations on the powder bed. After each layer is completed, the bed is lowered, a new layer of powder is added, and the process repeats until the object is fully built, following a scanning path determined by the part's geometry and chosen strategy (Figure 2.8 (a)). The main processing parameters include laser power (P), scanning velocity (v), hatch distance (h), layer thickness (t) and beam diameter. From the feedstock point of view, powder size and powder size distribution should be considered. The L-PBF process and these main parameters are schematically shown in Figure 2.8 (b). Due to the complexity of laser beam with material interaction (Figure 2.8 (c)), it is necessary to consider melt pool physics during designing L-PBF processing maps.
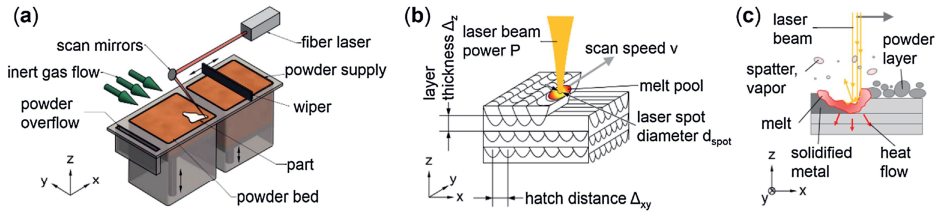
Figure 2.8. (a) The basic layout of an L-PBF machine; (b) a schematic of L-PBF processing parameters; (c) a beam matter interaction [31].

Extensive research on the fabrication of NiTi through L-PBF has been predominantly focused on manipulating the aforementioned processing parameters to achieve defect-free structural components while examining their impact on the microstructure and properties of NiTi. A considerable number of studies have concentrated on optimizing the volumetric energy input (expressed in $E_v = \dfrac{P}{v \times h \times t}$, J/mm^3) to identify suitable process windows for fabricating dense and structurally defect-free NiTi materials [32-34]. In the past, energy densities were primarily optimized using trial and error methods. However, the limited accuracy resulting from the inability to capture melt pool physics renders energy density only to a rough estimation for process parameter optimisation. Consequently, optimized energy densities tend to vary across different research works. For instance, Meier et al. [35] and Haberland et al. [36] reported an optimum processing energy density of 64.1 J/mm^3 for L-PBF NiTi, while Dadbakhsh et al. [37] found that dense L-PBF NiTi alloys can be obtained with an energy density ranging from 111 to 126 J/mm^3. It is important to note that optimizing L-PBF processing windows is a costly and time-consuming endeavour, which presents a challenge in exploring processing parameters across a wide range of design space.

Based on the identified knowledge gap, a physics-based analytical model is introduced in this study for the development of processing maps/windows, specifically for L-PBF of NiTi [38]. This model incorporates melt pool physics and criteria for defect formation, allowing for an extensive exploration of the processing space. The accuracy of this model has been demonstrated through experimental validations conducted under both low power (250 W) [38] and high-power (950 W) [39] laser conditions. A comprehensive presentation of the model and its results can be found in Chapter 3. Subsequently, researchers from Texas A&M University have employed the same methodology to determine optimal processing parameters for near-equiatomic (50.1 at. % Ni) and Ni-rich (50.8 at. % NiTi) NiTi shape memory alloys [40]. By utilizing the optimized L-PBF processing parameters, they have

successfully fabricated fully dense NiTi parts. Furthermore, through subsequent heat treatments applied to the fabricated NiTi alloys, they were able to achieve a shape memory strain of 6% and superelasticity of up to 4% [40].

In addition to studying the L-PBF process, another area of research focuses on comprehending the impact of this process on microstructure, mechanical properties, and functional characteristics. Numerous investigations have extensively explored the influence of various L-PBF processing parameters on microstructures, textures, phase transformation temperatures, superelasticity in Ni-rich NiTi, and shape memory effects in equiatomic NiTi. Soheil et al. [34] investigated the effect of laser power and scanning velocity on microstructure and superelasticity of Ni-rich NiTi and found that a sample fabricated with 100 W laser power and 125 mm/s scanning velocity exhibits a good superelasticity with a 5.7 % recoverable strain in the first cycle [34]. However, the relationships between processing parameters, microstructure, and the mechanisms behind enhanced superelasticity in L-PBF NiTi are still not well understood. Dadbakhsh et al. [37] argued that a low laser power combined with a low scanning speed leads to a pronounced shape memory effect, while high laser power coupled with a high scanning speed results in superelasticity. Other studies have also examined the effect of individual parameter variations, such as scanning velocity [33] and hatch distance [41] on functional properties of NiTi. Due to the existence of knowledge gaps in designing fully dense NiTi, optimized processing parameters differ across studies. Consequently, when discussing the effects of L-PBF processing parameters on microstructures and functional properties of NiTi, different and even conflicting conclusions have been drawn. This controversy makes it challenging to directly apply these conclusions to guide the design of high-performance L-PBF NiTi. Therefore, it is crucial to understand the dominant factors influencing functionalities of NiTi and to leverage these factors during the L-PBF process.

It is important to note that the achievable superelasticity has been primarily reported in L-PBF Ni-rich NiTi rather than in equiatomic or Ti-rich (Ni-lean) NiTi alloys. This observation can be explained by referring to Figure 2.9 [42]. Both the critical stress for martensitic transformation (σ_{SIM}) and the yield strength (σ_y) are temperature dependent. σ_{SIM} increases with temperature, while σ_y decreases with temperature. Consequently, the higher test temperature requires the greater stress to initiate the martensitic phase transformation. As a result, there exists a critical temperature above which superelasticity is absent. Above this temperature, σ_{SIM} surpasses σ_y, leading to plastic deformation. As mentioned in section 2.1.2, the martensite phase transformation temperatures increase with decreasing Ni content. Therefore, equiatomic and Ti-rich NiTi alloys have higher phase transformation temperatures

compared to Ni-rich NiTi. Consequently, the stress required to induce the martensitic transformation is higher for Ti-rich NiTi. However, unlike Ni, Ti has a very limited solid solubility in NiTi [14], which eliminates the possibility of solid strengthening and second phase strengthening induced by subsequent aging treatments in L-PBF NiTi. Additionally, due to a low nucleation rate during solidification, grain sizes in L-PBF-fabricated NiTi typically range from tens to hundreds of micrometres (excluding the low volumetric fraction of sub-grains or nanograins) [14]. This results in less pronounced grain refinement strengthening and lower yield strength. Consequently, achieving superelasticity in Ti-rich or equiatomic NiTi alloys fabricated via L-PBF remains a challenge. Attempts to achieve strengthening through fine grains or second-phase additions are impractical in this context.
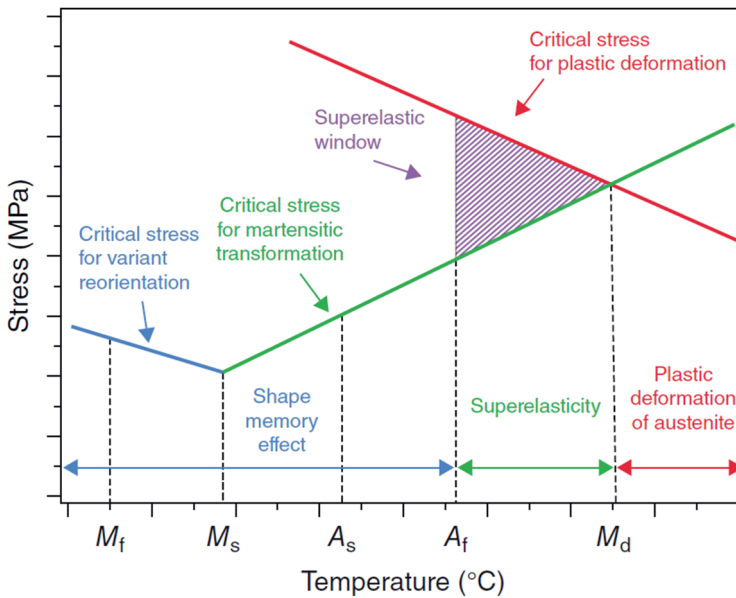
Figure 2.9. A schematic of relationship between critical stress for martensitic transformation and yield strength as function of temperature [42].

As highlighted in section 2.1.2, NiTi exhibits anisotropic functional properties across various crystallographic orientations. Consequently, the functional properties of NiTi can be tailored by manipulating its textures. In particular, the L-PBF technique offers the advantage of allowing the customization of temperature gradients and grain growth rates through the

application of appropriate processing parameters. Since each individual laser bead serves as the fundamental building block of an L-PBF component, the grain morphology and size are determined by each laser melt pool, as depicted in Figure 2.10. Therefore, a knowledge gap emerges regarding how to design L-PBF processing parameters to achieve desired customizable functional properties in NiTi. This knowledge gap can be further divided into two parts. The first part requires understanding the influence of crystallographic orientation on NiTi's functional properties. The second part involves determining how to design textures through L-PBF to achieve the desired functional outcomes.

2
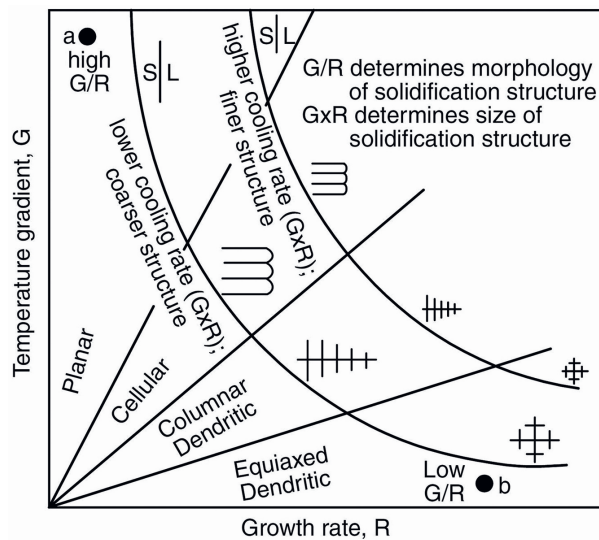
Figure 2.10. Effect of temperature gradient G and growth rate R on the morphology and size of solidification microstructure [44].

Mohammand et al. conducted investigations on the influence of scanning strategy [45] and hatch distance [46] on the texture of L-PBF NiTi. They found that samples with grains oriented along the [001] direction exhibited favorable superelasticity in Ni-rich NiTi. Dadbakhsh et al. [47] explored the impact of "artificial" textures, corresponding to different loading directions, by varying the orientation angles between the building direction and the L-PBF baseplate. They demonstrated that the highest spring back occurred in tests conducted along the building direction, while the highest thermal memory was observed in samples tested along the horizontal direction. However, the mechanism behind the grain orientation-

dependent anisotropy in L-PBF NiTi has not yet been fully elucidated, especially for Ti-Rich NiTi alloys. Furthermore, due to a lack of understanding regarding the melt pool physics in L-PBF NiTi, there is currently no general criterion for designing NiTi textures, and conclusions vary among different studies. Important to note, the fabricated textures in previous studies were relatively weak, with a maximum texture intensity of less than 10, and grains with inconsistent orientations still persisting within the same sample, even when a "strong" texture was claimed.

In order to address this knowledge gap, in this study, molecular dynamics was firstly utilized to predict the deformation behaviour of NiTi with different grain orientations. Subsequently, based on the obtained results concerning critical stresses for martensitic transformation, hardening rates during martensitic transformation, and recoverable abilities, a superelastic index was introduced to guide the selection of NiTi textures. Finally, employing a finite element model, thermal gradients and grain growth rates were obtained, which were utilized to achieve the desired NiTi texture. Through this proposed framework, a [001] fiber-textured L-PBF NiTi was successfully fabricated and showed exceptional superelasticity in Ti-rich NiTi without the need for post-treatments. Detailed findings and results related to this study can be found in Chapter 6.

Due to the complex interactions between the laser and NiTi, as well as non-equilibrium solidification, structural defects such as pores or cracks, crystal defects like dislocations and stacking faults, micro-segregation, and heterogeneous microstructures can be present in L-PBF NiTi. Post-treatments not only offer the opportunity to eliminate these structural defects but also influence the microstructure, residual stress, and precipitates. However, the majority of post-treatment studies have been focused on Ni-rich NiTi [48-50], as the introduction of achievable Ni_4Ti_3 phases through aging enhances superelastic and elastocaloric effects. To date, there have been very limited investigations into the post-treatment responses of L-PBF Ti-rich NiTi [51-53], with only mechanical properties being explored. Consequently, there is still a lack of understanding regarding the impact of heat-treated microstructures on the shape memory effect, both for the one-way and two-way shape memory effect. It should be noted that, despite the adverse effects of cracks and pores on mechanical properties, there is still a lack of research on the elimination of structural defects and the enhancement of mechanical/functional properties in L-PBF NiTi.

2.4. Conclusions

Due to the functionalities of NiTi and advancements in additive manufacturing, the 4D printing of shape memory alloys has attracted significant attention. Specifically, the laser

powder bed fusion (L-PBF) technique has been extensively explored in terms of processing parameter optimization for the fabrication of dense and high-performance 4D printed NiTi. However, there are still knowledge gaps pertaining to the development of comprehensive L-PBF process maps and a thorough understanding of the relationship between NiTi functionalities and L-PBF processing design. These gaps hinder development of 4D printed NiTi, leading to confusion among researchers and engineers when faced with inconsistent findings. Furthermore, the complexity of thermomechanical tests required for assessing the shape memory effect, along with the traditional concept of superelasticity absence in Ti-rich NiTi, has resulted in an emphasis on studies focusing on superelasticity in Ni-rich NiTi rather than Ti-rich NiTi. Consequently, there is a lack of understanding regarding the shape memory effect of L-PBF NiTi. Additionally, post-treatment, which is a crucial aspect of material research, has been primarily employed to investigate its impact on L-PBF NiTi functional properties. However, the effects of post-treatment on the elimination of structural defects and the evolution of microstructures in L-PBF NiTi remain unexplored.

2

References

[1] H. Sehitoglu, R. Hamilton, H.J. Maier, Y. Chumlyakov, Hysteresis in NiTi alloys, J. Phys. IV France 115 (2004) 3-10.

[2] P.K. Kumar, D.C. Lagoudas, Introduction to Shape Memory Alloys, Shape Memory Alloys: Modeling and Engineering Applications, Springer US, Boston, MA, 2008, pp. 1-51.

[3] H. Scherngell, A.C. Kneissl, Training and stability of the intrinsic two-way shape memory effect in Ni-Ti alloys, Scripta Mater. 39(2) (1998) 205-212.

[4] T. Waitz, T. Antretter, F.D. Fischer, H.P. Karnthaler, Size effects on martensitic phase transformations in nanocrystalline NiTi shape memory alloys, Mater. Sci. Technol. 24(8) (2008) 934-940.

[5] A. Ahadi, Q. Sun, Effects of grain size on the rate-dependent thermomechanical responses of nanostructured superelastic NiTi, Acta Mater. 76 (2014) 186-197.

[6] B. Xu, C. Yu, G. Kang, Phase field study on the microscopic mechanism of grain size dependent cyclic degradation of super-elasticity and shape memory effect in nano-polycrystalline NiTi alloys, Int. J. Plast. 145 (2021) 103075.

[7] K.C. Atli, I. Karaman, R.D. Noebe, D. Gaydosh, The effect of training on two-way shape memory effect of binary NiTi and NiTi based ternary high temperature shape memory alloys, Mater. Sci. Eng., A 560 (2013) 653-666.

[8] J.-N. Zhu, E. Borisov, X. Liang, R. Huizenga, A. Popovich, V. Bliznuk, R. Petrov, M. Hermans, V. Popovich, Controlling microstructure evolution and phase transformation behavior in additive manufacturing of nitinol shape memory alloys by tuning hatch distance, J. Mater. Sci. (2022) 1-19.

[9] J. Frenzel, E.P. George, A. Dlouhy, C. Somsen, M.F.X. Wagner, G. Eggeler, Influence of Ni on martensitic phase transformations in NiTi shape memory alloys, Acta Mater. 58(9) (2010) 3444-3458.

[10] K. Otsuka, X. Ren, Physical metallurgy of Ti–Ni-based shape memory alloys, Prog. Mater Sci. 50(5) (2005) 511-678.

[11] J. Cui, Y.S. Chu, O.O. Famodu, Y. Furuya, J. Hattrick-Simpers, R.D. James, A. Ludwig, S. Thienhaus, M. Wuttig, Z. Zhang, I. Takeuchi, Combinatorial search of thermoelastic shape-memory alloys with extremely small hysteresis width, Nat. Mater. 5(4) (2006) 286-290.

[12] C. Ying, J. Hai-chang, R. Li-jian, X. Li, Z. Xin-qing, Mechanical behavior in NiTiNb shape memory alloys with low Nb content, Intermetallics 19(2) (2011) 217-220.

[13] J. Van Humbeeck, Shape memory alloys with high transformation temperatures, Mater. Res. Bull. 47(10) (2012) 2966-2968.

[14] D. Holec, M. Friák, A. Dlouhý, J. Neugebauer, Ab initio study of point defects in NiTi-based alloys, Phys. Rev. B 89(1) (2014) 014110.

[15] M. Karimzadeh, M.R. Aboutalebi, M.T. Salehi, S.M. Abbasi, M. Morakabati, Adjustment of Aging Temperature for Reaching Superelasticity in Highly Ni-Rich Ti-51.5Ni NiTi Shape Memory Alloy, Mater. Manuf. Processes 31(8) (2016) 1014-1021.

[16] T. Simon, A. Kröger, C. Somsen, A. Dlouhy, G. Eggeler, On the multiplication of dislocations during martensitic transformations in NiTi shape memory alloys, Acta Mater. 58(5) (2010) 1850-1860.

[17] W.-N. Hsu, E. Polatidis, M. Šmíd, S. Van Petegem, N. Casati, H. Van Swygenhoven, Deformation and degradation of superelastic NiTi under multiaxial loading, Acta Mater. 167 (2019) 149-158.

[18] T.-x. Zhao, G.-z. Kang, C. Yu, Q.-h. Kan, Experimental investigation of the cyclic degradation of the one-way shape memory effect of NiTi alloys, Int. J. Miner. Metall. Mater. 26(12) (2019) 1539-1550.

[19] I. Ponikarova, S. Belyaev, N. Resnina, Degradation of two-way shape memory effect due to the relaxation of internal oriented stress in NiTi alloy on holding at 640÷700 K, Mech. Mater. 138 (2019) 103174.

[20] Y. Liu, Z.L. Xie, J. Van Humbeeck, L. Delaey, Effect of texture orientation on the martensite deformation of NiTi shape memory alloy sheet, Acta Mater. 47(2) (1999) 645-660.

[21] G. Laplanche, T. Birk, S. Schneider, J. Frenzel, G. Eggeler, Effect of temperature and texture on the reorientation of martensite variants in NiTi shape memory alloys, Acta Mater. 127 (2017) 143-152.

[22] G. Laplanche, J. Pfetzing-Micklich, G. Eggeler, Orientation dependence of stress-induced martensite formation during nanoindentation in NiTi shape memory alloys, Acta Mater. 68 (2014) 19-31.

2

[23] H. Sehitoglu, I. Karaman, R. Anderson, X. Zhang, K. Gall, H.J. Maier, Y. Chumlyakov, Compressive response of NiTi single crystals, Acta Mater. 48(13) (2000) 3311-3326.

[24] T. Nakahata, 4 - Industrial processing of titanium–nickel (Ti–Ni) shape memory alloys (SMAs) to achieve key properties, in: K. Yamauchi, I. Ohkata, K. Tsuchiya, S. Miyazaki (Eds.), Shape Memory and Superelastic Alloys, Woodhead Publishing2011, pp. 53-62.

[25] Z. Lekston, M. Zubko, K. Prusik, D. Stróż, Microstructure, Phase Transformations, and Properties of Hot-Extruded Ni-Rich NiTi Shape Memory Alloy, J. Mater. Eng. Perform. 23(7) (2014) 2362-2367.

[26] J.L. Murray, L.H. Bennett, H. Baker, Binary alloy phase diagrams, ASM International (OH)1986.

[27] Q. Zhou, M.D. Hayat, G. Chen, S. Cai, X. Qu, H. Tang, P. Cao, Selective electron beam melting of NiTi: Microstructure, phase transformation and mechanical properties, Mater. Sci. Eng., A 744 (2019) 290-298.

[28] C. Wang, X.P. Tan, Z. Du, S. Chandra, Z. Sun, C.W.J. Lim, S.B. Tor, C.S. Lim, C.H. Wong, Additive manufacturing of NiTi shape memory alloys using pre-mixed powders, J. Mater. Process. Technol. 271 (2019) 152-161.

[29] R.A. Abdul Kadir, R. Razali, N.H. Mohamad Nor, I. Subuki, M.H. Ismail, The Effect of Particles Shape and Size on Feedstock Flowibility and Chemical content of As-sintered NiTi Alloys, IOP Conference Series: Materials Science and Engineering 358(1) (2018) 012064.

[30] M.A. Wagner, J.L. Ocana-Pujol, A. Hadian, F. Clemens, R. Spolenak, Filament extrusion-based additive manufacturing of NiTi shape memory alloys, Mater. Des. 225 (2023) 111418.

[31] M.C.H. Karg, A. Munk, B. Ahuja, M.V. Backer, J.P. Schmitt, C. Stengel, S.V. Kuryntsev, M. Schmidt, Expanding particle size distribution and morphology of aluminium-silicon powders for Laser Beam Melting by dry coating with silica nanoparticles, J. Mater. Process. Technol. 264 (2019) 155-171.

[32] M. Elahinia, N. Shayesteh Moghaddam, M. Taheri Andani, A. Amerinatanzi, B.A. Bimber, R.F. Hamilton, Fabrication of NiTi through additive manufacturing: A review, Prog. Mater Sci. 83 (2016) 630-663.

[33] Z. Yu, Z. Xu, Y. Guo, R. Xin, R. Liu, C. Jiang, L. Li, Z. Zhang, L. Ren, Study on properties of SLM-NiTi shape memory alloy under the same energy density, J. Mater. Res. Technol. 13 (2021) 241-250.

[34] S. Saedi, N. Shayesteh Moghaddam, A. Amerinatanzi, M. Elahinia, H.E. Karaca, On the effects of selective laser melting process parameters on microstructure and thermomechanical response of Ni-rich NiTi, Acta Mater. 144 (2018) 552-560.

[35] H. Meier, C. Haberland, J. Frenzel, Structural and functional properties of NiTi shape memory alloys produced by selective laser melting, Innovative developments in design and manufacturing: advanced research in virtual and rapid prototyping (2011) 291-296.

[36] C. Haberland, M. Elahinia, J.M. Walker, H. Meier, J. Frenzel, On the development of high quality NiTi shape memory and pseudoelastic parts by additive manufacturing, Smart Mater. Struct. 23(10) (2014) 104002.

[37] S. Dadbakhsh, M. Speirs, J.-P. Kruth, J. Schrooten, J. Luyten, J. Van Humbeeck, Effect of SLM Parameters on Transformation Temperatures of Shape Memory Nickel Titanium Parts, Adv. Eng. Mater. 16(9) (2014) 1140-1146.

[38] J.-N. Zhu, E. Borisov, X. Liang, E. Farber, M.J.M. Hermans, V.A. Popovich, Predictive analytical modelling and experimental validation of processing maps in additive manufacturing of nitinol alloys, Addit. Manuf. 38 (2021) 101802.

[39] J.-N. Zhu, K. Liu, T. Riemslag, F.D. Tichelaar, E. Borisov, X. Yao, A. Popovich, R. Huizenga, M. Hermans, V. Popovich, Achieving superelasticity in additively manufactured Ni-lean NiTi by crystallographic design, Mater. Des. 230 (2023) 111949.

[40] L. Xue, K.C. Atli, S. Picak, C. Zhang, B. Zhang, A. Elwany, R. Arroyave, I. Karaman, Controlling martensitic transformation characteristics in defect-free NiTi shape memory alloys fabricated using laser powder bed fusion and a process optimization framework, Acta Mater. 215 (2021) 117017.

[41] S. Ehsan Saghaian, M. Nematollahi, G. Toker, A. Hinojos, N. Shayesteh Moghaddam, S. Saedi, C.Y. Lu, M. Javad Mahtabi, M.J. Mills, M. Elahinia, H.E. Karaca, Effect of hatch spacing and laser power on microstructure, texture, and thermomechanical properties of laser powder bed fusion (L-PBF) additively manufactured NiTi, Opt. Laser. Technol. 149 (2022) 107680.

[42] A.S. Turabi, S. Saedi, S.M. Saghaian, H.E. Karaca, M.H. Elahinia, Experimental Characterization of Shape Memory Alloys, Shape Memory Alloy Actuators2015, pp. 239-277.

[43] T. Bormann, B. Müller, M. Schinhammer, A. Kessler, P. Thalmann, M. de Wild, Microstructure of selective laser melted nickel–titanium, Mater. Charact. 94 (2014) 189-202.

2

[44] S. Kou, Welding metallurgy, New Jersey, USA 431(446) (2003) 223-225.

[45] K. Safaei, N.T. Andani, B. Poorganji, M.T. Andani, M. Elahinia, Controlling texture of NiTi alloy processed by laser powder bed fusion: Smart build orientation and scanning strategy, Addit. Manuf. Lett. 5 (2023) 100126.

[46] N. Shayesteh Moghaddam, S. Saedi, A. Amerinatanzi, A. Hinojos, A. Ramazani, J. Kundin, M.J. Mills, H. Karaca, M. Elahinia, Achieving superelasticity in additively manufactured NiTi in compression without post-process heat treatment, Sci. Rep. 9(1) (2019) 41.

[47] S. Dadbakhsh, B. Vrancken, J.P. Kruth, J. Luyten, J. Van Humbeeck, Texture and anisotropy in selective laser melting of NiTi alloy, Mater. Sci. Eng., A 650 (2016) 225-232.

[48] S. Saedi, A.S. Turabi, M. Taheri Andani, C. Haberland, H. Karaca, M. Elahinia, The influence of heat treatment on the thermomechanical response of Ni-rich NiTi alloys manufactured by selective laser melting, J. Alloys Compd. 677 (2016) 204-210.

[49] J. Gan, L. Duan, F. Li, Y. Che, Y. Zhou, S. Wen, C. Yan, Effect of laser energy density on the evolution of Ni_4Ti_3 precipitate and property of NiTi shape memory alloys prepared by selective laser melting, J. Alloys Compd. 869 (2021) 159338.

[50] Y. Cao, X. Zhou, D. Cong, H. Zheng, Y. Cao, Z. Nie, Z. Chen, S. Li, N. Xu, Z. Gao, W. Cai, Y. Wang, Large tunable elastocaloric effect in additively manufactured Ni–Ti shape memory alloys, Acta Mater. 194 (2020) 178-189.

[51] J. Fu, Z. Hu, X. Song, W. Zhai, Y. Long, H. Li, M. Fu, Micro selective laser melting of NiTi shape memory alloy: Defects, microstructures and thermal/mechanical properties, Opt. Laser. Technol. 131 (2020) 106374.

[52] S. Li, H. Hassanin, M.M. Attallah, N.J.E. Adkins, K. Essa, The development of TiNi-based negative Poisson's ratio structure using selective laser melting, Acta Mater. 105 (2016) 75-83.

[53] C. Tan, S. Li, K. Essa, P. Jamshidi, K. Zhou, W. Ma, M.M. Attallah, Laser Powder Bed Fusion of Ti-rich TiNi lattice structures: Process optimisation, geometrical integrity, and phase transformations, Int. J. Mach. Tools Manuf. 141 (2019) 19-29.

[54] J. Mohd Jani, M. Leary, A. Subic, M.A. Gibson, A review of shape memory alloy research, applications and opportunities, Mater. Des. 56 (2014) 1078-1113.

3

Development of Processing Maps in Laser Powder Bed Fusion NiTi

Abstract

Before investigating the effect of processing parameters of L-PBF on NiTi's microstructure, textures and functional properties, achieving high-quality and structurally defect-free L-PBF NiTi is a paramount prerequisite. In this chapter, analytical models predicting melt pool dimensions and defect formation criteria were synergistically used to develop processing maps demonstrating boundary conditions for the formation of such defects, as balling, keyhole-induced pores, and lack of fusion. Experimental validation has demonstrated that this method can provide an accurate estimation and guide manufacturability of defect-free NiTi alloys. Moreover, the crack formation phenomena were experimentally analyzed, which showed that a low linear energy density should be chosen to avoid cracks in the optimized process windows. Based on model predictions and experimental calibrations, NiTi samples with a relative density of more than 99 % were successfully fabricated.

3

3.1. Introduction

Recently, laser powder bed fusion (L-PBF), categorized as a technique of additive manufacturing (AM), is increasingly used for fabrication of NiTi shape memory alloys due to high design freedom and the feasibility of tailoring the microstructure and functional properties [1]. This AM method allows to overcome conventional NiTi fabrication problems and produce fully dense as well as porous or complex shaped internal and external structures. However, some defects such as balling, keyhole-induced pores, lack of fusion, and cracks may be introduced, due to not optimized processing parameters. Therefore, in order to take full advantage of L-PBF processing of high-quality parts, it is crucial to avoid defect formation. With the aim of a clear impression about different defects, the representative morphologies of these defects are shown in Figure 3.1.

Above mentioned defects are tightly related to L-PBF processing parameters. Balling (Figure 3.1 (a)) mainly originates from the low laser energy input, which results in insufficient liquid and high surface tension within each laser bead. In this case, balling is introduced by increasing surface tension [2]. The lack of fusion (Figure 3.1 (b)) is either caused by the metallic powders that are not fully melted in the previous deposit layer (due to the lack of energy input) or too large hatch distance and/or layer thickness, which results in an insufficient overlap among the laser tracks [3]. In contrast, keyhole-induced pores (Figure

3.1 (c)) occurs in the high laser energy processing regime, when an unstable keyhole-shaped melt pool collapses on itself, trapping gas bubbles from the vapor depression [4]. Due to rapid melting and rapid solidification under a high local laser energy input, a great temperature gradient and as a result a large residual thermal stress can be created in the fabricated parts. Hence, the high temperature gradient combined with the high residual stress often causes cracking in a fabricated part (Figure 3.1 (d)) [3]. In addition, elemental segregation towards the grain boundaries may result in weak/brittle phases, thereby increasing the chance of micro-cracking [5].
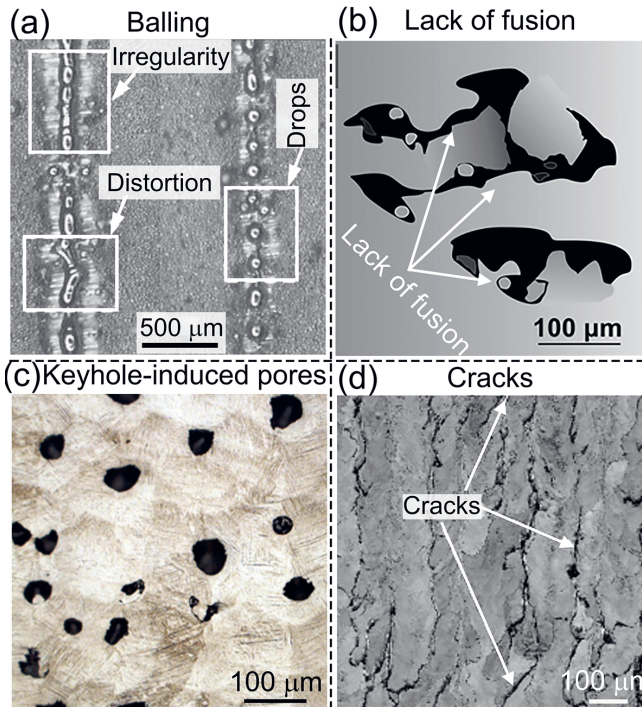
3

Figure 3.1 Different defects in L-PBF parts: (a) balling effect (reproduced with permission from [6] ©2010 Elsevier, The Netherlands.); (b) lack of fusion (reproduced with permission from [7] ©2019 John Wiley and Sons) and (c) keyhole-induced pores (reproduced with permission from [8] ©2016 Elsevier); (d) cracks (reproduced with permission from [9] ©2019 Elsevier).

In order to fabricate defects-free NiTi samples, L-PBF process windows need to be established, which is typically achieved by a time and energy consuming trial and error approach [1, 10, 11]. For convenience, researchers have often introduced the energy density, which combines several main processing parameters, to evaluate the final part quality and have found that defects can indeed be minimized by adjusting the energy density range [12]. As reported by Oliveira *et al.* [13], such two key process parameters as laser power and scanning velocity will affect maximum temperature of melt pools, which dictates the elemental evaporation, the number of molten powders and the melt pool mode (conduction or keyhole mode). In order to control elemental evaporation and eliminate lack of fusion, an appropriate linear energy density (laser power to scanning velocity ratio) should be selected first and then layer thickness/hatch distance should be adjusted accordingly [13]. The linear energy density (E_l) can be represented by the ratio of laser power (P) and scanning velocity (v) and can be expressed as Eq. (3.1):

$$E_l = \frac{P}{v}$$

(3.1).

The E_l is optimized to obtain desirable laser track shape, without the presence of balling and keyhole-induced pores [6, 14-17].

For L-PBF process, the volume energy density (E_v) (the second type) is commonly used to describe the combined effect of main processing parameters (including laser power (P, W), scanning velocity (v, mm/s), hatch distance (h, mm), and layer thickness (t, mm). This energy density quantifies the magnitude of energy input directed to the powder bed, and can be calculated using Eq. (3.2) [3, 18]:

$$E_v = \frac{P}{v \cdot h \cdot t}$$

(3.2).

It has been shown that high quality NiTi parts with a low defect density can be produced by L-PBF [19, 20]. Optimization of L-PBF process parameters for fabrication of NiTi parts has mainly been focused on determining the ideal volumetric energy density. As reported by Haberland *et al.* [21] and Meier *et al.* [22] the volumetric energy density of 85 J/mm^3 is the most optimal. However, Walker *et al.* [10] and Saedi *et al.* [23] argued that the volume energy density of approximately 55.5 J/mm^3 should be rather used to obtain fully dense L-PBF NiTi alloys. In contrast, Dadbakhsh reported that high quality L-PBF NiTi alloys can be fabricated with a high volumetric energy density of 111-126 J/mm^3 [24]. In the above-mentioned energy densities, laser beam diameter ($d_{Laser\ beam}$) and powder size (g_s) were not considered. In order

to develop a more generic definition of energy input during additive manufacturing, Oliveira *et al.* [25] proposed the Eq. (3.3) including all main process parameters:

$$ED = \beta \cdot \frac{P}{v \cdot h \cdot t} \tag{3.3},$$

where β is the dimensionless parameter defined as the ratio of powder grain size (g_s) and the diameter of the laser beam ($d_{Laser\ beam}$). Since the same batch of NiTi powder and constant laser beam size were used in this study, the Eq. (3.2) was rather used to calculate the volumetric energy density.

Prashanth *et al.,* pointed out that the energy density gives only an approximate estimation [26]. Bertoli *et al.*, also argued the limitation of volume energy density for selecting L-PBF processing parameters, due to inability of the energy density approach to capture melt pool physics [12]. In fact, the quality of L-PBF samples depends on the quality of the individual laser track and the overlap between the adjacent laser tracks (melt pool depth-to-layer thickness (D/t) and melt pool width-to-hatch distance (W/h)) [26-28]. Therefore, it is not surprising that consensus is not reached regarding an optimal linear or volumetric energy density as criterion for estimating defect free L-PBF parts. In order to fabricate defect-free L-PBF NiTi samples, melt pool dimensions and their tracks overlapping characteristics should be simultaneously considered.

Determination of processing conditions to achieve defect free components, including the effects of L-PBF processing parameters on the microstructural evolution and functional properties of L-PBF NiTi alloys was previously addressed [19, 23, 29, 30]. However, there is still no systemic investigation on the formation of defects induced by L-PBF processing of NiTi parts. The presence of defects in L-PBF parts is a well-known drawback and a critical issue, which can deteriorate mechanical and functional properties of NiTi alloys [1]. Therefore, it is essential to develop processing maps for L-PBF fabrication of high-quality NiTi parts and to investigate the effect of processing parameters on defect formation.

With the purpose of reducing laborious experimentation and achieving fast estimates of defects formation, the combination of melt pool dimensions based on analytical models and defect formation criteria has been proposed [28, 31-33]. Seede *et al.*, has proven the feasibility of combining the melt pool geometry and geometric criteria for avoiding defects formation (balling, keyhole-induced pores, and lack of fusion) and they have successfully fabricated an ultra-high strength martensitic steel using this method [27]. However, the approach relating melt pool dimensions and defects formation has not yet been applied to NiTi alloys.

In this chapter, the analytic models are utilized to predict melt pool dimensions and L-PBF processing maps are further designed based on the relationship between melt pool dimensions and defect formation criteria. Finally, process parameters for NiTi alloys are optimized and validated by fabrication of defect-free samples. Formation mechanisms of such defects as balling, keyhole-induced pores, lack of fusion and cracks are discussed in relation to L-PBF process parameters. Furthermore, micro-hardness and functional shape memory transformation properties of NiTi alloys fabricated with various L-PBF processing parameters are investigated. Hence, the final aim of this chapter is to systematically understand the defect formation mechanisms and develop processing maps allowing to guide defect-free processability in L-PBF NiTi parts.

3

Nomenclature	
L-PBF	Laser Powder Bed Fusion
AM	Additive Manufacturing
SMA	Shape memory alloy
E_l	Linear energy density, J/mm
E_v	Volumetric energy density, J/mm^3
P	Laser power, W
v	Scanning velocity, mm/s
h	Hatch distance, mm
t	Layer thickness, μm
D	Melt pool depth, μm
W	Melt pool width, μm
L	Melt pool length, μm
ΔH	The specific enthalpy for evaluating keyhole formation, J/m^3
h_s	The enthalpy at melting, J/m^3
A	Laser absorptivity
ρ	The density of material, kg/m^3
C_P	Heat capacity of material, J/(kg·K)
T_m	The melting temperature, K
T_b	The boiling temperature, K

a	The radius of laser beam, μm
σ	The Gaussian laser beam distribution parameter, μm
k	The thermal conductivity of material, W/(m·K)
α	The thermal diffusivity, m^2/s
s	Time, s
ρ_0	The electrical resistivity of the irradiated material, Ω/m
λ	The laser wavelength, nm
EDS	Energy-dispersive X-ray spectroscopy
M_s	Martensite starting temperature, ºC
BR	Building rate of Laser Powder Bed Fusion, mm^3/s
f_w	The overlapping ratio of width between adjacent laser tracks
f_D	The overlapping ratio of height between adjacent laser tracks

3.2. Methodology for L-PBF processing maps

3.2.1. Defects formation and criteria

Balling effect, keyhole-induced pores and lack of fusion are three common types of defects in L-PBF components [34]. Defect formation criteria are mainly based on geometrical considerations and empirically determined values taken from the literature [6, 12, 28, 33, 35]. Apart from these common defects, crack formation may take place when stresses induced by the heat introduced by laser processing exceed the strength of the material.

Balling is caused by laser energy induced non-stable melt pools [36]. Generally, there are two kinds of balling phenomena during L-PBF. Low laser energy results in insufficient liquid and poor wetting, which contributes to the formation of discontinuous scan lines with coarsened ball formation (referred to the first kind of balling phenomenon). High laser scanning speed can cause liquid splashes (micrometer-scaled) onto cohesive powder particles, which is considered as the second kind of balling phenomenon [16]. Due to large irregularities, distortion, and drops in the first kind of balling phenomenon, mechanical properties and the melt pool overlapping can be significantly affected [34]. Therefore, in

particular the first kind of balling should be avoided during L-PBF and will be the main defect considered in this study.

For the formation of first kind of balling formation, Yadroitsev *et al.* have proven that melt pool stability can be evaluated by the ratio of melt pool width (W) to its length (L) [6]. The necessary condition for the melt pool stability is:

$$\frac{\pi W}{L} > \sqrt{\frac{2}{3}} \qquad (3.4).$$

When excess energy is introduced by the laser, melt pools are formed in the keyhole mode [37]. Keyhole-induced pores can be caused by the entrainment of shielding gas, collapse of unstable keyholes, or premature solidification of the top surface [38, 39]. These pores cause stress concentration and have a negative effect on mechanical properties [40, 41]. Formation of keyhole-induced pores is a complex multi-physics process and a numerical framework based on the commercial software FLUENT has been proposed by We *et al.* [42], which successfully interprets the dynamic process of keyhole-induced pore formation and provides a solution to decrease porosity. King *et al.* have demonstrated that the depth of the melt pool has a linear relationship with the normalized enthalpy, and the keyhole-induced pore formation can be estimated by a criterion given in Eq. (3.5) [12]:

$$\frac{\Delta H}{h_s} = \frac{AP}{\pi h_s \sqrt{\alpha v a^3}} > \frac{\pi T_b}{T_m} \qquad (3.5),$$

where $\dfrac{\Delta H}{h_s}$ is the normalized enthalpy, ΔH (J/m³) is the specific enthalpy, $h_s = \rho C_p T_m$ (J/m³, ρ is the density and C_P is the heat capacity (J/(kg·K))) is the enthalpy at melting, A is laser absorptivity, α is the thermal diffusivity (m²/s), v is scanning velocity (mm/s), T_m melting temperature (K), and T_b is boiling temperature (K). In order to evaluate keyhole-induced pore formation during L-PBF, the 1/e radius (the resulting laser beam radius at which energy density is minimized to 1/e at the center of the laser beam) of the laser beam is treated as the laser spot size ($a = \sqrt{2}\sigma$, with s the Gaussian laser beam distribution parameter) [37].

Lack of fusion is a planar defect which occurs when insufficient heat is available to create an appropriate bonding between the newly deposited bead and the prior layers. When laser power, spot size and scanning speed (i.e., linear energy density) are selected, this type of defect results from inappropriate combination of hatch distance (h), layer thickness (t),

melt pool width (W) and depth (D). The hatch distance h is defined as the distance between the centre lines of adjacent tracks (indicated in Figure 3.2 (b)).

In order to avoid lack of fusion, a maximum hatch distance should be adjusted to ensure the good joining between the adjacent tracks [25]. The criteria for the maximum hatch distance have been proposed from geometric, energetic and thermal aspects [25]. In this work geometric criterion was used for its simplistic calculations, allowing to build relationships between process parameters and melt pool dimensions.

As proposed by Seede *et al.* [28], lack of fusion may occur for melt pools featuring parabola-shaped cross-sections, when h exceeds the maximum hatch distance h_{max}. The h_{max} can be calculated based on Eq. (3.6):

$$h_{max} = W\sqrt{1 - \frac{t}{(t+D)}} \qquad (3.6).$$

Therefore, the criterion for lack of fusion can be described by the Eq. (3.7), which is derived from Eq. (3.6):

$$(\frac{h}{W})^2 + \frac{t}{(t+D)} \geq 1 \qquad (3.7).$$

3.2.2. Melt pool dimension calculations.

As stated above, it is necessary to obtain melt pool dimensions for the evaluation of defects formation. Compared with finite-element model (FEM), analytical solutions are considered as simple and computationally inexpensive methods for predicting melt pool dimensions [28, 33, 43]. Eagar-Tsai (E-T) model has been proven to be an effective analytical model, which can provide a reasonable accurate estimation of the melt pool width and length [28, 31, 32, 44]. In the Eagar-Tsai model [45], a Gaussian distributed heat source is assumed, allowing to solve the differential equation analytically to obtain the temperature distribution and hence to achieve the melt pool profile. Based on the Eagar-Tsai model, the analytical form is re-derived as Eq. (3.8):

$$T = \frac{AP}{\pi k}\sqrt{\frac{\alpha}{\pi}}\int_0^{\infty} \frac{\exp[-\frac{z^2}{4\alpha s} - \frac{y^2+(x-vs)^2}{(4\alpha s + a_1^2)}]}{(4\alpha s + a_1^2)\sqrt{s}}ds \qquad (3.8),$$

where k is the thermal conductivity (W/(m·K)), α is the thermal diffusivity (m²/s), s is the time (s), a_1 is the radius of beam size, σ is the distribution parameter of the Gaussian distributed heat source. The scanning direction of the laser beam is along x and y in the transverse coordinate, and z is directed normal to the substrate surface.

For the convenience of the melt pool dimension calculations, the Eq. (3.8) can be put in dimensionless form by using the following dimensionless variables:

$x_N = \dfrac{x}{a_1}; y_N = \dfrac{y}{a_1}; z_N = \dfrac{z}{\sqrt{(\dfrac{\alpha a_1}{v})}}$ [32]. Furthermore, the parameter g, which is independent

of laser and material parameters, is introduced to describe the effect of scanning speed (v) on the temperature distribution [44]. Therefore, dimensionless variables and temperature distribution are expressed as follows in Eqs. (3.9) and (3.10) [44]:

$$T = T_S g(x_N, y_N, z_N, v) \qquad (3.9),$$

$$g(x_N, y_N, z_N, v) = \int_0^\infty \frac{\exp[-\dfrac{z_N^2}{4\tau} - \dfrac{y_N^2 + (x_N - \tau)^2}{(\dfrac{\alpha\tau}{va_1} + 1)}]}{(\dfrac{\alpha\tau}{va_1} + 1)\sqrt{\tau}} d\tau \qquad (3.10),$$

where, $T_S = \dfrac{AP}{\pi\rho C_p \sqrt{\alpha v a_1^3}}$ is the surface temperature, while the melt pool contour is

determined from the condition that T equals the melting point of the material. $T = T_m$ (T_m

is the melting point of material) and $\tau = \dfrac{s}{(\dfrac{a_1}{v})}$ is the dimensionless time. The readers were

encouraged to refer to the original study for more details about the development of thermal analytical solution [44].

Due to the fact that the E-T model is designed to investigate heat conduction-mode laser melting [31], the depth of melt pool will be underestimated by the change of the melt pool shape from the conduction mode melting to the keyhole mode melting [46]. An alternative model proposed by Gladush and Smurov, i.e. the G-S model, [35] is a good candidate for predicting melt pool depth, since it was derived for investigating keyhole welding, which is

consistent with the purpose of this work. Melt pool depth (D) can be described as a function of laser power (P), scanning speed (v) and laser beam size (a_1) (as shown in Eq. (3.11)):

$$D = \frac{AP}{2\pi k T_b} \ln\left(\frac{a_1 + \alpha/v}{a_1}\right) \tag{3.11},$$

where A is laser absorptivity, k is the thermal conductivity (W/(m·K)), T_b is the boiling temperature (K), and α is the thermal diffusivity (m^2/s).

3.2.3. Model parameters

Due to the preheating from neighboring laser tracks during L-PBF, the temperature and phase dependence of physical parameters should be considered. As reported by Ma *et al.* [30], the temperature of neighboring tracks can reach near the melting point during fabrication of NiTi parts. Therefore, temperature dependent properties at 1500 K (near the melting point), such as density and thermal diffusivity, were used in this study. Due to the lack of the experimental density data for NiTi, the density as a function of temperature is calculated by using Thermo-Calc software (Version 2020a) based on TCHEA2 (High Entropy Alloys version 2.1) database. Considering the fact that the crystal structure of the NiTi alloy is austenitic at high temperature [47], the heat capacity of austenitic NiTi is used in this study.

According to Drude's theory [27], the laser absorptivity A used in L-PBF can be estimated by using empirical Eq. (3.12) [27]:

$$A = 0.365\sqrt{\left(\frac{\rho_0}{\lambda}\right)} \tag{3.12},$$

where ρ_0 (Ω/m) is the electrical resistivity of the irradiated material and λ (nm) is the laser wavelength. Based on Eq. (3.12), the laser absorptivity of NiTi is 0.32, which is similar with that of Ti ($A_{Ti} = 0.36$) [53] and Ni-based alloys ($A_{Inconel\ 718} = 0.38$) [54]. NiTi properties and laser-related parameters are listed in Table 3.1.

Table 3.1 NiTi thermophysical properties and laser parameters.

Parameters	Values
Density (kg/m^3), ρ	6100
Heat capacity (J/(kg·K)), C_p	510 (austenite) [48]
Thermal conductivity (W/(m·K)), k	4.4 [49]
Thermal diffusivity (m^2/s), a	8e-6 [50]
Electrical resistivity (Ω/m), ρ_0	8.2e-8 (austenite) [51]
Melting temperature (K), T_m	1583
Boiling temperature (K), T_b	3033 [52]
Laser beam radius (μm), a_1	40
Laser wavelength (nm), λ	1070
Absorptivity, A	0.32

3.2.4. L-PBF fabrication

The NiTi samples were fabricated via L-PBF process by an Aconity3D Midi (Aconity3D GmbH, Germany) machine equipped with a laser source featuring a maximum power of 1000 W and a beam with a Gaussian distribution. Gas atomized NiTi powder (TLS Technik GmbH, Bitterfeld, Germany) with ~50.0 at. % content of Ni and spherical particles with D-values of 23 μm (D$_{10}$), 40 μm (D$_{50}$), 67 μm (D$_{90}$) was used in this study (Figure 3.2 (a)). Chemical composition of NiTi powder was measured by a combination of Energy-dispersive X-ray spectroscopy (EDS), Inductively Coupled Plasma Optical Emission Spectroscopy (ICP-EOS) and LECO combustion analysis and was confirmed to be Ni50.0 (at. %)–Ti with negligible impurity content (C, N, and O).
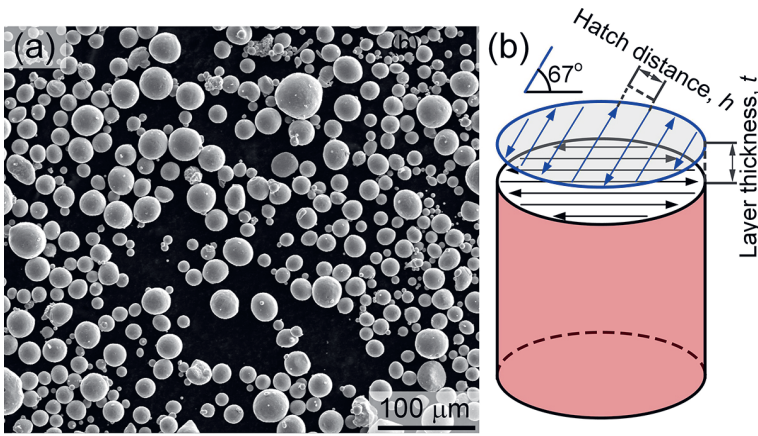
3

Figure 3.2. (a) SEM of the commercial NiTi powder and (b) the schematic of the applied L-PBF scanning strategy.

Table 3.2 L-PBF process parameters used for the fabrication A group NiTi samples.

	A1	A2	A3	A4	A5	A6	A7	A8	A9
Laser Power (W)	250	250	250	250	250	250	250	250	250
Scan velocity (mm/s)	1250	1250	1250	800	800	500	600	500	800
Hatch distance (µm)	100	120	140	120	140	140	140	120	187
Layer thickness (µm)	30	30	30	30	30	60	30	75	30
Laser beam diameter (µm)	80	80	80	80	80	80	80	80	80
Volumetric energy density (J/mm³)	67	56	48	87	74	60	99	56	56

As shown in Figure 3.2 (b), a bidirectional scanning strategy was conducted in each layer and a 67° scanning rotation between the adjacent layers was applied. When altering the scanning direction from layer to layer by 67°, it results in an increase of intertwined grain boundaries and thus inhibits the initiation and propagation of cracks [9]. L-PBF cylindrical samples (diameter of 6 mm and height of 20 mm) were fabricated on a NiTi base plate in Argon protection atmosphere. The volume energy density (E_v) was defined by Eq. (3.2). In this study, the accuracy of the developed model was validated by employing two different combinations of laser power and beam diameter: 250W - 80 µm and 950W - 500 µm. The variations in hatch distance, layer thickness, and scan velocity were considered. The samples

fabricated using the 250W - 80 μm combination were assigned to group A, while the samples fabricated using the 950W - 500 μm combination belonged to group B. The corresponding processing parameters are presented in Table 3.2 and Table 3.3, respectively. Processing conditions of the 250W - 80 μm and 950W - 500 μm are named as high and low laser power condition hereafter.

Table 3.3 L-PBF process parameters used for the fabrication of B group NiTi samples.

	B1	B2	B3	B4
Laser Power (W)	950	950	950	950
Scan velocity (mm/s)	2200	1900	1200	1060
Hatch distance (μm)	180	180	180	180
Layer thickness (μm)	50	50	50	50
Laser beam diameter (μm)	500	500	500	500
Volumetric energy density (J/mm^3)	48	56	88	100

3.2.5. Characterization

The relative density of the fabricated L-PBF samples was determined by the Archimedes method, using a theoretical maximum density of 6.45 kg/m^3. Samples for metallographic examination were ground, polished and etched in a reagent of HF (3.2 vol. %) + HNO$_3$ (14.1 vol. %) + H$_2$O (82.7 vol.%) for ~ 50−70 s [23]. The etched microstructure was examined using an optical microscope (OM, Keyence VHX-5000) and a scanning electron microscope (SEM, JEOL JSM 6500F) equipped with dispersive X-ray spectroscopy (EDS) analyser. Phase transformation behaviour was analysed by a differential scanning calorimetry (DSC, Perkin Elmer DSC 8000) with a cooling and heating rate of 10 K/min over a temperature range of 213 to 473 K. A sample of approximately 100 mg was sliced from the middle of L-PBF-NiTi samples for DSC analysis. Vickers hardness measurements were performed under the test force 0.3 kgf (further denoted as HV0.3) using an Automatic MicroHardness Tester (Buehler Vickers). In order to measure Ni content of bulk samples, at least 7 rectangular zones (180×250 μm^2, at 500× magnification) were measured by EDS (15 kV, beam current medium 13) on polished cross-sections and error bars were determined by calculating the standard deviation based on EDS results.

3.3. Results and Discussion

3.3.1. Analytical prediction of the melt pool dimensions

By solving Eqs. (3.9) and (3.10), temperature contour can be plotted by using dimensionless (normalized) term *g*. An example of a temperature contour plot and the melt pool boundary (indicated by the black line) with the heat input resulting from 250 W laser power and 1250 mm/s scanning velocity is shown in Figure 3.3 (a).
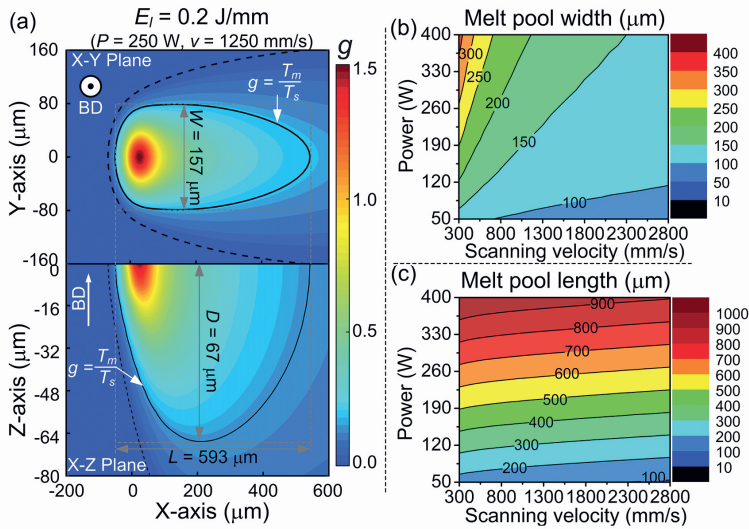

Figure 3.3. (a) Cross-sectional views (X-Y and X-Z planes) of the temperature contour (plotted by *g*) and the melt pool boundary (indicated by the black solid line, where $g = T_m/T_s$) from the E-T model; (b) melt pool width and (c) length as the function of the laser power and scanning velocity.

Based on the thermal results from the analytical solution of the E-T model, melt pool dimensions can be calculated. The melt pool width and length as functions of laser power (*P*) and scanning speed (*v*) are shown in Figure 3.3 (b) and (c), respectively. It can be seen that the melt pool width and length increase with increasing laser power or decreasing scanning speed (Figure 3.3 (b) and (c)), which means that both *P* and *v* are parameters significantly affecting the melt pool configuration and the thermal field within each laser track.

To verify the accuracy of the E-T model, experimental validations were carried out. Figure 3.4 (a) illustrates the applicability of E-T model for predicting melt pool widths, while Figures 3.4 (e)–(h) shows experimental results of the melt pool widths, which, as can be seen, match well with the values obtained from the analytical solutions. The minimum and maximum prediction error of melt pool width are ~3% and ~9%, respectively, which indicates reasonable accuracy of E-T model for predicting melt pool widths.

Figure 3.4 (b) shows that the E-T model (a red dashed line with solid rod symbol) underestimates the melt pool depth, which is consistent with results reported in the literature [28, 31, 32]. Since The Eagar-Tsai model is designed to describe conduction-mode laser melting and assumes constant thermophysical properties (ρ, C_P and k), it hard to obtain accurate melt pool depth estimation if L-PBF change from heat conduction to keyhole-mode, characteristic to the high energy input condition.

3

In order to achieve reasonably accurate estimations of the melt pool depth, Eq. (11) proposed by Gladush and Smurov (G-S model) for keyhole welding is used in this study. As shown in Figure 3.4 (b), the G-S model (a violet dashed line with open circles) has a better accuracy than the E-T model for predicting melt pool depths. The maximum deviation between the depth predicted by G-S model and experimentally measured depth is ~23 %, which is substantially lower than ~50 % deviation found for the E-T predicted depth. Therefore, the G-S model is further used for predicting melt pool depths. Melt pool depths predicted by the G-S model with various laser power and scanning velocity are shown in Figure 3.4 (c).

The criterion for keyhole-induced pore formation is determined by the normalized enthalpy $\dfrac{\Delta H}{h_s}$. The process map for keyhole-induced pore formation, based on Eq. (3.5) is presented in Figure 3.4 (d). As shown in Figure 3.4 (d), NiTi samples may exhibit keyhole-induced pore for scanning velocities up to 500 mm/s in a condition of constant laser power of 250 W, which is consistent with the experimental results (Figure 3.4 (h), keyhole-induced pores are marked by black dashed circles). It should be noted, that although keyhole-induced pore formation with its physical complexity is hard to be precisely described by the simple analytical equation (Eq. (3.5)), the approach by evaluating normalized enthalpy appears to be a simple and a rather good estimation.

Due to the difficulty of measuring the melt pool length and a lack of available data from the literature, it is hard to conduct a direct comparison between calculated and experimental

results. As reported by Prompoppatum *et al.* [32], if only room temperature thermal properties are used in the E-T model and there is a positive correlation between temperature and thermal diffusivity, the melt pool length will be overestimated. They proposed a correction factor to compensate for the lack of temperature-dependent properties and thus the prediction accuracy of melt pool lengths was improved [32]. Following a similar strategy and considering the fact that powder surrounding a melt pool has the temperature close to the melting point [30], high temperature (1500 K near the melting point) thermal properties of NiTi were used in the E-T model to improve the prediction accuracy. The validation of the melt pool length is discussed further in Section 3.3, in combination with the balling phenomena.

3
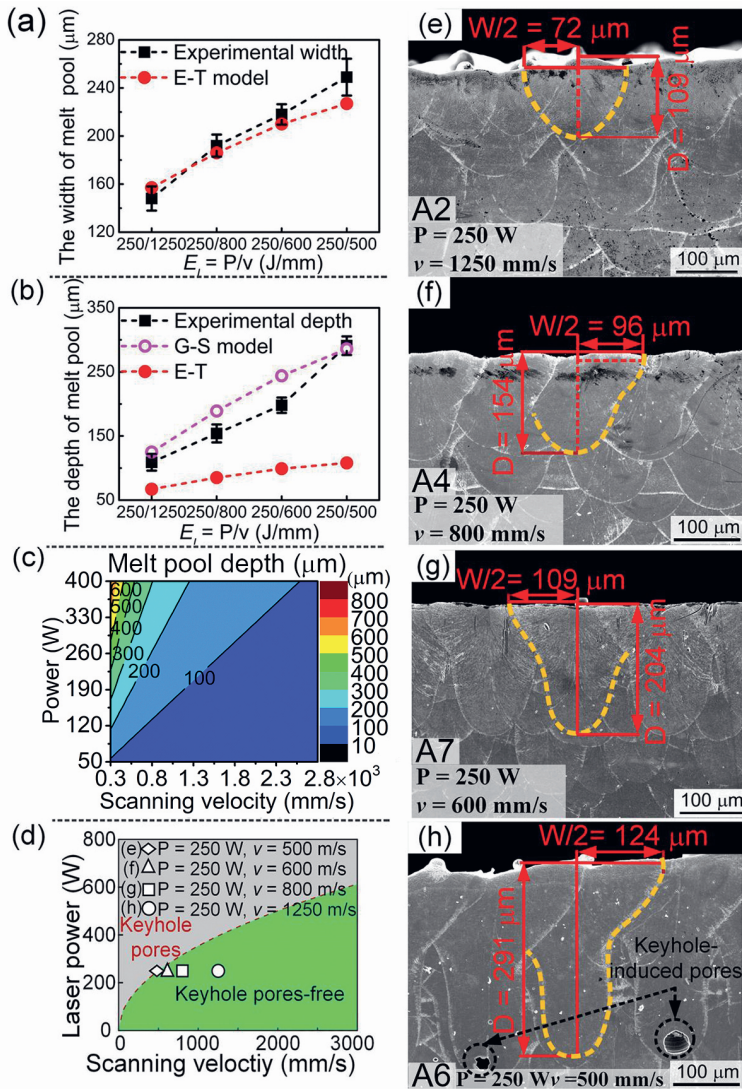
Figure 3.4. Comparison of the experimentally measured melt pools (a) widths and (b) depths between the E-T model and the G-S model predictions; (c) melt pool depths as a function of the laser power and scanning velocities based on the G-S model; (d) the process map for keyhole-induced pore formation; (e)-(h) cross-sectional L-PBF NiTi fabricated by the same laser power and different scanning velocities showing melt pool characteristics

55

3.3.2. Processing maps and experimental validation

As stated above, the analytical approaches can provide a reasonably accurate estimation of the melt pool dimension and the occurrence of keyholing. Therefore, processing maps for the L-PBF of NiTi alloys can be drawn by combining the defect formation criteria introduced in Section 3.1 and the melt pool dimensions predicted by the analytical approaches.

Processing maps with four linear energy density conditions are depicted in Figure 3.5. The experimental results of NiTi samples fabricated with various processing conditions, see Table 3.2, are indicated in the Figure 3.5.

According to these processing windows (Figure 3.5), the laser power should be in the range of 50-320 W to allow the fabrication of fully dense NiTi parts. Apart from creating defect free parts, the build rate (BR) should also be considered. The build rate (BR) can be expressed as:

$$BR = v \cdot h \cdot t \tag{3.13}.$$

Based on Eq. (3.2), *i.e.,* the volumetric energy density (E_v), a higher BR can be achieved when using a higher laser power for the condition of a constant E_v. Therefore, with respect to the balance of the high building rate and process reliability, a laser power of 250 W is chosen in this study.

Based on the defect criteria introduced in Section 3.1, both keyhole-induced pores and balling mainly depend on the heat-input related parameters (laser power, scanning velocity and laser beam size) and thermal physical properties. For NiTi and constant laser beam diameter of 80 µm, regimes of keyhole-induced pores and balling can be determined by laser power and scanning velocity. Hence, there are fixed regimes for keyhole-induced pores (the upper-left corner) and balling (the upper-right corner), as shown in Figure 3.5.

The lack of fusion is determined by melt pool dimensions (related to laser power and scanning velocity), hatch distance and layer thickness. Therefore, these parameters can be used to determine lack of fusion boundaries in the processing maps (as can be seen in Figure 3.5).

Figure 3.5 (a) shows that the fully dense region has narrowed with increasing hatch distance (from 100 to 140 µm) while keeping a constant layer thickness of 30 µm. Samples A1, A2 and A3 share the same position in the processing map (Figure 3.5 (a)), since these were fabricated with the same laser power of 250 W and a scanning velocity of 1250 mm/s.

Sample A3 (circled out in the solid green region, Figure 3.5 (a)) is near the boundaries of balling and lack of fusion.

Figure 3.5 (b) shows a processing map of samples A4, A5 and A9 with varying hatch distance from 120 to 187 μm and a lower scanning velocity of 800 mm/s (compare to 1250 mm/s in Figure 3.5 (a)). As can be seen, the fully dense area decreases with increasing hatch distance. The sample A9 falls into the lack of fusion regime (solid green region surrounded by the black dash line in Figure 3.5 (b)).

As shown in Figure 3.5 (c), boundaries for fully dense region can be determined (the solid green region) once hatch distance and layer thickness are selected. Positions of A3, A5 and A7 depend on the applied linear energy densities.
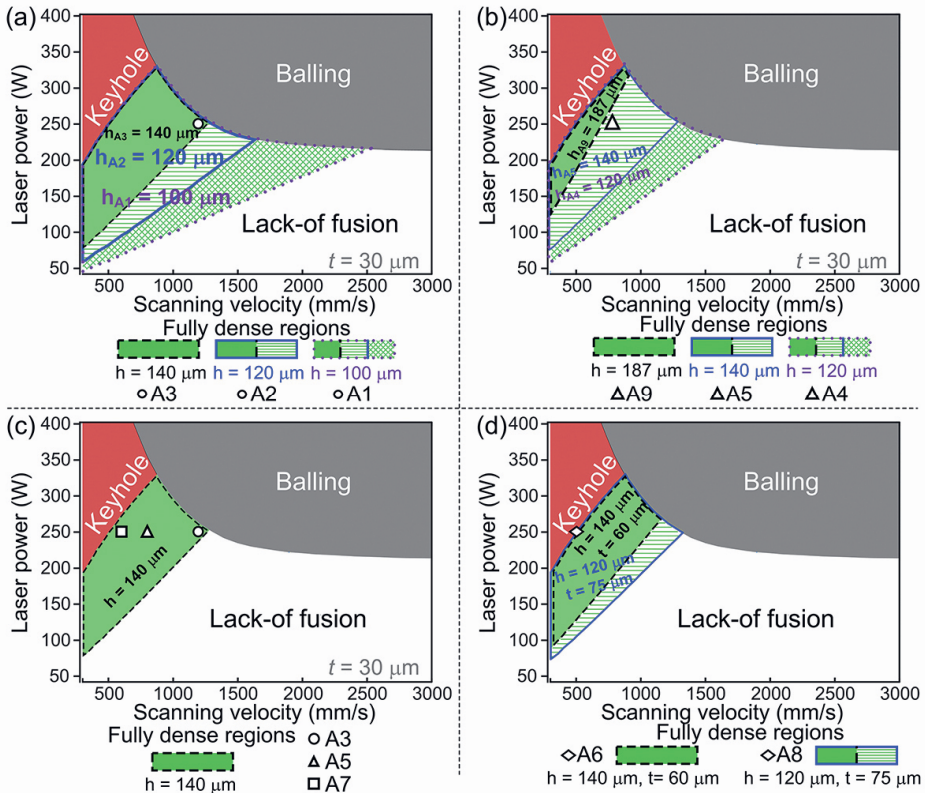
3

Figure 3.5. Processing maps for L-PBF of NiTi featuring locations of experimental data of samples fabricated with various processing parameters.

A processing map corresponding to simultaneous changes of hatch distance and layer thickness is shown in Figure 3.5 (d). The fully dense region of h =120 and t = 75 μm is indicated by the blue line (Figure 3.5 (d)) and that of h = 140 and t = 60 μm is indicated by the black dash line (Figure 3.5 (d)). Samples A6 and A8 (sharing the same position in the processing map and marked by a white diamond) are fabricated with a high linear energy density 250/500 (J/mm) and are both susceptible to keyhole-induced pore formation (Figure 3.5 (d)).

In order to quantitatively evaluate densification of L-PBF NiTi parts, the threshold of 99 % relative density is defined as a good densification level [55]. As seen in Figure 3.6, good densifications can be obtained in sample A2 and A8 with E_v of 56 J/mm^3 and A7 with E_v of 99 J/mm^3. These results demonstrate that the volumetric energy density can act as a rough guide in fabrication of dense NiTi parts. However, the suitability of E_v as a design parameter to describe L-PBF is limited due to its low accuracy on estimating relative density of L-PBF parts.
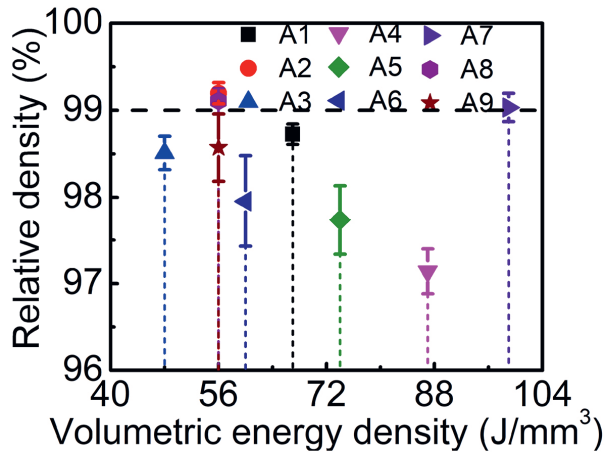

Figure 3.6. Measured relative density of L-PBF NiTi samples, fabricated with various processing parameters as a function of volume energy input (the threshold of 99 % relative density is marked by the black dash line for defining a good densification level).

3.3.2.1. Characterization of balling phenomena

Balling is a typical L-PBF process defect [1, 16]. Since L-PBF is carried out line-by-line and layer-by-layer. The balling may lead to discontinuities in the laser beads and may hinder the uniform deposition of subsequent powder layers [16]. Therefore, the factors affecting balling should be carefully considered for process optimization.

Figure 3.7 shows the top surface of samples A1–A3 produced with the same linear energy density (250/1250 J/mm), but with various hatch distances. Laser tracks with small-sized balling and small gaps can be seen in A3 (with a hatch distance of 140 µm) (Figure 3.7 (c)), which means that the linear energy density of 250/1250 (J/mm) and hatch distance of 140 µm is near the boundary of balling initiation. The result is also consistent with the prediction (Figure 3.5 (a)). Thus, the feasibility of analytical melt pool dimension prediction on the estimation of balling effect is justified.
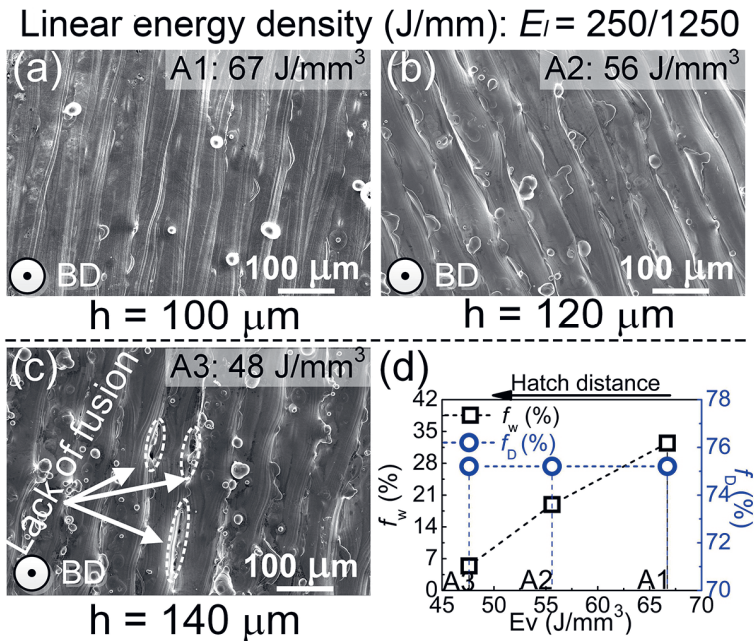
3

Figure 3.7. SEM micrographs of the top surfaces of L-PBF NiTi fabricated with the same linear energy of 250/1250 J/mm, but various hatch distances: (a) 100, (b) 120 and (c) 140 µm, (d) overlapping ratios of the melt pool width and height for samples A1–A3.

As shown in Figure 3.7, balling effect can be well alleviated via narrowing the hatch distance. The balling effect in samples A3 can be attributed to the constant laser power (250 W) combined with a high scanning velocity (1250 mm/s, compared with other samples A4–A9), causing melt pool instabilities, where the melt tends to have a large surface energy. Hence, rough laser tracks consisting of a number of small-sized balls are formed. Due to increased overlapping ratios (Figure 3.7 (d)), induced by reducing hatch distance, energy input increases and re-melt of previous tracks is enhanced, which can decrease the viscosity of the melt (the overlapping ratio of width is defined as $f_w = \dfrac{W - h}{W}$ and the overlapping ratio of height is defined as $f_D = \dfrac{D - t}{D}$, where W is the width of melt pool, h is hatch distance, D is the height of melt pool and t is the layer thickness). Therefore, the balling tendency can be decreased with narrowing the hatch distance.
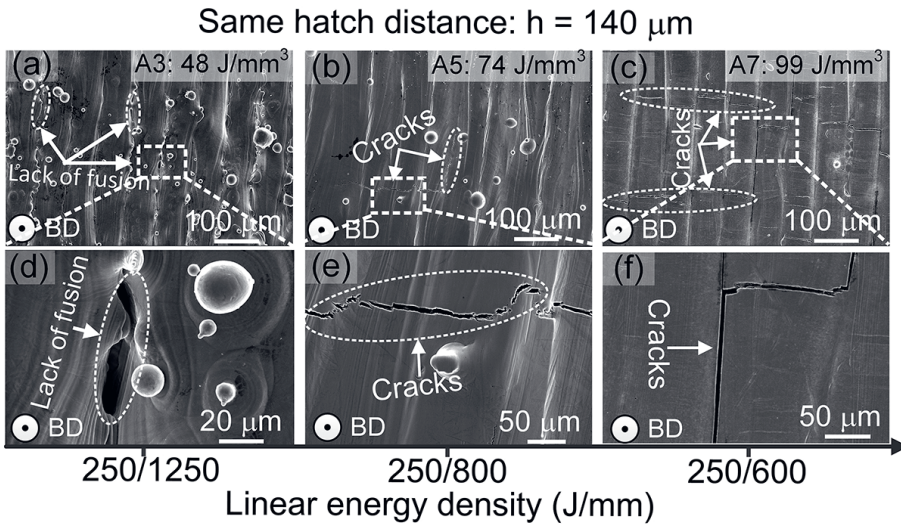

Figure 3.8. SEM images of the top surfaces of L-PBF NiTi alloys fabricated with various linear energy densities but a constant hatch distance 140 µm: (a) and (d) sample A3 with E_l = 250/1250 (J/mm); (b) and (e) sample A5 with E_l= 250/800 (J/mm); (c) and (f) sample A7 with E_l= 250/600 (J/mm).

For a better understanding of balling phenomena in L-PBF NiTi alloys, samples with various hatch distance (Figure 3.5 (b)) and linear energy density (Figure 3.5 (c)) were fabricated. As illustrated in the predicted process map (Figure 3.5 (b)), it is possible to avoid keyhole-induced pores and balling by using processing parameters with a laser power of 250 W and scanning velocity of 800 mm/s. As expected, with increasing the linear energy density, enabled by decreasing scanning velocity (Figures 3.8 (a)–(f)), continuous and balling-free laser tracks are produced, which is due to a sufficient liquid formation and a decrease of the melt viscosity [16]. It should however be noted that, although balling phenomena was eliminated, the cracks are introduced. Similar with the effect of hatch distance on balling phenomena of NiTi samples fabricated by linear energy density of 250/1250 (J/mm), the balling effect is also alleviated with decreasing hatch distance in NiTi samples fabricated by 250/800 (J/mm) (Figures 3.9 (a)–(f)).

3
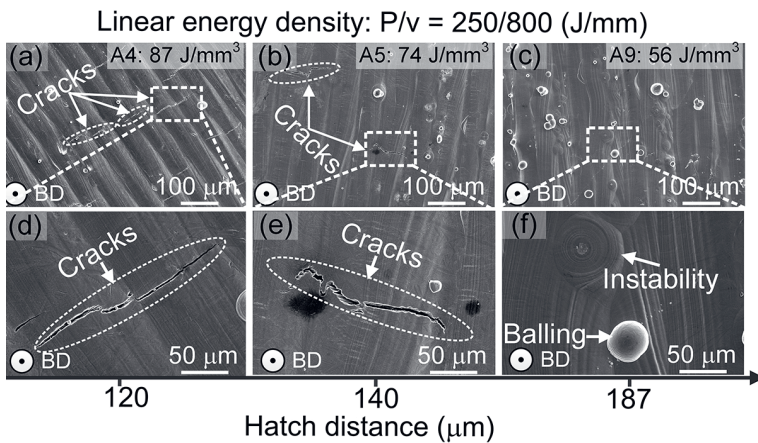
Figure 3.9. SEM images of the top surfaces of L-PBF NiTi alloys fabricated with various hatch distances but a constant linear energy density of 250/800 (J/mm): (a) and (d) A4 with h = 120 μm; (b) and (e) A5 with h = 140 μm; (c) and (f) A9 with h = 187 μm.

However, there are still cracks in the A4 sample (with narrowing hatch distance to 120 at E_l of 250/800 (J/mm), Figures 3.9 (a) and (d)). Considering the serious negative effect of cracks in AM parts, especially with respect to limiting functional properties, fatigue life and

fracture toughness, cracks should be always avoided [1, 56]. Therefore, the linear energy density E_l of 250/1250 (J/mm) was optimized in the current work and balling were controlled by narrowing the hatch distance. Crack formation in L-PBF NiTi parts will be discussed in Section 3.6.

3.3.2.2. Keyhole-induced pores

In section 3.1, it has been demonstrated and validated that keyhole-induced pores form in the condition of high linear energy density (i.e. a high laser power and a low scanning velocity). In order to estimate the effect of hatch distance and layer thickness on keyhole-induced pores, cylindrical NiTi samples were fabricated with various hatch distance and layer thickness, but a constant linear energy density of 250/500 J/mm (in the keyhole-induced pores region, Figure 3.5 (d)).

It can be seen that keyhole-induced pores and cracks are presented in sample A8 with hatch distance of 120 μm and layer thickness of 75 μm (Figures 3.10 (a), (c) and (e)). With increasing hatch distance to 140 μm and decreasing layer thickness to 60 μm, keyhole-induced pores still can be observed in sample A6 (Figures 3.10 (d) and (f)). Hence, it is demonstrated that heat input related parameters (laser power and scanning velocity) are main factors affecting keyhole-induced pore formation and thus should be carefully chosen. Moreover, although the degree of cracking is reduced, the balling phenomenon is exacerbated in sample A6 (Figure 3.10 (b)), which indicates the importance of hatch distance on cracks formation and balling effect. Based on characterization of samples A6 and A8, the reliability of processing map for predicting keyhole-induced pores is thus further confirmed (samples A6 and A8 in the keyhole-induced pore regime, Figure 3.5 (d)). Therefore, keyhole-induced pores are mainly dependent on heat input related parameters (laser power and scanning velocity), which should be chosen carefully to avoid introducing an excessive energy in melt pools.
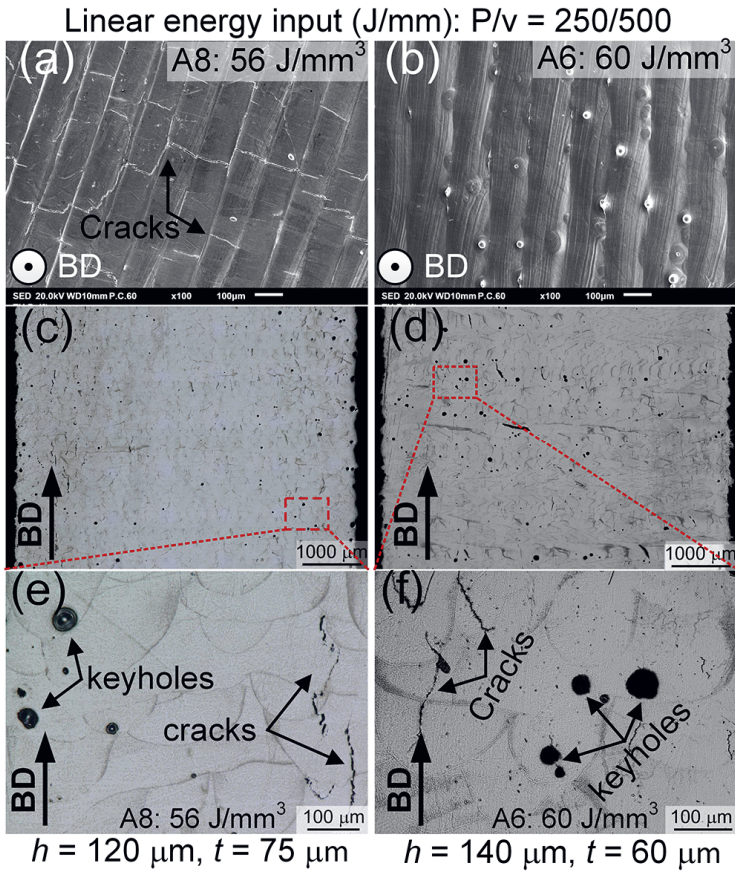
Figure 3.10. SEM of L-PBF NiTi alloys fabricated with the same linear energy level of 250/500 J/mm, but various hatch distance and layer thickness: (a), (c) and (e) h=120 μm, t=75 μm and (b), (d) and (f) h=140 μm, t=60 μm.

3.3.2.3. Lack of fusion

As can be seen in Figure 3.7 (c) and Figures 3.8 (a) and (d), lack of fusion occurs in sample A3 fabricated with processing parameters of $P = 250$ W, $v = 1250$ mm/s, $h = 140$ μm and $t = 30$ μm, which is consistent with the predicted process window, corresponding to the position of the white circle in the solid green zone of Figure 3.5 (a).

Figure 3.11. SEM of cross sections of L-PBF NiTi alloys fabricated with various processing parameters.

In order to have a more in-depth understanding of the defect's formation, the cross-sectional investigation of NiTi samples manufactured with various L-PBF process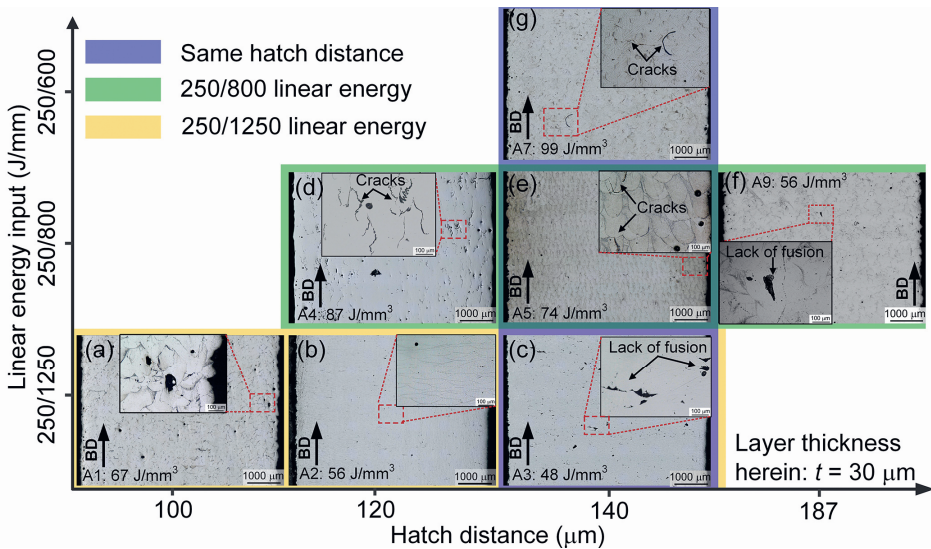ing parameters is provided in Figure 3.11. As can be seen, the condition of 250/1250 J/mm linear energy density (sample A2 with hatch distance of 120 μm (Figure 3.11 (b)), exhibits highest densification and is nearly defect-free. The large hatch distance in A3 resulted in irregular lack of fusion (Figure 3.11 (c)). This result is also consistent with the calculated prediction of lack of fusion (Figure 3.5 (a)). Compared with the sample A2, although there is enough overlapping of laser tracks for avoiding lack-of-fusion in A1, the narrow hatch distance can cause a high volumetric energy density. As a result, vaporization may become severe and cause formation of bubbles. Once the bubbles are trapped within the molten pools, pores can be formed [57].

Another sample featuring lack of fusion defect is sample A9 (Figure 3.11 (f)). Referring to the processing maps (Figure 3.5 (b)), the position of sample A9 is located in the region where lack of fusion is expected (solid green region is the fully dense region, in the condition of $h = 187$ and $t = 30$ μm). This indicates that the processing map can give a relatively good estimation on the occurrence of lack of fusion.

3.3.2.4. Cracks in L-PBF NiTi

Besides balling, keyhole-induced pores and lack of fusion, cracks in L-PBF NiTi parts cannot be tolerated. As shown in the top-view (Figure 3.8 and Figure 3.9) and cross-sectional representation (Figure 3.11), cracks usually exist in L-PBF NiTi samples with high volumetric energy densities (>74 J/mm^3). These high volumetric energy densities originate either from high linear energy densities or large overlapping of laser tracks (Figure 3.12 (a) and (b)), resulting from relatively low hatch distances.

With increasing linear energy density to 250/800 (J/mm), cracks become dominant defects for samples A4 (Figure 3.9 (a) and (d), and Figure 3.11 (d)) and A5 (Figure 3.8 (b) and (e), and Figure 3.11 (e)) with hatch distance of 120 and 140 µm, respectively. As expected, with further increasing linear energy density to 250/600 J/mm, cracks are produced, as demonstrated in A7 sample (Figure 3.8 (c) and (f), Figure 3.11 (g), and Figure 3.12 (a)).
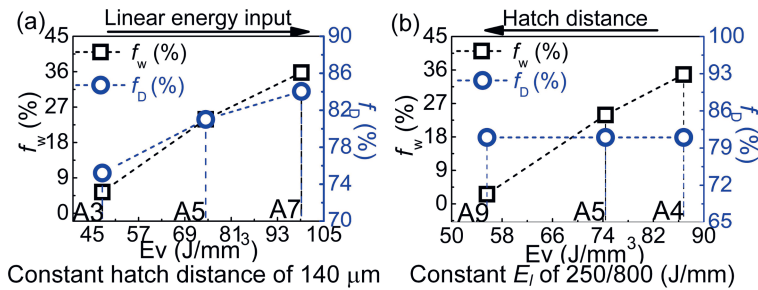
Figure 3.12. Overlapping ratios of melt pool width and height of various samples: (a) samples with constant hatch distance of 140 µm but various linear energy densities; (b) samples with constant linear energy density of 250/800 (J/mm) but various hatch distances ranging from 120 to 187 µm.

During cooling the deposited bead will experience solidification and thermal contraction, combined with transformation strains. If the induced strain exceeds a critical strain the material will crack. Therefore, larger beads, related to higher linear energy density are more susceptible to hot cracking. However, the strain rate also affects crack formation and is determined by the cooling rate, which also depends on the linear energy density. A lower strain rate associated with a higher linear energy density improves the crack resistance.

Therefore, both total strain and strain rate should be considered for crack sensitivity of the material.

It also should be noted that phase transformation and detwinning can be triggered by residual stress [58], as a result of the shape memory property of NiTi alloys, which brings a challenge and complexity in evaluation of residual stress in NiTi alloys. Although it is not the scope of this work it would be interesting to investigate these observations by experimental measurements of residual 3D stress in the L-PBF NiTi parts.

Therefore, considering defects of balling, keyhole-induced pores, lack of fusion and cracks together, the best quality among all studied herein process groups was found for A2 sample featuring a moderate hatch distance of 120 μm, which is consistent with the density measurements (Figure 3.6).

Although the developed herein processability maps do not show the boundary conditions for cracks formation, it still can be successfully applied with respect to balling, keyhole-induced pores and lack of fusion (Figure 3.5). Furthermore, by combining with the experimental results, it has been demonstrated that a low linear energy density contributes to avoiding the formation of cracks. Therefore, defect-free NiTi samples can be fabricated by choosing a low linear energy density in the good zone of process maps (the good zone is surrounded by solid blue line in Figure 3.5 (a)).

Predicting the formation of cracks remains a challenge. In the case of metallic materials manufactured through L-PBF, cracks may arise due to thermal stresses, elemental segregations, and solidification paths [56]. Given that cracks in L-PBF components can significantly compromise their mechanical properties and integration, it is important to prevent and mitigate crack formation. Chapter 7 delves into the mechanisms underlying the formation of cracks in equiatomic NiTi and presents corresponding strategies for crack healing.

3.3.2.5. Hardness, martensite phase transformation temperatures and Ni contents

In order to evaluate the processability of L-PBF NiTi alloys, it is important to consider its properties, such as hardness, shape memory effect, and superelasticity [59]. Hardness measurements were conducted in this work as it can provide a quick and direct evaluation of densification. In addition to NiTi hardness, the martensite starting temperature (M_s) determine the operating temperatures of NiTi alloys. Therefore, it is crucial to understand the relationship between M_s and the L-PBF processing conditions. As depicted in Figure 3.13,

the hardness generally decreases with increasing volumetric (from 240 to 190 HV, Figure 3.13 (a)) and linear energy density (from 240 to 203 HV, Figure 3.13 (b)). In contrast, the M_s increase from 55 to 67 °C with the increase of energy density (for both E_v and E_l). The reason for the changing trend of hardness is that high energy density ($E_v > 56$ J/mm^3 and $E_l >$ 250/1250 J/mm) results in large grain sizes [60], which causes the decrease of hardness. An exception is observed in sample A3 (Figure 3.13 (a)), where a lower hardness was achieved with decreasing E_v to 48 J/mm^3. The low hardness in the sample A3 is attributed to the occurrence lack of fusion (Figure 3.7 (c) and Figure 3.11 (c)). Figure 3.13 presents the micro-hardness measurements results, which vary between 190 and 240 HV among all samples. On the whole, these values are comparable with the hardness of NiTi fabricated by conventional extrusion methods (~219 – 227 HV) [61].
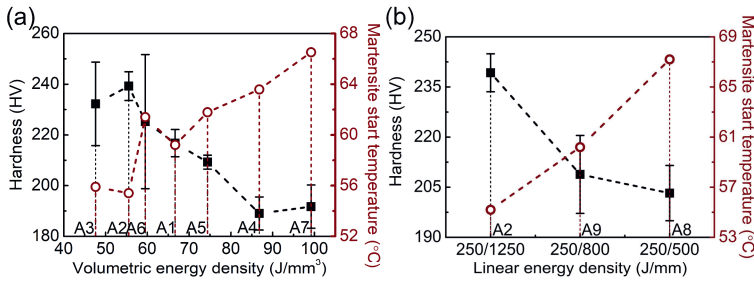
3

Figure 3.13. Micro-hardness of L-PBF samples as a function of (a) volumetric energy density and (b) linear energy density.
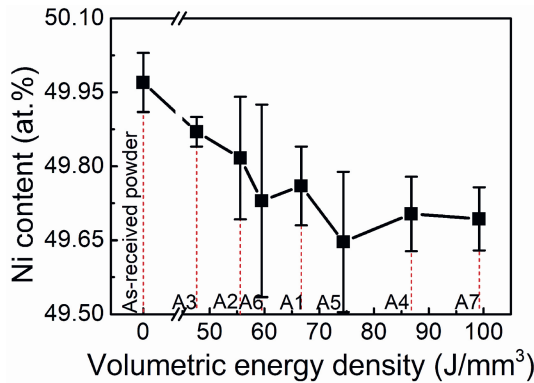

Figure 3.14. the Ni content as a function of volume energy density.

As shown in Figure 3.14, with increasing the volumetric energy density, the Ni content decreases. It indicates that more pronounced evaporation occurs at higher energy densities which has also been reported by previous research [28, 35]. Since phase transformation temperatures of NiTi increase with decreasing Ni content, there is an upward trend of M_s as a function of energy density. Hence, the lower the Ni content (with higher energy densities) the higher M_s temperature (see Figure 3.13 and Figure 3.14). In this work, the outlier A6 with the highest linear energy density of 250/500 (J/mm) among all studied herein samples has a relatively high M_s temperature due to a higher Ni evaporation, as seen in Figure 3.14.

It should be noted that sample A3 also shows an abnormal M_s temperature compared with the general upward trend of M_s temperature (Figure 3.13 (a)). Sample A3 compared to sample A2, has a larger hatch distance of 140 μm. As reported by Ma *et al.* [30]*, increasing hatch distance can introduce high dislocation density in NiTi samples, and the M_s temperature decreases with an increasing dislocation density due to introduction of more local misfits during phase transformations [62]. In addition, residual stresses, which are inevitable in L-PBF process due to high heating and cooling rates [1], can increase the transformation temperature of NiTi alloys [63]. Hence, both high dislocation density and residual stress could also contribute to the increase in M_s temperature.

3.3.2.6. Employing the developed model in the high laser condition

The motivation behind this chapter is to establish a versatile model for predicting NiTi L-PBF processing maps across a broad parameter range. Therefore, it becomes imperative to assess the accuracy of this model by employing L-PBF processing parameters that significantly differ from those of the A group. Consequently, B group samples were created using a high laser power (950 W) and a large beam diameter (500 μm) to serve as validation for the developed model, and detailed processing parameters are shown in the Table 3.3.
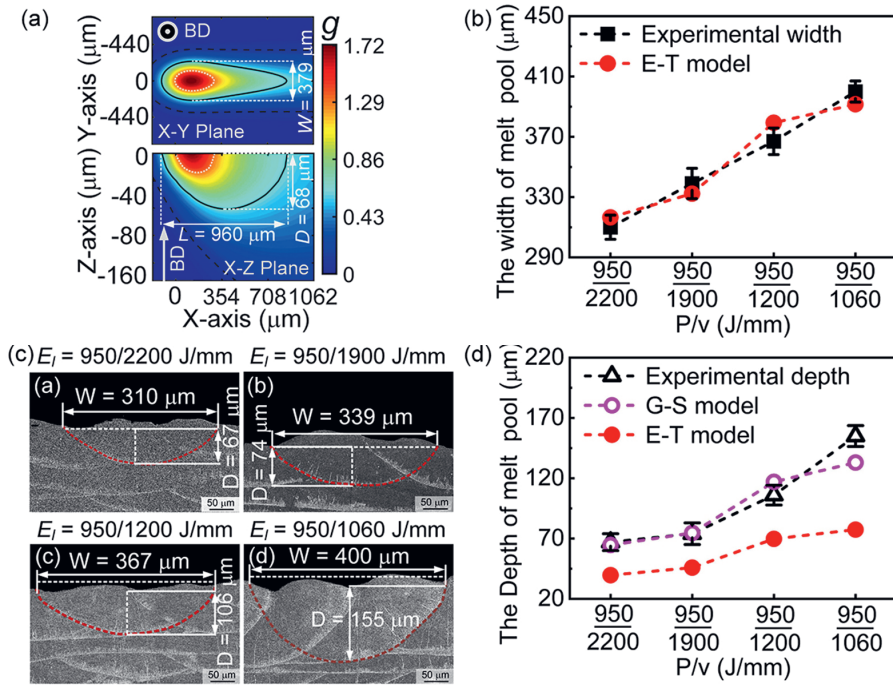
Figure 3.15. (a) A case with linear energy of $\dfrac{950 \text{ W}}{1200 \text{ mm/s}}$ (500 μm beam diameter): Cross-sectional views (X-Y and X-Z planes) of the temperature contour (plotted by g) and the melt pool boundary (indicated by the black solid line, where $g = T_m / T_s$) from the E-T model; Comparison of the experimentally measured melt pools (b) widths and (d) depths between the E-T model and the G-S model predictions for applied linear energy densities from B group samples; (c) cross-sectional pool melt shapes of L-PBF NiTi fabricated by B group processing conditions.

An example case of a temperature contour plot and the melt pool boundary (indicated by the black line) with the heat input resulting from 950 W laser power, 1200 mm/s scanning velocity and 500 μm beam diameter is shown in Figure 3.15 (a). By employing the developed model, melt pool width and depth were predicted. It can be seen that predicted melt pool widths (Figure 3.15 (b)) by using the E-T model can fit well with the experimental melt pool width (Figure 3.15 (c)). However, in terms of melt pool depth, the G-S model, concerning the keyhole melt pool, still shows a more accurate prediction than E-T model (Figure 3.15 (d)), despite conduction mode melt pools shown in samples with various linear energy input

(Figure 3.15 (c)). This can be explained by the element evaporation, one of the features of keyhole melt pool, which also presents in such conduction mode melt pools. Temperature contours in the example case also demonstrates that melt pool temperatures around the laser source is above NiTi boiling point (marked by grey dash line in Figure 3.15 (a)).

After confirming the accuracy of the model for melt pool dimension prediction in the high laser power and laser beam diameter condition, melt pool dimensions in a wider range of processing space are explored. The melt pool width, depth and length as functions of laser power (P) and scanning speed (v) are shown in Figure 3.16 (a) and (c), respectively.
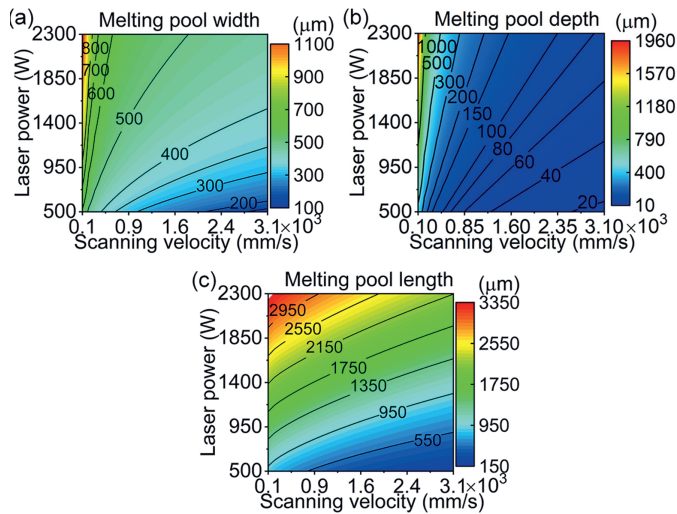
Figure 3.16. Melt pool (a)width, (b) depth and (c) length as the function of the laser power and scanning velocity for applying 500 μm beam diameter.

Similar with the process in the low laser power condition, a processing map considering a 500 μm beam diameter, 50 μm layer thickness and a 180 μm hatch distance is developed (Figure 3.17). By comparing experimental results, defect formation can be accurately predicted by the processing map. When applied linear energy density is lower than $\frac{950}{1900}$ J/mm, lack of fusion occurs in L-PBF NiTi samples (Figure 3.17). However, despite in the fully dense region, cracks still presents when the linear energy density above $\frac{950}{1060}$ J/mm (B4, Figure 3.17). Based on predicted processing map and experimental validation, the B3

sample with linear energy density of $\dfrac{950}{1200}$ J/mm is optimized as a defect-free sample in the condition of high laser power coupled with a large beam size (Figure 3.17).

3
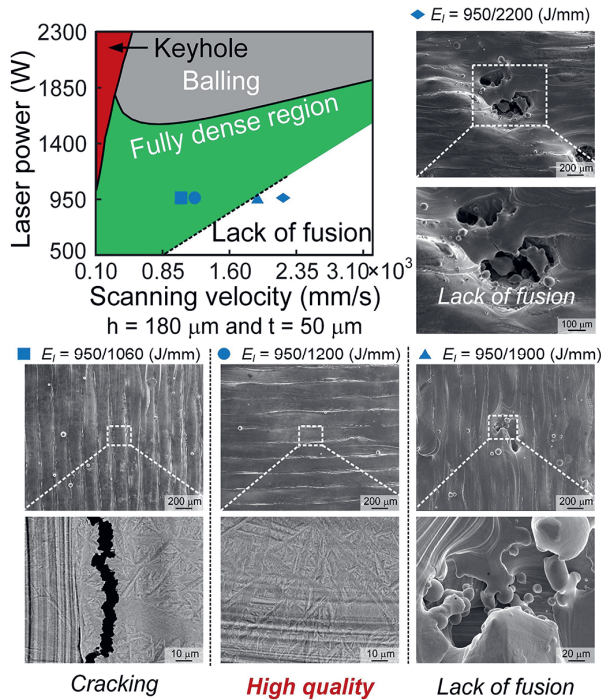
Figure 3.17. An L-PBF processing map for applying a 500 μm beam diameter, 50 μm layer thickness and a 180 μm hatch distance and corresponding SEM micrographs of the top surfaces of L-PBF NiTi fabricated with different linear energies.

It should be noted that the optimized defect-free sample B3 has an 88 J/mm^3 volumetric energy density, which is located in defected regime of 250 W laser power - 80 μm beam diameter condition. However, for the applied 56 J/mm^3 volumetric energy density, a defect-free E_v for the low laser power condition, leads to lack of fusion in the high laser power condition. Therefore, it further demonstrates that volumetric energy density cannot provide accurate estimation for the fabrication of defect-free L-PBF parts.
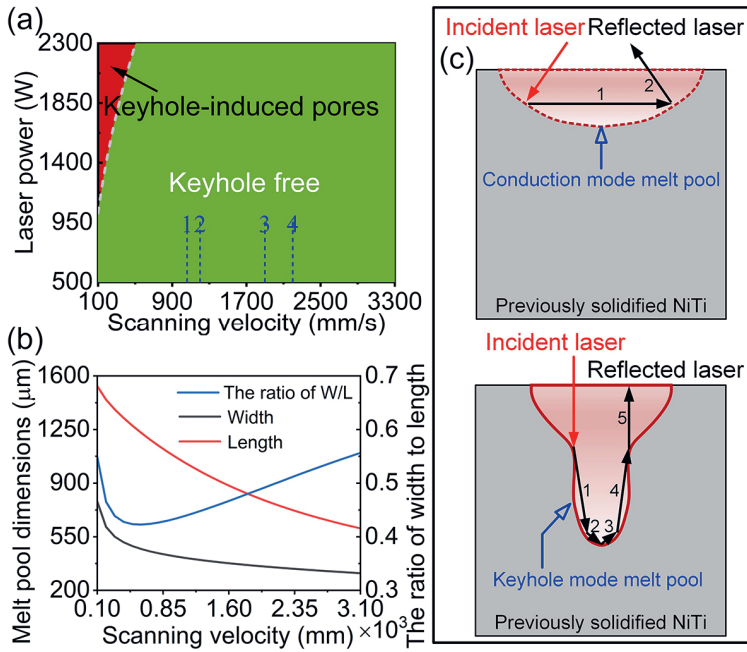
Figure 3.18. (a) The process map of keyhole-induced pores for applying 500 μm beam diameter; (b) width and length of melt pool and its ratio as a function of scanning velocity; (c) schematic diagram of the multiple reflection the laser under different beam diameter.

Based on Figure 3.17 and Figure 3.18 (a), in the condition of 950 W laser power and 500 μm beam diameter, L-PBF NiTi is not sensitive to balling and keyhole induced pores. As descripted in the Eq. 3.4, balling occurs when the ratio of melt pool width to length is smaller than ~0.26. In the circumstance of 950 W - 500 μm, the ratio of melt pool width to depth is always higher than 0.26 (Figure 3.18 (b)). Hence, balling is not sensitive in such conditions, which is also consistent with experimental results (Figure 3.17). For the keyhole, despite employing 950 W laser power, the beam diameter also increased to 500 μm. When

considering energy input per unit area ($E_{beam} = \dfrac{P}{\pi \cdot \left(\dfrac{d_{Laser\ beam}}{2} \right)^2}$, J/mm^2), the energy input for

the condition of 950W - 500 μm is ~ 4841 J/mm^2, while it is 12440 J/mm^2 for the condition of 250W - 80 μm. Therefore, high laser power condition has a lower energy input per unit area, which results in a less sensitivity to the keyhole melt pool. In addition, the increased beam size is achieved by positively defocusing laser beam, which makes beam divergent [64].

This divergent beam leads to the change of internal energy distribution (Figure 3.18 (c)), which further deceases the possibility of keyhole mode melt pool.

3.4. Conclusions

In this chapter, the feasibility of analytical models for predicting melt pool dimensions of L-PBF NiTi was demonstrated. Based on analytic solutions of the melt pool dimensions and defect formation criteria, L-BPF processing maps for fabricating NiTi alloys were drawn. The reliability of the L-BPF processing maps was validated for NiTi fabricated by different L-BPF processing conditions. The main conclusions of this work can be summarized as follows:

1. Fully dense L-PBF NiTi parts (> 99 %) can be successfully fabricated by utilizing the analytically developed process maps. However, cracks should be separately considered and can be inhibited by adopting desirable overlapping ratios of laser tracks and linear energy input.

2. Heat input related parameters, such as laser power and scanning velocity should be carefully chosen to achieve defect-free laser tracks. With a laser power of 250 W, scanning velocity should be higher than 500 mm/s to avoid keyholing and lower than 1250 mm/s to prevent NiTi parts from balling. Balling can be reduced by increasing hatch distance, but there is nearly no effect found on keyholing with changing hatch distance and layer thickness.

3. Hardness and M_s of L-PBF NiTi alloys was found to be sensitive to energy input (including both E_v and E_l). Hardness shows a decrease from 240 to 190 HV with increasing E_v from 56 to 99 J/mm^3. M_s shows an upward trend with increasing energy input, which increases from 55 to 67 ^{o}C. The increasing phase transformation temperatures is mainly attributed to Nickel evaporation during L-PBF.

4. The developed model is reliable in a wide range of L-PBF processing space. In the condition of 950 W laser power and 500 μm beam diameter condition, L-PBF is not sensitive to balling and keyhole induced pores when varying scanning velocities.

Thus, in this chapter, the use of proposed analytical approaches for the development and optimization of process parameters (including laser power, scanning velocity, hatch distance and layer thickness) for fabrication of defect-free NiTi alloys by using L-BPF manufacturing technique is demonstrated.

3

3

References

[1] M. Elahinia, N. Shayesteh Moghaddam, M. Taheri Andani, A. Amerinatanzi, B.A. Bimber, R.F. Hamilton, Fabrication of NiTi through additive manufacturing: A review, Progress in Materials Science 83 (2016) 630-663.

[2] M.H. Nasab, D. Gastaldi, N.F. Lecis, M. Vedani, On morphological surface features of the parts printed by selective laser melting (SLM), Additive Manufacturing 24 (2018) 373-377.

[3] B. Zhang, Y. Li, Q. Bai, Defect Formation Mechanisms in Selective Laser Melting: A Review, Chinese Journal of Mechanical Engineering 30(3) (2017) 515-527.

[4] J.-B. Forien, N.P. Calta, P.J. DePond, G.M. Guss, T.T. Roehling, M.J. Matthews, Detecting keyhole pore defects and monitoring process signatures during laser powder bed fusion: A correlation between in situ pyrometry and ex situ X-ray radiography, Additive Manufacturing 35 (2020) 101336.

[5] N.J. Harrison, I. Todd, K. Mumtaz, Reduction of micro-cracking in nickel superalloys processed by Selective Laser Melting: A fundamental alloy design approach, Acta Materialia 94 (2015) 59-68.

[6] I. Yadroitsev, A. Gusarov, I. Yadroitsava, I. Smurov, Single track formation in selective laser melting of metal powders, Journal of Materials Processing Technology 210(12) (2010) 1624-1631.

[7] A. Sola, A. Nouri, Microstructural porosity in additive manufacturing: The formation and detection of pores in metal parts fabricated by powder bed fusion, Journal of Advanced Manufacturing and Processing 1(3) (2019) e10021.

[8] G. Kasperovich, J. Haubrich, J. Gussone, G. Requena, Correlation between porosity and processing parameters in TiAl6V4 produced by selective laser melting, Materials & Design 105 (2016) 160-170.

[9] J. Braun, L. Kaserer, J. Stajkovic, K.H. Leitz, B. Tabernig, P. Singer, P. Leibenguth, C. Gspan, H. Kestler, G. Leichtfried, Molybdenum and tungsten manufactured by selective laser melting: Analysis of defect structure and solidification mechanisms, International Journal of Refractory Metals and Hard Materials 84 (2019) 104999.

[10] J. Walker, M. Elahinia, C. Haberland, An Investigation of Process Parameters on Selective Laser Melting of Nitinol, ASME 2013 Conference on Smart Materials, Adaptive Structures and Intelligent Systems, 2013.

3

[11] C. Zhao, H. Liang, S. Luo, J. Yang, Z. Wang, The effect of energy input on reaction, phase transition and shape memory effect of NiTi alloy by selective laser melting, Journal of Alloys and Compounds 817 (2020) 153288.

[12] U. Scipioni Bertoli, A.J. Wolfer, M.J. Matthews, J.-P.R. Delplanque, J.M. Schoenung, On the limitations of Volumetric Energy Density as a design parameter for Selective Laser Melting, Materials & Design 113 (2017) 331-340.

[13] J.P. Oliveira, A.D. LaLonde, J. Ma, Processing parameters in laser powder bed fusion metal additive manufacturing, Materials & Design 193 (2020) 108762.

[14] I. Yadroitsev, I. Yadroitsava, P. Bertrand, I. Smurov, Factor analysis of selective laser melting process parameters and geometrical characteristics of synthesized single tracks, Rapid Prototyping Journal 18(3) (2012) 201-208.

[15] L. Wang, Q.S. Wei, Y.S. Shi, J.H. Liu, W.T. He, Experimental Investigation into the Single-Track of Selective Laser Melting of IN625, Advanced Materials Research 233-235 (2011) 2844-2848.

[16] D. Gu, Y. Shen, Balling phenomena in direct laser sintering of stainless steel powder: Metallurgical mechanisms and control methods, Materials & Design 30(8) (2009) 2903-2910.

[17] R. Cunningham, C. Zhao, N. Parab, C. Kantzos, J. Pauza, K. Fezzaa, T. Sun, A.D. Rollett, Keyhole threshold and morphology in laser melting revealed by ultrahigh-speed x-ray imaging, Science 363(6429) (2019) 849.

[18] Z.X. Khoo, Y. Liu, J. An, C.K. Chua, Y.F. Shen, C.N. Kuo, A Review of Selective Laser Melted NiTi Shape Memory Alloy, Materials 11(4) (2018).

[19] C. Haberland, M. Elahinia, J.M. Walker, H. Meier, J. Frenzel, On the development of high quality NiTi shape memory and pseudoelastic parts by additive manufacturing, Smart Materials and Structures 23(10) (2014) 104002.

[20] E. Farber, J.-N. Zhu, A. Popovich, V. Popovich, A review of NiTi shape memory alloy as a smart material produced by additive manufacturing, Mater. Today. Proc. (2020).

[21] C. Haberland, H. Meier, J. Frenzel, On the properties of Ni-rich NiTi shape memory parts produced by selective laser melting, ASME 2012 Conference on Smart Materials, Adaptive Structures and Intelligent Systems, SMASIS 2012, 2012, pp. 97-104.

[22] H. Meier, C. Haberland, J. Frenzel, Structural and functional properties of NiTi shape memory alloys produced by Selective Laser Melting, Innovative Developments in Virtual and Physical Prototyping - Proceedings of the 5th International Conference on Advanced Research and Rapid Prototyping, 2012, pp. 291-296.

[23] S. Saedi, N. Shayesteh Moghaddam, A. Amerinatanzi, M. Elahinia, H.E. Karaca, On the effects of selective laser melting process parameters on microstructure and thermomechanical response of Ni-rich NiTi, Acta Materialia 144 (2018) 552-560.

[24] S. Dadbakhsh, M. Speirs, J.-P. Kruth, J. Schrooten, J. Luyten, J. Van Humbeeck, Effect of SLM Parameters on Transformation Temperatures of Shape Memory Nickel Titanium Parts, Advanced Engineering Materials 16(9) (2014) 1140-1146.

[25] J.P. Oliveira, T.G. Santos, R.M. Miranda, Revisiting fundamental welding concepts to improve additive manufacturing: From theory to practice, Progress in Materials Science 107 (2020) 100590.

[26] K.G. Prashanth, S. Scudino, T. Maity, J. Das, J. Eckert, Is the energy density a reliable parameter for materials synthesis by selective laser melting?, Materials Research Letters 5(6) (2017) 386-390.

[27] M. Letenneur, A. Kreitcberg, V. Brailovski, Optimization of Laser Powder Bed Fusion Processing Using a Combination of Melt Pool Modeling and Design of Experiment Approaches: Density Control, Journal of Manufacturing and Materials Processing 3(1) (2019).

[28] R. Seede, D. Shoukr, B. Zhang, A. Whitt, S. Gibbons, P. Flater, A. Elwany, R. Arroyave, I. Karaman, An ultra-high strength martensitic steel fabricated using selective laser melting additive manufacturing: Densification, microstructure, and mechanical properties, Acta Materialia 186 (2020) 199-214.

[29] S. Dadbakhsh, M. Speirs, J. Van Humbeeck, J.-P. Kruth, Laser additive manufacturing of bulk and porous shape-memory NiTi alloys: From processes to potential biomedical applications, MRS Bulletin 41(10) (2016) 765-774.

[30] J. Ma, B. Franco, G. Tapia, K. Karayagiz, L. Johnson, J. Liu, R. Arroyave, I. Karaman, A. Elwany, Spatial Control of Functional Response in 4D-Printed Active Metallic Structures, Scientific Reports 7(1) (2017) 46707.

3

[31] L. Johnson, M. Mahmoudi, B. Zhang, R. Seede, X. Huang, J.T. Maier, H.J. Maier, I. Karaman, A. Elwany, R. Arróyave, Assessing printability maps in additive manufacturing of metal alloys, Acta Materialia 176 (2019) 199-210.

[32] P. Promoppatum, S.-C. Yao, Analytical evaluation of defect generation for selective laser melting of metals, The International Journal of Advanced Manufacturing Technology 103(1-4) (2019) 1185-1198.

[33] M. Tang, P.C. Pistorius, J.L. Beuth, Prediction of lack-of-fusion porosity for powder bed fusion, Additive Manufacturing 14 (2017) 39-48.

[34] C. Teng, D. Pal, H. Gong, K. Zeng, K. Briggs, N. Patil, B. Stucker, A review of defect modeling in laser material processing, Additive Manufacturing 14 (2017) 137-147.

[35] G.G. Gladush, I. Smurov, Physics of laser materials processing: theory and experiment, Springer Science & Business Media2011.

[36] K. Tolochko Nikolay, E. Mozzharov Sergei, A. Yadroitsev Igor, T. Laoui, L. Froyen, I. Titov Victor, B. Ignatiev Michail, Balling processes during selective laser treatment of powders, Rapid Prototyp. J. 10(2) (2004) 78-87.

[37] A.A. Martin, N.P. Calta, S.A. Khairallah, J. Wang, P.J. Depond, A.Y. Fong, V. Thampy, G.M. Guss, A.M. Kiss, K.H. Stone, C.J. Tassone, J. Nelson Weker, M.F. Toney, T. van Buuren, M.J. Matthews, Dynamics of pore formation during laser powder bed fusion additive manufacturing, Nat Commun 10(1) (2019) 1987.

[38] B. Zhou, J. Zhou, H. Li, F. Lin, A study of the microstructures and mechanical properties of Ti6Al4V fabricated by SLM under vacuum, Materials Science and Engineering: A 724 (2018) 1-10.

[39] J. Zhou, H.-L. Tsai, Effects of electromagnetic force on melt flow and porosity prevention in pulsed laser keyhole welding, International Journal of Heat and Mass Transfer 50(11) (2007) 2217-2235.

[40] S. Leuders, M. Thöne, A. Riemer, T. Niendorf, T. Tröster, H.A. Richard, H.J. Maier, On the mechanical behaviour of titanium alloy TiAl6V4 manufactured by selective laser melting: Fatigue resistance and crack growth performance, International Journal of Fatigue 48 (2013) 300-307.

[41] H. Gong, K. Rafi, H. Gu, G.D. Janaki Ram, T. Starr, B. Stucker, Influence of defects on mechanical properties of Ti–6Al–4V components produced by selective laser melting and electron beam melting, Materials & Design 86 (2015) 545-554.

[42] W. Ke, X. Bu, J.P. Oliveira, W. Xu, Z. Wang, Z. Zeng, Modeling and numerical study of keyhole-induced porosity formation in laser beam oscillating welding of 5A06 aluminum alloy, Optics & Laser Technology 133 (2021) 106540.

[43] D.B. Hann, J. Iammi, J. Folkes, A simple methodology for predicting laser-weld properties from material and laser parameters, Journal of Physics D: Applied Physics 44(44) (2011) 445401.

[44] A.M. Rubenchik, W.E. King, S.S. Wu, Scaling laws for the additive manufacturing, Journal of Materials Processing Technology 257 (2018) 234-243.

[45] T.W. Eagar, N.S. TSAi, Temperature fields produced by traveling distributed heat sources, Weld. J. 62(12) (1983) 346-355.

[46] K.-H. Lee, G.J. Yun, A novel heat source model for analysis of melt Pool evolution in selective laser melting process, Additive Manufacturing 36 (2020) 101497.

[47] K. Otsuka, X. Ren, Physical metallurgy of Ti–Ni-based shape memory alloys, Progress in Materials Science 50(5) (2005) 511-678.

[48] H. Fang, M.B. Wong, Y. Bai, R. Luo, Effect of heating/cooling rates on the material properties of NiTi wires for civil structural applications, Construction and Building Materials 101 (2015) 447-455.

[49] C. Zanotti, P. Giuliani, P. Bassani, Z. Zhang, A. Chrysanthou, Comparison between the thermal properties of fully dense and porous NiTi SMAs, Intermetallics 18(1) (2010) 14-21.

[50] C. Zanotti, P. Giuliani, G. Riva, A. Tuissi, A. Chrysanthou, Thermal diffusivity of Ni–Ti SMAs, Journal of Alloys and Compounds 473(1-2) (2009) 231-237.

[51] J.W. Mwangi, L.T. Nguyen, V.D. Bui, T. Berger, H. Zeidler, A. Schubert, Nitinol manufacturing and micromachining: A review of processes and their suitability in processing medical-grade nitinol, Journal of Manufacturing Processes 38 (2019) 355-369.

[52] G.R. Mirshekari, A. Saatchi, A. Kermanpur, S.K. Sadrnezhaad, Laser welding of NiTi shape memory alloy: Comparison of the similar and dissimilar joints to AISI 304 stainless steel, Optics & Laser Technology 54 (2013) 151-158.

[53] F. Verhaeghe, T. Craeghs, J. Heulens, L. Pandelaers, A pragmatic model for selective laser melting with evaporation, Acta Materialia 57(20) (2009) 6006-6012.

3

[54] Y.S. Lee, W. Zhang, Modeling of heat transfer, fluid flow and solidification microstructure of nickel-base superalloy fabricated by laser powder bed fusion, Additive Manufacturing 12 (2016) 178-188.

[55] X.P. Li, K.M. O'Donnell, T.B. Sercombe, Selective laser melting of Al-12Si alloy: Enhanced densification via powder drying, Additive Manufacturing 10 (2016) 10-14.

[56] J.H. Martin, B.D. Yahata, J.M. Hundley, J.A. Mayer, T.A. Schaedler, T.M. Pollock, 3D printing of high-strength aluminium alloys, Nature 549(7672) (2017) 365-369.

[57] Y.H. Zhou, W.P. Li, L. Zhang, S.Y. Zhou, X. Jia, D.W. Wang, M. Yan, Selective laser melting of Ti–22Al–25Nb intermetallic: Significant effects of hatch distance on microstructural features and mechanical properties, Journal of Materials Processing Technology 276 (2020) 116398.

[58] Q. Zhou, M.D. Hayat, G. Chen, S. Cai, X. Qu, H. Tang, P. Cao, Selective electron beam melting of NiTi: Microstructure, phase transformation and mechanical properties, Materials Science and Engineering: A 744 (2019) 290-298.

[59] S. Shiva, I.A. Palani, S.K. Mishra, C.P. Paul, L.M. Kukreja, Investigations on the influence of composition in the development of Ni–Ti shape memory alloy using laser based additive manufacturing, Optics & Laser Technology 69 (2015) 44-51.

[60] T. Larimian, M. Kannan, D. Grzesiak, B. AlMangour, T. Borkar, Effect of energy density and scanning strategy on densification, microstructure and mechanical properties of 316L stainless steel processed via selective laser melting, Materials Science and Engineering: A 770 (2020) 138455.

[61] J. Luo, J.O. Bobanga, J.J. Lewandowski, Microstructural heterogeneity and texture of as-received, vacuum arc-cast, extruded, and re-extruded NiTi shape memory alloy, Journal of Alloys and Compounds 712 (2017) 494-509.

[62] M.F.X. Wagner, S.R. Dey, H. Gugel, J. Frenzel, C. Somsen, G. Eggeler, Effect of low-temperature precipitation on the transformation characteristics of Ni-rich NiTi shape memory alloys during thermal cycling, Intermetallics 18(6) (2010) 1172-1179.

[63] J.P. Oliveira, A.J. Cavaleiro, N. Schell, A. Stark, R.M. Miranda, J.L. Ocana, F.M. Braz Fernandes, Effects of laser processing on the transformation characteristics of NiTi: A contribute to additive manufacturing, Scripta Materialia 152 (2018) 122-126.

3

[64] X. Nie, Z. Chen, Y. Qi, H. Zhang, C. Zhang, Z. Xiao, H. Zhu, Effect of defocusing distance on laser powder bed fusion of high strength Al–Cu–Mg–Mn alloy, Virtual Phys. Prototyp. 15(3) (2020) 325-339.

3

3

4

Controlling Microstructure Evolution and Phase Transformation Behaviour in Additively Manufactured NiTi by tuning Hatch Distance

Abstract

Hatch distance, as an important L-PBF processing parameter, is often related to macro-scale structural defects, however its role on controlling the microstructure and functional properties is usually underestimated in L-PBF of NiTi. In this chapter, near-equiatomic NiTi (49.6 at. % Ni) parts were fabricated with various hatch distances to tailor the microstructure and their shape memory characteristics. Contrary to what is observed in Ni-rich NiTi alloys, in this chapter, it is demonstrated that phase transformation temperatures of L-PBF equiatomic NiTi do not decrease proportionally with hatch distance but rather relate to a critical hatch distance value. This critical value (120 μm) is derived from the synergistic effect of thermal stress and in-situ reheating. Below this value, epitaxial grain growth and in-situ recrystallization are enhanced. While above, irregular grains are formed, and dislocations induced by thermal stresses decrease. However, the critical value found herein is characterized by high dislocation density and fine grain size, resulting in a superior thermal cyclic stability. The proposed Finite Element Model (FEM) is proven to be an effective tool to understand and predict the effect of hatch distance on grain morphology and dislocation density evolutions in L-PBF NiTi SMAs. In this chapter, a comprehensive understanding for in-situ controlling L-PBF NiTi microstructure and functional characteristics, which contributes to designing 4-dimensional (4D) shape memory alloys, is provided.

4.1. Introduction

For the fabrication of L-PBF NiTi parts, main processing parameters include laser power (P, W), scanning velocity (v, mm s^{-1}), layer thickness (t, μm) and hatch distance (h, mm). In the past, most studies focused on investigating the effect of laser powers and scanning velocities (The linear energy density (E_l), shown in the eq. 3.1) on structural quality, microstructure evolution, and functional properties [1-5]. The layer thickness was usually chosen between 30–50 μm to achieve the balance among full-dense parts, stable powder spreading and desirable building rate [5-8]. However, the hatch distance was mainly selected as a fixed value to prevent structural defect formation (such as lack of fusion and surface roughness) [9-11], and its role in microstructural evolution, phase transformation behavior, and functional properties were underestimated and ignored.

As found in recent studies [12-14], the hatch distance is an unneglectable factor, which can affect not only structural defects but also exert a significant effect on the microstructure

and phase transformation temperatures (PTTs) in Ni-rich L-PBF NiTi alloys. However, microstructural evolution mechanisms and changes in phase transformation temperatures of L-PBF NiTi alloys with various hatch distances have not been revealed yet. For Ni–Ti alloys, it has been demonstrated that phase transformation behavior can be affected by the Ni/Ti ratio [15], precipitates [15, 16], dislocations [16, 17] and grain size [18, 19]. PTTs increase dramatically (around 100 K at. %$^{-1}$) with decreasing Ni content in Ni-rich NiTi alloys [15, 20]. While for equiatomic or Ti-rich NiTi alloys, PTTs almost do not change with the chemical composition ratio of Ni/Ti [20]. Similarly, precipitates only affect the PPTs significantly in Ni-rich rather than equiatomic or Ti-rich NiTi alloys [15, 21]. Dislocations can decrease PTTs by hindering martensite transformation during cooling [16]. Decreasing grain size can cause a suppression of the thermally induced martensitic phase transformation occurring, also resulting in a decreasing PTTs [18]. Due to a higher vapor pressure and lower boiling point of Ni compared with Ti in binary NiTi alloys [12, 14], Ni is preferentially evaporated from NiTi alloys and the chemical composition ratio of Ni/Ti decreases after L-PBF. Considering the sensitivity of transformation temperatures by Ni/Ti ratio and Ni-rich precipitates in Ni-rich alloys, an equiatomic (slightly Ti-rich) NiTi composition was selected to focus on understanding how to control phase transformation behavior and microstructure evolution by tuning the hatch distance.

In addition, it was found that dislocation density, impeding martensitic transformations, increases with widening the hatch distance [12], but only two hatch distance conditions were conducted/considered, which brings uncertainty about the relationship between the hatch distance and dislocation density.

In this work, L-PBF NiTi alloys with various hatch distances (100, 120, and 140 μm) were successfully fabricated. The effect of hatch distance on microstructure, dislocation density, phase transformation behavior and thermal-cyclic stability were systematically investigated by experiments as well as finite element modeling (FEM). An near equiatomic (slightly Ti-rich) NiTi composition (Ni: 49.6 at. %) was selected in this work in order to understand how to control phase transformation behavior and microstructure evolution by tuning hatch distance.

4.2. Materials and Methods

4.2.1. Experimental

4.2.1.1. Fabrication

Based on the optimization of processing parameters outlined in Chapter 3, it was determined that employing a laser power of 250W, in combination with a scanning velocity of 1250 mm/s, resulted in the production of laser beads free from balling defects. Chapter 4 aims to investigate the influence of the hatch distance (h). In this investigation, various hatch distances were tested while maintaining the other parameters constant (P = 250W, v = 1250 mm/s, and t = 30 μm). The samples with hatch distances of 100, 120, and 140 μm are denoted as A1, A2, and A3, respectively. A summary of the L-PBF processing parameters can be found in Table 3.1 of Chapter 3. For further information regarding the fabrication of L-PBF NiTi, please refer to Section 3.2.4 in Chapter 3.

4

4.2.1.2. Characterization

To investigate microstructure, cross sections along the building direction and the top view (perpendicular to the building direction) were prepared. Samples for metallographic examination were ground, polished, and etched in two types of etching solution. The first type etching solution consisting of HF (3.2 vol%), HNO_3 (14.1 vol%), and H_2O (82.7 vol%) was used to distinguish epitaxial grain growth [1]. A second solution consisting of 120 ml distilled water, 15 ml HCl, 15 g $Na_2S_2O_5$, 10 g $K_2S_2O_5$, and 2 g NH_4HF was used for identifying parent grains [22] (austenitic grains) with the help of linearly polarized light (LEICA DML 5000 light optical microscope). The average grain width was measured by the line intercept method [23] and the columnar architectures within molten pools were treated as different grains [24].

Details regarding hardness measurements and the investigation of phase transformation behaviour through DSC (Differential Scanning Calorimetry) can be found in the Section 3.2.4 in Chapter 3. All characteristic temperatures were determined by using the intersecting tangents method [25].

Dislocations and precipitates of fabricated NiTi samples were investigated using a JEM-2200FS transmission electron microscope (TEM) equipped with an energy dispersive spectrometer (EDS) system. The TEM specimens were prepared by electropolishing disks

with a diameter of 3 mm in a twin-jet electro-polisher using 10% perchloric acid and 90% ethanol as electrolytes.

Due to overlapping NiTi martensitic peaks at room temperature, it is difficult to investigate the broadening of XRD peaks. Hence, the high-temperature X-ray diffraction (XRD) for achieving parent phase phases was used in this work. All samples were heated to 423 K (higher than A_f, but not causing recovery/recrystallization [26]) during the XRD measurements. The XRD (Bruker D8 Discover diffractometer, Incoatec Microfocus Source (IµS)) measurements were conducted between 38° and 150° using a diffractometer with a Cu target, a step size of 0.04° 2θ and the counting time 20 s per frame. LaB_6 powder was used for the determination of the instrumental contributions to the peak width.

4.2.2. Finite Element Modelling

To study the effect of hatch distance on melt pool dimensions and their temperature field, Finite Element Analysis (FEA) was employed. A 3D thermal analysis model was developed using COMSOL Multiphysics Modelling Software (Version 5.5, COMSOL Ltd., Cambridge, UK).

4.2.2.1. Governing Equations and Volumetric Heat source

The thermal field was obtained by solving the following transient 3D heat conduction equation using the temperature-dependent thermal properties of the material:

$$\rho(T)C_p(T)\frac{\partial T}{\partial t} = Q + \nabla(k(T)\nabla T) \qquad (4.1),$$

where $\rho(T)$ (kg m^{-3}) is the temperature-dependent density, $C_p(T)$ (J kg^{-1} K^{-1}) is the temperature-dependent specific heat capacity, $k(T)$ (W m^{-1} k^{-1}) is the temperature-dependent thermal conductivity, and Q (W mm^{-3}) is the net volumetric heat flux.
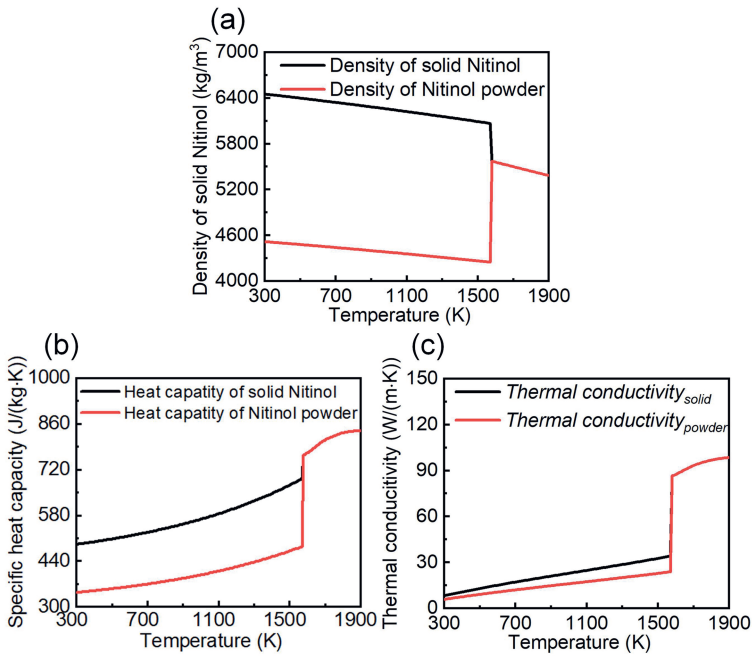
Figure 4.1. Temperature-dependent thermal-physical properties of Nitinol alloys used for FEA: (a) the density, (b) the specific heat capacity, and (c) the thermal conductivity.

The temperature-dependent thermal-physical properties [27, 28] used in this work were taken from literature or calculated by using Thermo-Calc software (Version 2020a, Thermo-Calc, Stockholm, Sweden) based on TCHEA2 (High Entropy Alloys version 2.1) database (Figure 4.1). In the solid state, powdered metal and the same metal in bulk form exhibit different thermal-physical properties. This difference can be simplified as a function of the porosity of the powder bed . Since the measured relative packing density of the powder is approximately 0.7, the temperature-dependent thermal-physical properties of Nitinol alloys in the powdered state before melting are proportionally decreased to approximately 70% of their original values.

Considering the thermocapillary flow within melt pools, artificially corrected factor α was induced as $k_2 = \alpha k_1$ (since only the conduction mode melt pool was shown in this work, α is selected as 2.5 [29]) when temperature is higher than the melting point of NiTi, where k_1 is the usual thermal conductivity of NiTi and k_2 is the modified one [29, 30].

Due to the lack of experimentally measured laser absorptivity, the Rosenthal equation was used to estimate the laser absorptivity of NiTi powder layers based on experimentally measured melt pool width [31]. The calculated laser absorptivity was found as 0.4 [31]. Although the Rosenthal equation relies on several restrictive assumptions [31]: only conduction is considered, heat of fusion is not included, thermal properties do not depend on temperature, and the calculation applies to remelting (no addition of powder), the estimated melt-pool sizes have been found to be realistic and close to experimentally measured values. Therefore, it is feasible to estimate laser absorptivity based on the Rosenthal equation and experimentally measured melt pool width.

The applied laser energy is separated into three portions, including reflection, absorption, and transmission of power. Only the absorbed energy is used to melt the powders and previously solidified layers. The laser energy can travel a certain depth along the powder bed. Therefore, the heat transfer through the depth direction on the powder bed was also considered in the present model. The laser penetration depth can be estimated based on the Beer-Lambert attenuation law. Therefore, the volumetric heat flux can be expressed as:

$$Q(x,y,z) = \frac{Q_0(x,y)}{\delta} \exp(-\frac{|z|}{\delta}) \qquad (4.2),$$

where Q_0 is the heat flux on the upper surface (W m^{-2}), $\delta = 65$ μm is the optical penetration depth (μm) of the used material [32], $|z|$ is the absolute value of the z-coordinate.

The distribution of surface heat flux Q_0 across the powder bed is presumed to be Gaussian, which can be mathematically represented as:

$$Q_0(x,y) = \frac{2AP}{\pi R^2} \exp(-\frac{2((x-vt)^2 + y^2)}{R^2}) \qquad (4.3),$$

where P is the laser power, A is the laser absorptivity of materials, and R is the laser beam radius at which the energy density is minimized to $1/e^2$ of that at the centre of the laser spot.

4.2.2.2. Geometrical description of modelling

To investigate the effect of hatch distance on melt pool dimensions and thermal gradients, single-track simulations are presented. The schematic of the designed geometry for investigating the effect of various hatch distances is shown in Figure 4.2. Considering

that hatch distances directly affect overlapping ratios between adjacent laser tracks, previously solidified parts should be included when applying various hatch distance conditions during FEM simulations. Therefore, the top layer was divided into two parts, i.e. the previously solidified part and the powder part. The hatch distance was reflected by the width of the overlapping zone and can be adjusted by changing the laser beam centreline position (Figure 4.2).
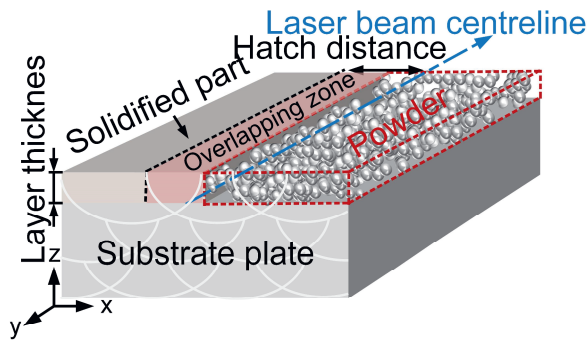
Figure 4.2. The schematic for simulation of various hatch distances in the single laser track.

To understand thermal histories during L-PBF processes, multiple tracks FEM simulations were carried out in the same layer. The 3D finite element model and the scanning strategy are shown in Figure 4.3. In total, 9 tracks were simulated to make L-PBF parts cooling down to the NiTi recrystallization temperature (873 K) [26].

Figure 4.3. (a) The 3D finite element model and (b) the scanning strategy.

4.3. Results

4.3.1. Microstructure evolution as a function of hatch distance

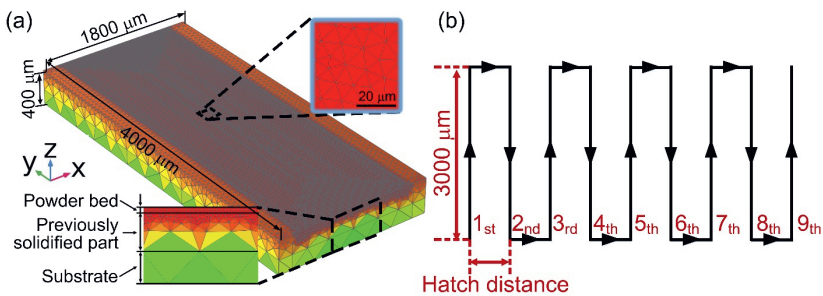Optical micrographs of samples A1–A3 fabricated with various hatch distances h of 100, 120, and 140 μm are shown in Figure 4.4. It can be seen that the grain size and morphology are highly affected by the hatch distances. From the top view of all samples, grain morphologies change from square-like (100 μm) to polygon-like and finally show irregular shaped (140 μm) (Figure 4.4 (a)–(c)). From the side view, the grains change from columnar to more equiaxed-like grains with increasing hatch distance (Figure 4.4 (d)–(f)). It should be noted that the grains in the sample with 140 μm hatch distance do not show epitaxial growth to subsequent layers, contrary to what is observed in samples with 100 and 120 μm hatch distances.
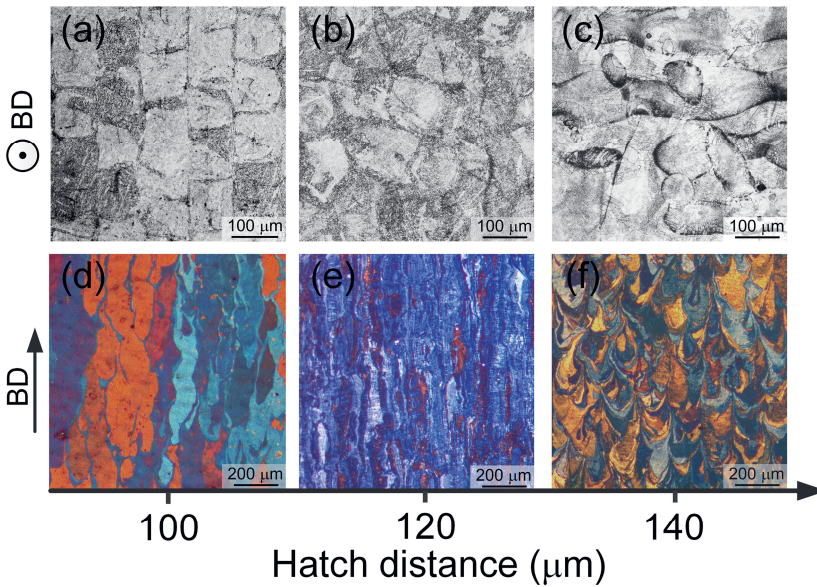

Figure 4.4. Optical micrographs for the NiTi alloys fabricated with different hatch distances h of (a, d) 100 μm, (b, e) 120 μm and (c, f) 140 μm. Pictures (a–c) display the cross-section perpendicular to the building direction (BD), and pictures (d–f) were taken under the polarized light condition (to show the grain boundaries of the parent phase) parallel to the building direction.

Figure 4.5 depicts the average grain width, length and aspect ratios (the ratio of grain length to the grain width) for the various hatch distance conditions. Both grain width and length show the monotonically decreasing trend with increasing the hatch distance (Figure 4.5 (a)). The average grain width decreases from ~58 to 29 µm and the average grain length decreases from ~454 to 167 µm (Figure 4.5 (a)). However, the length to width aspect ratio of the grains shows an initial increase and then a decrease (Figure 4.5 (b)), implying three types of grain growth characteristics for these three hatch distance conditions. With increasing hatch distance from 100 to 120 µm, fine width grains were obtained (due to the weakening of reheating induced grain growth [22] (Figure 4.4 (d) and (e))). Then, with further increasing hatch distance to 140 µm the grain growth changes from columnar grain growth (Figure 4.4 (e)) to equiaxed grain growth (Figure 4. 4 (f)).
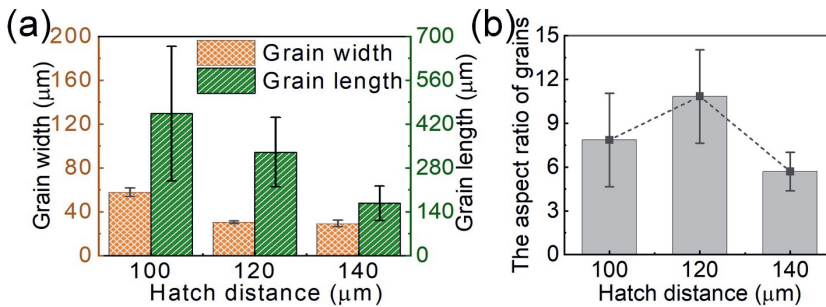

Figure 4.5. (a) The austenitic grain width and length (measured from Figure 4.4 (d)–(f)); (b) the aspect ratio (the ratio of grain length to the grain width) of grains in all hatch distance conditions.
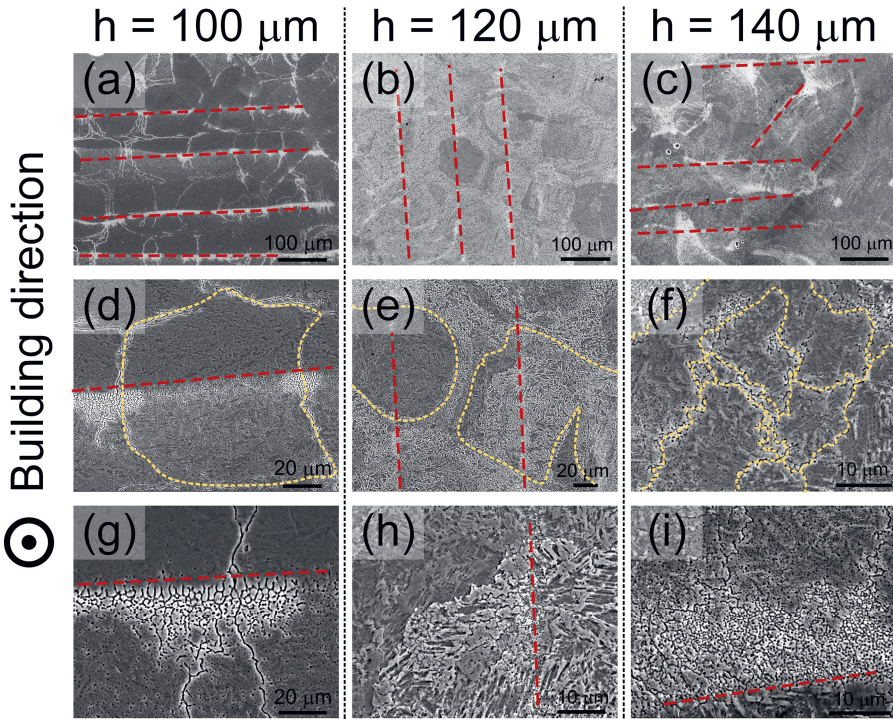
Figure 4.6. SEM micrographs for the NiTi alloys fabricated with different hatch distances of (a, d, and g) 100 μm, (b, e, and h) 120 μm and (c, f, and i) 140 μm. All pictures are depicted on the cross-section perpendicular to the building direction (BD) (Melt tracks were shown as red dash lines and parent grains were circled by yellow dash lines).

SEM observations on the top surfaces are shown in Figure 4.6. The melt tracks and corresponding boundaries can be traced in Figure 4.6 (a)–(c) (red dash lines). Parent grain (austenitic grains) boundaries are contoured by yellow dash lines in Figure 4.6 (d)–(e), which indicates grain morphology change from equiaxed to cellular structures with increasing hatch distance from 100 to 140 μm. As shown in Figure 4.6 (g)–(i), finer cellular structures were observed at melt track boundaries, and such microstructures are different from those fabricated via conventional methods (such as, wrought and powder metallurgy) [33-35]. These features result from heterogeneous nucleation induced by the re-melting of previously solidified tracks at the melt pool boundaries [36].

4.3.2. Micro-hardness, chemical composition and phase transformation

As shown in Figure 4.7 (a), the micro-hardness increases with hatch distance (from ~193 to 226 HV). It appears that the chemical composition changes, i.e. the Ni content increases with the hatch distance (due to reducing the extent of element evaporations) (Figure 4.7 (b)). To investigate the effect of hatch distance on the phase transformation behaviour of L-PBF NiTi samples, DSC measurements were conducted. Unlike the monotonically increasing correlation between the micro-hardness or Ni content and the hatch distance, the L-PBF NiTi sample produced with a 120 µm hatch distance shows the lowest phase transformation temperatures among all samples (Figure 4.7 (c) and (d) and Table 4.1). For NiTi SMAs, phase transformation temperatures mainly depend on Ni/Ti ratio [15] and dislocation densities [37]. Generally, the higher the Ni content the lower the phase transformation temperature [15]. Dislocations can hinder martensitic transition (a higher undercooling is required to trigger the B2 / B19′ transformation [38]), resulting in lower phase transformation temperatures. Since the Ni content increases linearly with the hatch distance (Figure 4.7 (b)), phase transformation temperatures should also have a linear relationship with the hatch distance that is if only Ni content plays the dominant role in phase transformation. However, by comparing Ni content and phase transformation temperatures, it is clear that an additional factor, such a dislocations, may also be involved. Therefore, to investigate the effect of hatch distance on dislocation densities in L-PBF NiTi samples, TEM, high-temperature XRD, and FEM simulations were conducted and presented in follow up sections.

4
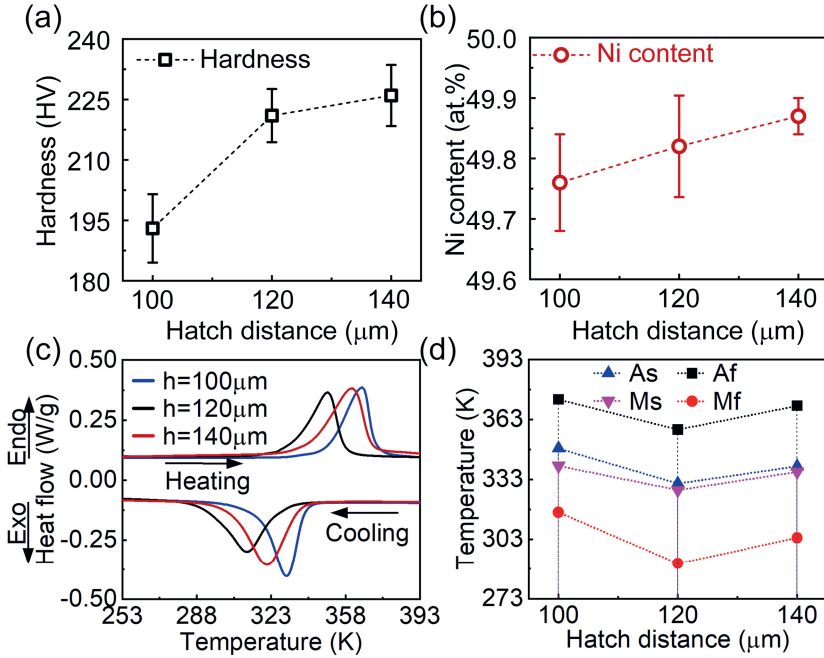
Figure 4.7. Samples with various hatch distance values: (a) Micro-hardness and (b) Ni content; (c) DSC curves and (d) corresponding phase transformation temperatures.

Table 4.1 Phase transformation temperatures determined by DSC.

Hatch distance (μm) Temperature (K)	100	120	140
Martensite start temperature (M_s)	339.8 ± 0.6	327.7 ± 0.9	336.8 ± 0.6
Martensite finish temperature (M_f)	314.4 ± 0.9	290.9 ± 0.6	303.8 ± 1.1
Austenite start temperature (A_s)	348.5 ± 0.3	331.0 ± 0.2	341.2 ± 0.2
Austenite finish temperature (A_f)	373.0 ± 0.3	357.9 ± 0.2	369.8 ± 1.2

4.3.3. TEM observation and high-temperature XRD

Figure 4.8 illustrates the representative TEM microstructure of the L-PBF NiTi alloys fabricated with various hatch distances. For all samples, nano-sized precipitates in the range of 20–60 nm (marked by orange arrows) were observed. Based on the EDS results, precipitates are $Ti_4Ni_2O_x$, which are commonly detected in near equiatomic NiTi alloys [39]. It should however be noted that the lattice parameters and crystal structure of Ti_2Ni phase and $Ti_4Ni_2O_X$ are the same, because O resides interstitially in the $Ti_4Ni_2O_x$ phase [40, 41].

For the sample with 100 µm hatch distance, serrated martensite phases with multiple bending were found (Figure 4.8 (a) and (b)). This feature originates from the shear force subjected to martensite with micro stresses [42]. Besides, the secondary twin structure was observed in the serrated martensite, which is indexed as the $\left\{11\bar{1}\right\}$ type I twin. Since the secondary twin is related to the local stress concentration [43], it further proved the existence of micro stress in the sample with 100 µm hatch distance. The micro stress field should be attributed to thermal stress induced by the high cooling rate during L-PBF process.

For the sample with the 140 µm hatch distance, martensite phases mainly consists of pure martensite structure of twins and secondary martensite twins (Figure 4.8 (c)). The TEM image of pure martensite twins and its corresponding selected area diffraction patterns (SADPs) are shown in Figure 4.8 (f) and (i). Some precipitates ($Ti_4Ni_2O_x$) are embedded into martensitic twin boundaries (Figure 4.8 (f)). $\langle 011 \rangle$ type II twins were determined by its SADPs, which is commonly found in the B19′ martensite [43]. The secondary martensite twins indicate the presence of the local stress concentration, which is similar with the sample with 100 µm hatch distance.

4
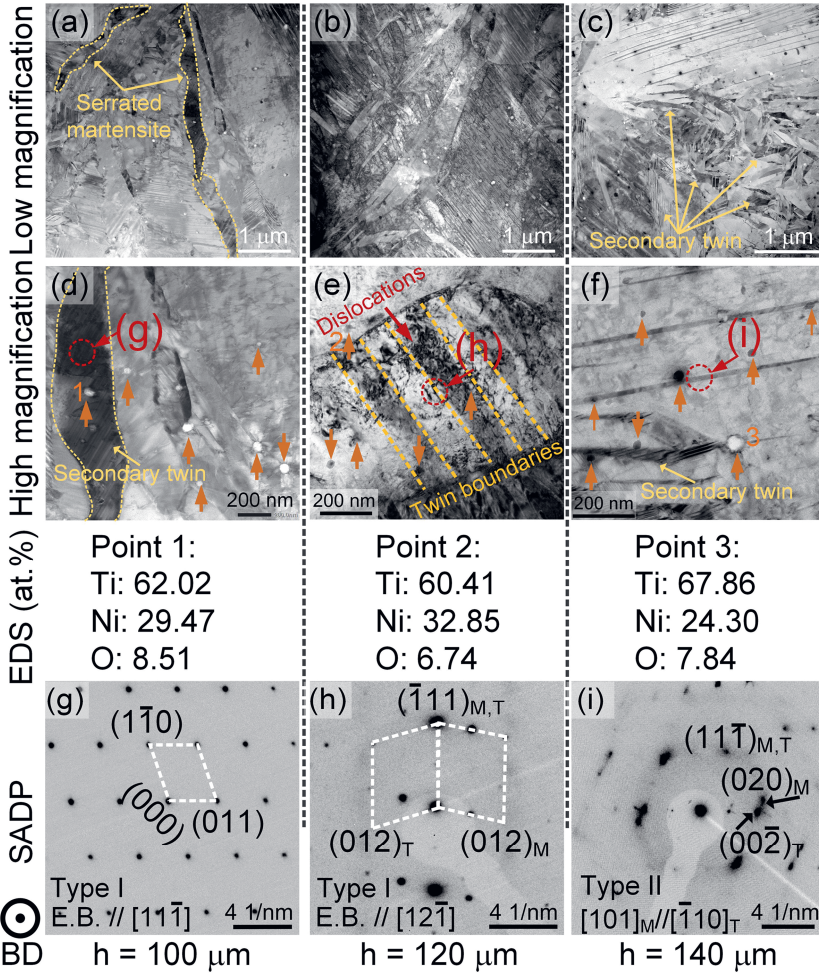
Figure 4.8. TEM images and corresponding selected area diffraction patterns of L-PBF NiTi fabricated with various hatch distances h of (a, d and g) 100 µm, (b, e and h) 120 µm, and (c, f and i) 140 µm (the upper part depicts low magnification and the lower part high magnification to distinguish the difference in dislocations and precipitates).

It should be noted that there are local micro stresses (implied by secondary martensite twins) in samples with the hatch distance of 100 and 140 µm, but dislocations were barely observed. These phenomena indicate there is no micro-plastic deformation in the samples

with the hatch distance of 100 and 140 μm. There are two possible reasons for the absence of micro-plastic deformation in L-PBF samples: (1) the local micro stress is not high enough to activate slip systems [44]; (2) reheating from follow-up laser tracks causes the elimination of dislocations [12]. The corresponding mechanisms are discussed in Section 4.1.

In contrast, dislocations were observed throughout the martensite matrix of the 120 μm hatch distance sample (Figure 4.8 (e)), showing a higher dislocation density in the 120 μm hatch distance samples. Based on SADPs in the sample with 120 μm, $\{11\overline{1}\}$ type I martensite twins were determined. Since this type of martensite twins are often observed in deformed NiTi alloys [45], it can further prove that dislocations are induced by micro plastic deformation in the sample with 120 μm. Considering that dislocations can hinder martensite transformation and lower phase transformation temperatures, the reason for the lowest phase transformation temperature in the 120 μm hatch distance sample (Figure 4.7 (d)) is attributed to its high dislocations density.

Although TEM observations can clearly show detailed microstructural characteristics, only locally representative areas were observed, and it is hard to quantitatively evaluate dislocation density on a larger scale. Therefore, to quantitatively investigate the dislocation density of these samples, high temperature XRD measurements were conducted.

In general, the micro-stain induced by dislocations and the crystallite size can cause the broadening of X-ray diffraction peak profiles. By calculating the full width at half maximum (FWHM) of the diffraction profiles, the peak broadening can be quantitatively evaluated [44, 46, 47]. Since the main phase is martensite (Monoclinic phase, B19′) at room temperature for all samples (Figure 4.9 (a)), many peaks are overlapping. This complicated the calculation of the FWHM. To overcome this issue, all samples were in-situ heated to 423 K (> A_f) to induce austenitization (Figure 4.9 (b)). Due to the simple peak profiles and the high symmetry of the high temperature parent phase (BCC, B2), the evaluation of HT X-ray diffraction profile broadening can then be smoothly performed. To improve accuracy of measured FWHM, the instrumental broadening ($\beta_{hkl(Instrumental)}$) was considered to achieve actual FWHM (β_{hkl}). The β_{hkl} can be acquired by using the as follows equation:

$$\beta_{hkl} = \sqrt{\beta_{hkl(Measured)}^2 - \beta_{hkl(Instrumental)}^2} \qquad (4.4).$$

To calculate instrumental broadening, LaB$_6$ powder is used as standard sample. The equation 4.4 is applied since the convolution of x-ray beam is in a shape of Gaussian distribution. For NiTi shape memory alloys, the (110)$_{B2}$ peak is usually chosen to investigate

dislocation density and coherently scattering region size by evaluating the peak broadening [66, 67]. The $(110)_{B2}$ peaks of all samples measured at 432 K and corresponding FWHM are shown in Figure 4.9. It can be seen that there are no other peaks around these 3 $(110)_{B2}$ austenite peaks (Figure 4.9 (b)), which indicates that all samples are austenitized by heating to 423 K.

4
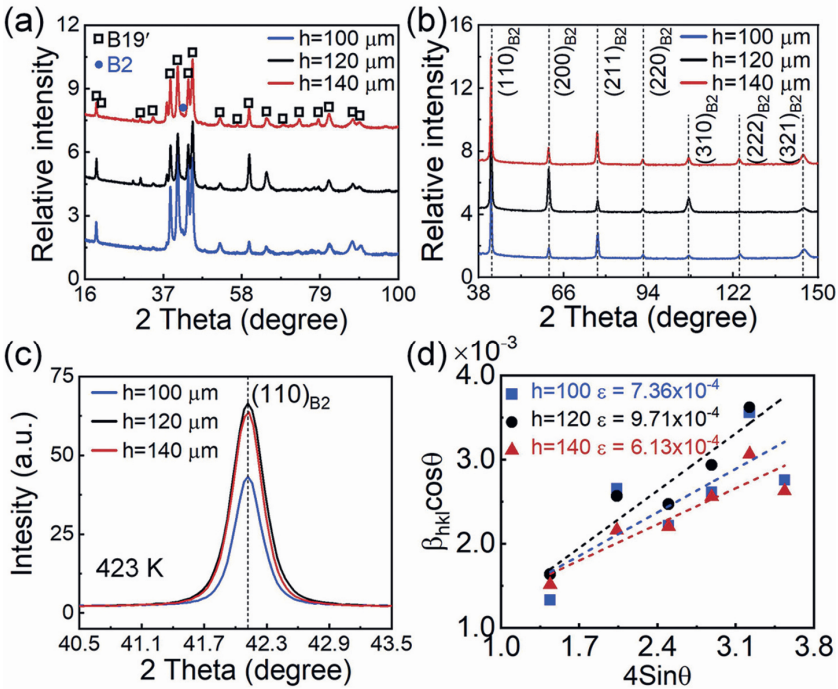
Figure 4.9. The $(110)_{B2}$ XRD peaks of L-PBF NiTi alloys were measured at (a) the room temperature (RT) and (b) at 423 K (> A_f); (c) the $(110)_{B2}$ peaks measured at 423K and (d) linear fitting demonstrating the values of micro strain ε varied with hatch distances.

To distinguish peak broadening contributions originating from either coherently scattering region size or micro-strain induced by dislocation, Williamson-Hall analysis based on uniform deformation model (UDM) is used [48, 49]. In the UDM, the Williamson-Hall equation can be written as

$$\beta_{hkl} \cos\theta = \frac{k\lambda}{D} + 4\varepsilon\sin\theta \qquad (4.5),$$

where β_{hkl} is the FWHM, θ is the diffraction angle and k is the shape factor (0.94) [48], λ is the wavelength of X-rays used (herein Cu-Kα1 wavelength = 1.540562 Å), D is coherently scattering region size and ε stands for micro-strain. By plotting $\beta_{hkl} \cos\theta$ versus the $4\sin\theta$, the coherently scattering region size can be estimated from the Y-intercept (the intercept is inversely proportional to the coherently scattering region size [50]) and micro-stain induced by dislocation is derived from the fitted slope [50-52] (results shown in Figure 4.9 (d)). Then, the dislocation density can be calculated from the obtained micro-strain based on the equation (4.6) [44]:

$$\rho = \frac{k}{F} \cdot \frac{\varepsilon^2}{\|b\|^2} \qquad (4.6),$$

where ρ is dislocation density and $\|b\|$ is the magnitude of Burgers vector, and F and k are constants chosen to be 1 and 14.4, respectively, for bcc crystal [75]. For BCC structure, the magnitude of Burgers vector is $\|b\| = \dfrac{a}{2\sqrt{u^2+v^2+w^2}}$, where a is the unit cell edge length of the crystal, and u, v and w are the components of the Burgers vector [53]. For NiTi, the slip direction is $\langle 111 \rangle$ [54] and a = 3.015 Å [55]. The magnitude of Burgers vector of B2 NiTi can be calculated: 2.61×10^{-10} m. The coherently scattering region size, micro-strain induced by dislocation and dislocation density of austenitic NiTi can be summarized in Table 4.2. The magnitude of dislocation densities calculated in this work is comparable to other reported works [44, 56]. The sample with 120 μm hatch distance has the highest dislocation density, which is consistent with DSC and TEM results.

It should also be noted that L-PBF NiTi consists of both relatively large grains and small size coherently scattering regions (measured by XRD) [57]. If the fraction of small size coherently scattering region is comparable with large size grains, peak-splitting will be observed in the XRD patterns [58]. A sharp single peak can be seen in Figure 4.9 (c), indicating negligible amount of small size coherently scattering regions. In this case, the change of phase transformation temperature of NiTi with various hatch distances mainly results from different dislocation densities, rather than coherently scattering regions.

4

Table 4.2 Calculated micro-strain and dislocation densities

Hatch distance (μm)	Coherently scattering regions (nm)	Micro-strain (%)	Dislocation density (m^{-2})
100	190	7.36×10^{-2}	1.2×10^{14}
120	478	9.71×10^{-2}	2.0×10^{14}
140	238	6.13×10^{-2}	7.9×10^{13}

To confirm the reason of various $(110)_{B2}$ FWHM in measured 3 samples, coherently scattering region sizes should be firstly determined. Since size induced peak broadening effect is pronounced only for coherently scattering region size less than 100 nm [64, 74], the smallest coherently scattering region size is ~190 nm which is much larger than the critical size. Hence, the micro-stain induced by dislocations is believed to be the main reason for XRD peak broadening.

By comparing FWHM of samples with various hatch distances, the sample with 120 μm has the largest FWHM (Figure 4.9 (d)), which indicates the highest dislocation density. Therefore, combining the DSC, TEM, and HT-XRD results, it can be proved that the sample fabricated with the moderate hatch distance of 120 μm can produce high density of dislocations.

4.3.3 The effect of hatch distance on the cyclic stability of L-PBF NiTi

For NiTi-based shape memory alloys, cyclic stability is essential to ensure their reliability during engineering applications [59]. To achieve this goal, expensive heat treatments, cold working, or severe plastic deformation techniques are generally used [60-63]. However, the above-mentioned methods might not be suitable for L-PBF parts since the pre-designed geometry could be changed [64]. Therefore, in-situ process tailoring of the microstructure is a good alternative to improve NiTi cyclic stability. This study showed that such processing parameter as hatch distance can significantly tailor the microstructure. Hence, it is important to investigate and understand the effect of hatch distance on the cyclic stability of L-PBF NiTi.

Figure 4.10 depicts the cyclic DSC response of L-PBF NiTi alloys fabricated with various hatch distances during multiple thermal cycling. The transformation temperatures

from the acquired data are generally measured by drawing tangents to the start and end regions of the transformation peak and the baseline of the heating and cooling curves. For all samples, the characteristic phase transformation temperatures decrease with increasing number of cycles (DSC curves gradually shift toward the lower temperature side in Figure 4.10 (a–c)). These phenomena are so-called thermal cyclic degradation, which is caused by the accumulation of dislocations and their effect on subsequent transformation cycles [59, 65]. By comparing changes of characteristic phase transformation temperatures after thermal cycling (Figure 4.10 (d)), the sample with 120 μm hatch distance has the best thermal-cyclic stability, and there is almost no change in the austenite finish temperature ($\Delta T_{Af} = 0$ °C) and the martensite starting temperature ($\Delta T_{Ms} = 0$ °C). In contrast, samples with 100 μm hatch distance show 8.2 and 7.6 °C temperature degradations for its A_f and M_s, respectively. For 140 μm hatch distance condition, the sample exhibits 6.8 and 4.6 °C temperature degradations. Therefore, the good thermal-cycling degradation resistance is shown in the samples with 120 μm hatch distance, indicating a stable working temperature window during thermal cycling.
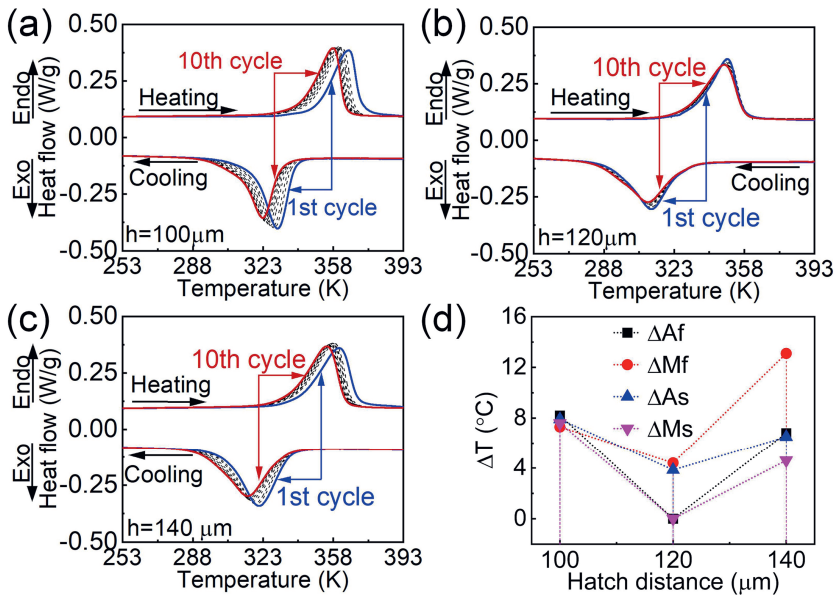
4

Figure 4.10. Effect of hatch distance on the cyclic stability of L-PBF NiTi, determined for 10 thermal cycles determined by DSC: (a) h = 100 μm, (b) h = 120 μm (c) h = 140 μm; (d) characteristic phase transformation temperatures change between the 1st and 10th cycles

For NiTi, high-density dislocations and ultra-fine grains (< 100 nm) can effectively improve functional stability by impeding dislocation movement during thermal cycling [66, 67]. Since small size coherently scattering regions have a very low fraction and their sizes are larger than 100 nm, thermal cyclic stability in all investigated herein L-PBF NiTi depends on only dislocation densities. The sample with h = 120 μm shows the best thermal cyclic stability due to the highest dislocation density (2.0×10^{14} m^{-2}). In contrast, the largest ΔT_{Mf} of 13.1 °C was seen in the sample with 140 μm hatch distance, which has the lowest dislocation density of 7.9×10^{13} m^{-2} (Table 4.2).

4.4. Discussion

4.4.1. The effect of hatch distance on microstructure

In the condition of constant laser power and scanning velocity, hatch distance can determine the overlapping between the adjacent laser tracks. A narrower hatch distance results in a higher overlapping ratio. In this case, more of the previously solidified part is involved in melting of the next laser track. Therefore, the effect of hatch distances on each laser track can be evaluated by tuning the ratio of previously solidified parts in FEM simulations (the schematic is shown in Figure 4.2). To obtain reliable simulation results and evaluate the predictability of the FEM, 2 more hatch distance values of 80 and 140 μm (beyond experimental observations of this work) were also included in FEM simulations.

As shown in Figure 4.11 (a)–(c), simulated melt pool dimensions are very close to that of the experimentally measured values (~ 3% deviation from experimentally measured melt pool width and depth in the h = 120 μm condition), which indicates the reasonable accuracy of FEM simulations. Based on the results from the single laser track FEM simulations, overlapping zones slightly decrease with increasing hatch distances (Figure 4.11 (a) and (d)) and there will be no overlap (melt pool width smaller than hatch distance) when the hatch distance is larger than 140 μm (Figure 4.11 (a)), which is consistent with the previous work [68]. In addition, the half widths and depths of melt pool (the part including overlapping zone) increase with hatch distance (Figure 4.11 (c)). The reason is attributed to a higher heat capacity, a higher density and a higher thermal conductivity in solid NiTi (lower hatch distance corresponding to more previously solidified parts) compared to NiTi powder, which is inversely proportional to the melt pool dimensions [31].
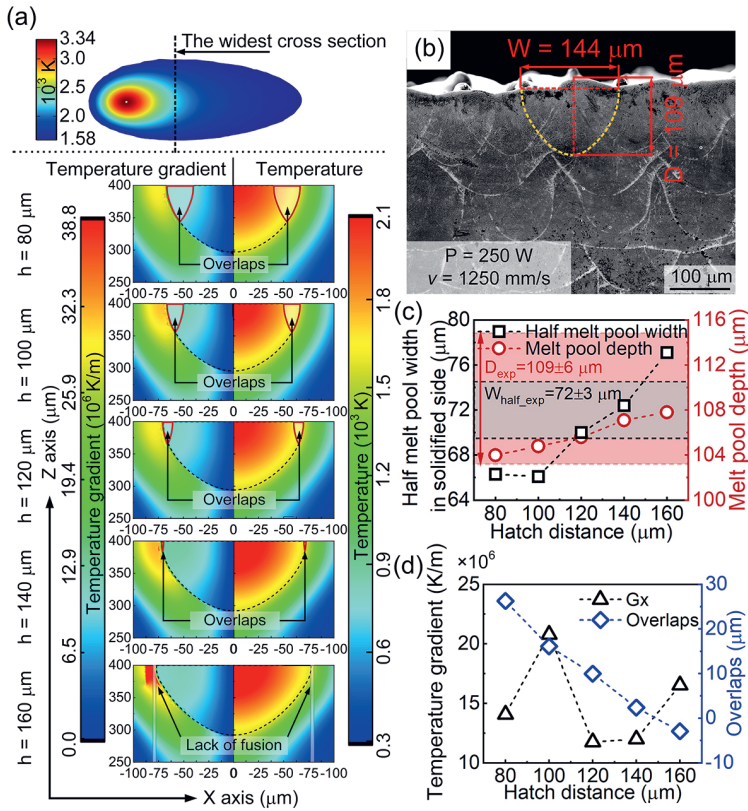
Figure 4.11. (a) The widest cross-section of the simulated melt pools featuring various hatch distance conditions: temperature gradients (the left side) and temperature fields (the right side) (solidus lines are shown as black dash lines); (b) the cross-sectional L-PBF NiTi fabricated by using E_l=250/1250 J mm^{-1} showing melt pool characteristics [68]; (c) half-width and depth of the melt pools as a function of hatch distance (derived from FEM simulations). Experimentally measured melt pool half-width and depth are shown as black and red dash lines, respectively; (d) temperature gradients in the solid-liquid interface (Z=399 μm) toward X axis as functions of hatch distance.

As reported by Bormann et al. [22], square-like grains from the top view of L-PBF NiTi parts (Figure 4.4 (a) and Figure 4.6 (d)) suggest epitaxial grain growth along the direction perpendicular to the laser beam movement. In this work, the square-like grains gradually disappear with increasing the hatch distance (Figure 4.4 (a)–(c) and Figure 4.6 (d)–(f)), indicating the fading of epitaxial grain growth. To understand the degradation of epitaxial

grain growth, the thermal gradient perpendicular to the laser beam movement direction (i.e., toward X axis, Gx) in various hatch distance conditions was calculated (Figure 4.11 (d)). Generally, grain growth during solidification tends to be along the direction of the largest temperature gradient [69, 70], which determines the epitaxial solidification during the L-PBF process [71]. Among all hatch distance conditions, the sample with the hatch distance of 100 µm has the highest temperature gradient of 2.1×10^7 K m^{-1} in front of the solid-liquid interface (Figure 4.11 (d)). Therefore, for the sample with 100 µm hatch distance it is easier to achieve the epitaxial grain growth than for the samples with other hatch distances. The simulated results also match well with the experimental observations (Figure 4.4 (a)–(c) and Figure 4.6 (d)–(f)).

It should be noted that temperature gradient toward X axis (Gx) increases again when the hatch distance is larger than 120 µm. However, since the overlap is small (even lack of fusion in the condition of 160 µm hatch distance) (Figure 4.11 (a)), there is no sufficient nucleation site for the epitaxial grain growth. Hence, the squared-like grains still degenerate into equiaxed grains even the Gx increases again (when h>120 µm).

4.4.2. Evolution of dislocations

The current work demonstrates that the hatch distance shows a significant influence on the dislocation density. The variation of phase transformation behaviour with hatch distance is believed to be the direct result of dislocations densities. With the aid of multiple laser track FEM simulations, the dislocation evolution can be connected with the thermal histories of L-PBF NiTi alloys [12].

The middle point between the first and second laser tacks is selected as the monitoring point (the schematic is shown in Figure 4.12 (a)), which can directly reflect the effect from the following laser tracks. The thermal history profiles of L-PBF NiTi in various hatch distance conditions (Figure 4.12 (b)) can be divided into 3 processes: 1) the first melting process (corresponding to the first peak); 2) the re-melting process (the second peak and its temperature is higher than the melting point of NiTi) and 3) the reheating process from the following laser tracks. It should be noted that even though the selected monitoring point will be remelted by the subsequent layer, it can still be considered capable of exhibiting representative features of the thermal histories of L-PBF NiTi fabricated with varying hatch distances.
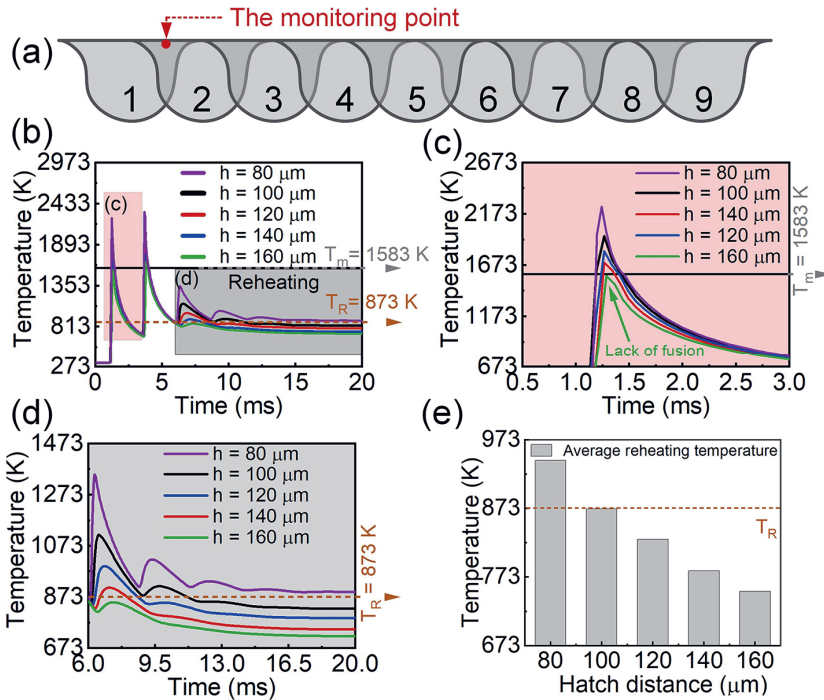
Figure 4.12. (a) The schematic of multiple laser tracks in FEM simulations and the corresponding monitoring point of thermal histories (the middle point between the first and second laser tracks, marked as the red point); (b) thermal histories of nine tracks for various hatch distances and enlarged zones for (c) the first track and (d) reheating from the following tracks; (e) The average reheating temperatures.

For the first melting process (Figure 4.12 (c)), the peak temperature in the monitoring point decreases with increasing hatch distance and is even lower than the melting point of NiTi when applying 160 μm hatch distance. In the reheating stage (Figure 4.12 (d)), the higher hatch distance value leads to the lower reheating temperature and the shorter cooling time to trigger in-situ annealing, which suggests less heat input for recrystallization of NiTi. By comparing the normalized reheating heat input (with respect to the reheating time) (Figure 4.12 (e), above the recrystallization temperature 873 K [26]), a narrower hatch distance results in a higher extent of reheating. This accounts for the lower dislocation density (due to recrystallization) (shown in Figure 4.8 (a) and (d)) and the large grain size (due to the grain growth) (Figure 4.4 (a) and (d)). Similar phenomena were also observed by Ma et al. [12]. With increasing hatch distance, the extent of reheating is weakened. Hence, more dislocations

due to micro-plastic deformation induced by thermal stress will remain in the large hatch distance condition.

It worth noting that there is not a specific recrystallization temperature theoretically defined for metallic materials. Generally, the driving force of recrystallization is the reduction of stored energy within the material, which is influenced by factors like grain size, defect density (such as dislocation density), stored elastic energy, and grain boundary types [72]. In this study, we have selected 873 K as the reference recrystallization temperature to provide a semi-quantitative evaluation of the recrystallization driving force among samples with varying hatch distances. Tadayyon et al. [26] observed in their study that heat treatment at 873 K can induce recrystallization. Given that the investigated NiTi alloy in their work shares similar alloying composition and grain sizes with our NiTi, 873 K is chosen as the recrystallization temperature indicator.

In this work, the dislocation density does not decrease monotonously with increasing hatch distance and is rather determined by the co-effect of the recrystallization triggered by in-situ reheating and the micro-plastic deformation induced by thermal stress (due to thermal shrinkage). For the L-PBF parts, when applying a higher hatch distance, there will be a smaller volume experiencing thermal shrinkage and this is believed to decrease thermal stress. In this case, a low hatch distance value indicates a high energy input for recrystallization but a high thermal stress level, and vice versa.

In this context, the narrower hatch distance can introduce more thermal stresses but also contributes to promoting in-situ recrystallization annealing. In contrast, the larger hatch distance can reduce thermal stresses, which is achieved by less volume thermal shrinkages and less heat input for recrystallization. Therefore, dislocations in L-PBF NiTi parts are a result of the competition between micro-plastic deformation induced by thermal stresses and in-situ recrystallization. In this study, when the hatch distance is lower than 120 µm, the in-situ recrystallization plays a detrimental role regarding dislocations. While applying the hatch distance larger than 120 µm, the in-situ recrystallization is weakened whereas the thermal shrinkage volume (related to dislocations) is also reduced. Finally, the 120 µm hatch distance is the critical value, which promotes the highest dislocation density in all studied cases. It should be noted that the discussion about thermal stress herein is mainly qualitative. To quantitatively evaluate thermal stress, Finite element Analysis including thermomechanical coupling between temperature and stress fields needs to be further carried out in future work.

As reported by Carroll et al. [73], dislocation substructures make the formation of B19′ more difficult in that they act as obstacles—an effect that can be seen in a shift of the Gibbs free energy curve of B19′ towards higher energies (Figure 4.13). Therefore, the sample with 120 μm hatch distance has the highest-density dislocation, indicating that makes the phase transformation equilibrium temperature towards lower temperatures. Accordingly, all four characteristic temperatures (A_s, A_f, M_s and M_f) of phase transformation in L-PBF NiTi with 120 μm hatch distance shows the lowest temperatures among all measured samples (Figure 4.7 and Table 4.1).
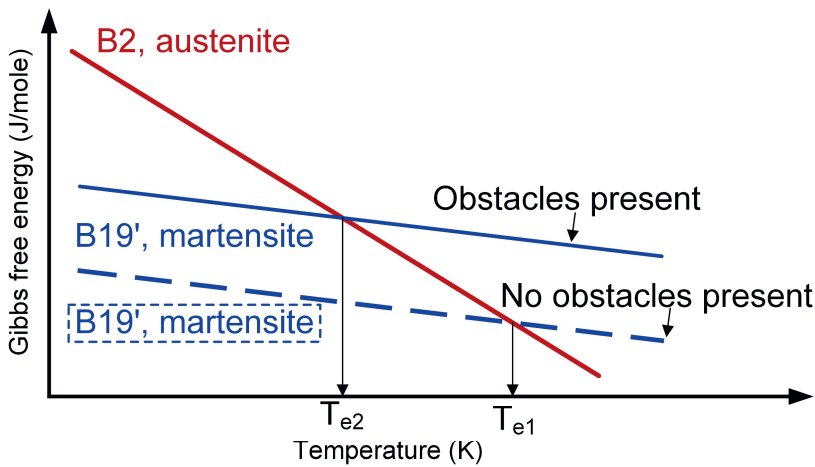
Figure 4.13. The schematic Gibbs free energy of austenite (B2) and martensite (B19′) as a function of temperature. The presence of obstacles (dislocations in this work) makes it energetically more difficult to form B19′ (reproduced based on [71]). T_{e1} is the equilibrium temperature between B2 and B19′ without dislocations and T_{e2} the equilibrium temperature between B2 and B19′ with the presence of dislocations.

Based on above results and discussions, it has been demonstrated that hatch distance is a significant and effective processing parameter, which can affect nano and micro structures of NiTi shape memory alloys. These structures in turn can determine phase transformation windows and thermal cyclic stability. For L-PBF process, the stable melt pool is determined by laser power and scanning velocity [68, 74], and layer thickness is often fixed in the regime

of 30–50 μm to ensure stable powder spreading [6]. Hence, hatch distance becomes a desirable processing parameter to be tuned during L-PBF process.

More work regarding cyclic thermal-mechanical testing to investigate the shape memory effect of L-PBF NiTi with various processing parameters was shown in the Chapter 5.

4.5. Conclusions

The present work investigated the effect of hatch distance on microstructure, phase transformation and thermal cyclic stability in NiTi alloys fabricated via laser powder bed fusion. The effect of hatch distance variation was studied, and it was shown that this parameter significantly affects the microstructure and dislocation evolution allowing for in-situ tailoring functional properties. The main findings can be summarized as follows:

1. NiTi austenitic grain size increases with increasing the hatch distance, and the grain's morphologies change from columnar to equiaxed. The squared-like grains from the top view of the 100 μm samples result from the enhanced epitaxial grain growth, which is attributed to a large thermal gradient along the transverse direction (relative to laser beam movement direction).

2. Phase transformation temperatures change linearly with hatch distance. The lowest phase transformation temperatures are observed in the 120 μm hatch distance samples and result from high dislocations density.

3. Combining TEM, HT-XRD, and FEM simulations, mechanisms of grain morphology and dislocation evolutions by applying various hatch distances are revealed. It has been shown that developed herein FEM models are appropriate tools to understand and predict microstructure evolution, which contributes to designing high-performance L-PBF NiTi shape memory alloys.

4. Due to the pre-existed high density dislocations, the samples with 120 μm hatch distance have a better ability to resist micro-plastic deformation induced by the phase transformation. As a result, the best thermal cyclic stability is found in all studied 120 μm samples.

5. Hatch distance can affect the number of heated volumes and reheating levels, which is related to thermal stresses and in-situ recrystallization. The thermal stress can

trigger dislocations by micro-plastic deformation and in-situ recrystallization can decrease dislocation densities. Through the competition between the two mentioned factors, different dislocation densities are shown in samples with various hatch distances.

In summary, the current results illustrate that the hatch distance should be of concern not only regarding the structural defects but also as a significant factor that contributes to tailoring microstructure, dislocation densities, phase transformation windows, and thermal cyclic stability in NiTi alloys. This work shows a new insight for fabricating in-situ tailorable L-PBF NiTi alloys and demonstrates a predictive model to evaluate further the various hatch distance effects. In the field of 4D printing metallic materials, phase transformation windows and microstructure (related to thermal-mechanical responses) are two concerning factors. Therefore, findings of this work provide a fundamental understanding about tailoring the two factors by tuning hatch distance, which can provide a novel pathway to design in-situ tailorable 4D NiTi shape memory alloys. More work related to the influence of hatch distance on the thermal-mechanical SME properties and functional fatigue in L-PBF NiTi has been shown in the Chapter 5.

4

References

[1] S. Saedi, N. Shayesteh Moghaddam, A. Amerinatanzi, M. Elahinia, H.E. Karaca, On the effects of selective laser melting process parameters on microstructure and thermomechanical response of Ni-rich NiTi, Acta Mater. 144 (2018) 552-560.

[2] S. Dadbakhsh, M. Speirs, J.-P. Kruth, J. Schrooten, J. Luyten, J. Van Humbeeck, Effect of SLM Parameters on Transformation Temperatures of Shape Memory Nickel Titanium Parts, Adv. Eng. Mater. 16(9) (2014) 1140-1146.

[3] T. Bormann, R. Schumacher, B. Müller, M. Mertmann, M. de Wild, Tailoring Selective Laser Melting Process Parameters for NiTi Implants, J. Mater. Eng. Perform. 21(12) (2012) 2519-2524.

[4] C. Haberland, M. Elahinia, J.M. Walker, H. Meier, J. Frenzel, On the development of high quality NiTi shape memory and pseudoelastic parts by additive manufacturing, Smart Mater. Struct. 23(10) (2014) 104002.

[5] L. Xue, K.C. Atli, S. Picak, C. Zhang, B. Zhang, A. Elwany, R. Arroyave, I. Karaman, Controlling martensitic transformation characteristics in defect-free NiTi shape memory alloys fabricated using laser powder bed fusion and a process optimization framework, Acta Mater. 215 (2021) 117017.

[6] Q.B. Nguyen, D.N. Luu, S.M.L. Nai, Z. Zhu, Z. Chen, J. Wei, The role of powder layer thickness on the quality of SLM printed parts, Arch. Civ. Mech. Eng. 18(3) (2018) 948-955.

[7] I.H. Ahn, Determination of a process window with consideration of effective layer thickness in SLM process, Int. J. Adv. Manuf. Technol. 105(10) (2019) 4181-4191.

[8] D. Herzog, V. Seyda, E. Wycisk, C. Emmelmann, Additive manufacturing of metals, Acta Mater. 117 (2016) 371-392.

[9] A.M. Khorasani, I. Gibson, A. Ghasemi, A. Ghaderi, A comprehensive study on variability of relative density in selective laser melting of Ti-6Al-4V, Virtual Phys. Prototyp. 14(4) (2019) 349-359.

[10] S. Greco, K. Gutzeit, H. Hotz, B. Kirsch, J.C. Aurich, Selective laser melting (SLM) of AISI 316L—impact of laser power, layer thickness, and hatch spacing on roughness, density, and microhardness at constant input energy density, Int. J. Adv. Manuf. Technol. 108(5) (2020) 1551-1562.

[11] M. Xia, D. Gu, G. Yu, D. Dai, H. Chen, Q. Shi, Influence of hatch spacing on heat and mass transfer, thermodynamics and laser processability during additive manufacturing of Inconel 718 alloy, Int. J. Mach. Tools Manuf. 109 (2016) 147-157.

[12] J. Ma, B. Franco, G. Tapia, K. Karayagiz, L. Johnson, J. Liu, R. Arroyave, I. Karaman, A. Elwany, Spatial Control of Functional Response in 4D-Printed Active Metallic Structures, Sci. Rep. 7(1) (2017) 46707.

[13] Y. Cao, X. Zhou, D. Cong, H. Zheng, Y. Cao, Z. Nie, Z. Chen, S. Li, N. Xu, Z. Gao, W. Cai, Y. Wang, Large tunable elastocaloric effect in additively manufactured Ni–Ti shape memory alloys, Acta Mater. 194 (2020) 178-189.

[14] I.D. McCue, G.M. Valentino, D.B. Trigg, A.M. Lennon, C.E. Hebert, D.P. Seker, S.M. Nimer, J.P. Mastandrea, M.M. Trexler, S.M. Storck, Controlled shape-morphing metallic components for deployable structures, Mater. Des. 208 (2021) 109935.

[15] J. Frenzel, E.P. George, A. Dlouhy, C. Somsen, M.F.X. Wagner, G. Eggeler, Influence of Ni on martensitic phase transformations in NiTi shape memory alloys, Acta Mater. 58(9) (2010) 3444-3458.

[16] J.K. Allafi, A. Dlouhy, K. Neuking, G. Eggeler, Influence of precipitation and dislocation substructure on phase transformation temperatures in a Ni-rich NiTi-shape memory alloy, J Phys Iv 11(PR8) (2001) 529-534.

[17] G.F. Eggeler, K. Neuking, A. Dlouhy, E. Kobus, Creep behavior of NiTi shape memory alloys and the effect of pre-creep on the martensitic phase transformation, Mater. Sci. Forum. (2000) 183-186.

[18] T. Waitz, T. Antretter, F.D. Fischer, N.K. Simha, H.P. Karnthaler, Size effects on the martensitic phase transformation of NiTi nanograins, J. Mech. Phys. Solids 55(2) (2007) 419-444.

[19] F.J. Gil, J.M. Manero, J.A. Planell, Effect of grain size on the martensitic transformation in NiTi alloy, J. Mater. Sci. 30(10) (1995) 2526-2530.

[20] W. Tang, B. Sundman, R. Sandström, C. Qiu, New modelling of the B2 phase and its associated martensitic transformation in the Ti–Ni system, Acta Mater. 47(12) (1999) 3457-3468.

[21] J. Zhu, H.-H. Wu, Y. Wu, H. Wang, T. Zhang, H. Xiao, Y. Wang, S.-Q. Shi, Influence of Ni_4Ti_3 precipitation on martensitic transformations in NiTi shape memory alloy: R phase transformation, Acta Mater. 207 (2021) 116665.

4

[22] T. Bormann, B. Müller, M. Schinhammer, A. Kessler, P. Thalmann, M. de Wild, Microstructure of selective laser melted nickel–titanium, Mater. Charact. 94 (2014) 189-202.

[23] S. Raghavan, B. Zhang, P. Wang, C.-N. Sun, M.L.S. Nai, T. Li, J. Wei, Effect of different heat treatments on the microstructure and mechanical properties in selective laser melted INCONEL 718 alloy, Mater. Manuf. Processes 32(14) (2017) 1588-1595.

[24] S. Luo, P. Gao, H. Yu, J. Yang, Z. Wang, X. Zeng, Selective laser melting of an equiatomic AlCrCuFeNi high-entropy alloy: Processability, non-equilibrium microstructure and mechanical behavior, J. Alloys Compd. 771 (2019) 387-397.

[25] M. Mahmoudi, G. Tapia, B. Franco, J. Ma, R. Arroyave, I. Karaman, A. Elwany, On the printability and transformation behavior of nickel-titanium shape memory alloys fabricated using laser powder-bed fusion additive manufacturing, J. Manuf. Process. 35 (2018) 672-680.

[26] G. Tadayyon, M. Mazinani, Y. Guo, S.M. Zebarjad, S.A.M. Tofail, M.J. Biggs, The effect of annealing on the mechanical properties and microstructural evolution of Ti-rich NiTi shape memory alloy, Mater. Sci. Eng., A 662 (2016) 564-577.

[27] A.K. Rai, H. Trpathy, R.N. Hajra, S. Raju, S. Saroja, Thermophysical properties of Ni based super alloy 617, J. Alloys Compd. 698 (2017) 442-450.

[28] C. Zanotti, P. Giuliani, G. Riva, A. Tuissi, A. Chrysanthou, Thermal diffusivity of Ni–Ti SMAs, J. Alloys Compd. 473(1) (2009) 231-237.

[29] C. Lampa, A.F.H. Kaplan, J. Powell, C. Magnusson, An analytical thermodynamic model of laser welding, J. Phys. D: Appl. Phys. 30(9) (1997) 1293-1299.

[30] Y. Li, K. Zhou, P. Tan, S.B. Tor, C.K. Chua, K.F. Leong, Modeling temperature and residual stress fields in selective laser melting, Int. J. Mech. Sci. 136 (2018) 24-35.

[31] M. Tang, P.C. Pistorius, J.L. Beuth, Prediction of lack-of-fusion porosity for powder bed fusion, Addit. Manuf. 14 (2017) 39-48.

[32] P. Fischer, V. Romano, H.P. Weber, N.P. Karapatis, E. Boillat, R. Glardon, Sintering of commercially pure titanium powder with a Nd:YAG laser source, Acta Mater. 51(6) (2003) 1651-1662.

[33] J.-T. Yeom, J.H. Kim, J.-K. Hong, S.W. Kim, C.-H. Park, T.H. Nam, K.-Y. Lee, Hot forging design of as-cast NiTi shape memory alloy, Mater. Res. Bull. 58 (2014) 234-238.

[34] J. Mentz, M. Bram, H.P. Buchkremer, D. Stöver, Improvement of Mechanical Properties of Powder Metallurgical NiTi Shape Memory Alloys, Adv. Eng. Mater. 8(4) (2006) 247-252.

[35] S. Parvizi, S.M. Hashemi, F. Asgarinia, M. Nematollahi, M. Elahinia, Effective parameters on the final properties of NiTi-based alloys manufactured by powder metallurgy methods: A review, Prog. Mater Sci. 117 (2021) 100739.

[36] F. Yan, W. Xiong, E.J. Faierson, Grain Structure Control of Additively Manufactured Metallic Materials, Materials 10(11) (2017) 1260.

[37] F. Khelfaoui, G. Guénin, Influence of the recovery and recrystallization processes on the martensitic transformation of cold worked equiatomic Ti–Ni alloy, Mater. Sci. Eng., A 355(1) (2003) 292-298.

[38] B. Maass, J. Burow, J. Frenzel, G. Eggeler, On the influence of crystal defects on the functional stability of NiTi based shape memory alloys, European Symposium on Martensitic Transformations (2009).

[39] M. Nishida, C.M. Wayman, T. Honma, Precipitation processes in near-equiatomic TiNi shape memory alloys, Metall. Trans. A 17(9) (1986) 1505-1515.

[40] G.S. Bigelow, S.A. Padula, A. Garg, D. Gaydosh, R.D. Noebe, Characterization of Ternary NiTiPd High-Temperature Shape-Memory Alloys under Load-Biased Thermal Cycling, Metall. Mater. Trans. A. Phys Metall Mater. Sci. 41(12) (2010) 3065-3079.

[41] D. Gu, C. Ma, D. Dai, J. Yang, K. Lin, H. Zhang, H. Zhang, Additively manufacturing-enabled hierarchical NiTi-based shape memory alloys with high strength and toughness, Virtual Phys. Prototyp. 16(sup1) (2021) S19-S38.

[42] G. Chen, J. Liu, Z. Dong, Y. Li, Y. Zhao, B. Zhang, J. Cao, Understanding mechanisms of shape memory function deterioration for nitinol alloy during non-equilibrium solidification by electron beam, J. Adv. Res. (2021).

[43] L. Hu, S. Jiang, S. Liu, Y. Zhang, Y. Zhao, C. Zhao, Transformation twinning and deformation twinning of NiTi shape memory alloy, Mater. Sci. Eng., A 660 (2016) 1-10.

[44] Y.H. Zhou, W.P. Li, D.W. Wang, L. Zhang, K. Ohara, J. Shen, T. Ebel, M. Yan, Selective laser melting enabled additive manufacturing of Ti–22Al–25Nb intermetallic: Excellent combination of strength and ductility, and unique microstructural features associated, Acta Mater. 173 (2019) 117-129.

4

[45] Q. Zhang, S. Hao, Y. Liu, Z. Xiong, W. Guo, Y. Yang, Y. Ren, L. Cui, L. Ren, Z. Zhang, The microstructure of a selective laser melting (SLM)-fabricated NiTi shape memory alloy with superior tensile property and shape memory recoverability, Appl. Mater. Today. 19 (2020) 100547.

[46] J. Fu, J.C. Brouwer, R.W.A. Hendrikx, I.M. Richardson, M.J.M. Hermans, Microstructure characterisation and mechanical properties of ODS Eurofer steel subject to designed heat treatments, Mater. Sci. Eng., A 770 (2020) 138568.

[47] T. Ungár, J. Gubicza, P. Hanák, I. Alexandrov, Densities and character of dislocations and size-distribution of subgrains in deformed metals by X-ray diffraction profile analysis, Mater. Sci. Eng., A 319-321 (2001) 274-278.

[48] K. Maniammal, G. Madhu, V. Biju, X-ray diffraction line profile analysis of nanostructured nickel oxide: Shape factor and convolution of crystallite size and microstrain contributions, Physica E: Low-dimensional Systems and Nanostructures 85 (2017) 214-222.

[49] V.D. Mote, Y. Purushotham, B.N. Dole, Williamson-Hall analysis in estimation of lattice strain in nanometer-sized ZnO particles, Journal of Theoretical and Applied Physics 6(1) (2012) 6.

[50] Y.-Y. Kim, A.S. Schenk, J. Ihli, A.N. Kulak, N.B.J. Hetherington, C.C. Tang, W.W. Schmahl, E. Griesshaber, G. Hyett, F.C. Meldrum, A critical analysis of calcium carbonate mesocrystals, Nat. Commun. 5(1) (2014) 4341.

[51] G.K. Williamson, W.H. Hall, X-ray line broadening from filed aluminium and wolfram, Acta Metall. 1(1) (1953) 22-31.

[52] V. Biju, N. Sugathan, V. Vrinda, S.L. Salini, Estimation of lattice strain in nanocrystalline silver from X-ray diffraction line broadening, J. Mater. Sci. 43(4) (2008) 1175-1179.

[53] G. Bokuchava, Materials microstructure characterization using high resolution time-of-flight neutron diffraction, Rom. J. Phys. 61(5-6) (2016) 903-925.

[54] Y.-S. Lin, M. Cak, V. Paidar, V. Vitek, Why is the slip direction different in different B2 alloys?, Acta Mater. 60(3) (2012) 881-888.

[55] C. Cayron, What EBSD and TKD Tell Us about the Crystallography of the Martensitic B2-B19′ Transformation in NiTi Shape Memory Alloys, Crystals 10(7) (2020) 562.

4

[56] Y.J. Yin, J.Q. Sun, J. Guo, X.F. Kan, D.C. Yang, Mechanism of high yield strength and yield ratio of 316 L stainless steel by additive manufacturing, Mater. Sci. Eng., A 744 (2019) 773-777.

[57] T. Waitz, V. Kazykhanov, H.P. Karnthaler, Martensitic phase transformations in nanocrystalline NiTi studied by TEM, Acta Mater. 52(1) (2004) 137-147.

[58] H. Natter, M.S. Löffler, C.E. Krill, R. Hempelmann, Crystallite growth of nanocrystalline transition metals studied in situ by high temperature synchrotron X-ray diffraction, Scripta Mater. 44(8) (2001) 2321-2325.

[59] M.F.X. Wagner, S.R. Dey, H. Gugel, J. Frenzel, C. Somsen, G. Eggeler, Effect of low-temperature precipitation on the transformation characteristics of Ni-rich NiTi shape memory alloys during thermal cycling, Intermetallics 18(6) (2010) 1172-1179.

[60] B. Kockar, I. Karaman, J.I. Kim, Y.I. Chumlyakov, J. Sharp, C.J. Yu, Thermomechanical cyclic response of an ultrafine-grained NiTi shape memory alloy, Acta Mater. 56(14) (2008) 3630-3646.

[61] D. Golberg, Y. Xu, Y. Murakami, K. Otsuka, T. Ueki, H. Horikawa, High-temperature shape memory effect in Ti50Pd50 − xNix (x = 10, 15, 20) alloys, Mater. Lett. 22(5) (1995) 241-248.

[62] D. Golberg, Y. Xu, Y. Murakami, S. Morito, K. Otsuka, T. Ueki, H. Horikawa, Characteristics of Ti50Pd30Ni20 high-temperature shape memory alloy, Intermetallics 3(1) (1995) 35-46.

[63] B. Kockar, I. Karaman, J.I. Kim, Y. Chumlyakov, A method to enhance cyclic reversibility of NiTiHf high temperature shape memory alloys, Scripta Mater. 54(12) (2006) 2203-2208.

[64] M. Attaran, The rise of 3-D printing: The advantages of additive manufacturing over traditional manufacturing, Bus. Horiz. 60(5) (2017) 677-688.

[65] H. Matsumoto, Transformation behaviour with thermal cycling in NiTi alloys, J. Alloys Compd. 350(1) (2003) 213-217.

[66] J. Burow, E. Prokofiev, C. Somsen, J. Frenzel, R. Valiev, G.F. Eggeler, Martensitic Transformations and Functional Stability in Ultra-Fine Grained NiTi Shape Memory Alloys, Mater. Sci. Forum. 584-586 (2008) 852-857.

4

[67] N.B. Morgan, C.M. Friend, A review of shape memory stability in NiTi alloys, J Phys Iv 11(Pr8) (2001) 325-332.

[68] J.-N. Zhu, E. Borisov, X. Liang, E. Farber, M.J.M. Hermans, V.A. Popovich, Predictive analytical modelling and experimental validation of processing maps in additive manufacturing of nitinol alloys, Addit. Manuf. 38 (2021) 101802.

[69] F. Yan, W. Xiong, E.J. Faierson, Grain Structure Control of Additively Manufactured Metallic Materials, Materials 10(11) (2017).

[70] S. Kou, Welding metallurgy, New Jersey, USA (2003) 431-446.

[71] L. Thijs, M.L. Montero Sistiaga, R. Wauthle, Q. Xie, J.-P. Kruth, J. Van Humbeeck, Strong morphological and crystallographic texture and resulting yield strength anisotropy in selective laser melted tantalum, Acta Mater. 61(12) (2013) 4657-4668.

[72] D. Raabe, 23 - Recovery and Recrystallization: Phenomena, Physics, Models, Simulation, in: D.E. Laughlin, K. Hono (Eds.) Physical Metallurgy (Fifth Edition), Elsevier, Oxford, 2014, pp. 2291-2397.

[73] M.C. Carroll, C. Somsen, G. Eggeler, Multiple-step martensitic transformations in Ni-rich NiTi shape memory alloys, Scripta Mater., 50 (2004) 187-192.

[74] R. Seede, D. Shoukr, B. Zhang, A. Whitt, S. Gibbons, P. Flater, A. Elwany, R. Arroyave, I. Karaman, An ultra-high strength martensitic steel fabricated using selective laser melting additive manufacturing: Densification, microstructure, and mechanical properties, Acta Mater. 186 (2020) 199-214.

[75] G.K. Williamson, R.E. Smallman, III. Dislocation densities in some annealed and cold-worked metals from measurements on the X-ray debye-scherrer spectrum, Philos. Mag., 1 (1956) 34-46.

4

5

Shape memory effect of as-fabricated L-PBF and heat treated NiTi

Abstract

To obtain customized 4D functional responses in NiTi structures, tailorable phase transformation temperatures and stress windows as well as one-way or two-way shape memory properties are required. To achieve this goal, various heat treatments, including direct aging, annealing and annealing followed by aging, were optimized for the Ti-rich NiTi (Ni49.6Ti (at. %)) fabricated by laser powder bed fusion (L-PBF). Microstructural evolution, phase transformation, precipitation and shape memory behaviour were systematically investigated by multiscale correlative microstructural, differential scanning calorimetry analysis and thermomechanical analysis. Based on optimized heat treatments, ~25 K phase transformation temperature windows and ~90 MPa stress windows were achieved for the one-way shape memory effect. Solutionized annealing was found to be the most effective way to improve one-way shape memory degradation resistance, due to the reduction of defects and solid solution strengthening. One of the main findings of this study is that the heterogonous microstructures between hard intergranular Ti_2NiO_x and soft NiTi matrix, induced by solutionized annealing with subsequent aging, result in strain partitioning and enclosing the internal stress state, which was found to promote a pronounced two-way shape memory effect response. The results of this work provide in-depth knowledge on tailoring and designing functional shape memory characteristics via heat treatments, which contributes to expanding L-PBF NiTi application fields, such as biomedical implants, aerospace components, and other advanced engineering applications.

5

5.1. Introduction

NiTi alloys, as functional materials, have been widely used in various industrial, high-tech and medical fields [1]. Generally, there are three main functions in NiTi SMAs, including superelasticity, elastocaloric and shape memory effects. Superelasticity and elastocaloric effect both are associated with reversible stress-induced martensitic transformation [2]. Depending on the conditions required for shape recovery, the shape memory effect is divided into the one-way shape memory effect (OWSME) and the two-way shape memory effect (TWSME) [3]. OWSME refers to the ability of a material to remember only one shape. When a material is deformed from its original shape, it can return to its original shape only by heating it above its recovery temperature (austenite finish temperature,

A_f)). If the material is deformed below the recovery temperature, it will remain in its deformed shape. TWSME, on the other hand, refers to a material capable to remember two different shapes, where shape changes spontaneously occur during heating and cooling without any external stress [4, 5]. Theses attractive functions make NiTi attractive for such smart applications as sensors, actuators, dampers and solid refrigeration [1].

However, the high reactivity and poor machinability of NiTi limit its design complexity, which is essential for smart device design. Laser powder bed fusion (L-PBF), categorized as additive manufacturing (AM), is considered an alternative technique allowing for more design flexibility of smart components [6]. Recently, NiTi with complex topological structures, designed for damping or medical applications, has been successfully fabricated by L-PBF [7, 8].

Due to the high heating and cooling rate in L-PBF (up to $\sim 10^6$ K·s^{-1}) [9], steep temperature gradient (in the magnitude of $\sim 10^7$ K·m^{-1}) [10, 11], layer-by-layer and track-by-track processing characteristics [12], produce materials having non-equilibrium solidification microstructures, including heterogeneous microstructures, metastable phases, micro-segregations and dislocations [13-15]. For NiTi, such non-equilibrium solidification microstructures affect its phase transformation temperatures and functional behavior. For instance, the compositional ratio of Ni/Ti in the NiTi matrix influences the martensitic phase transformation temperatures [16]. The deviation of matrix composition may result from element segregation or precipitation of second phases, which in turn, affects phase transformation temperatures [17]. Dislocations, associated with anisotropic stress fields [18], are commonly observed in the as-fabricated L-PBF NiTi [11], which impedes martensitic transformation during thermal cycling (decrease in martensite finish temperature) [11] and promotes the stress-induced formation of martensite during superelastic cycling (decrease in plateau stress in the forward transformation) [19].

The non-equilibrium features in L-PBF NiTi imply a possibility to tailor the phase transformation temperature and applied stress windows by controlling its microstructures. Heat treatments, as cost-effective and simple methods, are promising to tailor L-PBF NiTi functional properties. Recently, efforts have been made to study the effect of heat treatment on L-PBF NiTi. Tunable superelasticity and elastocaloric effects were achieved by applying heat treatments to control the precipitation of Ni_4Ti_3 in Ni-rich NiTi [20]. However, most heat treatment-related studies have been focused on Ni-rich NiTi [15, 20, 21], since the achievable Ni_4Ti_3 phases introduced by aging enhance the superelastic and elastocaloric effects. Until now, there are only very limited studies on the heat treatment responses of L-PBF Ti-rich NiTi [22-24], in which only mechanical properties were investigated. There is

still a lack of understanding of the effect of heat-treated microstructures on the shape memory effect. Moreover, the cyclic OWSME and TWSME of heat-treated L-PBF Ti-rich NiTi have never been investigated, which is important for a wide range of engineering applications [25]. Therefore, it is imperative to develop L-PBF Ti-rich NiTi with tunable OWSME and TWSME via applying appropriate heat treatments and understanding the relationship between microstructure and functional properties.

Due to the low crystallographic symmetry of NiTi martensite (B19′), polycrystalline NiTi shows different deformation behavior when applying various deformation modes (including uniaxial tension, compression, and shear) [26]. Especially, NiTi is very sensitive to strain hardening under compression during the SME test [26], which is associated with the generation of a high density of dislocations [27]. By contrast, under tension, there is no significant plastic deformation, and a flat stress plateau is observed, which is due to a high mobility of ⟨011⟩ type II twin junction planes of polycrystalline NiTi [27]. It indicates that residual strains or plastic deformation are easier to be accumulated, resulting in shape memory degradation under the cyclic compressive loading condition. Indeed, the superior shape memory effect of L-PBF NiTi was mainly reported for the tensile condition [28-31]. Therefore, it is still challenging for NiTi to achieve a stable shape memory effect under the compressive condition.

In this study, to understand the effect of heat treatments on microstructure evolution, phase transformation behavior and shape memory effect in L-PBF Ti-rich NiTi alloys, for different heat treatment schemes, including solutionized annealing, directly aging and annealing followed by aging, were applied. Nano-scaled structures were investigated by high-resolution transmission electron microscopy. The cyclic compressive-thermomechanical behavior of L-PBF NiTi without and with heat treatments was evaluated after 50 cycles. Finally, NiTi with tunable SME stress and temperature windows were successfully developed based on specific heat treatments. Relationships between microstructure, nano-precipitates and thermomechanical properties (including one-way and two-way shape memory effect) were discussed. Solutionized annealing was found to improve the OWSME degradation resistance, and subsequent aging helped to promote the TWSME response in L-PBE NiTi. To the author's best knowledge, this is the first systematic multiscale correlative investigation on microstructure, differential scanning calorimetry analysis (DSC), cyclic OWSME and TWSME of heat-treated L-PBF Ti-rich NiTi. This work may provide an insightful understanding of designing function-tunable 4D printing NiTi.

5

5.2. Materials and Methods

5.2.1. Material processing

Based on the Chapter 3, fully dense L-PBF NiTi were fabricated by the following L-PBF process parameters were used: 250 W laser power (P), 1250 mm/s scanning velocity (v), 120 μm hatch distance (h), 30 μm layer thickness (t) and 80 μm laser beam diameter. The as-fabricated NiTi sample is named AF hereafter.
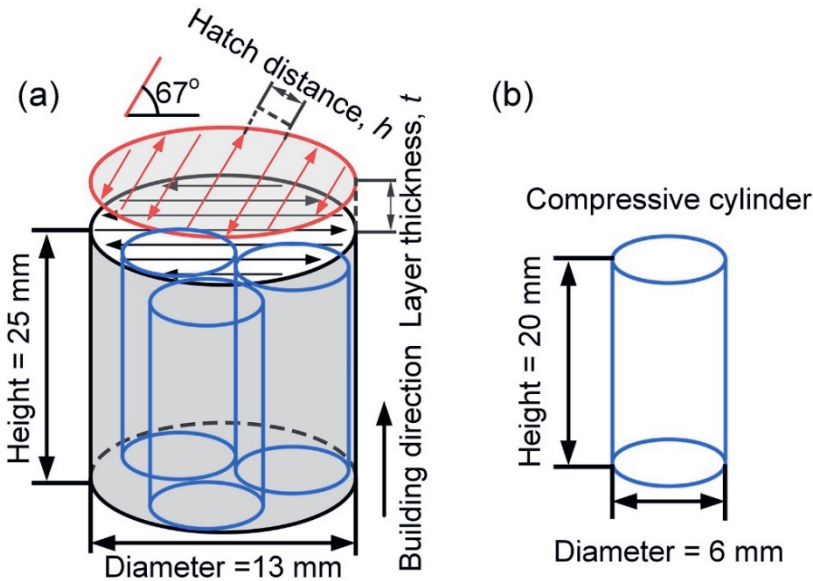

Figure 5.1 (a) The schematic of the applied L-PBF scanning strategy and (b) the machined cylinder for compressive tests by EDM.

To investigate the effect of heat treatments on the shape memory effect of Ti-rich L-PBF NiTi, three types of heat treatments were carried out on as-fabricated NiTi, i.e. solution annealing, directly aging and solution annealing followed by aging. Based on the NiTi binary phase diagram, $Ni_{49.6}Ti$ (at. %) is solid when the temperature is lower than 1298 K (Figure 2.1). To reduce the residual stress and homogenise the microstructure, solutionized annealing was carried out at 1223 K for 5.5 h followed by water quenching, referred to as S hereafter. For the direct aging, samples were held at 623 K for 18 h indicate by A hereafter. For the solution annealing followed by aging, samples were firstly held at 1223 K for 5.5 h and then

aged at 623 K for various holding durations (0.5–27 h). The optimized annealing 1223 K-5.5hs followed by aging 623 K-18 hs is named S+A hereafter. To prevent oxidation of NiTi, all samples were placed in stainless steel envelopes filled with argon during heat treatments. Post-process heat treatments details are summarized in Table 5.1.

Table 5.1 The overview of the post-heat treatments

Post treatments and designations	Temperature - duration
Directly aging, A	623 K - 18 hs
Solutionized annealing, S	1223 K - 5.5 hs
Solutionized annealing followed by aging, S+A	1223 K-5.5 hs + 623 K-18 hs

5.2.2 Thermomechanical tests

Thermomechanical compression tests were conducted using a 25 kN MTS 858 Table Top servo-hydraulic test platform. Using a strain control loop, a strain rate of 10^{-4} s^{-1} was employed when loading and unloading were performed. Samples were machined into cylinders with a dimension of ϕ 6 × 20 mm by electrical discharging machining (EDM) (Figure 5.1). The strain was measured by a ceramic rod extensometer with a gauge length of 12 mm (MTS model 632.53F-14), which was attached to the samples. The samples were heated up using an induction coil and cooled via three air-blowing nozzles. The temperature was controlled (and monitored) by a K-type thermocouple, spot welded at the middle of the sample.

A 3-step gradually increasing strain level test was applied to investigate the critical stress for phase transformation and strain recovery (Figure 5.2 (a)). "Hard" cyclic tests [32], where the same maximum nominal strain is reached for each cycle (50 cycles with a fixed maximum 4% strain), were applied to investigate the cyclic SME stability (Figure 5.2 (b)). Schematics of strain definitions and loading paths for the shape memory effect are shown in Figure 5.2 (c).

To investigate the two-way shape memory effect, The dilatation of the samples after 50 thermomechanical cycles as a function of temperature is determined using a dilatometer (TMA PT 1000/LT). A k-type thermocouple was spot welded onto the middle of sample. In the study, each sample is initially cooled to 203 K, then heated to 473 K, and finally cooled down to 273 K at a rate of 10 K per minute.
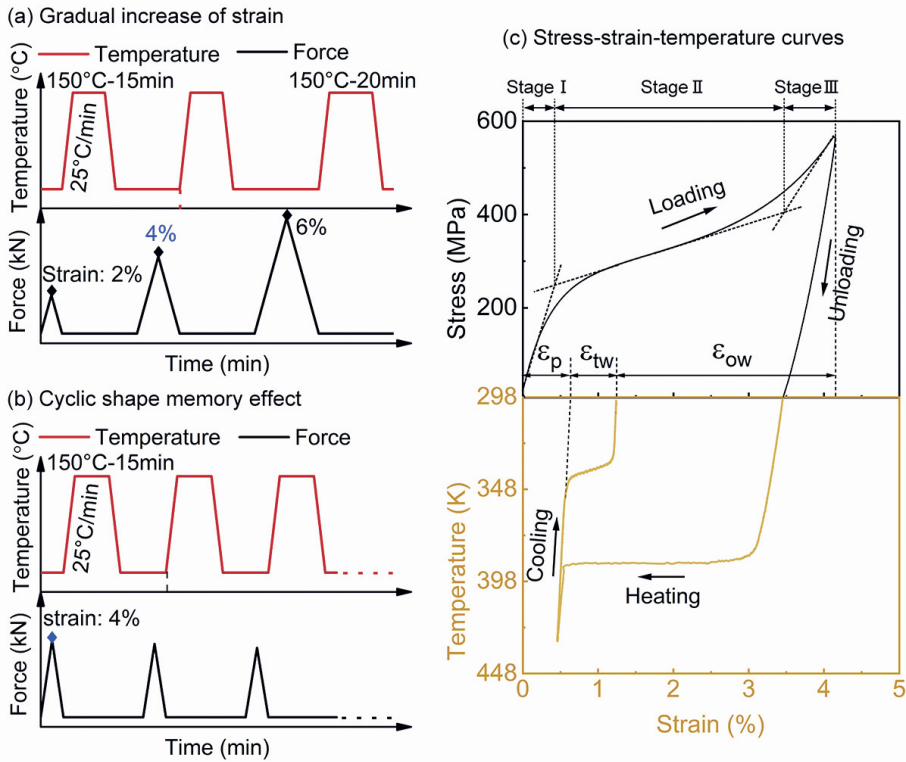
Figure 5.2. Schematics of (a) shape memory effect test with gradually increased strain and (b) cyclic shape memory effect, and (c) stress-strain-temperature curves, where ε_p is plastic strain, ε_{ow} is one-way shape memory strain and ε_{tw} is the two-way shape memory strain.

5.2.3 Characterizations

Before the metallographic examination, samples were ground, polished and tint etched, and the detailed procedure can be found in the previous work [11]. The etched microstructures were then examined via a Leica DMI 5000 optical microscope under the polarized light mode. For Vickers hardness measurements, a Durascan microhardness tester (Struers) was used. Polished samples were tested under the main load of 2kgf (HV_2) with a loading time of 10s. An average of 10 hardness values for each sample is reported. The series of indents were made at a distance of 2 mm.

To measure the size and distribution of precipitates, cross-sections of the samples were prepared and analyzed with a dual beam scanning electron microscope (Helios G4 P-FIB

UXe, Thermo Fisher Scientific, USA) equipped with a Xenon plasma focused ion beam (P-FIB). Protective Pt (mixed with 1.0 wt.% C) layers were first deposited on the polished surfaces of samples. Then, trenches were machine polished by the P-FIB.

Transmission electron microscopy (TEM) images were taken by FEI cubed titan Cs-corrected 80-300 kV transmission electron microscope and FEI Talos F200X scanning transmission electron microscope STEM. For the samples before thermomechanical tests, pre-sample preparation consisted of cutting and sawing a NiTi cylinder followed by mechanical polishing to around 20 µm thickness. Then, the thin foils were punched into discs with a diameter of 2.3 mm and glued on 3 mm Cu rings and subsequently milled to electron transparency by Ar ion. For the samples after thermomechanical tests, TEM foil samples were prepared by a Focused Ion Beam (FIB; FEI Helios 600i).

X-ray diffraction (XRD) analysis was carried out for phase identifications and phase fraction calculations in the as-fabricated and post-heat-treated samples. The measurements were carried out using the Bruker D8 Advance diffractometer in Cu-Kα radiation. The step size used was 0.03° in a 2θ range of 17°–120° with 45 kV voltage and 40 mA current.

Phase transformation behavior was analyzed by differential scanning calorimetry (DSC, Perkin Elmer DSC 8000) in a nitrogen atmosphere, with a cooling and heating rate of 10 K min^{-1} over a temperature range of 203–473 K. DSC samples with a dimension of ϕ 6×1 mm were prepared by EDM.

5

5.3. Results

5.3.1. Hardness and microstructure

Vickers hardness was used as a first indication of the effect of different heat treatments on NiTi properties. Figure 5.3 (a) shows the Vickers hardness variations of L-PBF NiTi with different heat treatment conditions. After heat treatments, all samples show higher hardness than the as-fabricated material (197 HV$_2$). The solutionized annealed (S) sample shows the smallest hardness deviation among all samples, indicating microstructural/chemical homogeneity. The sample after solutionized annealing (1223 K+5.5 h) followed by aging (623 K+18 h), referred to as S+A, has the highest hardness of 226 HV$_2$.
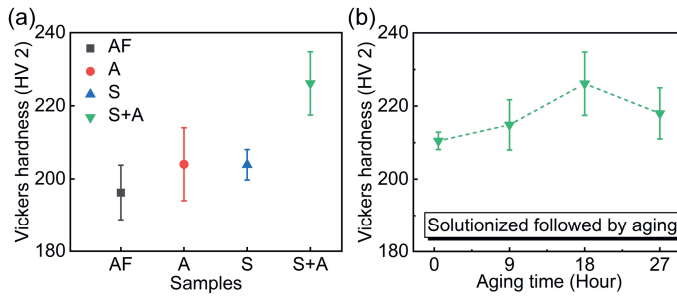
Figure 5.3. Vickers hardness for (a) different heat treatment conditions and (b) solutionized (1223 K+5.5 h) L-PBF NiTi with various subsequent aging duration at 623 K (0.5, 9, 18 and 27 hours respectively).

Since a higher hardness value usually indicates a greater strength [33, 34], implying a stronger ability of materials to resist deformation and dislocation movements and proliferation. Hence, to improve NiTi OWSME degradation resistance, a higher hardness is desirable. Based on the hardness results for different aging durations (Figure 5.3 (b)), 18 h is considered as the optimized aging time after solutionized annealing. With changing the aging time from 0.5 to 18 h, the hardness increases from ~210 to 226 HV_2. Increasing further the aging time to 27 h, results in a hardness decrease (from 226 to 218 HV_2), indicating an over-aging effect. Therefore, the 18 h aging is considered as a peak aging time resulting in the highest hardness among all the test aging durations.

Optical micrographs of L-PBF NiTi with different heat treatment conditions are shown in Figure 5.4. The top-view image of the as-fabricated sample shows a checkerboard grain structure with ~116 μm average grain size (Figure 5.4 (a)), which results from a bidirectional scanning strategy and epitaxial grain growth within the same deposition layer [35]. The cross-sectional image displays a columnar structure with curved austenitic grain boundaries (Figure 5.4 (e)). Such columnar grains grow nearly along BD over several deposition layers, showing a typical epitaxial grain growth [35]. Figure 5.4 (b–d) and (f–h) shows the microstructures of heat-treated samples from the top and cross-sectional views. Checkerboard grain structures from the top surface and columnar grain structures from the cross-sectional view remain after heat treatments, implying good thermal stability of the L-PBF NiTi samples. During solutionized annealing, the area of grain boundaries decreases, resulting in the enlargement of grains [35] (Table 5.2).
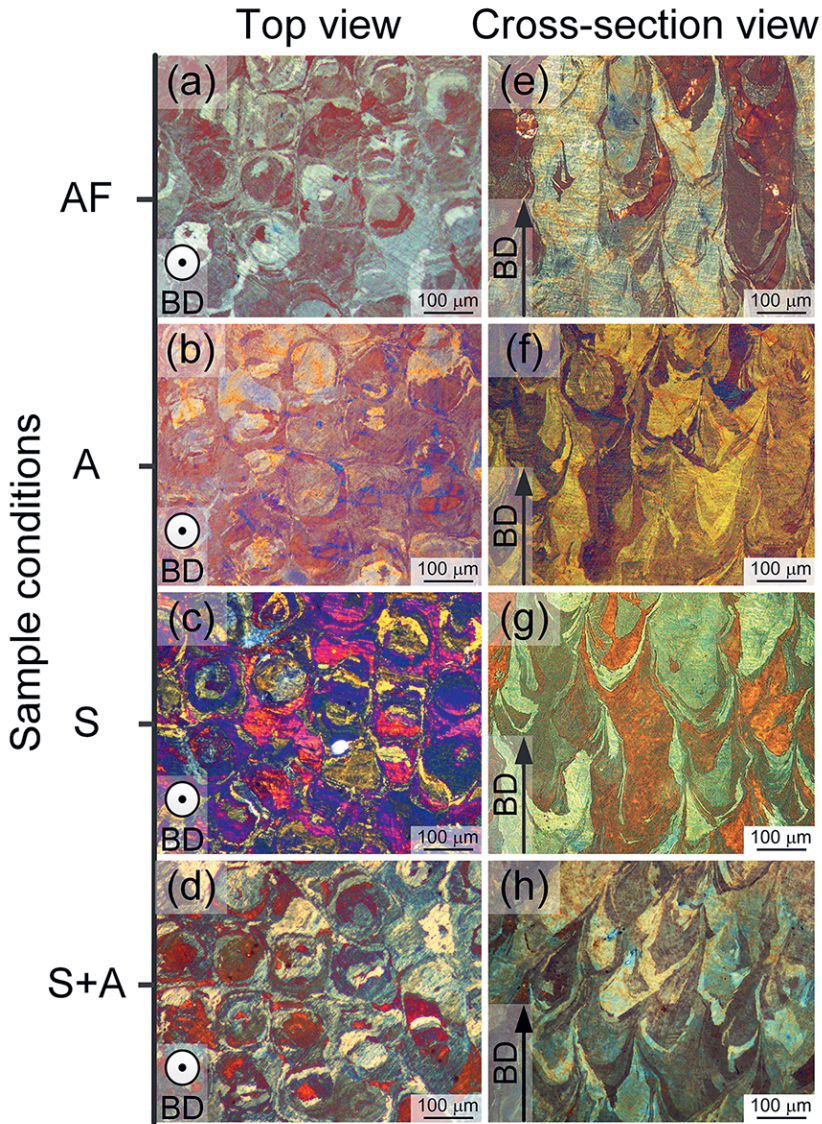
Figure 5.4. Optical microscopy images under polarized light from the top and cross-sectional views: (a) and (e) AF, (b) and (f) A, (c) and (g) S, (d) and (h) S+A L-PBF NiTi; Images (a)–(d) showing microstructures from the top view, and (e)–(h) cross-sectional microstructures.

Table 5.2 Comparison of grain sizes after heat treatments.

HT conditions	Grain size measure from top view (μm)	Grain length measure from cross-sectional view (μm)
AF	116 ± 4	160 ± 7
A	117 ± 5	172 ± 10
S	118 ± 3	184 ± 9
S+A	118 ± 5	196 ± 11

5.3.2. Phase transformation and phase identification

DSC curves, including initial NiTi powder, AF and samples with different heat treatments, are shown in Figure 5.5 (a), while their corresponding phase transformation temperatures (PTTs) are shown in Figure 5.5 (b). The NiTi powder has a broadened phase transformation temperature than other studied herein materials (Figure 5.5 (a) and (b)), which is attributed to the inhomogeneity of composition and particle size of NiTi powder [36]. Compared with the powder, the as-fabricated L-PBF sample has higher austenite start (A_s) and martensite finish (M_f) temperatures.. This results from the lower Ni content due to the evaporation of nickel during the L-PBF process, which has been demonstrated in the previous work [37]. All heat treatment procedures cause an increase in PTTs compared with the AF NiTi (Figure 5.5 (b)). The solutionized sample (S) shows the highest PTTs and the subsequent aging of the solutionized sample (S+A) decreases the PTT by ~ 5 K (Figure 5.5 (b)).

As seen in Figure 5.5 (c), only NiTi martensite (B19′) and austenite (BCC_B2) phases were detected by XRD in the as fabricated and heat-treated samples, indicating that oxidation was effectively avoided. It also should be mentioned that EDS analysis were carried out on all samples and there is almost no change in Ni and Ti content, which further demonstrates the avoidance of oxidation during heat treatments.
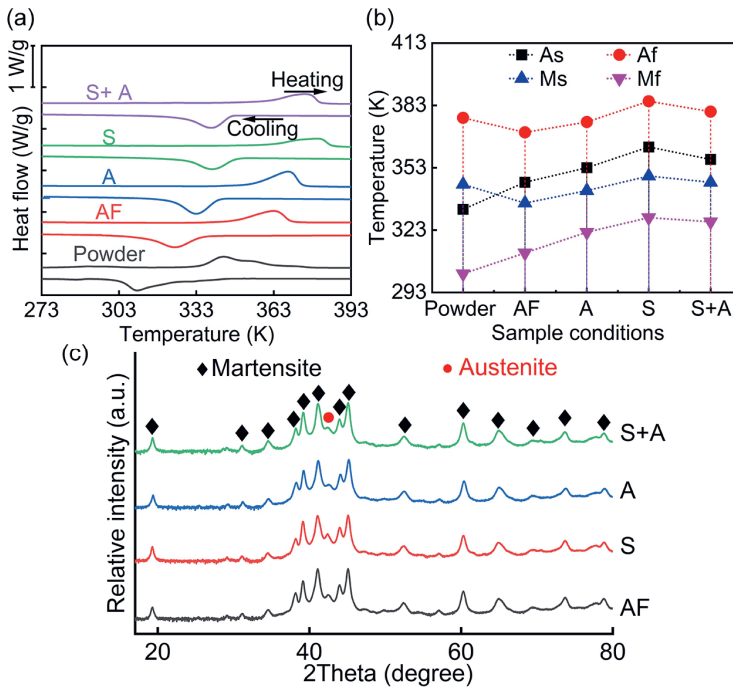
Figure 5.5 (a) DSC curves of NiTi powder and L-PBF NiTi for different heat treatment conditions, and (b) corresponding phase transformation temperatures (A_s austenite start temperature, A_f: austenite finish temperature, M_s: martensite start temperature and M_f: martensite finish temperature); (c) X-ray diffraction patterns of L-PBF NiTi without and with different heat treatment conditions.

5.3.3. The effect of aging time on precipitation in solutionized L-PBF NiTi

FIB was employed to polish the samples' cross sections to reveal precipitates in the samples with solutionized annealing followed by different aging times, as shown in Figure 5.6. With increasing aging time from 0.5 to 27 h, average sizes of the precipitates increase from ~140 to 350 nm (Figure 5.6). Aging for 18 h resulted in the highest measured hardness value (Figure 5.6 (b)). The growth of the precipitates in the sample with 27 h aging is accompanied by a loss in hardness (Figure 5.6 (b)).
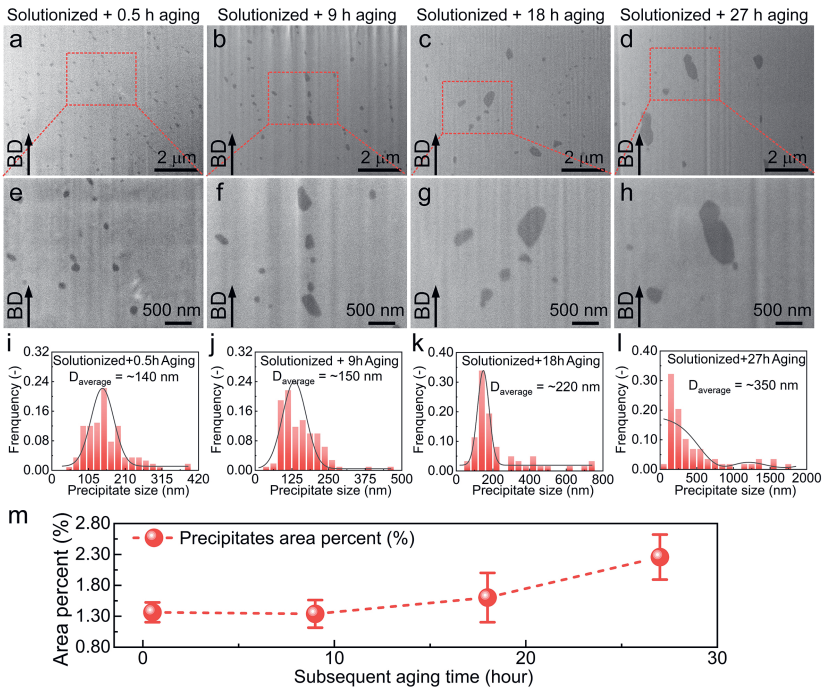
Figure 5.6. Cross-sectional SEM-FIB samples after solutionized annealing (1223 K+5.5 h) followed by 623 K aging with different aging durations: (a), (e) and (i) 0.5 h; (b), (f) and (j) 9 h; (c), (g) and (k) 18 h; (d), (h) and (l) 27 h. (m) The statistical area percent of precipitates in various samples.

5.3.4. Precipitates in as-fabricated and heat-treated L-PBF NiTi

As shown in the high-angle annular dark-field scanning transmission electron microscopy (HAADF-STEM) image (Figure 5.7), particles are dispersedly distributed within the matrix in the as-fabricated L-PBF NiTi. Particles were indexed as a pure Ti phase based on HRTEM and the corresponding fast Fourier transform (FFT) image. The formation of Ti particles in the matrix is attributed to the high solidification rate during L-PBF, where Ti solute gets trapped in the matrix. Ti particles were barely seen in the Ti-rich NiTi fabricated by conventional methods, such as casting and rolling, since these techniques do not induce a sufficiently high cooling rate. By contrast, the Ti_2NiO_x phase is commonly seen in NiTi fabricated by conventional techniques [17, 38, 39].
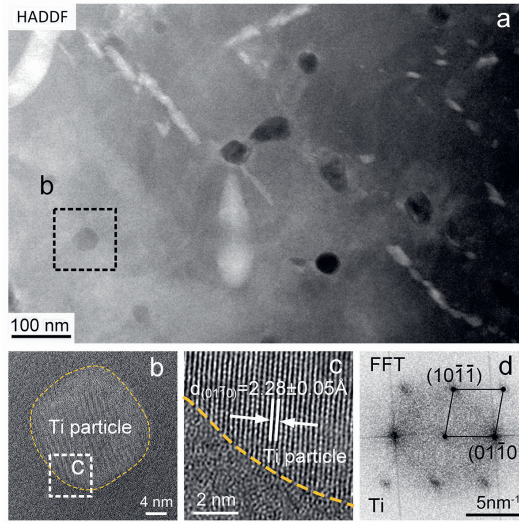
Figure 5.7. TEM of as-fabricated L-PBF NiTi sample: (a) HAADF-STEM; (b) HRTEM of precipitate Ti and corresponding (c) enlargement and (d) FFT.

Direct aging (A) promotes the formation of Ti_2NiO_x precipitates (Figure 5.8). Ti_2Ni crystal structure is determined by HRTEM and the corresponding FFT pattern (Figure 5.8 (d) and (e)). It should be noted that the presence of oxygen was confirmed by EDS mappings (Figure 5.8 (f)). Since oxygen has a certain solubility in Ti_2Ni [38], Ti_2NiO_x forms in directly aged L-PBF NiTi.
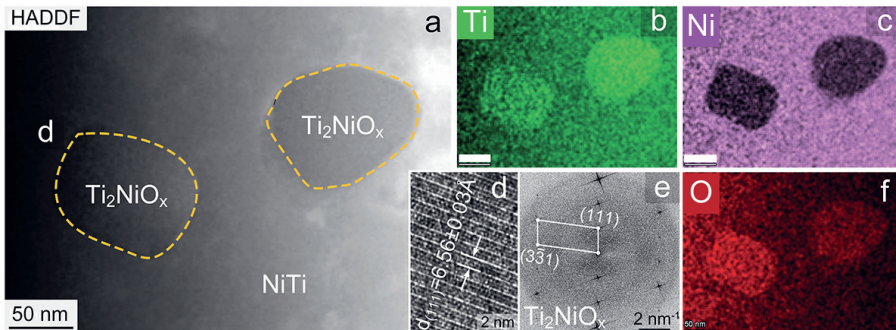
5

Figure 5.8. TEM images of aged for 18 h NiTi sample under 623 K: (a) HAADF-STEM; EDS mappings: (b) Ti, (c) Ni and (f) O; (d) The HRTEM of Ti_2NiO_x and (e) its FFT.

After 5.5 h of solutionized annealing under 1223 K, the NiTi sample shows clear martensite phase boundaries, and most precipitates are dissolved in the matrix (Figure 5.9 (a)). Typical $\{1\bar{1}1\}$ type I martensite twins (mirror symmetry between twin martensite variants) were found in the sample (Figure 5.9). The clear martensite twin boundaries and wide martensite laths indicate the relief of residual stresses and homogenization of the microstructure after solutionized annealing.
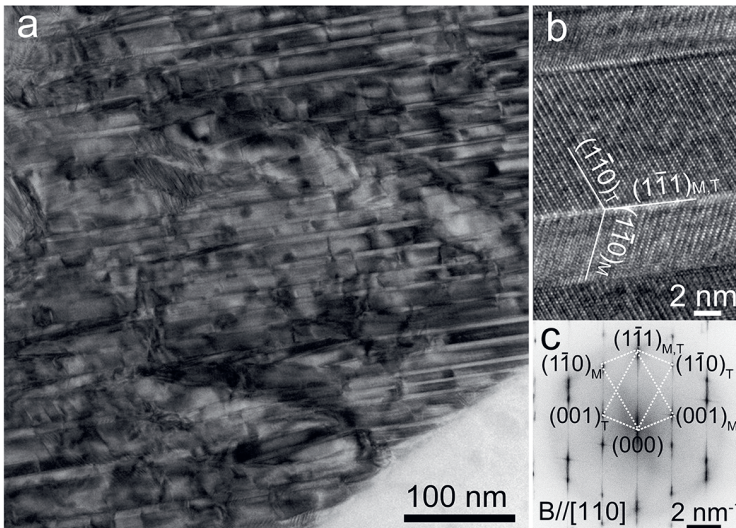

Figure 5.9. TEM images of S NiTi sample (1223 K + 5.5 h): (a) BF-TEM image, (b) typical type I twin martensite and (c) corresponding FFT images.

The 18 h aging of solutionized NiTi promotes intergranular precipitation (Figure 5.10 (a)). Based on the HRTEM and EDS results, the intergranular precipitates are identified as Ti_2NiO_x (Figure 5.10 (b)–(f)). Since grain boundaries are high-energy regions, the oversaturated Ti in NiTi matrix tends to precipitate along grain boundaries in a form of a Ti_2Ni-like phase. The Ti_2Ni can be further stabilized by oxygen to form the Ti_2NiO_x phase (Figure 5.10 (d)) [16].
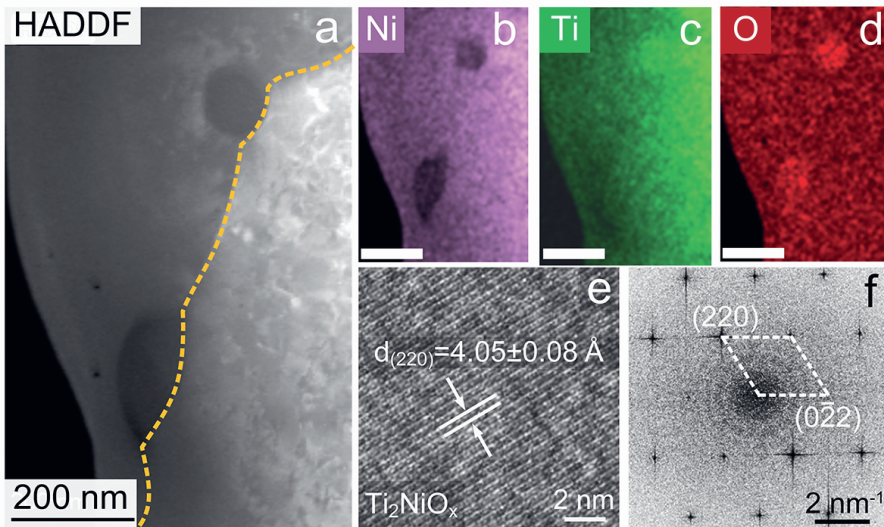
Figure 5.10. TEM images of the S+A sample: (a) HAADF-STEM and corresponding EDS mapping: (b) Ti, (c) Ni and (d) O; (e) The HRTEM of intergranular precipitate of Ti_2NiO_x and (f) its FFT.

5.3.5. Shape memory behavior

Figure 5.11 (a–d) shows the stress-strain curves of all samples under gradually increased strain levels. Thermo-mechanical behavior of all samples consists of three deformation stages [40], including the elastic deformation of twinned martensite (stage I), detwinning and martensite reorientation (stage II) and the elastic deformation of detwinned martensite (stage III) (Figure 5.11 (a–d), the corresponding deformation stages has been illustrated in the Figure 5.2 (c)). Work hardening occurs in all samples, indicating accumulation of dislocations during compression tests. The accumulated dislocations impede phase transformation-induced shape recovery during heating and cause plastic deformation [41]. The recovery ratio of all samples is given in Figure 5.11 (e) and shows that different heat treatments barely affect shape memory recovery. It should, however, be noted that heat treatments do improve the maximum true stress under the same strain level (Figure 5.11 (f)).
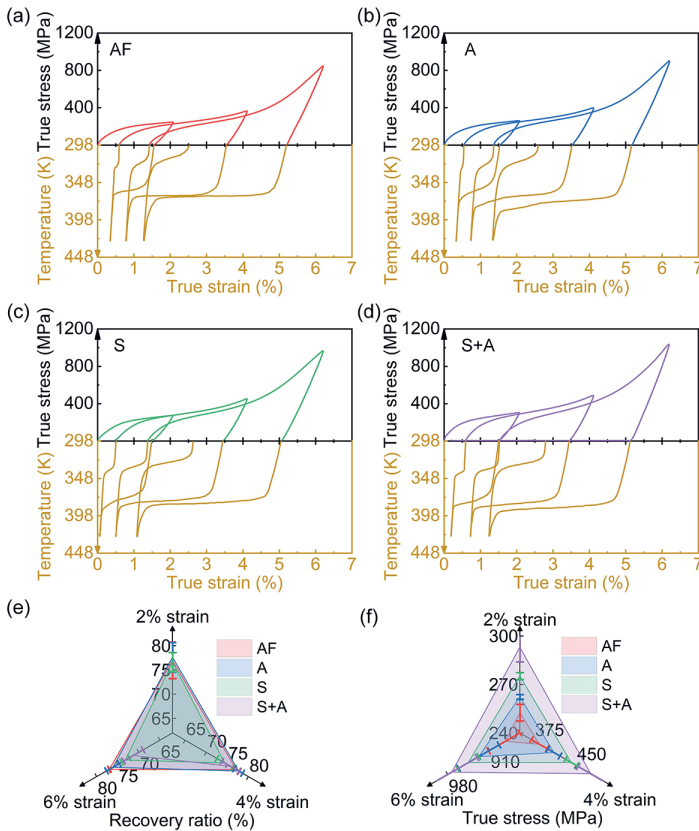
Figure 5.11. Stress-strain curves under gradually increased strain, and recovery ratio and maximum stress. (a) AF, (b) A, (c) S, (d) S+A, (e) recovery ratio, and (f) maximum stress.

The AF sample has the lowest stress value, with a peak stress of ~844 MPa. Due to the high heating and cooling rate, thermal residual stress can be present in the AF sample, which may provide additional stress for detwinning and martensite reorientation [42]. The aging treatment slightly increases the stress due to the formation of Ti_2NiO_x particles. Solution annealing induces Ti dissolution into the NiTi matrix, which provides solid solution strengthening for NiTi. Therefore, an increased stress is shown in the S sample compared with AF L-PBF NiTi. The S+A sample shows the highest stress for all strain levels and its peak stress reaches 935 MPa, which is in good agreement with observed hardness trends (Figure 5.3 (a)). The high stress is likely attributed to Ti_2NiO_x intergranular precipitation hardening.

5.3.6. Shape memory cyclic stability and two-way shape memory effect

To investigate shape memory degradation and TWSME, cyclic thermo-mechanical tests were carried out on samples with a nominal 4% engineering strain and 50 cycles. This strain level was chosen because 4 % strain corresponds to a strain where detwinning is completed and the onset of elastic deformation of detwinned martensite exists (Figure 5.11). As shown in the Figure 5.12, with cyclic thermo-mechanical tests (loading-unloading-heating-cooling-repeat), all samples show the degradation of the shape memory effect and accumulation of irrecoverable strain. During cooling, the strain shows non-linear changes, indicating the two-way shape memory effect (Figure 5.12) [43]. The two-way shape memory strain increases with the number of cycles.
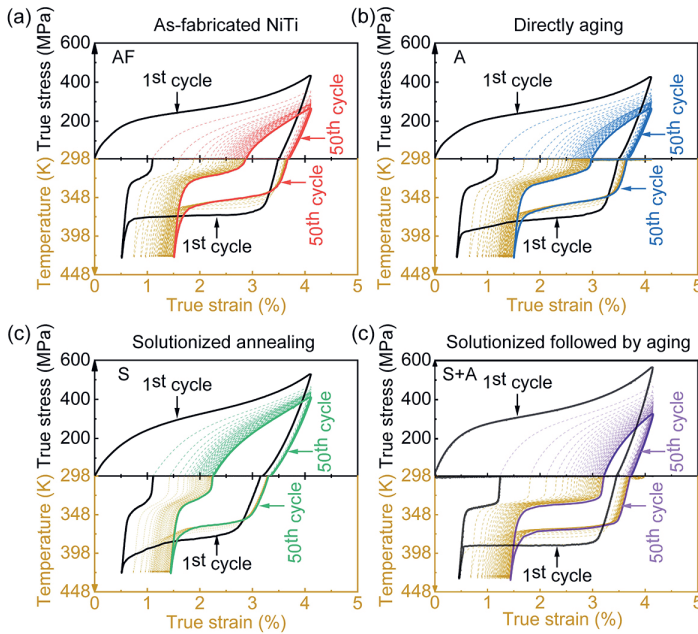

Figure 5.12. Stress-strain-temperature curves for 50 cycles under 4% deformation for (a) AF, (b) A, (c) S and (d) S+A.

As reported by Haberland et al., the conventionally processed NiTi degrades its OWSME to ~1.8% already within 15 cycles, even at a lower compression stress level (400 MPa) [44]. The solutionized NiTi reported in this study shows the highest shape memory degradation resistance and has ~1.8% recoverable strain (Figure 5.13) even after 50 thermo-mechanical cycles. By contrast, the S+A sample study herein exhibits the lowest recoverable strain (~0.8%) after 50 thermo-mechanical cycles. The as fabricated and directly aged NiTi have a similar shape memory degradation behavior (Figure 5.13), showing ~1.2 and 1.1 % recoverable strains after 50 cycles, respectively.
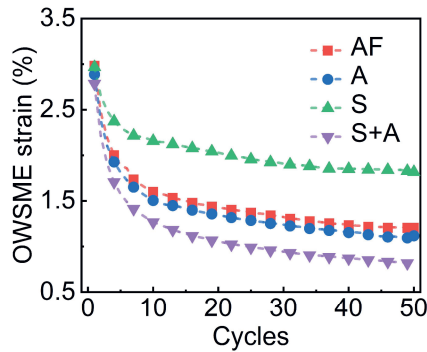

Figure 5.13. One-way shape memory effect (OWSME) strain as a function of cycles, under 4% engineering strain deformation.

The TWSME strain as a function of thermo-mechanical cycles is shown in Figure 5.14. The S+A sample shows the most pronounced two-way shape memory response, and its TWSME strain reaches to ~1.9 % after 50 thermomechanical cycles. However, the solutionized sample, exhibiting the highest shape memory degradation resistance, has the lowest TWSME strain (~1.1 % after 50 cycles). The directly aged NiTi has a slightly higher TWSME strain (~1.4 %) than the as-fabricated NiTi (~1.2%), which is an intermediate value. By comparing results of OWSME and TWSME strains, opposite trends can be observed. It indicates a direct correlation between shape memory degradation and two-way shape memory evolution, which is further discussed in section 5.4.2. It is important to note that the OWSME strain has decreased when taking the cooling-induced TWSME into account. However, in previous studies [30, 45], only the heating-strain curves instead of the heat-cooling-strain curves has been shown (Figure 5.11 and Figure 5.12). Therefore, the reported OWSME strains are usually overestimated.
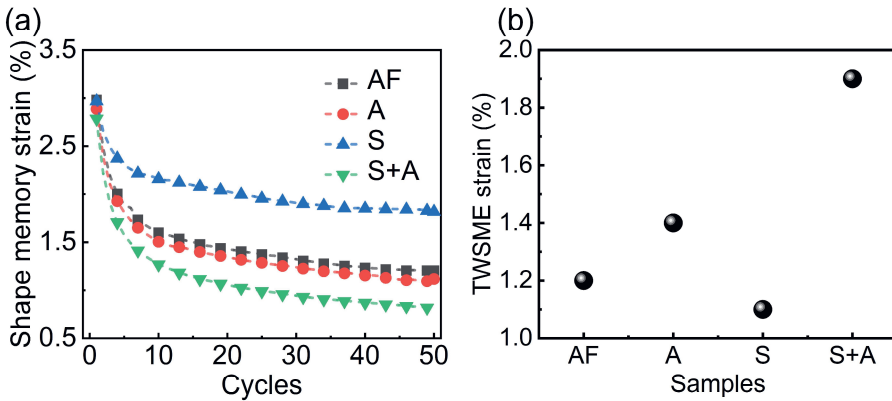
Figure 5.14 (a) Strain-temperature curves showing two-way shape memory effect (TWSME) of all samples after 50 thermomechanical cycles, and (b) TWSME strains of different samples.

5.4. Discussion

5.4.1. Effect of heat treatment on phase transformation temperatures

Figure 5.3 (a) illustrates the difference in hardness among the samples subjected to various heat treatments. Direct aging leads to an approximate 10 HV_2 increase in hardness compared to the as-fabricated samples. Since Ti particles in the as-fabricated NiTi is in the metastable state (Figure 5.7), the direct aging promotes the formation of Ti_2NiO_x precipitates (Figure 5.8), resulting in effective precipitation strengthening. Solutionized annealing also yields a similar hardness increment to direct aging (Figure 5.3 (a)), but the underlying strengthening mechanism differs. In the solutionized annealed sample, the enhanced hardness is primarily attributed to solid solution strengthening since most precipitates dissolve in the matrix (Figure 5.9). Meanwhile, the S+A sample demonstrates the highest hardness increase (~29 HV_2) due to the heat treatment's ability to promote nanoscale intergranular precipitates of Ti_2NiO_x (Figure 5.10). These precipitates play a dual role by contributing to precipitation strengthening and strengthening grain boundaries, effectively pinning dislocations.

Directly aged L-PBF NiTi (A) shows increased phase transformation temperatures (Figure 5.5 (a) and (b)). Based on the TEM results, direct aging promotes the formation of Ti_2NiO_x (Figure 5.8). Since pure Ti particles are the main precipitates in as-fabricated NiTi, direct aging makes Ni in NiTi matrix react with pure Ti to form the Ti_2Ni phase. Furthermore,

Ti_2Ni is further stabilized by oxygen to form Ti_2NiO_x. As described above, it results in a decrease of Ni content in NiTi and an increased phase transformation temperature [16].

Solutionized annealing of NiTi leads to higher phase transformation temperatures. This is attributed to 1) the dissolution of Ti and 2) the reduction of atomic-scale defects (such as voids and dislocations). The dissolved Ti causes a decreased Ni/Ti atomic ratio in the NiTi matrix, hence, increasing phase transformation temperatures [16]. Atomic-scaled defects inhibit martensite phase transformation, which can lower transformation temperatures [11]. A high annealing temperature (1223 K) allows NiTi to evolve to a more equilibrium state by eliminating or minimizing atomic defects. Therefore, the solutionized sample shows a further increase in phase transformation temperature.

Subsequent aging of solutionized NiTi slightly decreases its phase transformation temperature (Figure 5.5 (b)). Since aging promotes intergranular precipitation of Ti_2NiO_x (Figure 5.10), more Ti is precipitated than Ni. The Ti comes from the over-saturated Ti in NiTi matrix, which is induced by solutionized annealing followed by water quenching. Therefore, the increase in the Ni/Ti atomic ratio is the main reason for the decreased phase transformation temperatures.

5.4.2. Shape memory cyclic stability

The results described in Section 5.3.6 shows that heat treatment dramatically affects L-PBF NiTi shape memory stability and two-way shape memory evolution. To understand the effect of various precipitates and microstructures on the thermomechanical properties of NiTi, TEM was carried out on samples after thermomechanical testing.

The directly aged NiTi shows intermediate shape memory cyclic stability and TWSME among all tested samples (Figure 5.13 and Figure 5.14). Direct aging promotes Ti_2NiO_x formation within the NiTi matrix, which is an energy barrier for detwinning and martensite reorientation. After 50 cycles of shape memory testing, martensite variants become re-orientated along the loading and unloading direction (Figure 5.16). Notably, re-oriented martensite phase boundaries are decorated by precipitates (Figure 5.16). As precipitates create local lattice distortions, the mobility of martensite phase boundaries is limited. Hence, re-oriented martensite boundaries are pinned by nano-scaled precipitates. Since the direct aging was carried out at 623 K, which is lower than the typical recrystallization temperature of NiTi (~873 K) [46], dislocation and other meta-structures cannot be fully eliminated. Although direct aging promotes the formation of Ti_2NiO_x, the size of precipitates is ~45 nm,

which is similar to the ones in the as-fabricated sample (~36 nm). Hence, the directly aged sample shows similar thermomechanical behavior, i.e., comparable OWSME and TWSME after 50 cycles (Figure 5.13 and Figure 5.14). An increased phase transformation temperature in the directly aged sample is associated with the formation of Ti_2NiO_x.
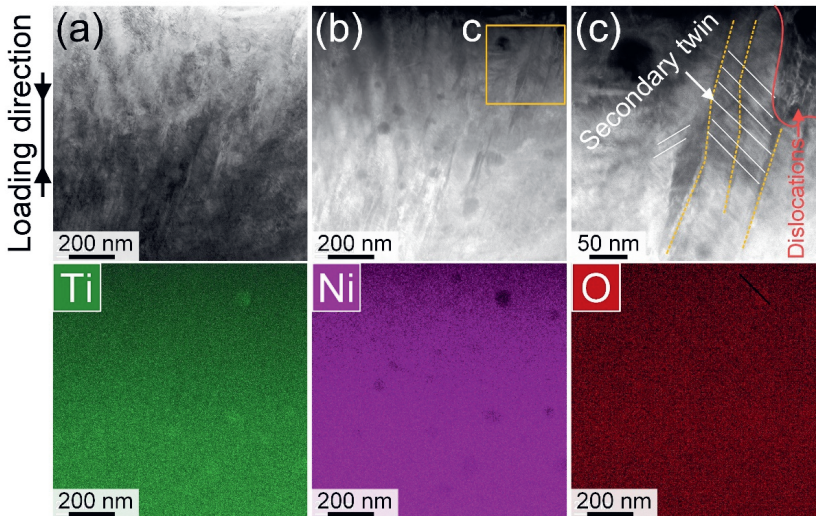

Figure 5.15. TEM images of as-fabricated L-PBF NiTi after 50 shape memory cycles: (a) BF image, (b) STEM-HAADF, (c) enlarge zone in (b); The EDS mappings of (a) are shown in the second row.

As shown in Figure 5.12, the S sample has the highest OWSME degradation resistance and correspondingly exhibits the lowest TWSME recoverable strain after 50 thermomechanical cycles. Since solutionized annealing was carried out at 1223 K, higher than the recrystallization temperature of NiTi, dislocations, meta-structures and residual stresses can be effectively eliminated. This is reflected by the large size of martensite and precipitate-free martensite twin boundaries (Figure 5.9). In addition, high-temperature solutionized annealing followed by water quenching also causes the dissolution of precipitates (solid-solution Ti). During thermomechanical cycles, the irrecoverable strain originates from the irreversible plastic deformation and the accumulation of the residual martensite phase. Solutionized annealing decreases the density of dislocations and metal-structures, which reduces irreversible plastic deformation induced by dislocation

141

proliferation. This also can be demonstrated by the STEM-HAADF image of solutionized sample after 50 thermomechanical cycles, where dislocations are barely seen. Its irrecoverable strain is mainly associated with the accumulation of residual detwinned martensite phases. As shown in Figure 5.17 (a)–(c), detwinned martensite is still present in the sample after heating to 423 K (higher than its $A_f \approx 386$ K), indicating that the transformation from detwinned martensite to austenite is suppressed. Therefore, the irreversible strain in the solutionized sample is attributed to the accumulation of irreversible martensite. Interestingly, the irreversible detwinned martensite phases appear near the undissolved large-size precipitates (Figure 5.17). Such precipitates create internal stress and inhibit phase transformation from detwinned martensite to austenite.
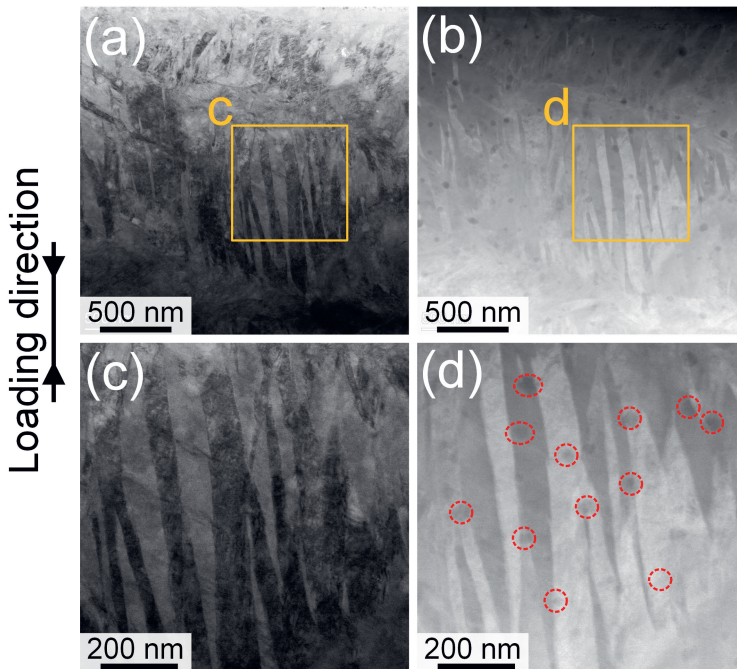

Figure 5.16. TEM images of directly aged NiTi after 50 shape memory cycles: (a) and (c) BF image; (b) and (d) STEM-HAADF image (precipitates were marked by red cycles).

The S+A sample shows the highest TWSME strain among samples (Figure 5.14). The TWSME originates from configured martensite plates by defects and directional internal stress by thermomechanical cycles [47]. It indicates that the S+A sample after thermomechanical cycles has the most effective internal stress state for triggering TWSME.

Such pronounced TWSME response can be attributed to the effective strain partitioning in the S+A sample. As shown in the TEM images of the S+A sample after 50 thermomechanical cycles (Figure 5.18), S+A effectively creates a heterogeneous structure around grain boundaries, i.e. nanoscale hard Ti_2NiO_x precipitates and soft NiTi matrix (Figure 5.18 (a)–(e)). In addition, due to the existence of Ti_2NiO_x, martensitic transformation in the surrounding NiTi matrix is suppressed. This is confirmed by TEM results. Since the TEM was performed at RT, which is lower than the M_f (~323 K, Figure 5.5 (a) and (b)), the martensitic phase should have been present rather than the observed austenitic NiTi (Figure 5.18 (d)).
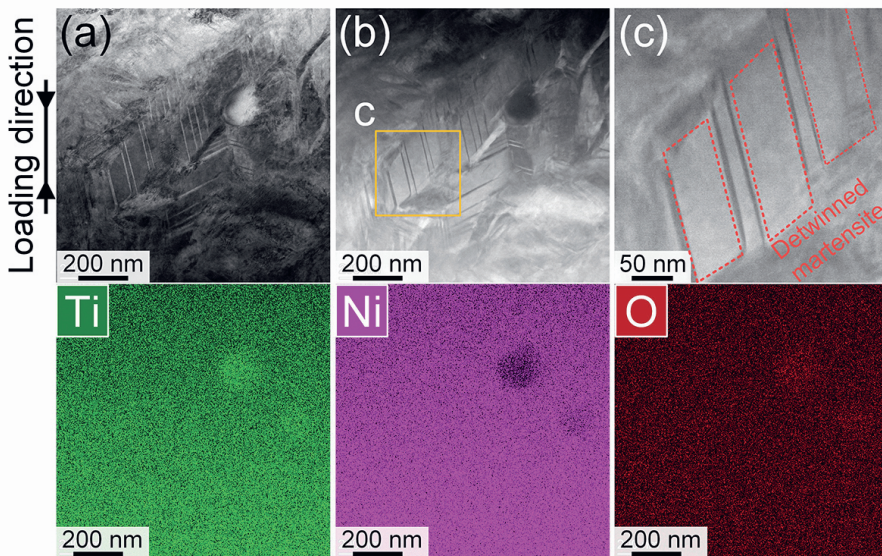

Figure 5.17. TEM images of S NiTi after 50 shape memory cycles: (a) BF image, (b) STEM-HAADF image, (c) enlarge zone in (b); The EDS mappings of (a) are shown in the second row.

It has been widely argued that heterogeneous structures can result in strain hardening due to the strain partitioning between soft and hard regions [48-50]. In this case, the S+A sample has the highest stress level under the same deformation among tested samples (Figure 5.11). Strain partitioning between NiTi and nanoscale Ni_4Ti_3 has been observed by Dong et al [51] in Ni-rich NiTi. They demonstrated that nanoscale precipitates, even with a low fraction, still allow for a considerable amount of applied stress. In this work, strain partitioning is induced between nanoscale Ti_2NiO_x and matrix. To the best of the authors' knowledge, this phenomenon is discovered for the first time in Ti-rich NiTi. Since there is a low cooling rate in conventional manufacturing methods, stable and coarse Ti_2NiO_x (several micrometers) precipitates are formed in the as-fabricated state, which cannot be further dissolved within the matrix after high-temperature solutionized annealing [52, 53]. By contrast, in this work, nanoscale pure Ti particles are found in as-fabricated Ti-rich L-PBF, which allows for its dissolution into the matrix (Figure 5.7) after solutionized annealing. Furthermore, the oversaturated Ti in the matrix precipitates in the form of nanoscale intergranular Ti_2NiO_x in the subsequent aging (Figure 5.10).

Therefore, the reason for a large TWSME in the S+A sample results from the as-following two aspects: (1) the hard region, consisting of intergranular Ti_2NiO_x precipitates and surrounding distorted austenite matrix, promotes strain partitioning and makes stress within grains more directional, which is favorable for TWSME; (2) the intergranular Ti_2NiO_x precipitates effectively encloses directional internal stress within each grain, further enhancing TWSME.
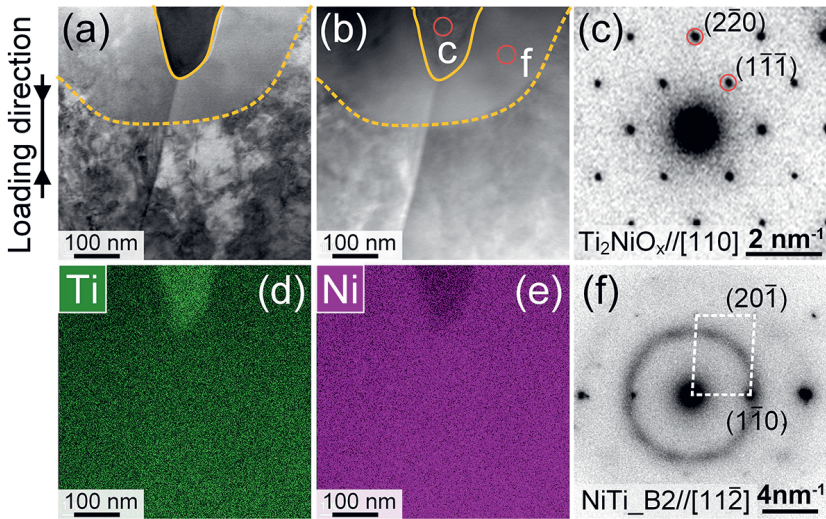
5

Figure 5.18. TEM images of the S+A sample after 50 shape memory cycles: (a) BF image, (b) STEM-HAADF image, (c) SAED of precipitate, (d) and (e) EDS mapping of (a), and (f) SAED of matrix near the precipitate.

5.5. Conclusions

In this work, the effect of various heat treatments on microstructural evolution, phase transformation, and shape memory behavior was systematically investigated in the L-PBF Ti-rich NiTi. The main conclusions are summarized below:

1. Heat treatments were found to mainly affect nano-scaled precipitates and atomic defects, while grain sizes and morphologies were not significantly affected. Direct aging promotes intragranular precipitation of the Ti_2NiO_x phase, while solutionized annealing dissolves metastable Ti particles into the NiTi matrix and reduces atomic defects. Intergranular Ti_2NiO_x precipitates were shown in the solutionized and aged sample.

2. All heat treatments increase phase transformation temperatures compared with those in the as-fabricated state, which was found to be due to an increase in the atomic Ti/Ni ratio in the NiTi matrix and a decrease in atomic defect density.

3. For the single thermomechanical test with gradually increased strain level, the optimized heat treatments allow tailoring the stress window without any sacrifice in

the recovery of one-way shape memory strain. For the cyclic thermomechanical tests, solutionized annealing dramatically improved OWSME degradation resistance due to the elimination of microstructural defects, while S+A gave the most pronounced TWSME response due to strain partitioning induced by the heterogonous microstructures between hard intergranular Ti_2NiO_x and soft NiTi matrix.

Relationships between heat treatments, microstructures and functional responses in the L-PBF NiTi are revealed based on multiscale correlative characterization. These findings can be used to enhance the one-way and two-way shape memory degradation resistance of L-PBF NiTi. Furthermore, this work also provides an alternative way to tailor SME temperature and stress windows increasing the attractiveness of 4D-printed NiTi.

5

References

[1] J. Mohd Jani, M. Leary, A. Subic, M.A. Gibson, A review of shape memory alloy research, applications and opportunities, Mater. Des. 56 (2014) 1078-1113.

[2] A. Ahadi, T. Kawasaki, S. Harjo, W.-S. Ko, Q. Sun, K. Tsuchiya, Reversible elastocaloric effect at ultra-low temperatures in nanocrystalline shape memory alloys, Acta Mater. 165 (2019) 109-117.

[3] X.M. Zhang, J. Fernandez, J.M. Guilemany, Role of external applied stress on the two-way shape memory effect, Mater. Sci. Eng., A 438-440 (2006) 431-435.

[4] T. Omori, J. Wang, Y. Sutou, R. Kainuma, K. Ishida, Two-Way Shape Memory Effect Induced by Bending Deformation in Ductile Cu-Al-Mn Alloys, Mater. Trans. 43(7) (2002) 1676-1683.

[5] B. Xu, G. Kang, Q. Kan, C. Yu, X. Xie, Phase field simulation on the cyclic degeneration of one-way shape memory effect of NiTi shape memory alloy single crystal, Int. J. Mech. Sci. 168 (2020) 105303.

[6] S.L. Sing, W.Y. Yeong, Laser powder bed fusion for metal additive manufacturing: perspectives on recent developments, Virtual Phys. Prototyp. 15(3) (2020) 359-370.

[7] Z. Yan, J.-N. Zhu, E. Borisov, T. Riemslag, S.P. Scott, M. Hermans, J. Jovanova, V. Popovich, Superelastic response and damping behavior of additively manufactured Nitinol architectured materials, Addit. Manuf. 68 (2023) 103505.

[8] Y. Guo, Z. Xu, Q. Wang, S. Zu, M. Liu, Z. Yu, Z. Zhang, L. Ren, Corrosion resistance and biocompatibility of graphene oxide coating on the surface of the additively manufactured NiTi alloy, Prog. Org. Coat. 164 (2022) 106722.

[9] Y. Tian, J.A. Muñiz-Lerma, M. Brochu, Nickel-based superalloy microstructure obtained by pulsed laser powder bed fusion, Mater. Charact. 131 (2017) 306-315.

[10] M.-S. Pham, B. Dovgyy, P.A. Hooper, C.M. Gourlay, A. Piglione, The role of side-branching in microstructure development in laser powder-bed fusion, Nat. Commun. 11(1) (2020) 749.

[11] J.-N. Zhu, E. Borisov, X. Liang, R. Huizenga, A. Popovich, V. Bliznuk, R. Petrov, M. Hermans, V. Popovich, Controlling microstructure evolution and phase transformation behavior in additive manufacturing of nitinol shape memory alloys by tuning hatch distance, J. Mater. Sci. 57(10) (2022) 6066-6084.

5

[12] H.R. Kotadia, G. Gibbons, A. Das, P.D. Howes, A review of Laser Powder Bed Fusion Additive Manufacturing of aluminium alloys: Microstructure and properties, Addit. Manuf. 46 (2021) 102155.

[13] L. Xu, Z. Chai, B. Peng, W. Zhou, X. Chen, Effect of heat treatment on microstructures and mechanical properties of Inconel 718 additively manufactured using gradient laser power, Mater. Sci. Eng., A 868 (2023) 144754.

[14] T. Pinomaa, M. Lindroos, M. Walbrühl, N. Provatas, A. Laukkanen, The significance of spatial length scales and solute segregation in strengthening rapid solidification microstructures of 316L stainless steel, Acta Mater. 184 (2020) 1-16.

[15] J. Gan, L. Duan, F. Li, Y. Che, Y. Zhou, S. Wen, C. Yan, Effect of laser energy density on the evolution of Ni4Ti3 precipitate and property of NiTi shape memory alloys prepared by selective laser melting, J. Alloys Compd. 869 (2021) 159338.

[16] J. Frenzel, E.P. George, A. Dlouhy, C. Somsen, M.F.X. Wagner, G. Eggeler, Influence of Ni on martensitic phase transformations in NiTi shape memory alloys, Acta Mater. 58(9) (2010) 3444-3458.

[17] G. Tadayyon, M. Mazinani, Y. Guo, S.M. Zebarjad, S.A.M. Tofail, M.J.P. Biggs, Study of the microstructure evolution of heat treated Ti-rich NiTi shape memory alloy, Mater. Charact. 112 (2016) 11-19.

[18] A. Falvo, F. Furgiuele, C. Maletta, Two-way shape memory effect of a Ti rich NiTi alloy: experimental measurements and numerical simulations, Smart Mater. Struct. 16(3) (2007) 771.

[19] T. Simon, A. Kröger, C. Somsen, A. Dlouhy, G. Eggeler, On the multiplication of dislocations during martensitic transformations in NiTi shape memory alloys, Acta Mater. 58(5) (2010) 1850-1860.

[20] Y. Cao, X. Zhou, D. Cong, H. Zheng, Y. Cao, Z. Nie, Z. Chen, S. Li, N. Xu, Z. Gao, W. Cai, Y. Wang, Large tunable elastocaloric effect in additively manufactured Ni–Ti shape memory alloys, Acta Mater. 194 (2020) 178-189.

[21] S. Saedi, A.S. Turabi, M. Taheri Andani, C. Haberland, H. Karaca, M. Elahinia, The influence of heat treatment on the thermomechanical response of Ni-rich NiTi alloys manufactured by selective laser melting, J. Alloys Compd. 677 (2016) 204-210.

5

[22] J. Fu, Z. Hu, X. Song, W. Zhai, Y. Long, H. Li, M. Fu, Micro selective laser melting of NiTi shape memory alloy: Defects, microstructures and thermal/mechanical properties, Opt. Laser. Technol. 131 (2020) 106374.

[23] S. Li, H. Hassanin, M.M. Attallah, N.J.E. Adkins, K. Essa, The development of TiNi-based negative Poisson's ratio structure using selective laser melting, Acta Mater. 105 (2016) 75-83.

[24] C. Tan, S. Li, K. Essa, P. Jamshidi, K. Zhou, W. Ma, M.M. Attallah, Laser Powder Bed Fusion of Ti-rich TiNi lattice structures: Process optimisation, geometrical integrity, and phase transformations, Int. J. Mach. Tools Manuf. 141 (2019) 19-29.

[25] T.-x. Zhao, G.-z. Kang, C. Yu, Q.-h. Kan, Experimental investigation of the cyclic degradation of the one-way shape memory effect of NiTi alloys, Int. J. Miner. Metall. Mater. 26(12) (2019) 1539-1550.

[26] L. Orgéas, D. Favier, Stress-induced martensitic transformation of a NiTi alloy in isothermal shear, tension and compression, Acta Mater. 46(15) (1998) 5579-5591.

[27] Y. Liu, Z. Xie, J. Van Humbeeck, L. Delaey, Asymmetry of stress–strain curves under tension and compression for NiTi shape memory alloys, Acta Mater. 46(12) (1998) 4325-4338.

[28] Z. Yu, Z. Xu, Y. Guo, R. Xin, R. Liu, C. Jiang, L. Li, Z. Zhang, L. Ren, Study on properties of SLM-NiTi shape memory alloy under the same energy density, J. Mater. Res. Technol. 13 (2021) 241-250.

[29] H.Z. Lu, C. Yang, X. Luo, H.W. Ma, B. Song, Y.Y. Li, L.C. Zhang, Ultrahigh-performance TiNi shape memory alloy by 4D printing, Mater. Sci. Eng., A 763 (2019) 138166.

[30] Q. Zhang, S. Hao, Y. Liu, Z. Xiong, W. Guo, Y. Yang, Y. Ren, L. Cui, L. Ren, Z. Zhang, The microstructure of a selective laser melting (SLM)-fabricated NiTi shape memory alloy with superior tensile property and shape memory recoverability, Appl. Mater. Today. 19 (2020) 100547.

[31] N. Shayesteh Moghaddam, S.E. Saghaian, A. Amerinatanzi, H. Ibrahim, P. Li, G.P. Toker, H.E. Karaca, M. Elahinia, Anisotropic tensile and actuation properties of NiTi fabricated with selective laser melting, Mater. Sci. Eng., A 724 (2018) 220-230.

[32] B. Erbstoeszer, B. Armstrong, M. Taya, K. Inoue, Stabilization of the shape memory effect in NiTi: an experimental investigation, Scripta Mater. 42(12) (2000) 1145-1150.

5

[33] M.E. Mitwally, M. Farag, Effect of cold work and annealing on the structure and characteristics of NiTi alloy, Mater. Sci. Eng., A 519(1) (2009) 155-166.

[34] P. Zhang, S.X. Li, Z.F. Zhang, General relationship between strength and hardness, Mater. Sci. Eng., A 529 (2011) 62-73.

[35] T. Bormann, B. Müller, M. Schinhammer, A. Kessler, P. Thalmann, M. de Wild, Microstructure of selective laser melted nickel–titanium, Mater. Charact. 94 (2014) 189-202.

[36] M. Speirs, B. Van Hooreweder, J. Van Humbeeck, J.P. Kruth, Fatigue behaviour of NiTi shape memory alloy scaffolds produced by SLM, a unit cell design comparison, J. Mech. Behav. Biomed. Mater. 70 (2017) 53-59.

[37] J.-N. Zhu, E. Borisov, X. Liang, E. Farber, M.J.M. Hermans, V.A. Popovich, Predictive analytical modelling and experimental validation of processing maps in additive manufacturing of nitinol alloys, Addit. Manuf. 38 (2021) 101802.

[38] J. Mentz, J. Frenzel, M.F.X. Wagner, K. Neuking, G. Eggeler, H.P. Buchkremer, D. Stöver, Powder metallurgical processing of NiTi shape memory alloys with elevated transformation temperatures, Mater. Sci. Eng., A 491(1) (2008) 270-278.

[39] A. Foroozmehr, A. Kermanpur, F. Ashrafizadeh, Y. Kabiri, Investigating microstructural evolution during homogenization of the equiatomic NiTi shape memory alloy produced by vacuum arc remelting, Mater. Sci. Eng., A 528(27) (2011) 7952-7955.

[40] Y. Liu, Z. Xie, J.V. Humbeeck, L. Delaey, Y. Liu, On the deformation of the twinned domain in Niti shape memory alloys, Philos. Mag. A 80(8) (2000) 1935-1953.

[41] C. Yu, G. Kang, Q. Kan, X. Xu, Physical mechanism based crystal plasticity model of NiTi shape memory alloys addressing the thermo-mechanical cyclic degeneration of shape memory effect, Mech. Mater. 112 (2017) 1-17.

[42] Q. Zhou, M.D. Hayat, G. Chen, S. Cai, X. Qu, H. Tang, P. Cao, Selective electron beam melting of NiTi: Microstructure, phase transformation and mechanical properties, Mater. Sci. Eng., A 744 (2019) 290-298.

[43] I. Kaya, H. Tobe, H.E. Karaca, M. Nagasako, R. Kainuma, Y. Chumlyakov, Positive and negative two-way shape memory effect in [111]-oriented $Ni_{51}Ti_{49}$ single crystals, Mater. Sci. Eng., A 639 (2015) 42-53.

[44] C. Haberland, M. Elahinia, J. Walker, H. Meier, J. Frenzel, Additive Manufacturing of Shape Memory Devices and Pseudoelastic Components, 2013.

5

[45] Z. Xiong, Z. Li, Z. Sun, S. Hao, Y. Yang, M. Li, C. Song, P. Qiu, L. Cui, Selective laser melting of NiTi alloy with superior tensile property and shape memory effect, Journal of Materials Science & Technology 35(10) (2019) 2238-2242.

[46] G. Tadayyon, M. Mazinani, Y. Guo, S.M. Zebarjad, S.A.M. Tofail, M.J. Biggs, The effect of annealing on the mechanical properties and microstructural evolution of Ti-rich NiTi shape memory alloy, Mater. Sci. Eng., A 662 (2016) 564-577.

[47] C. Lexcellent, S. Leclercq, B. Gabry, G. Bourbon, The two way shape memory effect of shape memory alloys: an experimental study and a phenomenological model, Int. J. Plast. 16(10) (2000) 1155-1168.

[48] J. Li, W. Lu, S. Chen, C. Liu, Revealing extra strengthening and strain hardening in heterogeneous two-phase nanostructures, Int. J. Plast. 126 (2020) 102626.

[49] M.N. Hasan, Y.F. Liu, X.H. An, J. Gu, M. Song, Y. Cao, Y.S. Li, Y.T. Zhu, X.Z. Liao, Simultaneously enhancing strength and ductility of a high-entropy alloy via gradient hierarchical microstructures, Int. J. Plast. 123 (2019) 178-195.

[50] F. He, Z. Yang, S. Liu, D. Chen, W. Lin, T. Yang, D. Wei, Z. Wang, J. Wang, J.-j. Kai, Strain partitioning enables excellent tensile ductility in precipitated heterogeneous high-entropy alloys with gigapascal yield strength, Int. J. Plast. 144 (2021) 103022.

[51] Y.H. Dong, D.Y. Cong, Z.H. Nie, Z.B. He, L.F. Li, Z.L. Wang, Y. Ren, Y.D. Wang, Stress transfer during different deformation stages in a nano-precipitate-strengthened Ni-Ti shape memory alloy, Appl. Phys. Lett. 107(20) (2015) 201901.

[52] M. Kaya, A. Buğutekin, N. Orhan, Effect of Solution Treatment on Thermal Conductivity of Porous NiTi Shape Memory Alloy, Int. J. Thermophys. 32(3) (2011) 665-673.

[53] C.-l. Chu, J.-C.Y. Chung, P.-K. Chu, Effects of heat treatment on characteristics of porous Ni-rich NiTi SMA prepared by SHS technique, Trans. Nonferrous Met. Soc. 16(1) (2006) 49-53.

5

6

Achieving Superelasticity in Additively Manufactured Ni-Lean NiTi by Crystallographic Design

Abstract

Superelastic metallic materials possessing large recoverable strains are widely used in automotive, aerospace and energy conversion industries. Superelastic materials working at high temperatures and with a wide temperature range are increasingly required for demanding applications. Until recently, high temperature superelasticity has only been achievable with multicomponent alloys fabricated by complex processes. In this study, a novel framework of multi-scale models enabling texture and microstructure design is proposed for high-performance NiTi fabrication via laser powder bed fusion. Based on the developed framework, a Ni-lean Ni (49.4 at. %)-Ti alloy is, for the first time, endowed with a 4% high-temperature compressive superelasticity. A $\langle 001 \rangle$ texture, unfavorable for plastic slip, is created to realize enhanced functionality. The unprecedented superelasticity can be maintained up to 453K, which is comparable with but has a wider superelastic temperature range (~110 K) than rare earth alloyed NiTi alloys, previously only realizable with grain refinement, and other complicated post-processing operations. At the same time, its shape memory stability is also improved due to existing textured $\langle 100 \rangle$ martensite and intergranular precipitation of Ti_2NiOx. This discovery reframes the way of designing superior performance NiTi based alloys through directly tailoring crystallographic orientations during additive manufacturing.

6

6.1. Introduction

Reversible martensitic transformation, a diffusionless solid-solid phase transition [1], gives shape memory alloys (SMAs) unique functional properties. Depending on the initial phase states before deformation, the properties are divided into superelasticity and shape memory effect (SME). Superelasticity (also termed pseudoelasticity), a rubber-like behavior, makes SMAs recover their deformation after unloading [2]. Unlike traditional metallic materials, superelastic SMAs can recover several percent of strain. SME is a capability of SMAs to regain their original shapes after deformation by heating [3]. Due to its attractive functional properties [4, 5], SMAs are widely utilized as actuators, sensors, dampers and medical implants [6]. However, superelasticity with higher operating temperatures and a wider superelastic temperature is required [7] in such emerging applications as aerospace, energy and vehicle engineering fields. At the same time, to improve energy utilizing

efficiency and reduce costs, SMAs with multi-functions, a high temperature superelasticity and a stable SME, are highly desired.

Nitinol (NiTi), as the most commercially successful shape memory alloy, cannot meet this challenge. Traditionally, high-temperature superelasticity has been achieved by increasing phase-transformation temperatures whilst inhibiting dislocation slip through lattice distortion [8], grain refinement [9] or precipitation strengthening [10]. These require complex processing combinations of multicomponent alloying [7, 8], severe-plastic deformation [9] and heat treatments [10, 11]. For instance, $Ti_{20}Hf_{15}Zr_{15}Cu_{25}Ni_{25}$ [8], $Ti_{16.67}Zr_{16.67}Hf_{16.67}Ni_{25}Co_{10}Cu_{15}$ [12] and severely cold rolled Ti-44Ni-5Cu-1Al [13] have been demonstrated to have potential for enhancing high-temperature superelasticity. However, such methods are costly and complex, limiting superelastic products only in form of sheets, tubes and wires.

Nowadays, to minimize greenhouse gas emissions and energy consumption, alloy sustainability should be taken into account. To fulfil this goal, SMAs with simplified alloying components and high superelastic temperature windows need to be developed [14]. It is known that Ni-lean NiTi exhibits martensitic phase transformation in a higher temperature (can reach ~373 K) [15], which potentially allows it to achieve high-temperature superelasticity. Nonetheless, due to relatively low yield stress and lack of precipitates blocking dislocation movements, plastic deformation usually occurs prior to stress-induced martensite transformation (SIMT) in the Ni-lean NiTi [16]. Therefore, Ni-lean binary NiTi cannot reveal superelasticity in an as-fabricated state without post-treatments. Limited by conventional processes, traditional concepts of inducing superelasticity are to increase dislocation movement barriers (induced by robust phase interfaces or grain boundaries) [13, 17] and improve phase transformation compatibility between austenite and stress-induced martensite [18]. This still inevitably involves multicomponent alloying and complex deformation processes followed by heat treatments.

Crystalline materials can exhibit anisotropic mechanical and functional properties due to preferred crystallographic orientation [19]. Utilizing such anisotropy in Ni-lean NiTi is a promising way to induce high-temperature superelasticity, instead of alloying with rare elements. This introduces a few challenges: 1) is there a preferred crystallographic orientation that can introduce superelasticity in Ni-lean NiTi; 2) how to screen the desirable crystallographic orientation; 3) how to fabricate Ni-lean NiTi with specifically orientated grains. Therefore, quantitative predictions about the effect of crystallographic orientations on NiTi superelasticity and a suitable processing technique should be investigated. Specifically, in the present study, the molecular dynamics (MD) in single crystal NiTi was employed to

6

screen appropriate crystallographic orientations for superelastic behavior. Considering the fact that single-crystal fabrication is still challenging, single-crystal-like polycrystalline Ni-lean NiTi consisting of large columnar grains are considered as alternatives [20]. Laser powder bed fusion (L-PBF), a type of an additive manufacturing (AM) technique [21], was applied to fabricate NiTi with designed microstructure. It offers sufficient flexibility to tailor grain morphologies and orientation via tuning L-PBF processing parameters. Furthermore, finite element modeling was carried out to bridge gaps between MD-optimized crystallographic orientations and the design of L-PBF processing parameters.

In this study, for the first time, a superelasticity with a high and wide temperature window was reported in a Ni-lean Ni (49.4 at. %)-Ti fabricated by additive manufacturing. This was achieved by employing multi-scaled models enabling microstructural design and functional property prediction, which opens up a new way of designing high-performance materials by controlling functional anisotropy.

6.2. Methodology

6.2.1. Molecular dynamics simulations

Molecular dynamic (MD) simulations were performed on an open-source code LAMMPS [22]. The modified embedded-atom method (MEAM) potential developed by Ko et al. was applied to describe interatomic interactions [23]. To investigate superelastic behavior at different temperatures, single crystal models, including [100], [110], and [111] orientations, were used. The single crystal model size was ~21×10.5×10.5 nm^3 containing ~1.7×10^5 atoms. All model sizes slightly varied for each respective configuration to ensure that the model size is an integer multiple of the crystal plane distance. The primitive cell was taken from the literature [24]. To more accurately understand the superelastic behavior in polycrystalline NiTi, the compressive behavior of bicrystal models for [100], [110], and [111] textures were studied. Bicrystal models with nearly the same orientations were built with Atomsk [25], and the model's size was ~23×16×16 nm^3 containing ~4.5×10^5 atoms. A three-dimensional periodic boundary condition was applied. To simulate the non-elastic deformation in a real material, 0.5% percent of atoms were removed in each model as point defects. After 1×10^{-10} s relaxation, the thickness of grain boundaries is about four atomic layers. Phase transformation temperatures were determined by heating and cooling, and the temperature change rate was set as 0.5 K / ps optimized by Ko et al. [23].

6

In MD models, dislocations and nanoscale Ti_2Ni precipitates in NiTi are not taken into account. To mimic a fiber texture, The two grains in the model have similar orientations and a high aspect ratio. Three dimensional periodic boundary condition is applied, which makes the grain with thickness of about 80 Å infinitely expand in the other two dimensions. The bicrystal model is built with Voronoi tessellation method in ATOMSK by assigning the centre points and the orientation of each grain. The misorientations for the two grains with respect to the denoted orientation, i.e. [100], [110], and [111], are represented with three angles, corresponding to the rotation of the grain around global X, Y, and Z axis, respectively. The value of misorientations are randomly chosen to be about 3 . In this aspect, the grain boundary in the bicrystal is built by three independent rotations and therefore it is a random grain boundary.

Bicrystal models were uniaxially compressed to 4% engineering strain at 353K, and single crystal models were uniaxially compressed to 8% engineering strain at different temperatures. The length of the simulation box decreases along compressive direction, and sizes along the rest two directions were allowed to expand or shrink to maintain the corresponding stress components near zero. When the compression strain reaches the maximum value, the load was removed and the change of the model's size in the following 2×10^{-11} s was recorded. The adaptive common neighbor analysis (A-CNA) is applied to identify the atomic structure during loading, especially the martensitic phase induced by stress which is of most concern. Data analysis and atomic visualizations were carried out on the OVITO [26].

6.2.2. Finite element modeling

Details about the finite element model, heat source description and thermophysical properties of NiTi can be found in the section 4.2.2 of Chapter 4.

6.2.3. Thermodynamic calculations and grain morphology selection

Classical and solute-trapped Scheil-Gulliver solidification models were simulated using Thermo-Calc software (version 2021b) with the TCHEA2 database. The solution content of Ti in the NiTi BCC_B2 phase as a function of the solid faction was derived from Scheil-Gulliver solidification models.

By utilizing an analytical model, grain morphologies were deduced based on thermal gradient (G) and solidification rate (R). The model is formulated as [27]:

$$\frac{G^n}{R} = a \left\{ \sqrt[3]{\frac{-4\pi N_0}{3\ln[1-\varphi]}} \times \frac{1}{n+1} \right\}^n \qquad (6.1),$$

where $a = 1.25 \times 10^6$ (K$^{3.4}$/m·s) and $n = 3.4$ are material-dependent constants (fitted by the constitutional tip undercooling based on the Thermo-calc TCHEA2 database), $N_0 = 2 \times 10^{15}$ m^{-3} is the nuclei density for Ni-based alloys [27] and φ is a grain morphology factor. When morphology mainly consists of columnar grains, $\varphi = 0.05$ and if there are equiaxed grains, $\varphi = 0.8$. G and R can be calculated based on FEM results.

6.2.4. Material fabrication

Details about L-PBF NiTi fabrication can be found in the section 3.2.4 of Chapter 3. For high laser power condition, B3 was chosen. For the low laser condition, A2 was chosen. The optimized L-PBF processing parameters are listed in Table 6.1. For convenience, the B2 was named as $\langle 001 \rangle_{BD}$ textured NiTi and A2 was named as non-textured NiTi.

Table 6.1 L-PBF process parameters used in this work for NiTi fabrication.

	Non-textured	$\langle 001 \rangle_{BD}$ textured
Laser Power (W), P	250	950
Scan velocity (mm/s), v	1250	1200
Hatch distance (μm), h	120	180
Layer thickness (μm), t	30	50
Laser beam diameter (μm)	80	500
Volumetric energy density (J/mm^3)	56	88

To investigate compressive superelasticity and the SME, cylindrical samples of 13 mm diameter and 25 mm height (along the building direction) were built and then machined into eight compressive cuboids (4×4×8 mm) using electrical discharge machining (EDM). Samples were ground and polished to remove EDM damage.

6

6.2.5. Microstructural characterization

Metallographic procedures, chemical etching solution and differential scanning calorimetry can be found in the section 4.2.1 of Chapter 2. Nickel contents were determined by ICP-OES and EDS, which were introduced in the section of 3.2.5 of the Chapter 3.

An FEI cubed titan Cs-corrected 80-300 kV transmission electron microscopy (TEM) was employed for microstructural characterization at the nanoscale. Elemental mapping was performed, and high-angle annular dark field (HAADF) images were produced in a scanning transmission electron microscopy (STEM) mode. TEM samples were mechanically polished to ~20 μm thickness, and then punched into 2.3 mm discs and glued on 3 mm diameter Cu rings. The thin disc samples were then further milled to electron transparency by Ar ions.

Phase identification was determined by two-dimensional X-ray diffraction (2D-XRD) using a Bruker D8 Discover diffractometer with Cu Kα radiation and 2D Eiger2 R 500K detector. Data evaluation was carried out by Bruker software DiffracSuite. EVA vs 5.2. Texture was measured by a Bruker D8 Discover diffractometer with Eulerian cradle in parallel beam geometry with Co Kα radiation. Samples were heated to 373 K by a positive temperature coefficient heating element to ensure an austenitic state. Bruker software DiffracSuite.Diffrac 4.1 was used for Data evaluation.

For in-situ heating and cooling XRD measurements, NiTi samples were first immersed in liquid nitrogen to ensure a fully martensitic state. Temperature changes were achieved by using an Anton Paar DHS 1100 hot-stage with a temperature range from room temperature (RT) to 423 K. XRD scans were measured over a 2θ range between 15º and 100º at RT and between 38º and 150º at 423 K. The scanning step size was 0.04º and the counting time per step was 1 s. The in-situ heating and cooling during XRD were performed using still frames within a 2θ range between 37.6º and 47.0º since martensite B19' and R phase peaks are mainly located within this range. The counting time per step was 20 s per frame.

For high-temperature texture measurements, four pole figures of NiTi BCC_B2 phase, (110), (200), (211) and (310) were measured at 423 K. The rotational angle, φ, was scanned from 0 to 360º in steps of 5º. The tilt angle, ψ, was scanned from 0–70º in steps of 5º. The harmonic series expansion method was used to obtain the orientation distribution functions (ODFs) and recalculated pole figures. Based on ODFs, the inverse pole figures can be plotted.

6.2.6. Mechanical testing

Superelasticity and shape memory effects were tested on an MTS 858 tabletop hydraulic test machine by applying uniaxial compression. A strain rate of 1.0×10^{-4} s^{-1} was applied and strains were measured by a contact-based high-temperature ceramic extensometer (632.53F-14, MTS). The temperature change was controlled by induction heating and air flow cooling. The temperature was measured by 3 K-type thermocouples welded onto the NiTi sample surfaces.

Prior to superelasticity tests, samples were heated to 423 K (65 K above austenite finish temperature) and then cooled to 353 K to ensure an austenitic state. Before SME testing, samples were quenched in liquid nitrogen to ensure a fully martensitic state. Schematics of strain definitions and loading paths for superelasticity and the shape memory effect are shown in Figure 6.1. Strains were measured by a high-temperature ceramic extensometer. All samples were loaded and unloaded along the building direction. To investigate the superelastic temperature range, samples were trained (200 cycles) with 6% nominal engineering strain to remove the phase transformation-induced plasticity [28]. In this work, samples with at least 85% recoverable strain ratio are considered to exhibit superelastic behavior.
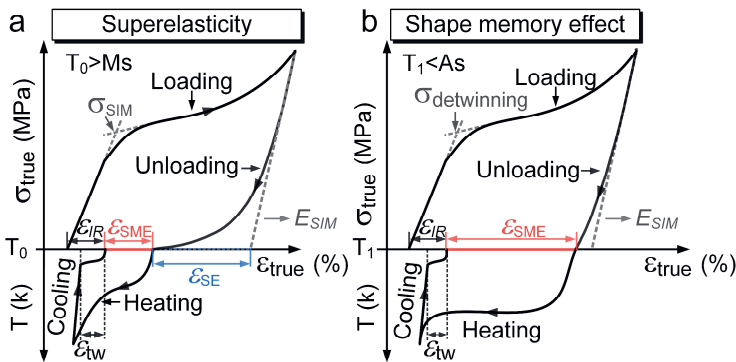

Figure 6.1. Schematics of strain definitions and loading path for (a) superelasticity and (b) shape memory effect. Where, T_0 is a testing temperature for superelasticity, T_1 is a testing temperature for shape memory effect, M_s is the martensite starting temperature, A_s is the austenite starting temperature, σ_{SIM} is the critical stress for stress-induced martensite, $\sigma_{detwinning}$ is the critical stress for detwinning, E_{SIM} is the elasticity modulus of stress-induced martensite, ε_{SE} is the superelasticity strain, ε_{SME} is the shape memory effect strain and ε_{IR} is the irreversible strain.

6.3. Results

6.3.1. Evaluation of superelastic capability

The initiation of superelasticity is determined by the critical stress (σ_{SIM}) for stress-induced martensite transformation (SIMT). Superelasticity disappearance occurs when the required stress of SIMT is higher than the critical stress for plastic slip (usually yield stress, σ_y). Desirable crystallographic orientations theoretically could make NiTi show a low hardening rate during SIMT, a relatively low σ_{SIM} and large recoverable strain.
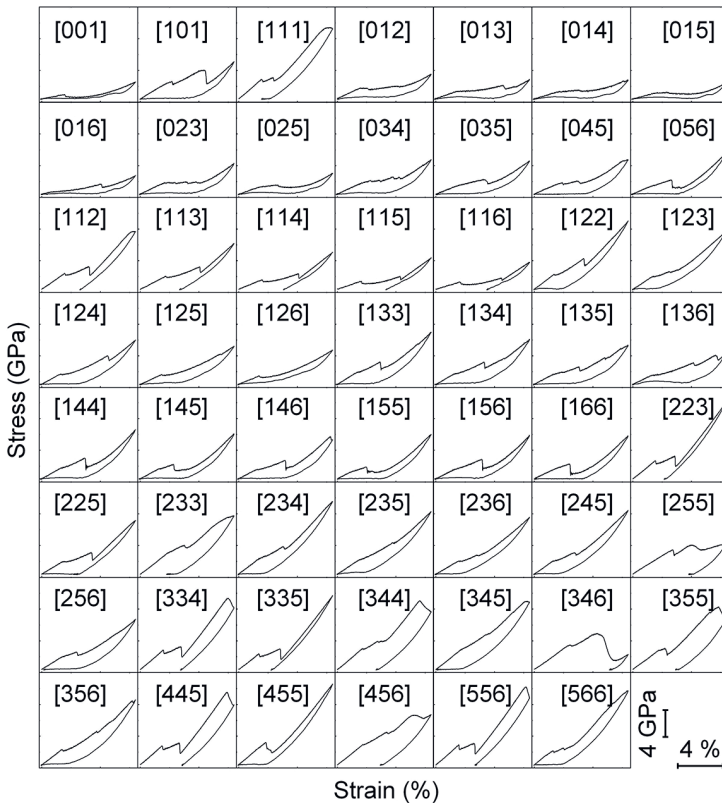

Figure 6.2. Molecular dynamics (MD) simulated compressive strain-stress curves along 55 crystallographic orientations.

To screen desirable NiTi crystallographic orientations, compression (at the test temperature 15 K above A_f) of single crystals was simulated by employing molecular dynamics (MD). In total, 55 crystallographic orientations were considered in this work, while the corresponding MD simulated compressive curves are shown in Figure 6.2.
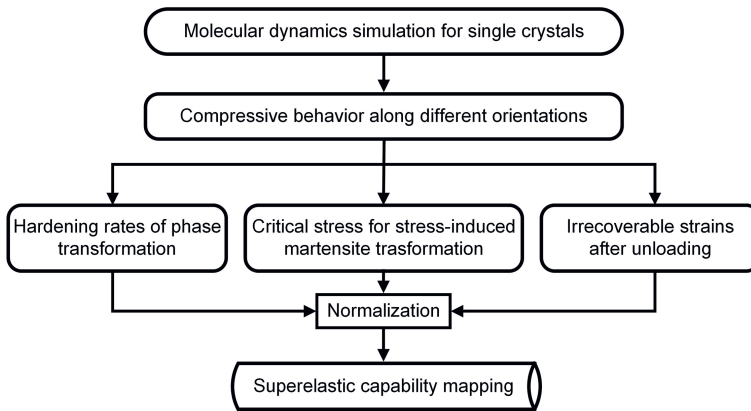

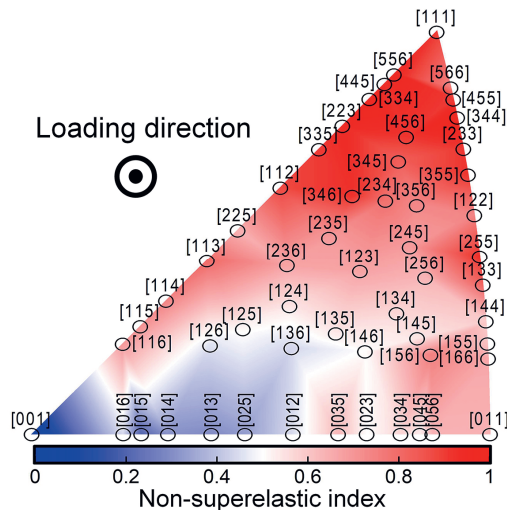Figure 6.3. A flowchart of the screening method for desirable crystallographic orientations.

Figure 6.4. The superelastic capability as a function of crystallographic orientation. The legend is, a dimensionless figure of merit to evaluate superelastic capability, non-superelastic index, and the smaller index value indicates better superelasticity.

The screening process developed in this work is illustrated in a flowchart diagram (Figure 6.3). To integrally evaluate the superelastic capabilities of NiTi with various crystallographic orientations, the hardening rate, σ_{SIM} and the irrecoverable strain were separately normalized by scaling between 0 and 1 to make it dimensionless. Then, the overall normalization was made based on the equal-weighted summation of the three factors as a dimensionless figure of merit to access superelastic capabilities. The lower value of the dimensionless figure of merit indicates the more desirable crystallographic orientation for releasing superelasticity.

For convenience, the dimensionless figure of merit is termed the "non-superelastic index", and all calculated non-superelastic indices are summarized in an inverse pole figure (Figure 6.4). As shown in the Figure 6.4, only orientations close to [001] show high possibilities for desirable superelastic capabilities. Considering the fact that low-index orientations are more common in materials, the [001] oriented NiTi is selected to be further fabricated.

To further confirm the capability of $\langle 001 \rangle$ orientated NiTi of inducing superelasticity, three typical low-Miller-index bicrystal models with periodic boundary conditions, either $\langle 001 \rangle$, $\langle 110 \rangle$ or $\langle 111 \rangle$ orientations, were applied to simulate the compressive behavior of polycrystalline NiTi. The $\langle 001 \rangle$ model shows the lowest σ_{SIM}, near-zero hardening rate and largest recoverable strain (Figure 6.5 (a) and (d)), indicating a more favorable orientation for compression to activate SIMT and a better strain recoverability. Although the $\langle 110 \rangle$ orientation also shows superelasticity based on molecular dynamics results (Figure 6.5 (b) and (d)), the high superelastic stress, SIMT instability (dropped stress during SIMT, Figure 6. 5 (b) ②–④), and large stress hysteresis may cause undesirable fatigue damage and low durability of functional parts [29]. For the $\langle 111 \rangle$ model, the high σ_{SIM} and hardening rate of SIMT results in more martensite variants (Figure 6.5 (c) ④), which induces the interlocking effect of SIM variants and leads to poor strain recoverable ability after unloading. Therefore, it further demonstrates that NiTi with $\langle 001 \rangle$ orientated grains manifest a stable superelasticity.
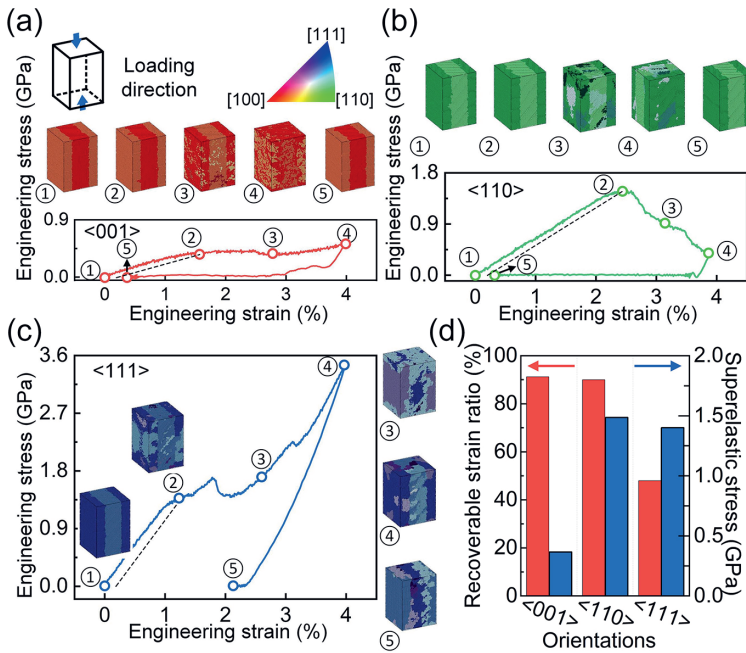
Figure 6.5. MD simulations of 4% engineering strain compressive deformation of bicrystal NiTi periodic boundary conditions at 353 K, showing the behaviour of (a) either $\langle 001 \rangle$ (b) $\langle 110 \rangle$ and (c) $\langle 111 \rangle$ orientations; Corresponding simulated microstructures at different deformation stages are shown above the simulated stress-strain curves: ① the starting state, ② the critical point for stress-induced martensite transformation, ③ the intermediate state between ② and ④, ④ the position with 4% strain, and ⑤ the unloading state; the 0.2% strain offset method was used to identify critical stress for the stress-induced martensite transformation and different colour domains within the simulated microstructures indicate grains with different orientations and martensite variants. (d) The recoverable strain ratios and superelastic stresses of various oriented models.

6.3.2. Microstructure design and validation

The L-PBF process was employed to design $\langle 001 \rangle$ textured polycrystalline NiTi. In cubic crystal structured materials [30], solidified grains prefer to grow along $\langle 001 \rangle$ directions parallel to the local heat flow direction (NiTi has a body-centered-cubic structure

at high temperature, BBC_B2) [30]. To fabricate NiTi with pronounced $\langle 001 \rangle$ texture, the thermal gradient direction should be parallel to the building direction (the layer-increasing direction) and columnar-shaped grains are required.
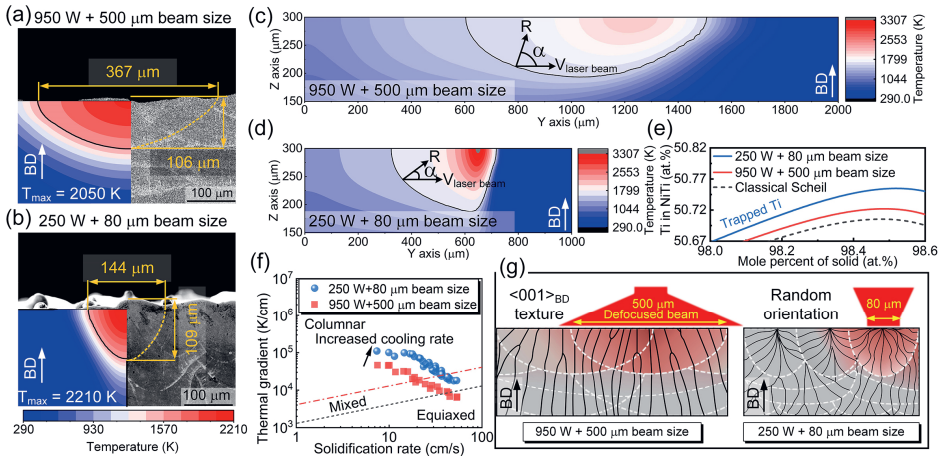

Figure 6.6. Experimental and finite element simulated cross-sectional views of L-PBF NiTi melt pool characteristics for: (a) 950 W laser power with 500 µm beam diameter and (b) 250 W laser power with 80 µm beam diameter. Side-views (parallel to track deposition) of FEM simulated melt pools for (c) the processing condition of 950 W laser power, 1200 mm/s scanning velocity and 500 µm beam diameter and (d) the processing condition of 250 W laser power, 1250 mm/s scanning velocity and 80 µm beam diameter. (e) Ti in BCC NiTi phase as a function of the fraction of solid evaluated by a classic and solute trapping Scheil model. (f) Calculated microstructure selection map for Ni-Ti based on finite element analysis. (g) Schematic of grain growth over several deposition layers with two optimised processing conditions.

Grains grow parallel to the maximum thermal gradient perpendicular to solid-liquid interfaces (can be considered as melt pool boundaries) [31]. To ensure grain growth along the building direction to form a $\langle 001 \rangle$ texture, a wider and shallower melt pool is preferable for local thermal gradients with a consistent direction [32]. The featured melt pool can be achieved by applying a divergent laser beam with a positive defocus [33]. Here, a divergent laser beam with a 500 µm beam diameter was employed. The L-PBF processing parameter

optimization for such processing condition can be found in the section 3.3.2.6 of the Chapter 3. For comparison, L-PBF NiTi fabricated with the optimized E_l of 250/1250 J/mm is used as a reference [34], displaying a narrow and deep melt pool (Figure 3.4 (e) in the section 3.3.2 of the Chapter 3). For convenience, the processing condition of 950 W laser power, 1200 mm/s scanning velocity and 500 μm beam diameter is referred as the high laser power condition and the processing condition of 250 W laser power, 1250 mm/s scanning velocity and 80 μm beam diameter is referred as the low laser power condition.

To predict grain morphologies of L-PBF NiTi fabricated by using the optimized E_l of 950/1200 J/mm, finite-element modeling (FEM) and analytical modeling of grain morphology selection were conducted. Temperature fields, temperature gradients (values and directions) and melt pool shapes were predicted by FEM and the results obtained serve as further input for grain morphology prediction. Due to the large beam diameter, the energy input is more divergent, which results in smaller temperature gradients (Figure 6.6 (a), (c), and (f)) than the low laser power condition (Figure 6.6 (b), (d), and (f)). The simulated melt pool width and height match well with experimental results, indicating reliable FEM simulated results (Figure 6.6 (a) and (b)).

The grain morphology selection is related to temperature gradients and solidification rates. The temperature gradients are extracted from FEM results and the solidification rates (R) are calculated based on the equation (6.2):

$$R = V_{laser} \times \cos\alpha \qquad (6.2),$$

where V_{laser} is the laser beam scanning velocity and α is the angle between the local thermal gradient at the fusion boundary and the laser scanning direction. The developed grain morphology map shows that both applied processing conditions induce columnar grains (Figure 6.6 (f)). Melt pool cross-sectional boundaries show that the high laser power coupled with a large beam size results in a small variation of fusion boundary curvature of ~0.5 (Figure 6.6 (a)). This promotes grain growth in a more consistent orientation along the building direction to form elongated $\langle 001 \rangle$ columnar grains. By contrast, the large melt pool boundary curvature of ~1.4 at the low laser power condition (Figure 6.6 (b)) leads to the frequent change of epitaxial grain growth direction with subsequent depositing layers, causing the formation of random texture. The grain growth behavior is illustrated in the Figure 6.6 (g).
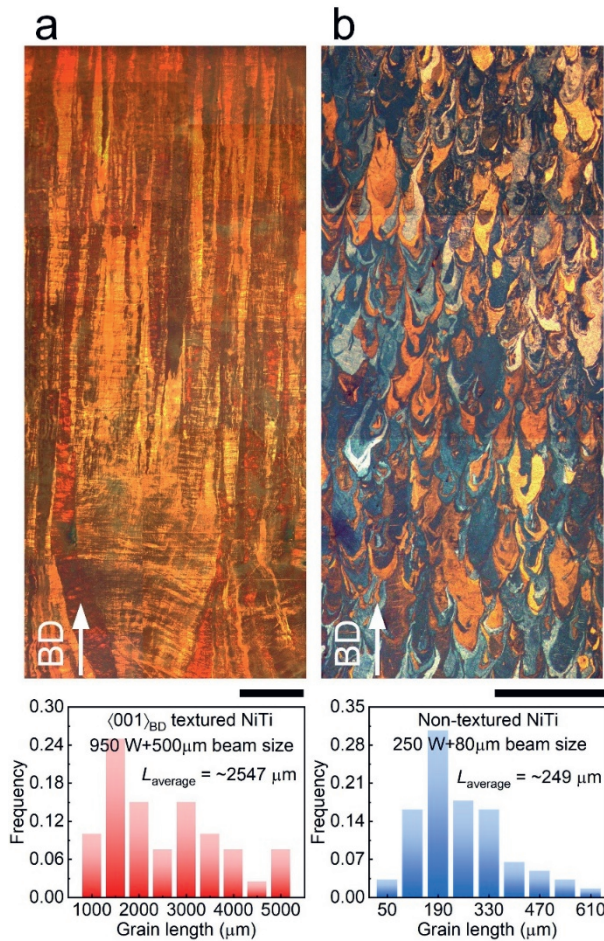
6

Figure 6.7. Optical microscopy images of samples with (a) 950 W laser and 500 μm beam diameter and (b) 250 W laser and 80 μm beam diameter, showing austenite grain size and morphology, and corresponding grain length statistics; All scale bars are 500 μm.

To validate the predictions, bulk NiTi parts were fabricated by L-PBF. To avoid structural defects in the high laser power condition, hatch distance (h) and layer thickness (t) were optimized based on the previously developed model as h = 180 μm and t = 50 μm (the section 3.3.2.6 of the Chapter 3) [35]. For the low laser power condition, the common optimized processing parameters were applied for fabricating the reference NiTi sample [34]. As expected, the L-PBF NiTi with the high 950 W laser power condition shows columnar

polycrystalline features with millimeter-scaled grains (length of ~2.5 mm, Figure 6.7) and a strong $\langle 001 \rangle$ texture along the building direction (referred to $\langle 001 \rangle_{BD}$ texture hereafter) (Figure 6.8 (a) and (b)). The processing condition of low 250 W laser power with focused beam of 80 µm diameter leads to randomly oriented grains (Figure 6.8 (c) and (d), referred to non-texture hereafter).
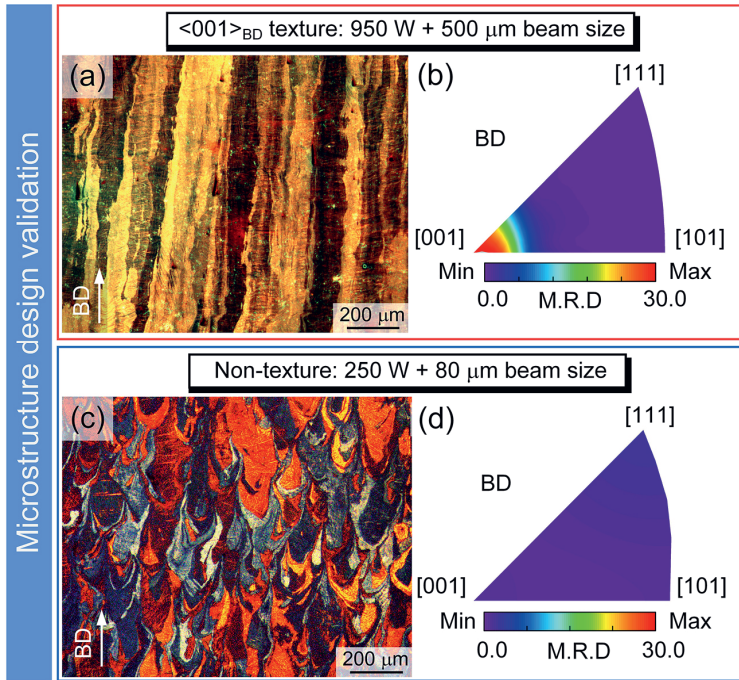

Figure 6.8. Cross-sectional polarized light optical microstructure showing parent austenitic grains of L-PBF NiTi, and inverse pole figures measured by XRD at 473 K to ensure fully austenitic BCC_B2 phase: (a) and (b) for 950 W laser power with 500 µm beam diameter; (c) and (d) for 250 W laser power with 80 µm beam diameter. M.R.D. stands for multiples of a random distribution.

It should however be noted that despite the different grain orientations and sizes, the two materials show similar phase-transformation temperatures (Figure 6.9 (a)) because phase-transformation temperatures are mainly controlled by the Ni content [15], which is ~49.4 ± 0.1 at.% (considered as Ni-lean, Figure 6.9 (b)) for both fabrications. Notably, Ni-

lean NiTi has previously always been considered as showing poor superelasticity, unless cold working coupled with complex heat treatments (HTs) were performed [36]. The $\langle 001 \rangle_{BD}$ textured NiTi fabricated in this work also shows homogenous elemental distribution (Figure 6.10), overcoming the drawback of element segregation with the directional solidification technique. In addition, the high laser power (950 W) coupled with a large beam size (500 µm) is not only promoting a desirable $\langle 001 \rangle$ texture formation but also improving the building rate (calculated by $v \times h \times t$) of NiTi AM fabrication from 4.5 to 10.8 mm^3/s.
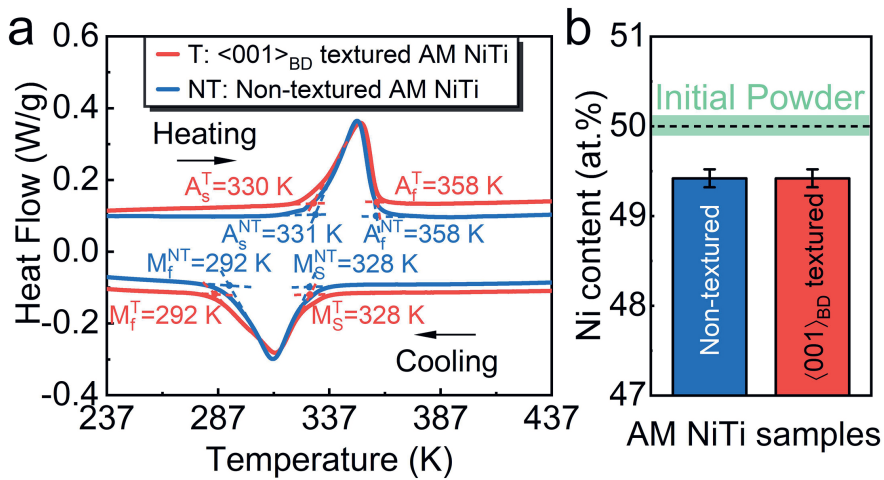
Figure 6.9. (a) DSC of as fabricated $\langle 001 \rangle_{BD}$ textured and non-textured AM NiTi; where, martensite start temperature is denoted as M_s, martensite finish temperature as M_f, austenite start temperature as A_s and austenite finish temperature as A_f. (b) Ni content of $\langle 001 \rangle_{BD}$ textured and non-textured AM NiTi samples measured by inductively coupled plasma-optical emission spectrometry (ICP-OES) with 0.1 at. % accuracy. T is $\langle 001 \rangle_{BD}$ texture and NT is non-texture.

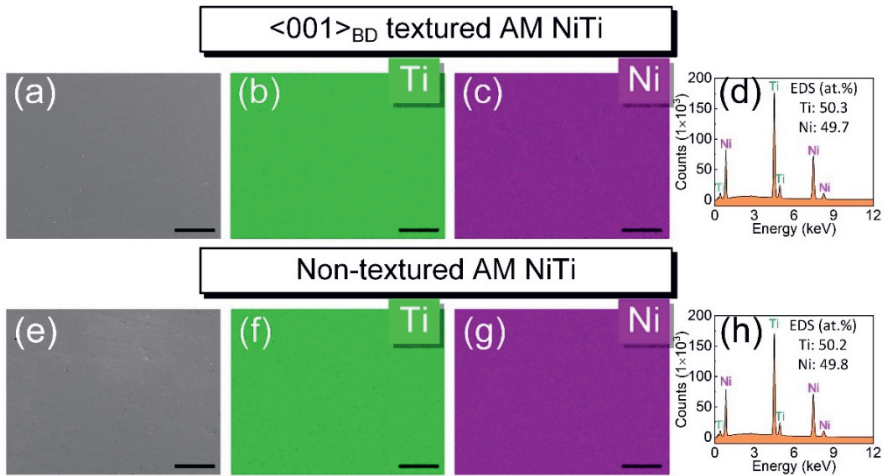Figure 6.10. (a) SEM image of $\langle 001 \rangle_{BD}$ textured AM NiTi sample and its corresponding energy dispersive spectroscopy (EDS) maps of (b) Ti and (c) Ni and (d) EDS spectrum, showing homogeneous elemental distribution; (e) SEM image of non-textured AM NiTi sample and its corresponding energy dispersive spectroscopy (EDS) mappings of (f) Ti and (g) Ni and (h) EDS spectrum; All scale bars are 100 μm.

6.3.3. Phase identifications and microstructure characterization

Considering the crystallographic textures in designed herein AM NiTi, a 2D-XRD technique was employed to identify phases. At RT (~300 K), B19′ martensite is the main phase in both AM NiTi samples (Figure 6.11). When the temperature is heated to 423 K, all B19' martensite variants transform into B2 austenite phase. Since the strong [001] texture in the $\langle 001 \rangle_{BD}$ textured sample, the (110)$_{B2}$ diffraction was shown after a 45° tilt relative to a horizontal plane (Figure 6.11 (a)). Fewer Debye Scherrer diffraction rings and a strong single ring in the $\langle 001 \rangle_{BD}$ textured sample indicate a preferred texture. For the cooling stage, the B2 → M$_{B19'}$ transformation occurs when the temperature is lower than 318 K (Figure 6. 11 (a)), which is consistent with DSC results (Figure 6.9 (a)). With cooling back to RT, the R phase with a small fraction was detected (Figure 6.11). The R phase is commonly seen in the NiTi and acts as an intermedia phase between B2 and B19′ phases [24]. Since the transformation temperature range of B2 → R is within the temperature range of B2 → B19′, the overlapped endothermic peaks cannot be observed by DSC (Figure 6.9).
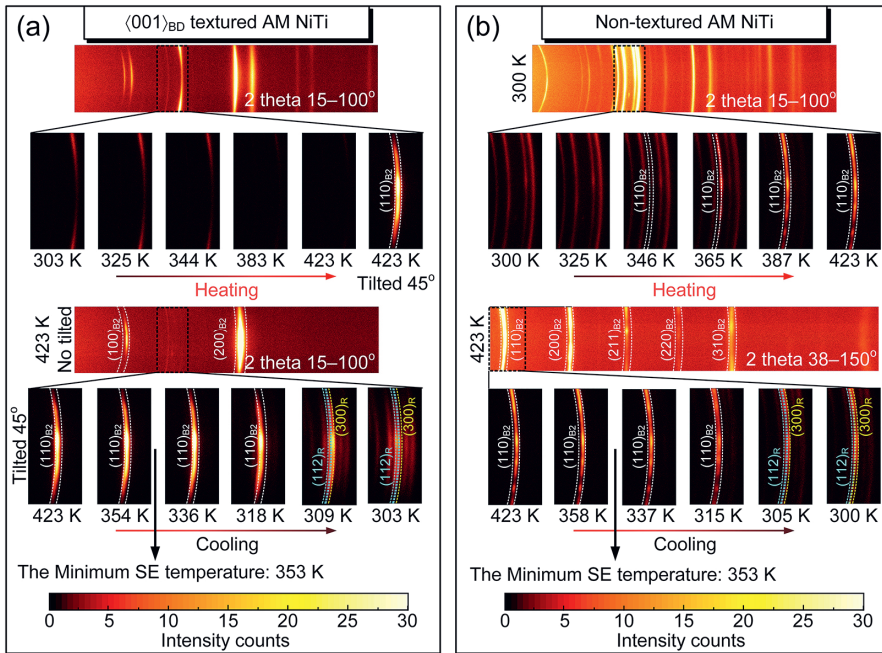
6

Figure 6.11. In-situ heating and cooling two-dimensional X-ray diffraction (2D-XRD) patterns: (a) $\langle 001 \rangle_{BD}$ textured and (b) non-textured AM NiTi samples: Before superelasticity tests, samples were heated to 423 K and then cooled to testing temperatures (> 353 K) to ensure an austenitic state (marked by black arrows in (a) and (b)). Only the austenite B2 phase and intermediate R phase were marked in 2D XRD patterns and the rest peaks are martensite B19′ phase.

Employing different AM processing conditions also affects the morphology and width of the martensite (B19′) phase. The $\langle 001 \rangle_{BD}$ textured AM NiTi (see Figure 6.12 (a) and (c)) shows a ~10 times wider martensite spacing than the non-textured AM NiTi (Figure 6.12 (b) and (d)). Besides, the $\langle 001 \rangle_{BD}$ textured AM NiTi also shows a strong $\langle 100 \rangle$ and relatively weak $\langle 011 \rangle$ martensitic poles (Figure 6.12 (e)). Based on the lattice correspondence of the $[001]_{B2} \| [100]_{B19'}$ and $[001]_{B2} \| [011]_{B19'}$ [37], the textured martensite phase (B19′) inherits the orientation from $\langle 001 \rangle$ textured austenite (BCC_B2) phase (Figure 6.8 (d)).
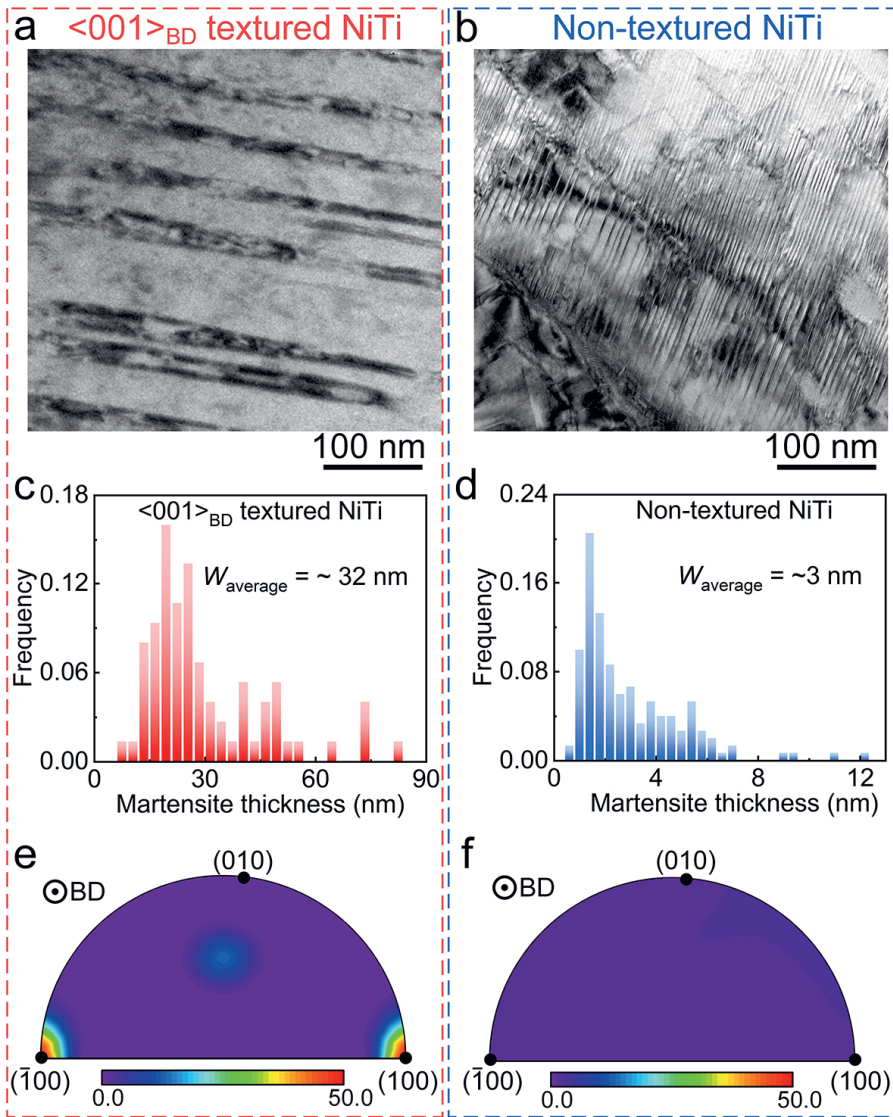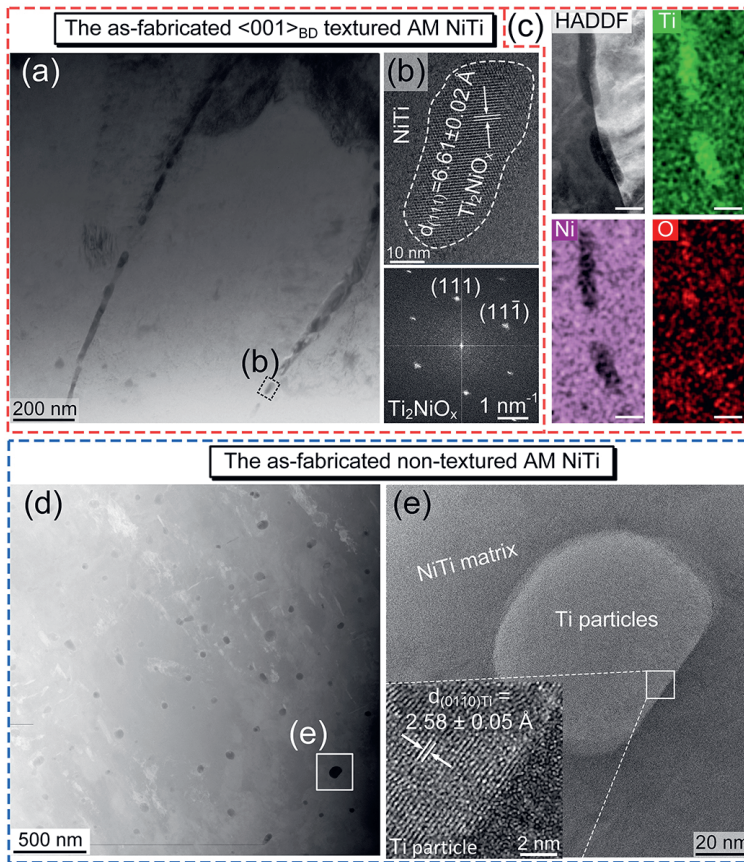
Figure 6.12. Bright-field TEM images of (a, c) $\langle 001 \rangle_{BD}$ textured and (b, d) non-textured AM NiTi samples, showing martensite size and morphology, and corresponding martensite width statistics; IPFs of B19' martensite phase measured by XRD in (e) $\langle 001 \rangle_{BD}$ textured and (f) non-textured AM NiTi samples measured at RT; All scale bars are 100 nm.

173

Figure 6.13. (a) Bright-field TEM image of as-fabricated $\langle 001 \rangle_{BD}$ textured NiTi sample. (b) HRTEM and corresponding fast Fourier transform (FFT) images of the $Ti_4Ni_2O_x$ precipitate in (b), and beam direction is close to $[1\bar{1}0]$; (c) A HAADF image and corresponding EDS mappings of typical grain boundary precipitates. (d) High-angle annular dark field-scanning transmission electron microscopy (HAADF-STEM) images of the non-textured NiTi samples and (e) an enlarged precipitate observed by high-resolution transmission electron microscopy (HRTEM) with corresponding indexed result showing Ti particle in NiTi matrix (enlarged zone of (d), marked by a white square frame).

In the nanoscale, the precipitate behavior in the as fabricated $\langle 001 \rangle_{BD}$ textured AM NiTi is quite distinct from that in the reference non-textured AM NiTi. Ti_2NiOx precipitates along

grain boundaries were observed by TEM (Figure 6.13 (a)–(c)) in the $\langle 001 \rangle_{BD}$ textured AM NiTi. By contrast, only pure Ti particles formed within grains in the non-textured sample (Figure 6.13 (d) and (e)).

6.3.4. Functional properties of L-PBF NiTi

6.3.4.1. Superelasticity

To evaluate the superelasticity of AM NiTi with designed different textures, the samples were tested at 353 K (25 K above the martensite start temperature) to ensure a fully austenitic state. For the $\langle 001 \rangle_{BD}$ textured NiTi, pronounced superelasticity was shown (the red line in Figure 6.14 (a)). In contrast, the non-textured sample showed no superelasticity at 353 K (the red line in Figure 6.14 (b)). It demonstrates the improved superelasticity in the designed $\langle 001 \rangle_{BD}$ textured NiTi. To the best of the authors' knowledge, this superelasticity in a Ni-lean NiTi alloy is the first demonstrated for an AM material without any additional post processing.

To investigate superelastic temperature ranges, various loading temperatures were applied. The $\langle 001 \rangle_{BD}$ textured AM NiTi shows superior superelasticity (4% recoverable strain from 353 K to 413 K) with a large temperature range of ~110 K and its highest superelastic temperature can reach up to 453 K (Figure 6.14 (a)). As a comparison, the reference sample of the non-textured AM NiTi does not show any stable superelasticity from 343 to 373 K (Figure 6.14 (b)), and it is already plastically deformed when tested above 363 K (Figure 6.15). The achieved superelasticity in the $\langle 001 \rangle_{BD}$ textured AM NiTi is remarkable as it is comparable with NiTi-Hf alloys [38]. Notably, NiTi-Hf alloys only have a narrow 20 K superelastic temperature range [39], while the textured NiTi designed in this work has a temperature window in excess of 5 times wider. It should be noted that the $\langle 001 \rangle_{BD}$ textured AM NiTi partially loses its part of superelasticity when the temperature is higher than 413 K, and its recoverable strain ratio decreases to 86 % at 453 K. Such irrecoverable strain results from transformation- and reorientation-induced plasticity [40], which is due to the high stress level when test temperatures above 413 K (peak stresses > 750 MPa, Figure 6.14 (a)).
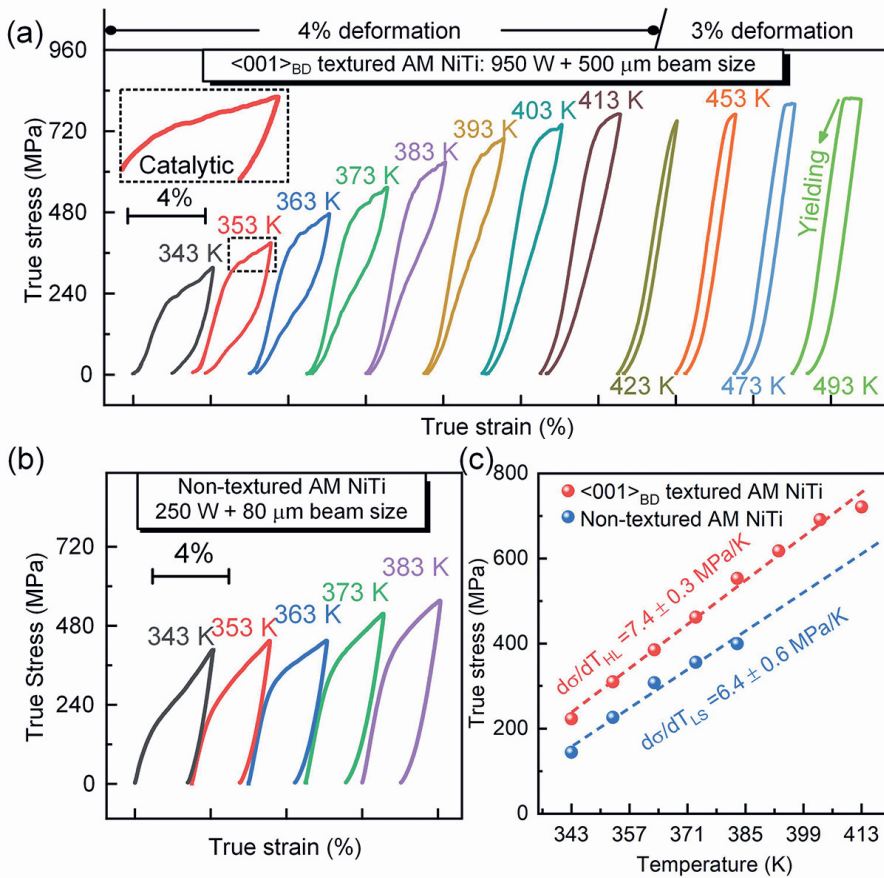
Figure 6.14. True stress (σ_{true}) - true strain (ε_{true}) curves as a function of temperatures for (a) $\langle 001 \rangle_{BD}$ textured and (b) non-textured samples. (c) The critical transformation stress as a function of test temperatures for $\langle 001 \rangle_{BD}$ textured and non-textured AM NiTi samples.
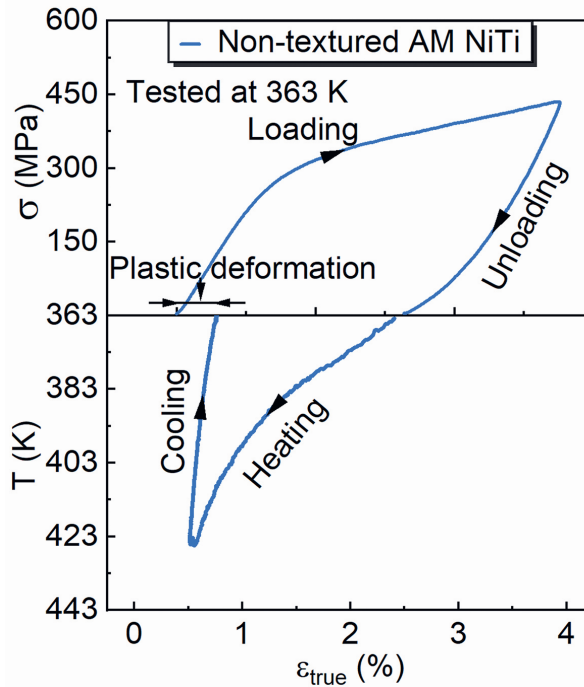
6

Figure 6.15. The true stress (σ_{true}) - true strain (ε_{true}) - temperature (T) curve of a non-textured AM NiTi sample measured at 363 K (35 K above the martensite start temperature), showing no superelasticity and the occurrence of plastic deformation.

6.3.4.2. Shape memory effect

The SME, as another important function of NiTi alloys, was also investigated. With a 4% compressive engineering strain, the $\langle 001 \rangle_{BD}$ textured NiTi has almost 100% recoverable strain (Figure 6.16 (a)) at the first SME cycle, which is if not considering the induced two-way shape-memory effect (illustrated in Figure 6.1). The non-textured NiTi, as a comparison, has ~18% residual deformation (0.7% true strain) (Figure 6.16 (b)). The $\langle 001 \rangle_{BD}$ textured NiTi also shows better cyclic SME stability. After 50 SME cycles, the $\langle 001 \rangle_{BD}$ textured NiTi still has ~1.6% recoverable strain, which is ~33% higher than the reference non-textured NiTi (Figure 6.16 (c)). Even with the higher shape memory recoverable strain, the $\langle 001 \rangle_{BD}$ textured NiTi still has comparable two-way shape memory strain (~0.6) with the non-textured NiTi (Figure 6.16 (d)).

6
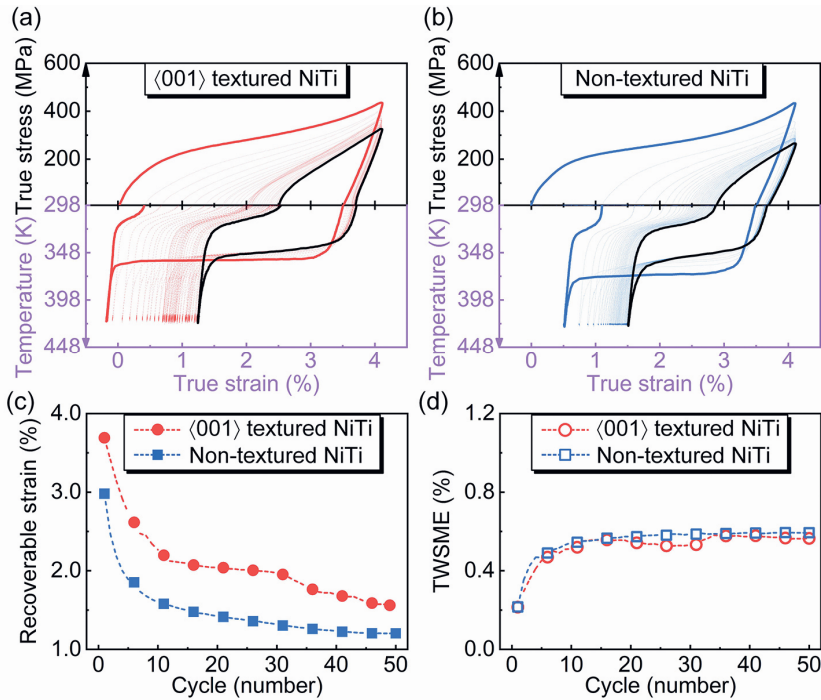
Figure 6.16. True stress (σ_{true}) - true strain (ε_{true}) - temperature (T) curves of (a) as-fabricated $\langle 001 \rangle_{BD}$ textured and (b) non-textured samples measured at RT showing shape memory effect. (c) The recoverable strain is a function of the number of cycles. (d) The two-way shape memory strain is a function of the number of cycles.

6.4. Discussion

6.4.1. Occurrences of superelasticity in $\langle 001 \rangle$ textured NiTi

Our results clearly show that the achieved $\langle 001 \rangle_{BD}$ texture can effectively induce superelasticity in Ni-lean NiTi. Based on the molecular dynamics simulation results, relatively low stress triggers stress-induced martensite transformation in $\langle 001 \rangle$ orientated grains (Figure 6.5). This is due to the high resolved shear stress factor in $\langle 001 \rangle$ orientated NiTi [41, 42]. As reported by Sehitoglu *et al.* [42]*,* the [001] single crystal has the lowest Schmid factors of austenite and martensite phases, which resulting in the enhanced recoverable strains and superelasticity. In this study, the fabricated polycrystalline $\langle 001 \rangle$

orientated NiTi is single-crystal-like, hence, a superelastic behavior, similar with the [001] single crystal, was presented.

According to the post-translational modifications analysis, the deformed NiTi in the MD bicrystal models can be divided into different domains with different local lattice orientations. These domains were distinguished by various colors (Figure 6.5 (a)–(c)). The number of domains can directly reflect the ability of coordinating deformation in MD bicrystal models with various orientations. The $\langle 001 \rangle$ orientated NiTi shows the minimum number of 3 domains, indicating a good ability to coordinate deformation. Therefore, a relatively weak hardening effect is shown in the $\langle 001 \rangle$ orientated NiTi during SIMT (Figure 6.5 (a)).
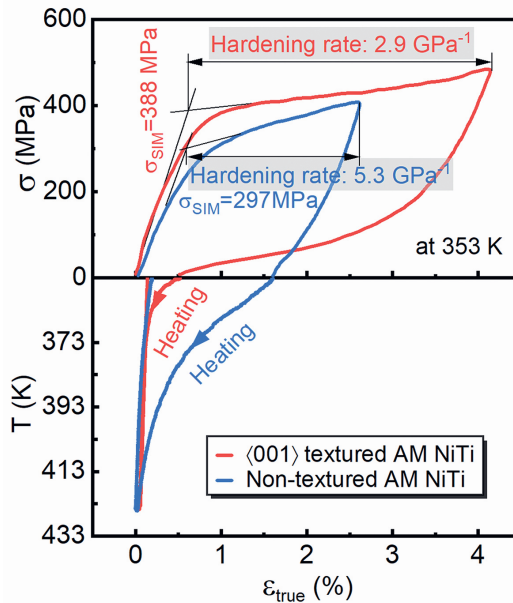
Figure 6.17. The true stress (σ_{true})-true strain (ε_{true})-temperature (T) curves. Loading and unloading were conducted at 353 K. Subsequent heating and cooling were employed to confirm that the irreversible strains after unloading result from residual martensite.

In experimental results, the SIMT in the $\langle 001 \rangle_{BD}$ textured AM NiTi proceeds in a catalytic manner [43], i.e., showing a fluctuation feature during the SIMT (Figure 6.17). This

phenomenon further demonstrates that $\langle 001 \rangle$ textured grains are more favorable for SIMT. By contrast, the non-textured AM NiTi containing some $\langle 111 \rangle$ orientated grains show no superelasticity. The reason can be attributed to the significant hardening effect, especially for $\langle 111 \rangle$ orientated grains, during SIMT. The SIMT hardening is directly shown in the MD simulations and is also demonstrated by Sehitoglu *et al*. [42]. Due to the existence of six correspondent variant pairs, hardening effect is more pronounced in $\langle 111 \rangle$ orientated grains, which leads to early yielding of the austenite and martensite phases and limited SIMT [42].
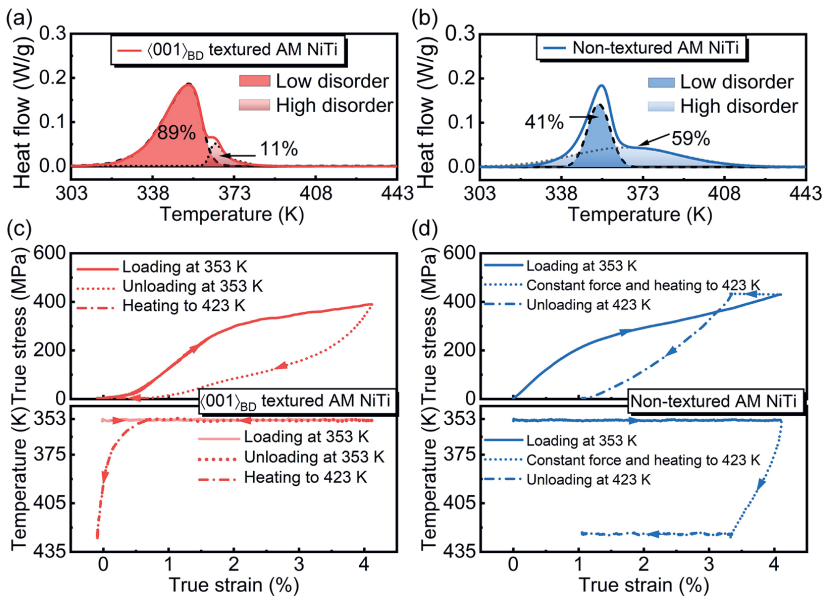
Figure 6.18. Heating of differential scanning calorimetry (DSC) curves for (a) the $\langle 001 \rangle_{BD}$ textured and (b) the non-textured samples after 4% engineering strain under compression; True stress (σ_{true}) - true strain (ε_{true}) - temperature (T) curves of (c) the $\langle 001 \rangle_{BD}$ textured NiTi (loading and unloading at 353 K and heating the sample to 423 K) and (d) the non-textured samples non-textured sample (loading at 353 K, constant applied force and heating the sample to 423 K, and unloading at 423 K).

To understand why texture can control the occurrence of superelasticity even in NiTi with a Ni-lean composition, DSC tests were conducted on the two samples with distinct textures after 4% compressive deformation at 353 K. The DSC results showed additional shoulder peaks during heating (Figure 6.18 (a) and (b)), indicating an increase in austenite-finish temperature. Especially for the non-textured sample (Figure 6.18 (b)), the austenite-finish temperature of the deformed state (A_f^d) increases by 66 K to 424 K, compared with its initial non-deformed state ($A_f^{\text{Non-textured NiTi}} \approx A_f^{\langle 001 \rangle_{\text{BD}} \text{ textured NiTi}} = 358\,\text{K}$). By contrast, there is only a 26 K increase of A_f^d for the $\langle 001 \rangle_{\text{BD}}$ textured sample (Figure 6.18 (a)). The DSC results indicate that lower reverse phase transformation resistance (stress-induced martensite to austenite) exists in the $\langle 001 \rangle_{\text{BD}}$ textured AM NiTi, leading to the occurrence of superelasticity.

To quantitatively evaluate the phase transformation compatibility between stress-induced martensite and austenite, the required additional austenite-finish temperature increments ($\Delta A_f = A_f^d - A_f$) were compared, and a lower ΔA_f means better phase transformation compatibility. The non-textured sample shows 2.5 times higher $\Delta A_f^{\text{Non-textured NiTi}}$ (66 K) and a higher fraction of 59% stress-induced martensite affected by deformation (the high disorder part in Figure 6. 18 (a) and (b)) than the $\langle 001 \rangle_{\text{BD}}$ textured sample ($\Delta A_f^{\langle 001 \rangle_{\text{BD}} \text{ textured NiTi}}$ = 26 K and the high disorder part fraction is 11%). The result demonstrates that the designed $\langle 001 \rangle_{\text{BD}}$ texture is favorable for improving the SIMT compatibility between parent phases and the stress-induced martensite [44, 45], which reduces the imposed elastic and interfacial energy resistance [46]. The improved compatibility in the $\langle 001 \rangle_{\text{BD}}$ textured AM NiTi directly promotes reverse transformation from stress-induced martensite to austenite during unloading at a constant temperature (Figure 6.18 (c)), leading to the emergence of superelasticity. In contrast, the non-textured sample shows an irreversible transformation during unloading and the absence of superelasticity (Figure 6.14 (b)), unless extra heating is induced to trigger the reverse transformation (Figure 6.18 (d)).

6

6.4.2. Superelastic temperature ranges

Based on Clausius-Clapeyron relationship [18], the σ_{SIM} increases with increasing temperatures. Theoretically, the yield stress (σ_y) of NiTi decreases with increasing temperatures [47]. When above a critical temperature, $\sigma_{SIM} > \sigma_y$ occurs and the superelasticity is limited to below the critical temperature [47]. The high temperature superelasticity with a wide temperature range requires low superelastic stress temperature dependence ($d\sigma_{SIM} / dT$) and/or yield stress temperature dependence ($d\sigma_y / dT$). In this work, the $\langle 001 \rangle_{BD}$ textured AM NiTi displays a relatively high superelastic stress temperature dependence ($d\sigma_{SIM} / dT$) of ~7.4 MPa/K (Figure 6.14 (c)). Hence, the high temperature superelasticity could be attributed to the anti-yielding ability of the $\langle 001 \rangle_{BD}$ textured AM NiTi. To demonstrate this statement, Schmid factors (describing resolved shear stress for slip) of NiTi with various orientations were calculated to evaluate the anti-yielding ability (Figure 6.19). The $\langle 001 \rangle$ orientated NiTi crystal has the lowest Schmid factor of 0.00 in the typical NiTi $\langle 001 \rangle \{110\}$ slip system [42] (Figure 6.19), showing in theory no plastic slip. The MD single crystal model also demonstrates that the $\langle 001 \rangle$ orientation also shows remarkable stability against yielding as a function of temperature (Figure 6.20 (a)). In contrast, the $\langle 111 \rangle$ orientation has a rapid decrease in yield stress (Figure 6.20 (c)), which is consistent with results reported by Sehitoglu *et al*. [42]. In the non-textured NiTi, some grains also orientate along $\langle 111 \rangle$ (a weak $\langle 111 \rangle$ texture intensity of 2.2 in Figure 6.8 (d)), which directly cause a poor superelastic response. Therefore, the exceptional anti-yielding ability of $\langle 001 \rangle$ textured NiTi contributes to superior high-temperature superelasticity (up to 453 K) with a wide temperature range of ~110 K.

6
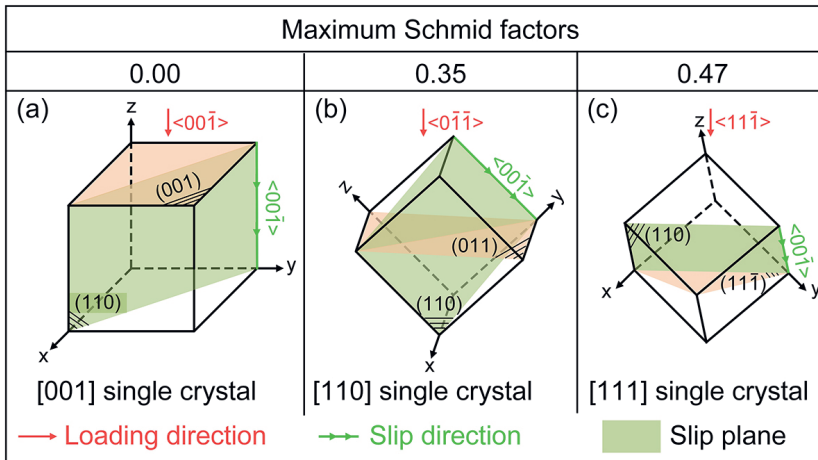
Figure 6.19. Schematics of plasticity initiations with an activated $\langle 001\rangle\{110\}$ slip system [42] in BCC_B2 NiTi: Loading along (a) [001]; (b) [110]; and (c) [111] directions.
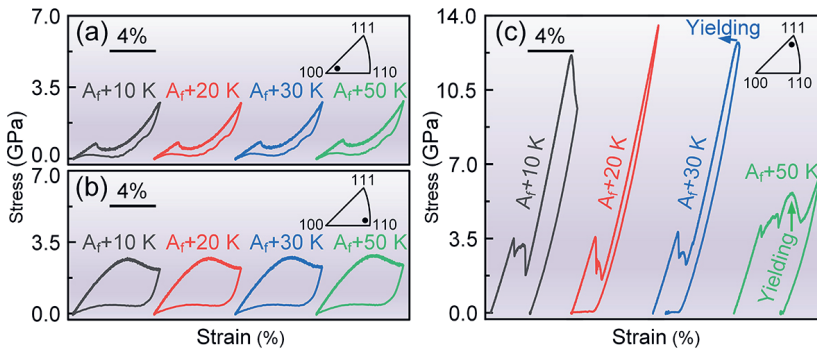
Figure 6.20. MD simulated compressive strain (ε)-stress (σ) curves of single crystal NiTi with 8% strain deformation at different temperatures, showing behaviour for (a) [100], (b) [011] and (c) [111] orientations. All austenite finish temperatures (A_f) are 425 K.

6.4.3. Stability of shape memory effect

A better shape memory recoverability and a higher SME cyclic stability were shown in the $\langle 001\rangle_{BD}$ textured AM NiTi as compared to the reference non-textured AM NiTi (Figure 6.16). For the shape memory effect, the deformation stage is associated with the detwinning and reorientation of martensite variants, and deformation recovery is achieved by thermal-

183

induced phase transformation via $M_{detwinned} \to A$. Due to inconsistent orientations of self-accommodated martensite before deforming and intrinsic lattice mismatch between austenite (BCC_B2) and martensite (B19′), dislocation and residual martensite accumulate to induce irrecoverable strain after cyclic SME tests [44, 48]. In this work, a strong $\langle 100 \rangle_{B19'}$ martensitic texture at RT, inherited from the $\langle 001 \rangle_{B2}$ austenitic texture, was shown in the $\langle 001 \rangle_{BD}$ textured AM NiTi. Such orientated martensite phases reduce interactions and interlocking effect of CVPs during detwinning and martensite reorientation resistance is also weakened accordingly. After cyclic SME tests, the martensite variants with greater width in the $\langle 001 \rangle_{BD}$ textured AM NiTi (Figure 6.21 (a)) indicate smaller internal stress and better compatibility between martensite and austenite [44]. By contrast, due to a higher internal stress in the cyclic SME tested non-textured AM NiTi, fine laminated martensite variants become dominant (Figure 6.21 (b)).
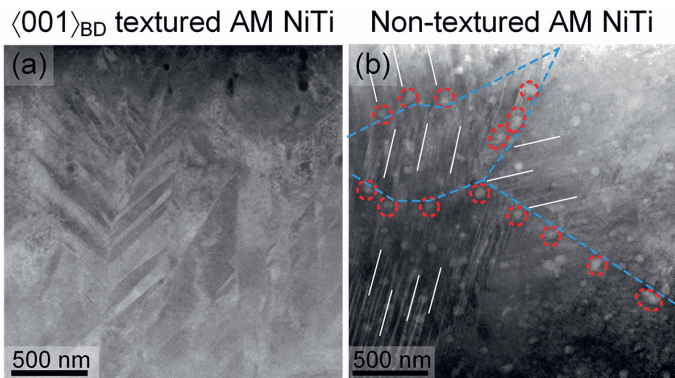
Figure 6.21. Samples after 50 shape memory effect cycles: (a) a HAADF-STEM image of the $\langle 001 \rangle_{BD}$ textured sample; (b) An annular dark-field STEM image in the non-textured sample and pure Ti particles were marked by red dash circles, martensite variant orientations were marked by solid white lines.

Precipitation behavior also affects SME stability. In the $\langle 001 \rangle_{BD}$ textured AM NiTi, the grain boundary precipitation of the Ti_2NiO_x phase effectively pins dislocations grain boundaries decorated with Ti_2NiO_x precipitates block dislocation movements, which is seen in the TEM images (Figure 6.22). By contrast, pure Ti particles formed within grains in the

non-textured sample hinder martensite variant reorientations (Figure 6.21 (b)). The precipitation behavior is determined by the solidification rate, which was calculated based on FEM and solute trapping Scheil models (Figure 6.6 (c)–(f)). In the non-textured NiTi, a higher solidification rate results in more Ti being trapped into NiTi matrix and a more rapid cooling rate limits trapped Ti to react with NiTi to form $Ti_2Ni(O_x)$. Therefore, a better SME stability shown in the $\langle 001 \rangle_{BD}$ textured AM NiTi attributes to the following two reasons: 1) the $\langle 100 \rangle_{B19'}$ martensitic texture coordinates detwinning and reorientation of martensite variants; 2) intergranular precipitates pin dislocations.
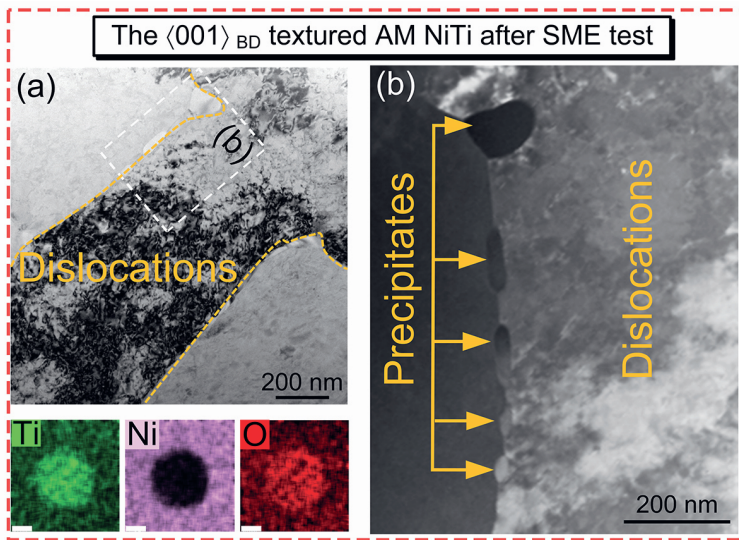
Figure 6.22. (a) a bright field TEM image of the $\langle 001 \rangle_{BD}$ textured sample after 50 shape memory effect cycles showing the dislocations pinned by precipitates segregated along the grain boundaries and EDS maps of Ti, Ni, and O of a typical precipitate (all scale bars are 20 nm). (b) An enlarged HAADF-STEM image from a zone in (a).

6.4.4. Comparison of functional properties with other NiTi-based alloys

In this work, the wide superelastic temperature ranges, the high-temperature superelasticity, and the high critical stress temperature dependence allow binary Ni-lean NiTi to operate at elevated temperatures with wide tailorable stress windows (Figure 6.23 (a)). The

properties obtained are superior to complex multicomponent single crystal (SX) or polycrystalline NiTi-based alloys (such as NiTi-Hf and NiTi-Hf-Pd) fabricated by deformation processes coupled with long-time heat treatments (HT) [39, 49]. By taking advantage of the additive manufacturing technique and using microstructure design concepts developed in this work, functionally graded NiTi. Such design flexibility opens a new path toward novel multifunctional and smart devices.
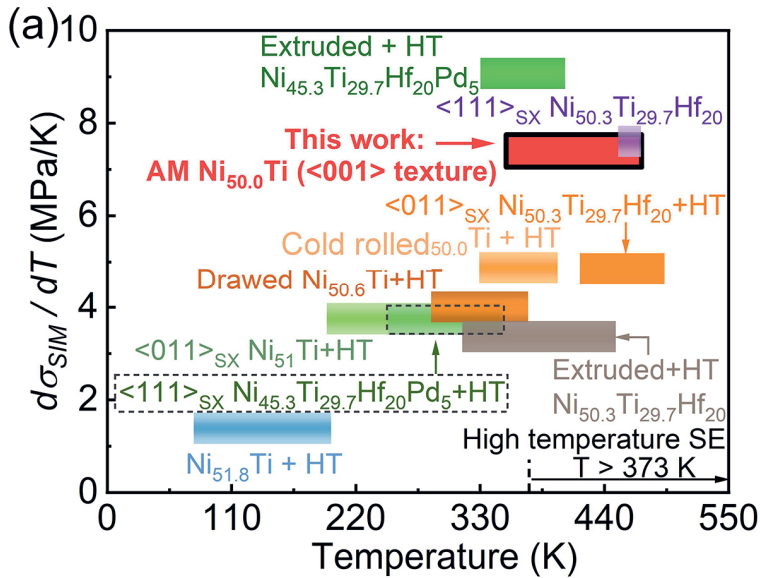
Figure 6. 23. An overview of the superelastic temperature range (by temperature and the critical stress temperature dependence ($d\sigma_{SIM} / dT$)) for known NiTi-based alloys fabricated by different processes (SX, HT and SE are abbreviations of single crystal, heat treatment and superelasticity, respectively).

6.5. Conclusions

In summary, the proposed framework based on a synergy between finite-element, analytical and molecular-dynamic models, and additive manufacturing can help to achieve theory-guided microstructure and functional property design in NiTi SMAs. This discovery opens a new pathway to designing high-performance functional materials via additive manufacturing through controlling functional anisotropy. The specific conclusions are as follows:

1. The relationship between crystallographic orientations and superelasticity of NiTi SMAs has been studied via molecular dynamics, taking into account the critical stress for stress-induced martensite transformation, hardening rate during stress-induced transformation and recoverable strain. An orientation map of superelasticity has been drawn and crystallographic orientations close to $\langle 001 \rangle$ were found more favorable for superelasticity.

2. Based on predictions of temperature fields and grain morphologies, single-crystal-like polycrystalline Ni-lean NiTi with a strong $\langle 001 \rangle$ texture has been successfully fabricated via a laser powder bed fusion additive manufacturing technique.

3. An unprecedented superelasticity up to 453K with a high and wide temperature window (~110 K) in a Ni-lean Ni (49.4 at.%)-Ti is achieved in the $\langle 001 \rangle$ textured additively manufactured NiTi, which is associated with the superior anti-yielding ability of the designed $\langle 001 \rangle$ texture and the improved phase transformation compatibility between austenite and stress-induced martensite.

4. The designed additive manufacturing processing condition can enhance superelasticity and improve shape memory stability simultaneously. The improved shape memory stability is attributed to the formation of $\langle 100 \rangle$ textured martensite and the dislocation movement blocked by grain decorated with Ti_2NiO_x precipitates.

6

References

[1] T. Omori, R. Kainuma, Alloys with long memories, Nature 502(7469) (2013) 42-44.

[2] X. Ren, K. Otsuka, Origin of rubber-like behaviour in metal alloys, Nature 389(6651) (1997) 579-582.

[3] E. Alarcon, L. Heller, E. de Prado, J. Kopeček, Temperature and microstructure dependent tensile behavior of coarse grained superelastic NiTi, Mater. Des. 226 (2023) 111617.

[4] D. Dye, Towards practical actuators, Nat. Mater. 14(8) (2015) 760-761.

[5] X. Huang, G.J. Ackland, K.M. Rabe, Crystal structures and shape-memory behaviour of NiTi, Nat. Mater. 2(5) (2003) 307-311.

[6] Y. Song, X. Chen, V. Dabade, T.W. Shield, R.D. James, Enhanced reversibility and unusual microstructure of a phase-transforming material, Nature 502(7469) (2013) 85-88.

[7] J. Van Humbeeck, Shape memory alloys with high transformation temperatures, Mater. Res. Bull. 47(10) (2012) 2966-2968.

[8] S. Li, D. Cong, Z. Chen, S. Li, C. Song, Y. Cao, Z. Nie, Y. Wang, A high-entropy high-temperature shape memory alloy with large and complete superelastic recovery, Mater. Res. Lett. 9(6) (2021) 263-269.

[9] P. Hua, M. Xia, Y. Onuki, Q. Sun, Nanocomposite NiTi shape memory alloy with high strength and fatigue resistance, Nat Nanotechnol. 16(4) (2021) 409-413.

[10] H.E. Karaca, S.M. Saghaian, G. Ded, H. Tobe, B. Basaran, H.J. Maier, R.D. Noebe, Y.I. Chumlyakov, Effects of nanoprecipitation on the shape memory and material properties of an Ni-rich NiTiHf high temperature shape memory alloy, Acta Mater. 61(19) (2013) 7422-7431.

[11] J. Zhang, T. Chen, W. Li, J. Bednarcik, A.-C. Dippel, High temperature superelasticity realized in equiatomic Ti-Ni conventional shape memory alloy by severe cold rolling, Mater. Des. 193 (2020) 108875.

[12] C.-H. Chen, Y.-J. Chen, Shape memory characteristics of (TiZrHf)50Ni25Co10Cu15 high entropy shape memory alloy, Scripta Mater. 162 (2019) 185-189.

6

[13] H. Chen, F. Xiao, Z. Li, X. Jin, L. Mañosa, A. Planes, Elastocaloric effect with a broad temperature window and low energy loss in a nanograin Ti-44Ni-5Cu-1Al (at.%) shape memory alloy, Phys. Rev. Mater. 5(1) (2021) 015201.

[14] X. Li, K. Lu, Improving sustainability with simpler alloys, Science 364(6442) (2019) 733-734.

[15] J. Frenzel, E.P. George, A. Dlouhy, C. Somsen, M.F.X. Wagner, G. Eggeler, Influence of Ni on martensitic phase transformations in NiTi shape memory alloys, Acta Mater. 58(9) (2010) 3444-3458.

[16] S. Saedi, A.S. Turabi, M. Taheri Andani, C. Haberland, H. Karaca, M. Elahinia, The influence of heat treatment on the thermomechanical response of Ni-rich NiTi alloys manufactured by selective laser melting, J. Alloys Compd. 677 (2016) 204-210.

[17] S.M. Saghaian, H.E. Karaca, H. Tobe, A.S. Turabi, S. Saedi, S.E. Saghaian, Y.I. Chumlyakov, R.D. Noebe, High strength NiTiHf shape memory alloys with tailorable properties, Acta Mater. 134 (2017) 211-220.

[18] J. Xia, Y. Noguchi, X. Xu, T. Odaira, Y. Kimura, M. Nagasako, T. Omori, R. Kainuma, Iron-based superelastic alloys with near-constant critical stress temperature dependence, Science 369(6505) (2020) 855-858.

[19] X. Chong, M. Hu, P. Wu, Q. Shan, Y.H. Jiang, Z.L. Li, J. Feng, Tailoring the anisotropic mechanical properties of hexagonal M7X3 (M=Fe, Cr, W, Mo; X=C, B) by multialloying, Acta Mater. 169 (2019) 193-208.

[20] J.C. Guo, P. Rong, L. Wang, W.J. Chen, S.X. Han, R.N. Yang, X.W. Lei, W.J. Yao, N. Wang, A comparable study on stray grain susceptibilities on different crystallographic planes in single crystal superalloys, Acta Mater. 205 (2021) 116558.

[21] B. Blakey-Milner, P. Gradl, G. Snedden, M. Brooks, J. Pitot, E. Lopez, M. Leary, F. Berto, A. du Plessis, Metal additive manufacturing in aerospace: A review, Mater. Des. 209 (2021) 110008.

[22] S. Plimpton, Fast parallel algorithms for short-range molecular dynamics, J. Comput. Phys. 117(1) (1995) 1-19.

[23] W.-S. Ko, B. Grabowski, J. Neugebauer, Development and application of a Ni-Ti interatomic potential with high predictive accuracy of the martensitic phase transition, Phys. Rev. B 92(13) (2015) 134107.

6

[24] K. Otsuka, X. Ren, Physical metallurgy of Ti–Ni-based shape memory alloys, Prog. Mater Sci. 50(5) (2005) 511-678.

[25] P. Hirel, Atomsk: A tool for manipulating and converting atomic data files, Comput. Phys. Commun. 197 (2015) 212-219.

[26] A. Stukowski, Visualization and analysis of atomistic simulation data with OVITO–the Open Visualization Tool, Modell. Simul. Mater. Sci. Eng. 18(1) (2009) 015012.

[27] M. Gäumann, C. Bezençon, P. Canalis, W. Kurz, Single-crystal laser deposition of superalloys: processing–microstructure maps, Acta Mater. 49(6) (2001) 1051-1062.

[28] S. Miyazaki, T. Imai, Y. Igo, K. Otsuka, Effect of cyclic deformation on the pseudoelasticity characteristics of Ti-Ni alloys, Metall. Trans. A 17(1) (1986) 115-120.

[29] D. Wang, S. Hou, Y. Wang, X. Ding, S. Ren, X. Ren, Y. Wang, Superelasticity of slim hysteresis over a wide temperature range by nanodomains of martensite, Acta Mater. 66 (2014) 349-359.

[30] H.L. Wei, J. Mazumder, T. DebRoy, Evolution of solidification texture during additive manufacturing, Sci. Rep. 5(1) (2015) 16446.

[31] E.H. Amara, R. Fabbro, Modelling of gas jet effect on the melt pool movements during deep penetration laser welding, J. Phys. D: Appl. Phys. 41(5) (2008) 055503.

[32] M. Garibaldi, I. Ashcroft, M. Simonelli, R. Hague, Metallurgy of high-silicon steel parts produced using Selective Laser Melting, Acta Mater. 110 (2016) 207-216.

[33] J. Metelkova, Y. Kinds, K. Kempen, C. de Formanoir, A. Witvrouw, B. Van Hooreweder, On the influence of laser defocusing in Selective Laser Melting of 316L, Addit. Manuf. 23 (2018) 161-169.

[34] M. Elahinia, N. Shayesteh Moghaddam, M. Taheri Andani, A. Amerinatanzi, B.A. Bimber, R.F. Hamilton, Fabrication of NiTi through additive manufacturing: A review, Prog. Mater Sci. 83 (2016) 630-663.

[35] J.-N. Zhu, E. Borisov, X. Liang, E. Farber, M.J.M. Hermans, V.A. Popovich, Predictive analytical modelling and experimental validation of processing maps in additive manufacturing of nitinol alloys, Addit. Manuf. 38 (2021) 101802.

[36] S. Miyazaki, My Experience with Ti–Ni-Based and Ti-Based Shape Memory Alloys, Shape Mem. Superelasticity 3(4) (2017) 279-314.

6

[37] Y. Liu, The superelastic anisotropy in a NiTi shape memory alloy thin sheet, Acta Mater. 95 (2015) 411-427.

[38] G.P. Toker, M. Nematollahi, S.E. Saghaian, K.S. Baghbaderani, O. Benafan, M. Elahinia, H.E. Karaca, Shape memory behavior of NiTiHf alloys fabricated by selective laser melting, Scripta Mater. 178 (2020) 361-365.

[39] H.E. Karaca, S.M. Saghaian, B. Basaran, G.S. Bigelow, R.D. Noebe, Y.I. Chumlyakov, Compressive response of nickel-rich NiTiHf high-temperature shape memory single crystals along the [111] orientation, Scripta Mater. 65(7) (2011) 577-580.

[40] C. Yu, G. Kang, Q. Kan, X. Xu, Physical mechanism based crystal plasticity model of NiTi shape memory alloys addressing the thermo-mechanical cyclic degeneration of shape memory effect, Mech. Mater. 112 (2017) 1-17.

[41] K. Gall, H. Sehitoglu, Y.I. Chumlyakov, I.V. Kireeva, Tension–compression asymmetry of the stress–strain response in aged single crystal and polycrystalline NiTi, Acta Mater. 47(4) (1999) 1203-1217.

[42] H. Sehitoglu, I. Karaman, R. Anderson, X. Zhang, K. Gall, H.J. Maier, Y. Chumlyakov, Compressive response of NiTi single crystals, Acta Mater. 48(13) (2000) 3311-3326.

[43] S.C. Mao, J.F. Luo, Z. Zhang, M.H. Wu, Y. Liu, X.D. Han, EBSD studies of the stress-induced B2−B19′ martensitic transformation in NiTi tubes under uniaxial tension and compression, Acta Mater. 58(9) (2010) 3357-3366.

[44] J. Cui, Y.S. Chu, O.O. Famodu, Y. Furuya, J. Hattrick-Simpers, R.D. James, A. Ludwig, S. Thienhaus, M. Wuttig, Z. Zhang, I. Takeuchi, Combinatorial search of thermoelastic shape-memory alloys with extremely small hysteresis width, Nat. Mater. 5(4) (2006) 286-290.

[45] P. Šittner, P. Sedlák, H. Seiner, P. Sedmák, J. Pilch, R. Delville, L. Heller, L. Kadeřávek, On the coupling between martensitic transformation and plasticity in NiTi: Experiments and continuum based modelling, Prog. Mater Sci. 98 (2018) 249-298.

[46] Y. Liu, S.P. Galvin, Criteria for pseudoelasticity in near-equiatomic NiTi shape memory alloys, Acta Mater. 45(11) (1997) 4431-4439.

[47] A.S. Turabi, S. Saedi, S.M. Saghaian, H.E. Karaca, M.H. Elahinia, Experimental Characterization of Shape Memory Alloys, Shape Memory Alloy Actuators2015, pp. 239-277.

6

[48] K. Chu, Q. Sun, Reducing functional fatigue, transition stress and hysteresis of NiTi micropillars by one-step overstressed plastic deformation, Scripta Mater. 201 (2021) 113958.

[49] E.E. Timofeeva, N.Y. Surikov, A.I. Tagiltsev, A.S. Eftifeeva, A.A. Neyman, E.Y. Panchenko, Y.I. Chumlyakov, The superelasticity and shape memory effect in Ni-rich Ti-51.5Ni single crystals after one-step and two-step ageing, Mater. Sci. Eng., A 796 (2020) 140025.

6

7

Healing Cracks in Additively Manufactured NiTi

The contents of this chapter have been published as a journal paper: Jia-Ning Zhu, Zhaoying Ding, Evgenii Borisov, Xiyu Yao, Johannes C. Brouwer, Anatoly Popovich, Marcel Hermans, and Vera Popovich. "Healing cracks in additively manufactured NiTi shape memory alloys." *Virtual and Physical Prototyping* 18, no. 1 (2023): e2246437.

Abstract

The pursuit of enhancing NiTi superelasticity through laser powder bed fusion (L-PBF) and [001] texture creation poses a challenge due to heightened susceptibility to hot cracking in the resulting microstructure with columnar grains. This limitation restricts NiTi's application and contributes to material waste. To overcome this, an approach of utilizing spark plasma sintering (SPS) to heal directional cracks in [001] textured L-PBF NiTi shape memory alloy is introduced. Diffusion bonding and oxygen utilization for Ti_2NiO_x formation successfully heal the cracks. SPS enhances mechanical properties, superelasticity at higher temperatures, and two-way shape memory strain during thermomechanical cycling. This work provides an alternative solution for healing cracks in L-PBF parts, enabling the sustainable reuse of cracked materials. By implementing SPS, this approach effectively addresses hot cracking limitations, expanding the application potential of L-PBF NiTi parts while improving their functional and mechanical properties.

7.1. Introduction

Nickel-titanium (NiTi) exhibits superelasticity and shape memory effect due to reversible martensitic transformation (SIMT) [1], making it a desirable material for a range of applications, including medical devices and industrial smart components [2-4]. Despite these attractive functionalities, NiTi's fabrication remains challenging, and its poor machinability limits its potential [5]. Laser powder bed fusion (L-PBF), an emerging additive manufacturing technique [6, 7], offers unprecedented design freedom [5], enabling the production of complex parts [8] and the design of microstructures and crystallographic orientations [9, 10].

NiTi exhibits anisotropic functional properties when deformed along different crystallographic orientations, showing distinct superelasticity. NiTi with [001] crystallographic orientation is demonstrated to be desirable for releasing superelasticity based on phenomenological models [11], molecular dynamics, and experiments [10]. However, fabricating [001] textured NiTi is still challenging. For NiTi components, crystallographic orientation can be manipulated through plastic deformation processes or solidification. Limited by the slip systems of NiTi, only [111] or [011] textured microstructures can be achieved by plastic deformation processes, such as rolling and drawing [12, 13]. The cubic crystal structure of solidified NiTi allows grains to grow along

7

195

the maximum thermal gradient direction during solidification, creating [001] textured NiTi through directional solidification or single crystal growth from melts (e.g., the Bridgman technique) [14]. However, above-mentioned solidification methods result in serious chemical compositional non-uniformity due to lower cooling rates [15]. By manipulating L-PBF processing parameters, temperature gradients and grain growth rates can be controlled [16], enabling the creation of single-crystal-like NiTi with [001] columnar grains, dramatically enhancing NiTi superelasticity [10].

However, despite the advantages of L-PBF [001] textured NiTi with columnar grains, these microstructures are susceptible to hot cracking due to restricted liquid feeding in long channels of interdendritic regions [17]. Hot cracking can significantly reduce the mechanical properties of NiTi, leading to negative effects on durability and integrity [18]. Therefore, it is crucial, particularly for safety-critical applications, to heal cracks in L-PBF NiTi parts and to utilize cracking materials in a more sustainable way.

To date, there has been limited research on healing cracks in NiTi, particularly in additively manufactured parts. Since cracks for L-PBF [001] textured NiTi mainly propagate along grain boundaries parallel to the building direction [10], intergranular crack flanks need to be filled, and effective bonding among interfaces is required. In-situ precipitation between crack flanks is a promising way to heal cracks [19]. To heal cracks, a directional force and elevated temperature are required. The directional force, perpendicular to the crack propagation direction, narrows or closes crack flanks, while the elevated temperature promotes diffusion precipitation to create bonding between crack flanks. Since elevated temperature may result in weakened texture by recrystallization, the healing process should be as short as possible to preserve the [001] texture.

A technique for healing cracks in L-PBF [001] textured NiTi is crucial. Heat treatment can provide heat to promote diffusion but lacks the force to assist bonding. Although hot isostatic pressing (HIP) involves the simultaneous application of high temperature and high pressure to a sample, the pressure is applied uniformly in all directions [20], which is suitable for healing microcracks. As reported by Vilanova [21], HIP is unable to heal cracks beyond 6 μm width for laser powder bed fusion parts. Spark plasma sintering (SPS) heats materials rapidly and provides uniaxial pressure [22], making it a promising technique for healing directional cracks. However, until now, crack healing of L-PBF NiTi has not been explored by applying SPS.

The objective of this study is to investigate the feasibility of using SPS to heal cracks in L-PBF NiTi and to determine the microstructure and superelasticity of the healed parts. This

investigation aims to contribute to the understanding of how SPS can be used to heal cracks in NiTi and emphasizes the importance of using NiTi in a more sustainable way by reducing waste and optimizing its performance. Furthermore, this study will provide insights into the mechanisms of crack healing in NiTi and the role of microstructure in determining its functional properties, which can apply to healing cracks in other alloy systems.

7.2. Materials and Methods

7.2.1. Material processing

Cracked L-PBF NiTi samples were intentionally fabricated. The processing parameters are as follows: a 950 W laser power, a 1060 mm/s scanning velocity, a 180 µm hatch distance, a 50 µm layer thickness, and a 500 µm laser beam diameter. Details about sample fabrication can be found in Chapter 3 [10].

Crack healing was conducted in a spark plasma sintering furnace (FCT SPS system, type KCE-FCT HP D-25-SI, Germany). Each cracked sample was loaded into a graphite die with an inner diameter of 20 mm (ISO-68, Toyo Tanso, Japan), and its cracking direction (parallel to the L-PBF building) is perpendicular to the SPS loading direction (Figure 7.1 (b)).
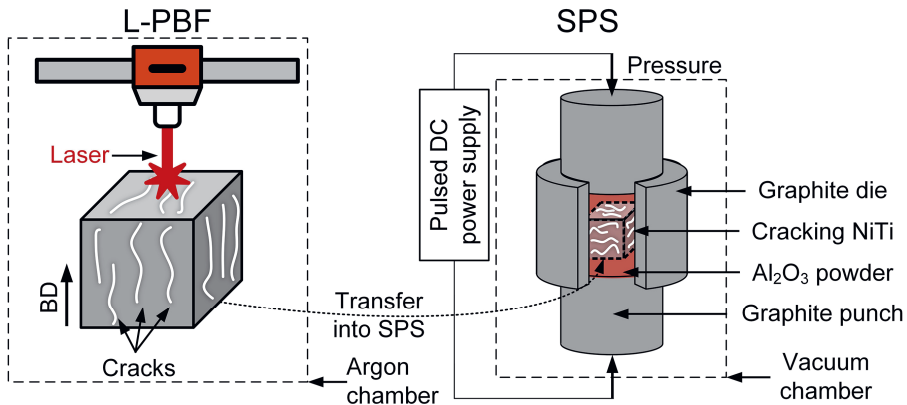

Figure 7.1. Schematics for laser powder fusion and spark plasma sintering.

To support cracked samples, the gap between the graphite die and the sample was filled with Al$_2$O$_3$ powders. The choice of Al$_2$O$_3$ powders as supporting materials stems from their high hardness, stiffness, and melting point. These properties endow Al$_2$O$_3$ with exceptional temperature stability, rendering it a fitting choice for the supporting materials during SPS. The SPS furnace was evacuated and flushed two times with Ar-gas of 5N purity (Linde, The Netherlands). The SPS healing process was conducted under the following procedures. First, the furnace was heated up to the target temperature in a range of 1223–1423 K with a heating rate of 100 K/min. The target pressure in a range of 13–22 MPa was applied with the duration in a range of 0.4–2 hours. Finally, the pressure was released, and the sample was cooled naturally to room temperature.

In order to achieve crack healing in L-PBF NiTi, various combinations of SPS pressure, temperature, and duration were optimized. It is crucial to prevent plastic deformation during the SPS healing process to preserve the [001] texture in NiTi. Therefore, the applied pressure during SPS should be lower than the yield strength of NiTi at the specific temperature. Since there is a lack of experimental data on NiTi yield strength above 673 K, an analytical fitting was performed based on reported values [23]. Considering that the yield strength of NiTi decreases with increasing temperature and becomes zero above the melting point of NiTi (1583 K), a three-phase exponential decay function was used for the analytical fitting.
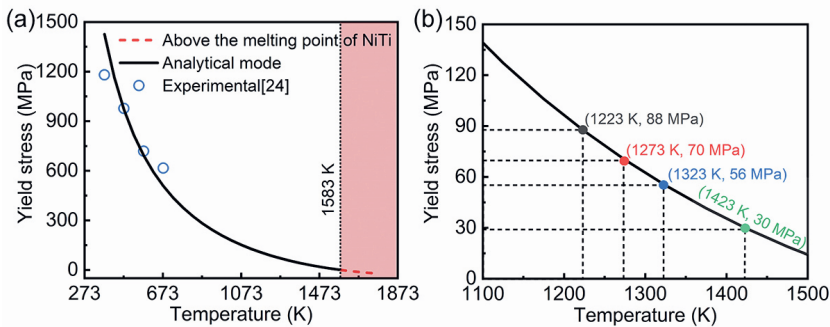

Figure 7.2. Predicted temperature-dependent yield strength of NiTi versus the experimental results of NiTi yield stress [23].

The predicted curve is shown in Figure 7.2, and predicted yield strength of NiTi fits well with reported values. The enlarged image in Figure 7.2 (b) reveals that the minimum

predicted yield strength for all investigated temperatures is 37 MPa. The maximum SPS pressure of 22 MPa is selected to prevent significant plastic deformation after the SPS healing process. The SPS processing parameters and corresponding sample labels are shown in the Table 7.1. Optical microscopy images of NiTi with various SPS conditions are shown in the Figure 7.3. It can be seen that a relative low temperature results in non-fully healing and residual cracks (< 1273 K) and high temperature with 22 MPa lead to plastic deformation (1423 K)
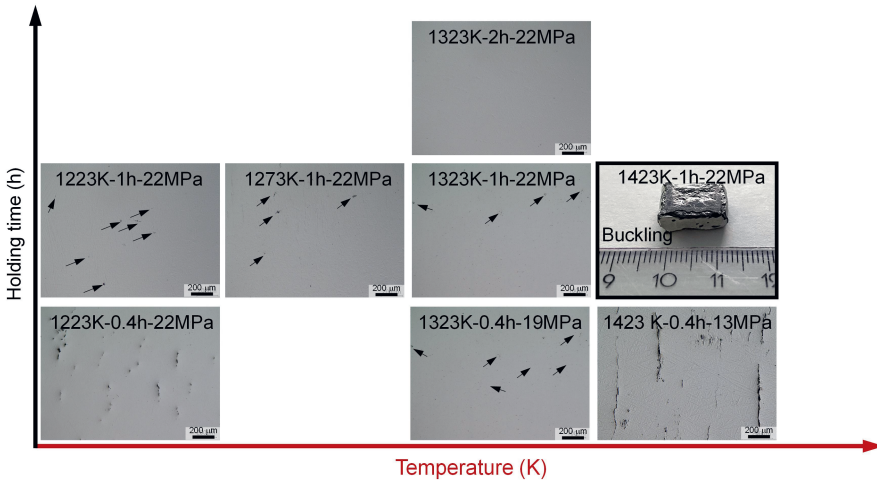
Figure 7.3. Optical microstructure of NiTi processed by various SPS parameters (shown in the figure in the format of "Temperature (K)-Holding time (h)-Pressure (MPa)"). All images are with 200 µm scale bars. Micro-cracks are marked by black arrows in the figure.

7

Table 7.1 SPS processing parameters for healing NiTi cracks.

SPS processing parameters	Temperature (K)	Holding time (h)	Pressure (MPa)
Semi-healed NiTi	1323	1.0	22
Fully healed NiTi	1323	2.0	22

7.2.2. Characterization

Before the metallographic examination, samples were ground, polished and tint etched, and the detailed procedure can be found in the section 4.2.1 of the Chapter 4 [9]. Procedures and setting details of X-ray diffraction (XRD) analysis and differential scanning calorimetry (DSC) were same with and described in the section 6.2.5 of the Chapter 6 [10].

Scanning electron microscopy (SEM) images and element analysis were captured by using a JEOL JSM 6500F (JEOL, Japan) equipped with an ultra-dry energy dispersive spectrometer (EDS) detector (Thermo Fisher Noran).

Transmission electron microscopy (TEM) images were taken by an FEI Talos F200X TEM FEI Talos F200X TEM equipment. TEM high-angle annular dark field (HAADF) observation, selected area electron diffraction (SAED), and energy dispersive spectroscopy (EDS) operations were also conducted. TEM foil samples were prepared by a focused Ga^+ ion beam (FIB; FEI Helios 600i).

Relative density of materials was determined by the Archimedes method, using a theoretical maximum density of 6.45 g/cm^3. The crack length density is estimated based on the ratio of crack length and measured area [24], and the crack length was measured by using Image J to do statistical analysis for three optical microscopy images with ×200 magnification. Oxygen contents were measured by a Bruker oxygen-hydrogen analyser (G8 GALILEO).

7.2.3. Mechanical tests

Vickers hardness measurements were performed under the test force 1.0 kgf (further denoted as HV1) using an Automatic Microhardness Tester (Buehler Vickers). To evaluate the local mechanical properties of various NiTi samples, instrumented indentation tests were conducted at room temperature using a Zwick ZHU2.5 instrument. To avoid stress concentrations, a spherical ball indenter with a diameter of 0.5 mm was employed. Description about superelasticity tests can be found in the section 6.2.6 of the Chapter 6 [10]. All samples were loaded and unloaded along the L-PBF building direction.

7

7.3. Results

7.3.1. Microstructures, texture and phase transformation

The cross-sectional images along the building direction (BD) are shown in Figure 7.4. For the as-fabricated NiTi, cracks mainly propagate along the building direction (Figure 7.4 (a)) and penetrate multiple layers (Figure 7.4 (b)), and its average crack length density was found ~5.9 ×10^{-3} mm^{-1}. It can be seen that SPS can effectively heal cracks in L-PBF NiTi. By applying 22 MPa pressure under 1323 K with 1 h duration, cracks have been significantly eliminated and its crack length density decreases to ~9.5×10^{-4} mm^{-1} (Figure 7.4). To fully heal cracks, the pressure and heat holding time was prolonged to 2 hours. As shown in Figure 7.4 (e) and (f), cracks were fully healed. This indicates the feasibility of the SPS for healing L-PBF NiTi cracks. The increased relative density in the fully healed NiTi (~99.7 %) also indicates a densification induced by enclosing crack flanks (Figure 7.5 (a)).
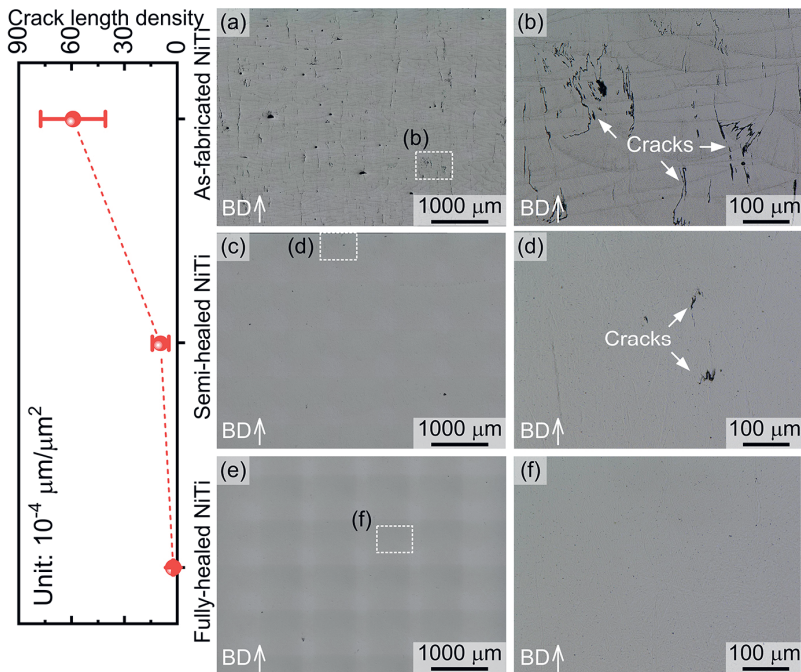

Figure 7.4. Crack length densities and optical microstructures: (a) and (b) as-fabricated NiTi; (c) and (d) Semi-healed NiTi; (e) and (f) Fully healed NiTi.
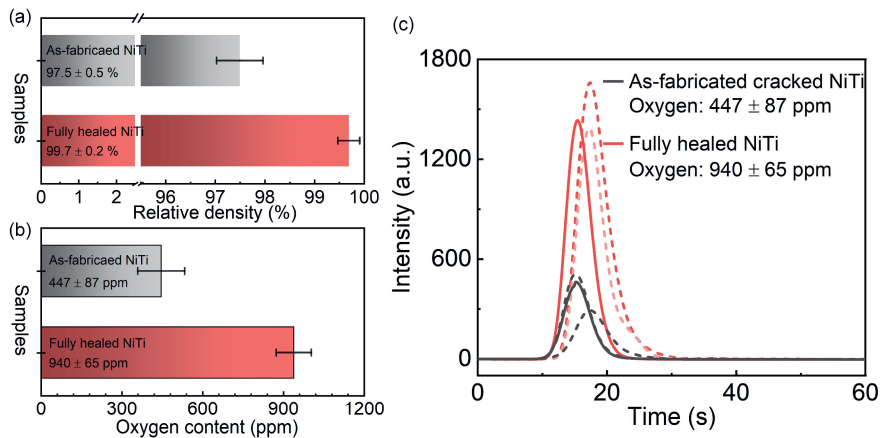
Figure 7.5. (a) Measured relative density of as-fabricated cracked and fully healed NiTi samples. There is an increased relative density after SPS healing process, indicating the elimination of crack flanks. (b) and (c) Measured oxygen contents in as-fabricated cracked and fully healed NiTi samples by using a Bruker oxygen-hydrogen analyser (G8 GALILEO). Dash lines are repeated curves. After the SPS process, an increased oxygen content can be seen.

To further understand the crack healing mechanism, microstructures were further examined by tint OM, SEM and EDS. As shown in the polarized light OM image (Figure 7.6 (a)), intergranular cracks are dominant in the as-fabricated NiTi. By revealing melt pool boundaries, these intergranular cracks exist at melt pool centrelines. These hot cracks are resulting from solidification shrinkage at the final solidification zone when dendrites solidify in a columnar manner [17]. The backscattered electron (BSE) images of semi-healed NiTi are shown in Figure 7.6 (c) and (d). The healed cracks (dark grey longitudinal part in Figure 7. 6 (d)) show more Ti than the NiTi matrix (Figure 7.6 (f)), indicating that formed Ti-rich precipitates contribute to NiTi crack healing. The area around the unhealed crack (Figure 7.6 (e)) shows an even higher content of Ti than the Ti-rich precipitates (Figure 7.6 (f)). Therefore, it is possible to further deduce the crack healing mechanism by analysing microstructural features around unhealed and healed cracks. In the fully healed sample, there are two types of precipitate morphologies (Figure 7.6 (g) and (h)). The elongated precipitates along the building direction are responsible for crack healing and the dispersive particles originated from intragranular precipitation.
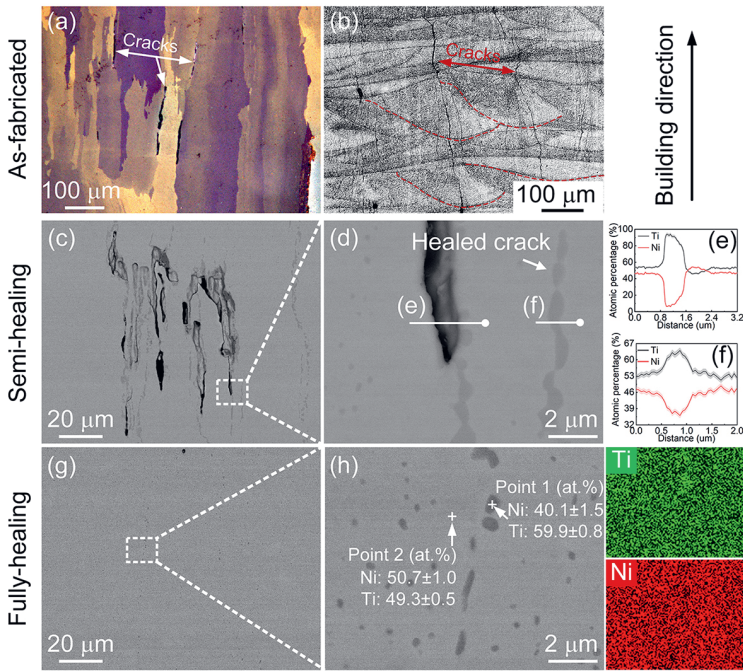
Figure 7.6. As-fabricated NiTi with cracks: optical microstructures showing (a) parent (austenite) phase at the polarized light and (b) melt pool features at the normal light. (c) BSE microstructures of the semi-healed NiTi and (d) its corresponding enlarged image; (e) and (d) EDS line scanning from (d). (g) and (h) BSE microstructures of fully healed NiTi and corresponding EDS mappings from (h). All images showing microstructures along the building direction.

XRD measurements were conducted at room temperature to identify phases. As shown in the XRD patterns, all samples, including cracked L-PBF, semi-healed and fully healed NiTi, have B19′ as the main phase, and small peaks, corresponding to residual austenite (BCC_B2) and Ti_2NiO_x, are also present. To compare phase transformation temperature changes before and after the healing process, DSC measurements were carried on as fabricated and fully healed NiTi. After the SPS healing process, phase transformation temperatures were increased, and the corresponding temperatures are shown in Figure 7.7 (b) and Table 7.2. There is a ~22 K increase of austenite finish temperature and a ~8 J/g increase in the forward phase transformation enthalpy (Figure 7.7 (b) and Table 7.2)

7

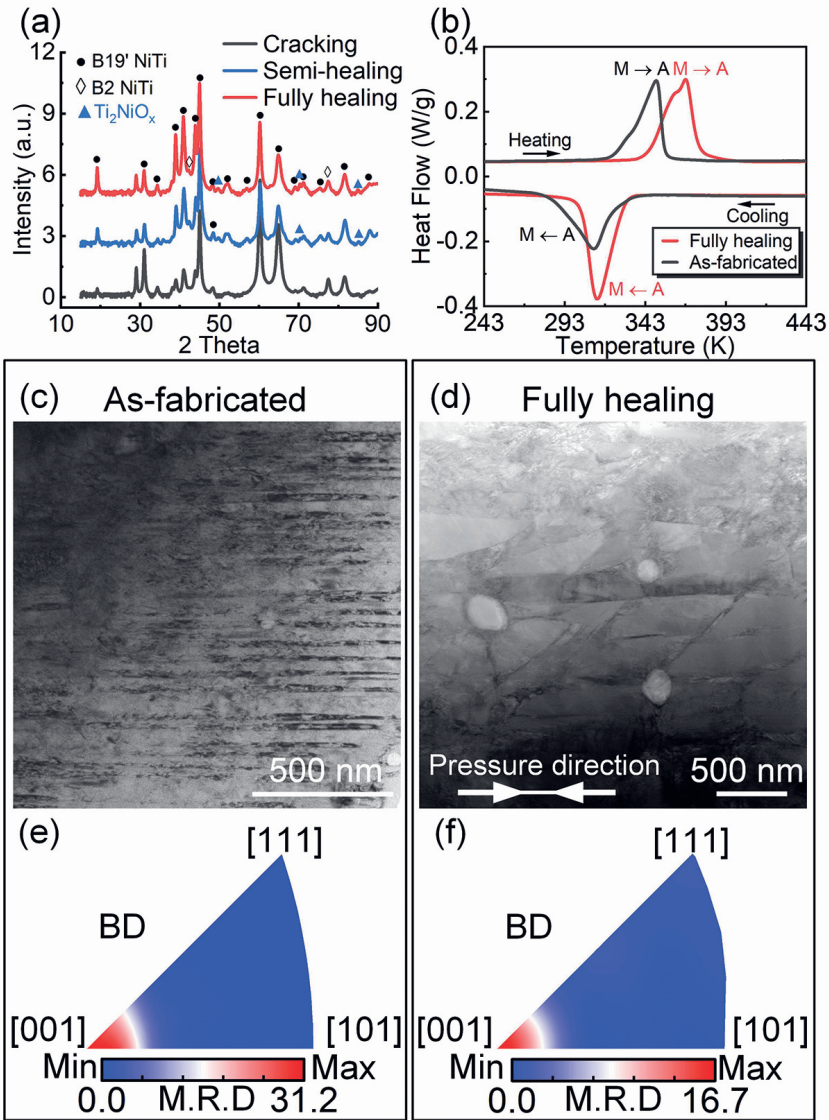Figure 7.7. (a) XRD patterns of NiTi without and with different healing processes; (b) DSC curves of as-fabricated NiTi and fully-healed NiTi; TEM images of (c) as-fabricated NiTi (the bright field image) and (d) fully-healed NiTi (the angle annular dark field image); Inverse pole figures (IPFs) measured by XRD at 473 K, showing texture of the austenite phase: (e) as-fabricated NiTi and (f) fully-healed NiTi.

The TEM images (Figure 7.7 (c) and (d)) also demonstrate that martensite is the main phase at room temperature for as fabricated and fully healing samples, which is consistent with XRD and DSC results (Figure 7.7 (a) and (b)). The fully healed sample has wider martensite phases (~269 nm) than that (~32 nm) in the as-fabricated NiTi. Interestingly, the morphology of martensite in the fully healed NiTi has a tilted brick-like structure and the tilt direction is consistent with the SPS pressure direction (Figure 7.7 (d)). It is worth noting that, despite the high-temperature SPS, the strong [001] texture remains in the fully healed sample (Figure 7.7 (f)). Compared with the as-fabricated NiTi, there is a ~ 50% decrease in the [001] texture intensity in the fully healed sample (Figure 7.7 (e) and (f)). The columnar grain morphology in the fully healed NiTi further indicates that the desirable [001] orientated grains for enhancing superelasticity are preserved (Figure 7.8).
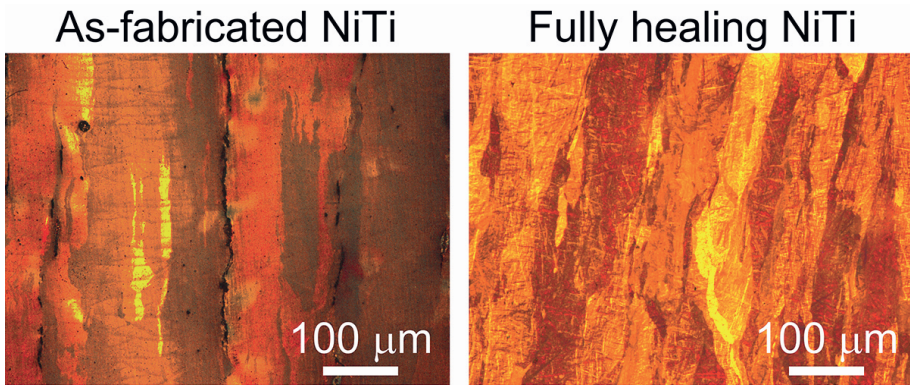
Figure 7.8. Optical microstructure images taken under the polarized light condition showing parent phase grain morphologies before and after the SPS healing process. The columnar grains parallel to the L-PBF building direction are still preserved after the healing process. This is consistent with the texture measurement (Figure 7.7 (e) and (f)).

Due to the resolution limitation of EDS equipped in the SEM, it is hard to analyse elements across grain boundaries of as-fabricated NiTi. Here, the STEM-EDS technique was applied to understand the elemental distribution along the crack flanks of the as-fabricated NiTi. As shown in the Figure 7.9 (a)–(e), more titanium and oxygen segregate along the grain boundary, indicating that hot cracking may result from these elemental segregations. The distance of elemental segregation is ~14 nm.

Table 7.2 Phase transformation temperatures determined by DSC tests.

Temperature (K) Samples	M_s	M_f	M_p	A_s	A_f	A_p	$\Delta H_{A \leftrightarrow M}$ (J/g)
As-fabricated NiTi	327	282	311	322	356	350	23.9
Fully healed NiTi	332	303	312	344	378	368	31.7

*M_s is the Martensite start temperature, M_f is the Martensite finish temperature, M_p is the peak temperature of the forward transformation (A→M), A_s is the austenite start temperature, A_f is the austenite finish temperature, A_p is the peak temperature of the reverse transformation (M→A), $\Delta H_{A \leftrightarrow M}$ is the forward transformation enthalpy.

To reveal the cracking healing mechanism, the semi-healed (as an intermediate state) and the fully healed NiTi were further analysed by TEM. The FIB technique was applied to exact the TEM sample including the unhealed crack (Figure 7.9 (f)). There is an elongated precipitate along the flanks of the crack (Figure 7.9 (g)). Based on the selected area electron diffraction (SAED) (Figure 7.9 (h)) and EDS point analysis, the precipitate is determined as Ti containing oxygen (~11.9 ± 1.4 at. %) (hereafter referred to as Ti(O)). Compared with the as-fabricated cracked NiTi, the width of Ti increases to ~346 nm in the semi-healed NiTi. Therefore, the SPS process can promote the diffusion of Ti to the crack location.

To confirm precipitates along healed cracks in the fully heal sample, a TEM sample was prepared by FIB near the position of elongated precipitates. The interested area is shown in the Figure 7.9 (i) and the precipitate marked by the red arrows is used as a location reference. The SAED pattern (Figure 7.9 (k)) demonstrate that final precipitates along healed cracks in the fully healed sample are Ti_2NiO_x (Figure 7.9 (j)), which is also consistent with the XRD result (Figure 7.7 (a)).

7
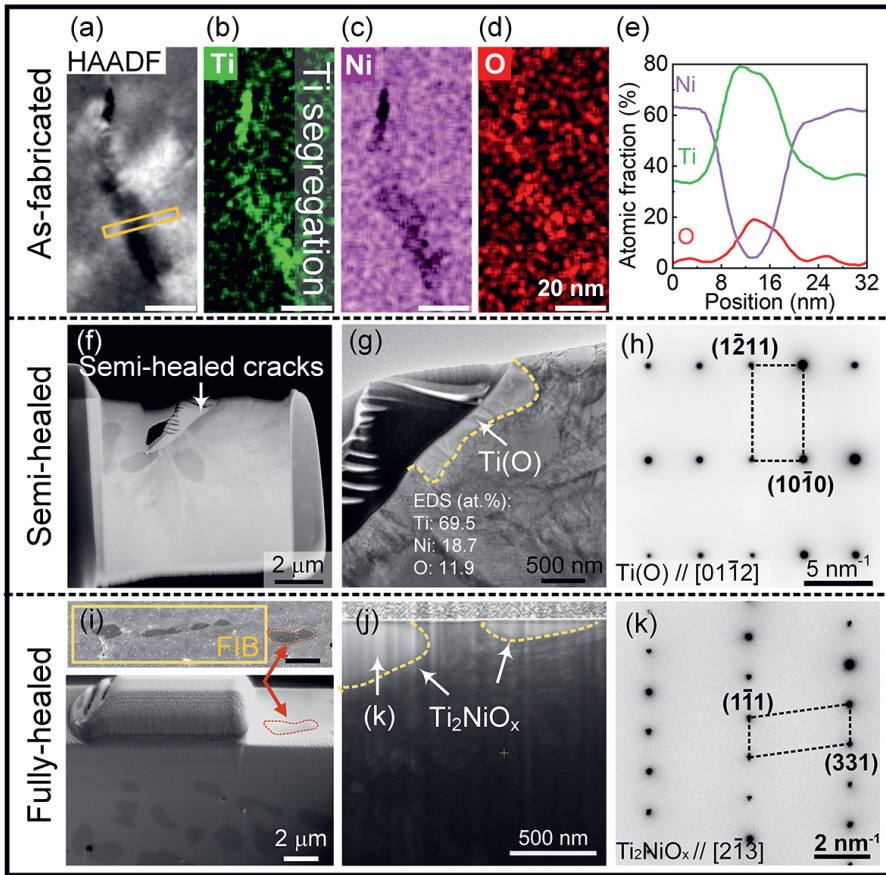
Figure 7.9. (a) The STEM-HAADF image of as-fabricated NiTi and its corresponding EDS mappings, i.e., (b) Ti, (c) Ni and (d) O, and (e) a line scanning from (a); (f) and (g) TEM images of semi-healed NiTi and SAED pattern of Ti(O) from (g); (i) and (j) TEM images of fully healed NiTi and SAED pattern of Ti_2NiO_x from (k).

7.3.2. Mechanical and Functional properties of fully healed NiTi

The purpose of this study is to heal cracks and preserve the superior superelasticity of [001] textured NiTi. To investigate the effect of the SPS treatment on mechanical properties of NiTi, instrumented indentation was conducted. Indentation displacement-force curves with varying maximum forces of 10, 20 and 30 N are shown in the Figure 7.10 (a). The fully healed NiTi always shows lower displacement values than the as-fabricated cracked NiTi under different force levels (Figure 7.10 (a)). This indicates an improved strength of NiTi

after the SPS healing process. The fully healed sample also has a higher Vickers hardness (229 ± 3 HV1) than the as-fabricated cracked NiTi (188 ± 13 HV1) (Figure 7.10 (b)). The large deviation in hardness values of the as-fabricated cracked NiTi results from uniformly distributed cracks. Therefore, the SPS process not only contributes to the crack healing but also improves NiTi strength.
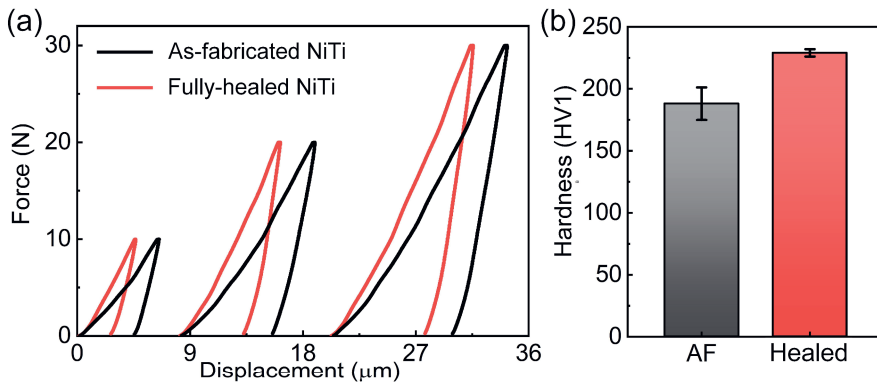
Figure 7.10. (a) Displacement-force curves and (b) Vickers hardness of as-fabricated cracked and fully healed NiTi.

To verify whether the superelasticity still remain in the fully healed sample, thermomechanical tests were conducted. The as fabricated [001] NiTi shows an expected superelasticity (Figure 7.11 (a)), despite the existence of cracks. This is due to that the loading or unloading direction is parallel to the crack propagation direction, which makes strain or stress continuously transfer within samples. Hence, the [001] orientation still can play an effective role on enhancing superelasticity. With thermomechanical cycles under a constant nominal deformation of 4% strain, the superelastic strain value almost remains constant as ~3.2% and residual strain accumulate to 0.5% after 50 cycles. The accumulation of residual strain results from phase transformation induced plasticity and can reach a saturated state after cycles.
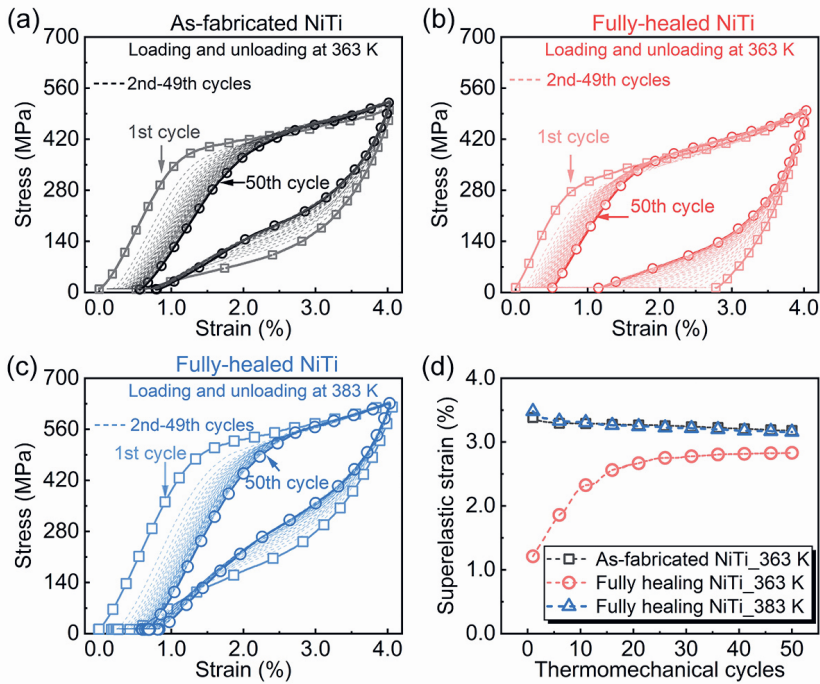
Figure 7.11. Cyclic thermomechanical tests: (a) as fabricated and (b) fully healed NiTi under 363 K loading and unloading, and (c) fully healed NiTi under 383 K loading and unloading. (d) Superelastic strains as a function of thermomechanical cycles

Under the same loading and unloading temperature of 363 K, the fully healed sample also shows superelastic behaviour (Figure 7.11 (b)). At the first thermomechanical cycle, the recoverable strain is only ~1.3%. Surprisingly, its superelasticity is enhanced with the number of cycles and the superelastic strain increases to 2.9 % after 50 thermomechanical cycles (~223 % increase of superelastic strain compared with the first cycle). Compared with the literature, superelasticity usually degrades with thermomechanical cycling. To best of authors' knowledge. it is, for the first time, found in additive manufactured NiTi that superelasticity is enhanced by thermomechanical cycling.

7

7.4. Discussion

7.4.1. Cracking and healing mechanism

7.4.1.1. Crack formation

Before discussing the crack healing mechanism, it is important to understand the crack formation mechanism. NiTi cracking is intergranular (Figure 7.3 (a)), which is a typical feature of solidification cracking (or hot cracking) [25]. The solidification behaviour of Ni (49.6 at. %)-Ti is calculated based on the Scheil-Gulliver model (Figure 7.12 (a)). Since this model assumes that no diffusion occurs in solid phases and infinitely fast diffusion occurs in the liquid, it is suitable for L-PBF solidification with a high cooling rate. At the final stage of solidification (the solid fraction is higher than 0.9), the solidification temperature range is ~237 K (Figure 7.12 (a)).
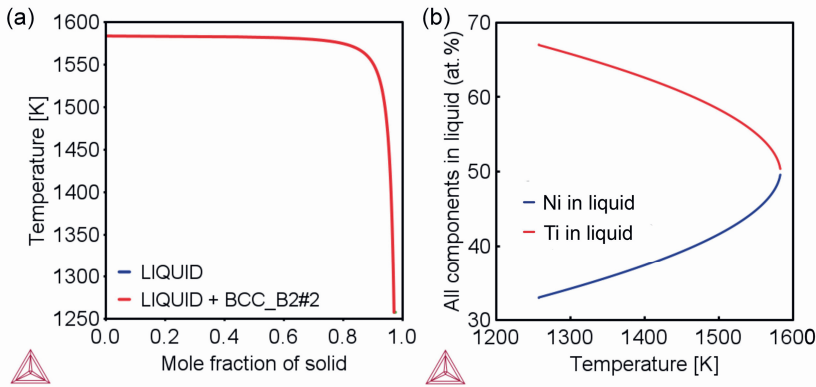
Figure 7.12. (a) The solidification path of Ni (49.6 at. %)-Ti based on the Scheil-Gulliver model. (b) the content of Ni and Ti in the liquid as a function of temperature.

As reported by Kou [26], the solidification cracking susceptibility can be evaluated by the steepness of the curve of T vs $(f_S)^{1/2}$ when $(f_S)^{1/2}$ is close to 1, where T is the temperature and f_S is the solid fraction. For Ni (49.6 at. %)-Ti, the steepness of $\dfrac{\Delta T}{(f_S)^{1/2}}$ is ~7431 K, which is ~1.8 times higher than the high cracking susceptibility of 7075 Al alloy [27]. The high cracking susceptibility of NiTi indicates that cracking along grain boundaries is prone to occur due to stresses introduced by solidification shrinkage and thermal contraction.

Due to the solute redistribution during the solidification of Ni (49.6 at. %)-Ti alloy, Ti enriches the residual liquid (Figure 7.12 (b)). In the solidification microstructure, dendrites grow and merge forming grains, and at the grain boundaries liquid films may remain. Therefore, Ti segregation can be observed along the grain boundaries (Figure 7.9 (a)–(e)).

7.4.1.2. Crack healing

As shown in Figure 7.6 and Figure 7.9, the healing of cracks is achieved by the participation of diffusion bonding. The 1323 K-1 h-22 MPa SPS healing process results in the formation of Ti(O). Despite the L-PBF and SPS processes are under Ar (purity of 99.99%) protection, oxygen is inevitable and can be found in NiTi [28]. As Ti is a reactive element, Ti is easy to react with oxygen at high temperate [29]. The Ti-O binary phase diagram (Figure 7.13) shows that Ti has a large solubility of oxygen, and its solubility of oxygen can reach to ~32 at. % at 1323 K (the SPS processing temperature). The EDS result at the semi-healed NiTi shows that ~11.9 at. % oxygen is present within Ti (Figure 7.9 (g)), which is lower than the maximum solubility of oxygen in Ti. Therefore, Ti(O) exists in the semi-healed cracking interface.
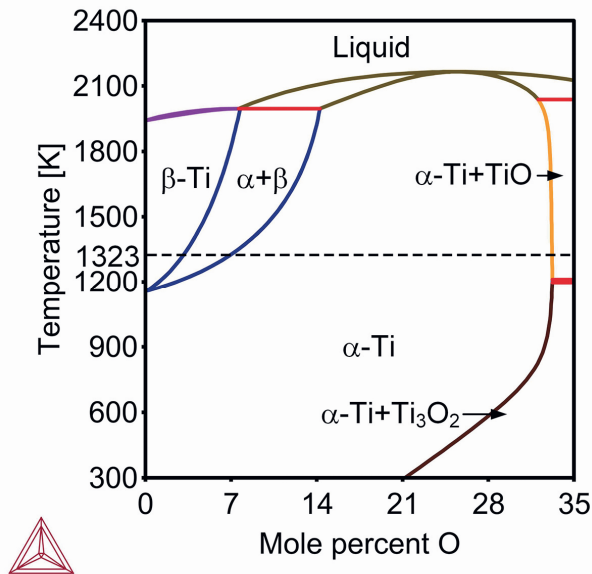

Figure 7.13. The binary phase diagram of Ti-O.

For the entire system, the Ti(O) does not exist in a state of thermodynamic equilibrium. With increasing holding duration to 2 h under 1323 K and 22 MPa, the Ti_2NiO_x phase forms by consuming Ti(O) and the chemical bonding is created, which closes cracks. In the Ni-Ti system, the diffusion rate of Ti into Ni is much higher than that of Ni into Ti [30]. At 1223 K, close to the SPS processing temperature of 1323 K, the diffusion rate of Ti is 2.0×10^{-10} cm^{-2}, which is two orders of magnitude higher than that of Ni (1.5×10^{-12} cm^{-2}). Meanwhile, there is a concentration difference of Ti between Ti(O) and NiTi matrix. Therefore, increasing the duration of the SPS process promotes Ti atoms to diffuse from Ti(O) into NiTi. Based on the Ni-Ti phase diagram [1], NiTi has a limited solubility of Ti and the increase of Ti in NiTi results in the formation a Ti_2Ni phase. Furthermore, oxygen can stabilize Ti_2Ni phase [31], and Ti_2NiO_x is finally present to act as the crack bonding phase (Figure 7.9 (g) and (h) and Figure 7.9 (i)–(k)). The formation of Ti_2Ni phase has been also observed in the interface of Ti and NiTi of Ni-Ti diffusion couples [30].

Based on the above discussion, the chemical reaction of the whole healing process can be summarized as follows:

$$Ti + O \rightarrow Ti(O) \tag{7.1}$$

$$Ti(O) + NiTi \rightarrow Ti_2NiO_x \tag{7.2}$$
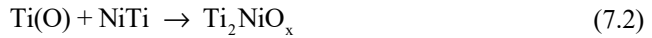
As external oxygen participates in the healing process, these reactions will result in volume expansion. The increased oxygen levels in the fully healed NiTi (940 ppm), compared with the as-fabricated cracked NiTi, (447 ppm) has been confirmed by oxygen measurement (Figure 7.5 (c)). Additionally, in the fully healed NiTi crack flanks can be further closed by the applied pressure.

Therefore, the crack healing is attributed to the synergistic effect from the following sequential three aspects: (1) Crack flanks are closed by external pressure provided by SPS; (2) the remaining gaps at the flanks are filled by Ti_2NO_x due to the volume expansion reaction; (3) Chemical bonding is created by diffusion and remains effective after releasing pressure. It should be mentioned that oxygen is usually considered as an undesirable contamination for L-PBF NiTi, as it deteriorates a printability of NiTi [28]. In this study, the oxygen was utilized to heal cracks in NiTi. The ability of Ti_2NiO_x in crack healing is further demonstrated by EBSD in a larger scale (compared with TEM results shown in the Figure 7.9) (Figure 7.14).
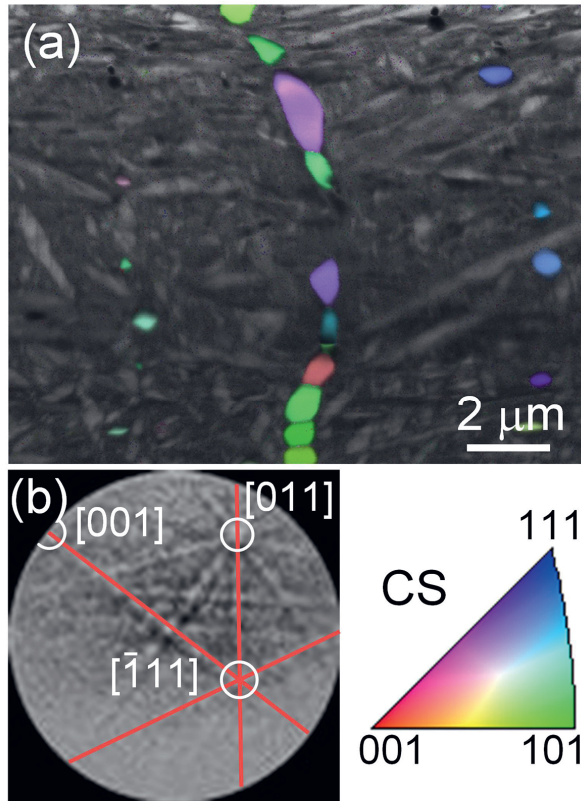
Figure 7.14. (a) A EBSD map with the Ti_2NiO_x phase inverse pole figure colour map overlaid on an image quality map (showing the morphology of B19′ martensite variants) in the fully healed NiTi. (b) A Kikuchi pattern obtained from the Ti_2NO_x phase. CS: cross-section. This EBSD result further demonstrates the formation of Ti_2NiO_x and its role in the healing of NiTi cracks.

7.4.2. Phase transformation temperatures and superelastic behaviour

DSC results show that the SPS healing process increases NiTi phase transformation temperatures (Figure 7.7 (b) and Table 7.2). For the forward transformation, the main difference between as-fabricated cracked and fully healed NiTi is shown in the martensite finish temperature (M_f). The M_f *in* the fully healed NiTi is 21K higher than that in the as-fabricated cracked NiTi. A higher M_f suggests that a decreased driving force is necessary to facilitate the transformation [32]. It has been reported that crystal defects, such as dislocations [33], point defects [34] and grain boundaries [35], can impede martensite transformation and

result in the decrease of phase transformation temperatures. In this study, the fully healed NiTi underwent a high-temperature treatment (1323 K), higher than the NiTi recrystallization temperature [36], which can eliminate crystal defects [37]. Therefore, an increased martensitic transformation temperature is found in the fully healed NiTi. In addition, the SPS healing process promotes the formation of Ti_2NiO_x by decreasing the Ni content in NiTi matrix, which further increase phase transformation temperatures [31].

Due to the increased phase transformation temperatures, the fully healed NiTi shows distinct superelastic behaviour from the as-fabricated cracked NiTi (Figure 7.11 (a) and (b)) at the same loading temperature of 363 K. As the loading temperature of 363 K is lower than the A_f = 368 K of fully healed NiTi, there is a lack of sufficient driving force to trigger the reserve transformation from stress-induced martensite to austenite [38]. Therefore, a small superelastic strain of ~1.2 % (Figure 7.11 (c)) is present after the first thermomechanical cycle. When increasing the test temperature to 383 K (above A_f of fully healed NiTi), desirable superelastic ability, comparable with the as-fabricated NiTi, is shown in the fully healed NiTi (Figure 7.11 (c) and (d)).

It should be noted that, the superelasticity of fully healed NiTi shows an unusual enhancement with thermomechanical cycles, which is different from the commonly seen superelastic degradation [39-41]. For cyclic thermomechanical NiTi, there are two generally accepted viewpoints: (1) the functional degradation of NiTi is due to dislocation accumulation and plastic deformation accompanying martensite transformation [39-41]; (2) oriented internal stresses, induced by thermomechanical cycles, can promote phase transformation and narrow the stress hysteresis [42-44]. Therefore, it can be concluded that the enhanced superelasticity in the fully healed NiTi tested at 363 K is due to the dominance of internal stress assisted phase transformation. In other words, the orientated internal stress induced by thermomechanical cycles is more effective to evoke the reverse transformation during unloading. It provides an additional driving force to promote superelastic strain, even when there is irrecoverable plastic strain caused by dislocation accumulation.
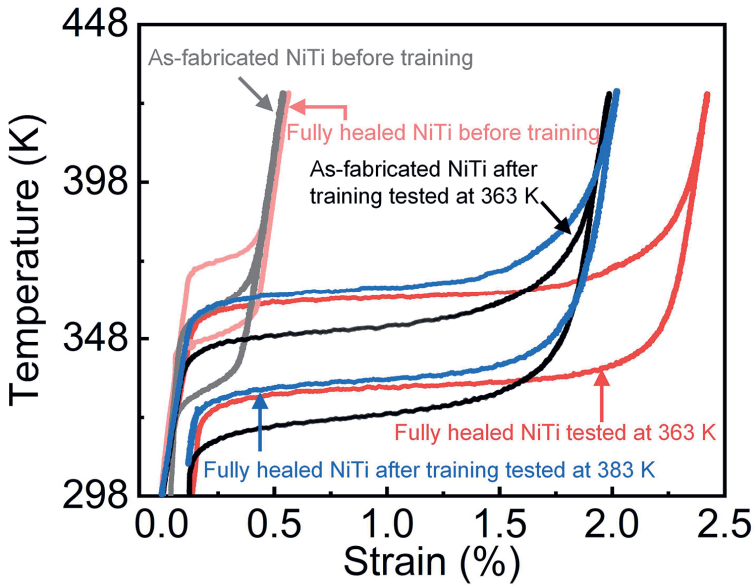
Figure 7.15. Two-way shape memory effect response of as fabricated and fully healed NiTi before and after thermomechanical training.

The level of internal stress within samples can be estimated by two-way shape memory behaviour. After thermomechanical cycles, samples show decreased phase transformation temperatures (Figure 7.15). This is because internal stresses induced by thermomechanical cycles decrease the required thermal driving force of phase transformations. As the superelastic behaviour obeys the Clausius-Clapeyron relationship [1, 45], the internal stress can be quantitatively related to the M_s shift, i.e.:

$$\frac{d\sigma}{dM_s} = \frac{\Delta H \times \rho}{\varepsilon \times T_0} \tag{7.3},$$

where $d\sigma$ is the internal stress (MPa), dM_s (K) is the martensite start temperature shift, ΔH (J/g) is the enthalpy of transformation (measured by DSC shown in the Table 7. 2), ρ = 6.45 g/cm^3 is the NiTi density [46], ε = 0.08 (-) is a transformation strain [45] and T$_0$, herein using the equilibrium temperature of the reserve transformation ($\frac{M_P + A_p}{2}$), is 330 K for as-fabricated cracked NiTi and 340 K for the fully healed NiTi. Based on strain-temperature curves of samples before and after thermal mechanical tests (Figure 7.15) and

considering the M_s shift, the as-fabricated cracked NiTi has a ~7 K shift, and the fully healed NiTi has 17 K and 13 K shifts for tests under 363 K and 383 K, respectively. By calculating the eq. (3), the internal stress for the as-fabricated cracked and the fully healed NiTi tests under 363 K and 383 K, are 41, 129 and 98 MPa. Such estimation also fits well with the two-way shape memory behaviour (Figure 7.15). The fully healed NiTi tested at 363 K has the largest two-way shape memory strain, indicating a highest internal stress.

It is worthy to note that the as-fabricated cracked NiTi after 363 K thermomechanical cycles (the dark black line in the Figure 7. 15) and the fully healed NiTi after 383 K thermomechanical cycles (the blue line in the Figure 7.15) has similar two-way shape memory strains (Figure 7.15), despite ~ 2 times higher estimated internal stress in the fully healed NiTi. This is not contradictory, as based on the Clausius-Clapeyron relationship (eq. 7.3), critical stresses for martensitic phase transformation increase with temperature. The fully healed NiTi after training tested at 383 K (the blue line in the Figure 7.15) has a ~6 K higher M_s than the as-fabricated cracked NiTi after training tested at 363 K (the dark black line in the Figure 7.15). This increased phase transformation results in a ~46 MPa increase of critical stress for martensitic transformation. After excluding the temperature effect on phase transformation stresses, the fully healed NiTi after training tested at 383 K has an equivalent 52 MPa internal stress, which is comparable with the internal stress of 41 MPa in the as-fabricated crack NiTi.

Therefore, the gradually enhanced superelastic ability with thermomechanical cycles and the large two-way shape memory strain (~2.4 %) in fully healed NiTi is attributed to a higher internal stress level. It should be highlighted that such two-way shape memory strain is superior, as it is comparable with the heat-treated cold-drawn NiTi even at a higher deformation level (~8.5 % training deformation [47] and an 8% pre-strain [45]). The reason higher internal stress can be induced into full healed NiTi may result from the presence of intergranular Ti_2NiO_x precipitates. In the Chapter 5, it has been demonstrated that intergranular Ti_2NiO_x precipitates contributes to enclosing internal stress by strain partitioning. The effect of Ti_2NiO_x on the two-way effect in the fully healed NiTi is worthy to be further investigated.

7

7.5. Conclusions

In this study, the crack-healing of [001]-textured L-PBF NiTi using SPS (Spark Plasma Sintering) was successfully demonstrated. Under optimized processing conditions, SPS can successfully eliminate cracks induced by the L-PBF process. The mechanism of crack-healing, as well as the mechanical and functional properties were systematically examined. The main conclusions can be summarized as follows:

1. Spark plasma sintering is demonstrated as an effective method for healing hot cracks in [001]-textured L-PBF NiTi. Cracks are healed through diffusion bonding, and the flanks in the cracks are filled with in-situ formed Ti_2NiO_x precipitates.

2. This work utilized oxygen, which is traditionally considered detrimental to L-PBF parts, in the healing process. The oxygen engages in the following reactions: $Ti + O \rightarrow Ti(O)$ and $Ti(O) + NiTi \rightarrow Ti_2NiO_x$.

3. The SPS healing process improves the mechanical properties of NiTi by eliminating cracks and increases the stable superelastic temperature by 20 K compared to the as-fabricated L-PBF cracked NiTi.

4. An unusual enhancement in superelasticity is observed in the SPS-healed NiTi with thermomechanical cycles. This phenomenon can be attributed to the dominant effect of internal stress on reducing the critical stress required for phase transformation.

5. The SPS-healed NiTi shows a pronounced two-way shape memory response, resulting in approximately 2.4% two-way shape memory strain under a maximum training strain of 4%. This effect is due to high internal stress level in the SPS-healed NiTi.

Findings of this study indicate that SPS is a promising technique for healing hot cracks in L-PBF NiTi and can improve NiTi's mechanical properties and superelasticity. The revealed crack-healing mechanism also provides novel insights for designing crack-healing strategies in other alloy systems.

7

References

[1] K. Otsuka, X. Ren, Physical metallurgy of Ti–Ni-based shape memory alloys, Prog. Mater Sci. 50(5) (2005) 511-678.

[2] J. Mohd Jani, M. Leary, A. Subic, M.A. Gibson, A review of shape memory alloy research, applications and opportunities, Mater. Des. 56 (2014) 1078-1113.

[3] D. Dye, Towards practical actuators, Nat. Mater. 14(8) (2015) 760-761.

[4] X. Ren, K. Otsuka, Origin of rubber-like behaviour in metal alloys, Nature 389(6651) (1997) 579-582.

[5] M. Elahinia, N. Shayesteh Moghaddam, M. Taheri Andani, A. Amerinatanzi, B.A. Bimber, R.F. Hamilton, Fabrication of NiTi through additive manufacturing: A review, Prog. Mater Sci. 83 (2016) 630-663.

[6] Z.X. Khoo, J.E.M. Teoh, Y. Liu, C.K. Chua, S. Yang, J. An, K.F. Leong, W.Y. Yeong, 3D printing of smart materials: A review on recent progresses in 4D printing, Virtual Phys. Prototyp. 10(3) (2015) 103-122.

[7] S.L. Sing, W.Y. Yeong, Laser powder bed fusion for metal additive manufacturing: perspectives on recent developments, Virtual Phys. Prototyp. 15(3) (2020) 359-370.

[8] Z. Yan, J.-N. Zhu, E. Borisov, T. Riemslag, S.P. Scott, M. Hermans, J. Jovanova, V. Popovich, Superelastic response and damping behavior of additively manufactured Nitinol architectured materials, Addit. Manuf. 68 (2023) 103505.

[9] J.-N. Zhu, E. Borisov, X. Liang, R. Huizenga, A. Popovich, V. Bliznuk, R. Petrov, M. Hermans, V. Popovich, Controlling microstructure evolution and phase transformation behavior in additive manufacturing of nitinol shape memory alloys by tuning hatch distance, J. Mater. Sci. 57(10) (2022) 6066-6084.

[10] J.-N. Zhu, K. Liu, T. Riemslag, F.D. Tichelaar, E. Borisov, X. Yao, A. Popovich, R. Huizenga, M. Hermans, V. Popovich, Achieving superelasticity in additively manufactured Ni-lean NiTi by crystallographic design, Mater. Des. 230 (2023) 111949.

[11] M. Gäumann, C. Bezençon, P. Canalis, W. Kurz, Single-crystal laser deposition of superalloys: processing–microstructure maps, Acta Mater. 49(6) (2001) 1051-1062.

[12] G. Laplanche, A. Kazuch, G. Eggeler, Processing of NiTi shape memory sheets – Microstructural heterogeneity and evolution of texture, J. Alloys Compd. 651 (2015) 333-339.

7

[13] K. Gall, T.J. Lim, D.L. McDowell, H. Sehitoglu, Y.I. Chumlyakov, The role of intergranular constraint on the stress-induced martensitic transformation in textured polycrystalline NiTi, Int. J. Plast. 16(10) (2000) 1189-1214.

[14] H. Sehitoglu, I. Karaman, R. Anderson, X. Zhang, K. Gall, H.J. Maier, Y. Chumlyakov, Compressive response of NiTi single crystals, Acta Mater. 48(13) (2000) 3311-3326.

[15] P. Capper, Bulk Bridgman growth of cadmium mercury telluride for IR applications, J Mater Sci Mater Electron. 12(8) (2001) 423-428.

[16] P. Köhnen, M. Létang, M. Voshage, J.H. Schleifenbaum, C. Haase, Understanding the process-microstructure correlations for tailoring the mechanical properties of L-PBF produced austenitic advanced high strength steel, Addit. Manuf. 30 (2019) 100914.

[17] J.H. Martin, B.D. Yahata, J.M. Hundley, J.A. Mayer, T.A. Schaedler, T.M. Pollock, 3D printing of high-strength aluminium alloys, Nature 549(7672) (2017) 365-369.

[18] P.A. Rometsch, Y. Zhu, X. Wu, A. Huang, Review of high-strength aluminium alloys for additive manufacturing by laser powder bed fusion, Mater. Des. 219 (2022) 110779.

[19] J. Huang, L. Guo, L. Zhong, Synergistic healing mechanism of self-healing ceramics coating, Ceram. Int. 48(5) (2022) 6520-6527.

[20] R.A. Stevens, P.E.J. Flewitt, Hot isostatic pressing to remove porosity & creep damage, Mater. Des. 3(3) (1982) 461-469.

[21] M. Vilanova, F. Garciandia, S. Sainz, D. Jorge-Badiola, T. Guraya, M. San Sebastian, The limit of hot isostatic pressing for healing cracks present in an additively manufactured nickel superalloy, J. Mater. Process. Technol. 300 (2022) 117398.

[22] Z.-Y. Hu, Z.-H. Zhang, X.-W. Cheng, F.-C. Wang, Y.-F. Zhang, S.-L. Li, A review of multi-physical fields induced phenomena and effects in spark plasma sintering: Fundamentals and applications, Mater. Des. 191 (2020) 108662.

[23] R.R. Adharapurapu, F. Jiang, K.S. Vecchio, G.T. Gray, Response of NiTi shape memory alloy at high strain rate: A systematic investigation of temperature effects on tension–compression asymmetry, Acta Mater. 54(17) (2006) 4609-4620.

[24] Z. Zhou, Q. Lei, Z. Yan, Z. Wang, Y. Shang, Y. Li, H. Qi, L. Jiang, Y. Liu, L. Huang, Effects of process parameters on microstructure and cracking susceptibility of a single crystal superalloy fabricated by directed energy deposition, Mater. Des. 198 (2021) 109296.

7

[25] S. Kou, Solidification and liquation cracking issues in welding, JOM 55(6) (2003) 37-42.

[26] S. Kou, A criterion for cracking during solidification, Acta Mater. 88 (2015) 366-374.

[27] S. Kou, A simple index for predicting the susceptibility to solidification cracking, Weld. J 94(12) (2015) 374-388.

[28] X. Wang, J. Yu, J. Liu, L. Chen, Q. Yang, H. Wei, J. Sun, Z. Wang, Z. Zhang, G. Zhao, J. Van Humbeeck, Effect of process parameters on the phase transformation behavior and tensile properties of NiTi shape memory alloys fabricated by selective laser melting, Addit. Manuf. 36 (2020) 101545.

[29] Y. Inoue, N. Hiraide, A. Hayashi, K. Ushioda, Effect of Titanium on Oxidation Behavior of High-Purity Ferritic Stainless Steel, Mater. Trans. 60(9) (2019) 1968-1976.

[30] L. Hu, Y. Xue, F. Shi, Intermetallic formation and mechanical properties of Ni-Ti diffusion couples, Mater. Des. 130 (2017) 175-182.

[31] J. Frenzel, E.P. George, A. Dlouhy, C. Somsen, M.F.X. Wagner, G. Eggeler, Influence of Ni on martensitic phase transformations in NiTi shape memory alloys, Acta Mater. 58(9) (2010) 3444-3458.

[32] R.F. Hamilton, T.A. Palmer, B.A. Bimber, Spatial characterization of the thermal-induced phase transformation throughout as-deposited additive manufactured NiTi bulk builds, Scripta Mater. 101 (2015) 56-59.

[33] T. Simon, A. Kröger, C. Somsen, A. Dlouhy, G. Eggeler, On the multiplication of dislocations during martensitic transformations in NiTi shape memory alloys, Acta Mater. 58(5) (2010) 1850-1860.

[34] A. Mansouri Tehrani, H. Shahrokhshahi, N. Parvin, J. Brgoch, Influencing the martensitic phase transformation in NiTi through point defects, J. Appl. Phys. 118(1) (2015).

[35] W.-S. Ko, S.B. Maisel, B. Grabowski, J.B. Jeon, J. Neugebauer, Atomic scale processes of phase transformations in nanocrystalline NiTi shape-memory alloys, Acta Mater. 123 (2017) 90-101.

[36] G. Tadayyon, M. Mazinani, Y. Guo, S.M. Zebarjad, S.A.M. Tofail, M.J. Biggs, The effect of annealing on the mechanical properties and microstructural evolution of Ti-rich NiTi shape memory alloy, Mater. Sci. Eng., A 662 (2016) 564-577.

7

[37] K.K. Alaneme, E.A. Okotete, Recrystallization mechanisms and microstructure development in emerging metallic materials: A review, Journal of Science: Advanced Materials and Devices 4(1) (2019) 19-33.

[38] X. Huang, Y. Liu, Effect of annealing on the transformation behavior and superelasticity of NiTi shape memory alloy, Scripta Mater. 45(2) (2001) 153-160.

[39] D. Song, C. Yu, C. Zhang, G. Kang, Superelasticity degradation of NiTi shape memory alloy in wide ranges of temperature and loading level: Experimental observation and micromechanical constitutive model, Int. J. Plast. 161 (2023) 103487.

[40] W.-N. Hsu, E. Polatidis, M. Šmíd, S. Van Petegem, N. Casati, H. Van Swygenhoven, Deformation and degradation of superelastic NiTi under multiaxial loading, Acta Mater. 167 (2019) 149-158.

[41] O. Tyc, L. Heller, P. Šittner, Lattice Defects Generated by Cyclic Thermomechanical Loading of Superelastic NiTi Wire, Shape Mem. Superelasticity 7(1) (2021) 65-88.

[42] K. Wada, Y. Liu, Thermomechanical training and the shape recovery characteristics of NiTi alloys, Mater. Sci. Eng., A 481-482 (2008) 166-169.

[43] I. Ponikarova, S. Belyaev, N. Resnina, Degradation of two-way shape memory effect due to the relaxation of internal oriented stress in NiTi alloy on holding at 640÷700 K, Mech. Mater. 138 (2019) 103174.

[44] X. Wang, B. Xu, Z. Yue, Phase transformation behavior of pseudoelastic NiTi shape memory alloys under large strain, J. Alloys Compd. 463(1) (2008) 417-422.

[45] S. Eucken, T.W. Duerig, The effects of pseudoelastic prestraining on the tensile behaviour and two-way shape memory effect in aged NiTi, Acta Metall. 37(8) (1989) 2245-2252.

[46] J.-N. Zhu, E. Borisov, X. Liang, E. Farber, M.J.M. Hermans, V.A. Popovich, Predictive analytical modelling and experimental validation of processing maps in additive manufacturing of nitinol alloys, Addit. Manuf. 38 (2021) 101802.

[47] H. Scherngell, A.C. Kneissl, Training and stability of the intrinsic two-way shape memory effect in Ni-Ti alloys, Scripta Mater. 39(2) (1998) 205-212.

7

7

8

General Discussion and Conclusions

The motivation behind this research was to develop 4D printed smart metallic materials. At the inception of the PhD project, the focus of 4D printing was primarily on polymers, with minimal research conducted on metallic shape memory materials. Hence, the aim of this research was to fill this gap by exploring the potential of metallic materials. Specifically, a near equiatomic NiTi shape memory alloy (slight Ni-lean 49.6 at. % Ni) was selected as the prime candidate to demonstrate the shape memory function as the fourth dimensional response of 3D printed metallic materials. Throughout this research, significant efforts were dedicated to achieving an integrated design approach for additively manufactured NiTi shape memory alloys. The research design framework can be summarized as a progression from optimisation of processing parameters to microstructure, followed by functional properties and subsequent post-treatment considerations. This comprehensive approach allowed for a multiscale systematic exploration of the relationship between process parameters, resulting microstructure, functional characteristics and the potential for post-treatments to enhance the material's performance.

The fabrication of fully dense and structural defect-free L-PBF NiTi, as one of the overarching challenges in the L-PBF field, has been firstly investigated in this study. Departing from conventional methods of L-PBF parameter optimization that rely on trial-and-error and empirical results, a novel computational approach was presented. The model proposed in this study leverages melt pool physics and defect formation criteria to predict L-PBF NiTi processing maps. By considering key L-PBF processing parameters such as laser power, scanning velocity, hatch distance, layer thickness, and laser beam diameter, this model enables the exploration of suitable processing parameters across a wide range of conditions. Notably, the model is based on analytical solutions, resulting in a low computational cost. It can evaluate approximately 600 L-PBF processing combinations within a mere ~13 minutes on a typical computer with a 4-core CPU. To validate the accuracy of this predictive model, experiments were conduced using two distinct sets of L-PBF processing conditions: low laser power (250 W) with a small beam diameter (80 μm), and high laser power (950 W) with a large beam diameter (500 μm). The experimental results confirmed the reliability and effectiveness of the predictive model in guiding the fabrication of defect-free L-PBF NiTi components.

Following the optimization of processing parameters, an optimal process has been identified as that a laser power of 250W, combined with a scanning velocity of 1250 mm/s, yields laser beads devoid of balling defects. Building upon this optimized linear energy input, a systematic investigation has been conducted to analyse the impact of hatch distance on various aspects, including thermal histories, grain size and morphology, dislocation structure

8

and density, and phase transformation behaviour. The findings of this study reveal that the hatch distance significantly influences thermal histories, which, in turn, affects dislocation densities and subsequently influences the cyclic stability of thermally induced martensitic transformations. To establish comprehensive relationships between L-PBF parameters, microstructures, and functional properties, a methodology that integrates a finite element thermal model with experimental validation was developed. The results of this study demonstrate that the martensitic phase transformation characteristics of NiTi are highly dependent on thermal histories, influenced by phenomena such as remelting and reheating. This proposed methodology can also be applied to investigate the effects of other L-PBF processing parameters on the phase transformation behaviour of NiTi.

After gaining insights into thermal-induced phase transformations in L-PBF NiTi, the investigation delved into stress-induced phase transformations. For this purpose, dense L-PBF NiTi specimens fabricated using optimized parameters were selected, namely a 250 W laser power, 1250 mm/s scanning velocity, 120 µm hatch distance, and 30 µm layer thickness. Then, the as-fabricated L-PBF NiTi as well as its heat-treated counterparts have been proceeded to investigate shape memory effect. Observations of this study revealed that all L-PBF NiTi alloys, both with and without heat treatments, exhibit a shape memory effect. However, variations in shape recovery ability, shape memory degradation behaviour, and two-way shape memory effect were evident among the samples. These differences were attributed to variations in microstructure before and after the heat treatments. To enhance specific functionalities of L-PBF NiTi, employing heat treatments is highly recommended. For instance, solutionized annealing can improve the shape memory degradation resistance by eliminating crystallographic defects. Furthermore, a combination of solutionized annealing and subsequent aging can lead to an enhanced two-way shape memory response. This is achieved by inducing intergranular precipitates through the designed heat treatment, resulting in heterogenous structures comprising of a soft matrix and hard precipitates. The presence of such heterogenous structures facilitates strain partitioning, confining internal stress within individual grains. The findings from this aspect of the study provide valuable guidance for the tailored design of shape memory effects through the utilization of appropriate heat treatments.

However, despite achieving a tailorable shape memory effect in L-PBF Ni-lean NiTi, the absence of another important function, superelasticity, remains a challenge. This is primarily due to the lack of strengthening factors such as solid-solution strengthening and precipitation strengthening in Ni-lean NiTi, caused by its very limited solid solubility of Ti in NiTi. Furthermore, the low solidification nucleation rate in NiTi leads to a weak Hall-

8

Petch strengthening. Additionally, the critical stress for stress-induced martensitic transformation follows the Clapeyron-Clausius law, expressing that the critical stress increases with increasing temperatures. As a result, Ni-lean NiTi, with a higher austenite finish temperature compared to Ni-rich NiTi, undergoes plastic deformation prior to the stress-induced martensitic transition in L-PBF Ni-lean NiTi, resulting in the absence of superelasticity.

To overcome this challenge, it is proposed to utilize the functional and mechanical anisotropy of NiTi to design NiTi with preferred grain orientations that promote superelasticity, while discouraging plastic yielding. This design approach involves three steps: 1) grain orientation selection, 2) fabrication of NiTi with the intended preferred grain orientations, and 3) experimental validation of superelasticity in Ni-lean NiTi. The selection of grain orientations is accomplished through molecular dynamics and Schmid factor calculations, confirming that [001] textured NiTi holds the greatest potential for realising superelasticity in Ni-lean NiTi. Based on the developed processing maps and the thermal field simulations conducted by finite element models, criteria for selecting grain morphology were derived. L-PBF processing parameters are optimized for the fabrication of [001] textured Ni-lean NiTi. Finally, through experimental validation, an unprecedented superelasticity was achieved in L-PBF Ni-lean NiTi. The superelastic temperature can be maintained up to 453 K, comparable to rare earth alloyed NiTi alloys, but with a wider superelastic temperature range of approximately 110K. This remarkable discovery revolutionizes the design of superior-performing NiTi-based alloys by directly tailoring crystallographic orientations during additive manufacturing. So far, both of the main functions of NiTi, i.e. the shape memory effect, and superelasticity, can be achieved using the L-PBF technique in Ni-lean NiTi, laying the basis for designing functionally graded NiTi materials with the defined alloying compositions.

Although superelasticity is achieved in L-PBF Ni-lean NiTi, there is a side effect to be considered: fabricated NiTi with [001] textured columnar grains exhibit a high hot-cracking sensitivity, necessitating careful selection of L-PBF processing parameters. In order to address this issue and enable the sustainable reuse of cracked NiTi samples, an investigation on NiTi crack healing was initiated. Through the utilization of spark plasma sintering (SPS), hot cracks induced by element segregation and thermal stresses are effectively healed. The healing mechanism involves the application of force and heat during SPS, which facilitate the closure of Ti-segregated crack flanks by diffusion bonding. As a result, in addition to preserving superelasticity, the mechanical properties and two-way shape memory response of the SPS-healed NiTi are significantly improved. This improvement can be attributed to

8

the formation of healing Ti_2NiO_x precipitates around the cracking flanks. By effectively addressing the mitigation of hot cracking, this approach expands the application potential of L-PBF NiTi parts while simultaneously enhancing their functional and mechanical properties.

The findings and methodologies presented in this research provide a solid basis for further advancements in 4D printing of metallic materials. The knowledge gained from this study could also be extended to other metallic materials and additive manufacturing techniques, enabling the development of a broader range of smart materials with advanced functionalities. Overall, this research contributes to the growing field of 4D printing and paves the way for the design and fabrication of innovative metallic materials with tailored properties and functions.

8

9

Recommendations

9

This study has undertaken the development of 4D printing techniques for smart metallic materials, with a specific focus on Ti-rich NiTi shape memory alloys. Utilizing the laser powder bed fusion (L-PBF) technique, a significant progress in establishing a comprehensive processing framework was achieved. Efforts of this study included the optimization of L-PBF process parameters, as well as the exploration of tailored microstructure, texture and resulting functionalities. Additionally, suitable post-treatment processes to enhance the functional and mechanical properties of L-PBF NiTi were investigated. Upon the outcomes of this research, the following recommendations are formulated:

1. Cracks pose a significant challenge to the functional and mechanical properties of L-PBF NiTi. Despite the observation of cracking phenomena, a reliable model for predicting crack formation in L-PBF NiTi is still lacking. To effectively address this issue, a comprehensive model should be developed, taking into account the thermal histories and thermal stress influenced by different processing parameters in combination with the solidification behaviour of the material.

2. The significance of crystallographic orientations on the functional properties of NiTi has been demonstrated in this study. To further enhance the design accuracy of superelasticity in NiTi through L-PBF, it is recommended to develop integrated models that incorporate grain and texture predictions, as well as predictions of the superelastic behaviour based on the anticipated microstructure. These comprehensive models will facilitate more precise control over the desired functional characteristics of NiTi components.

3. With emerging design demands, there is a growing need for NiTi materials with multistage functional responses. Functionally graded NiTi shape memory alloys (SMAs) present a promising solution to address this challenge. Leveraging the capabilities of the L-PBF technique, it becomes possible to tailor microstructures and chemical compositions in situ, thereby enabling the creation of functionally graded NiTi materials. This work has successfully achieved graded microstructures and textures by controlling L-PBF processing parameters. However, it is important to consider the influence of element evaporation on the chemical composition changes and establish a quantifiable relationship between the NiTi's chemical composition, element evaporation, and phase transformation temperatures. Leveraging from the results of this PhD dissertation, the initial results on achieving functionally graded NiTi with chemical gradients and microstructural gradients are shown in Figure 9.1 and Figure 9.2, respectively.
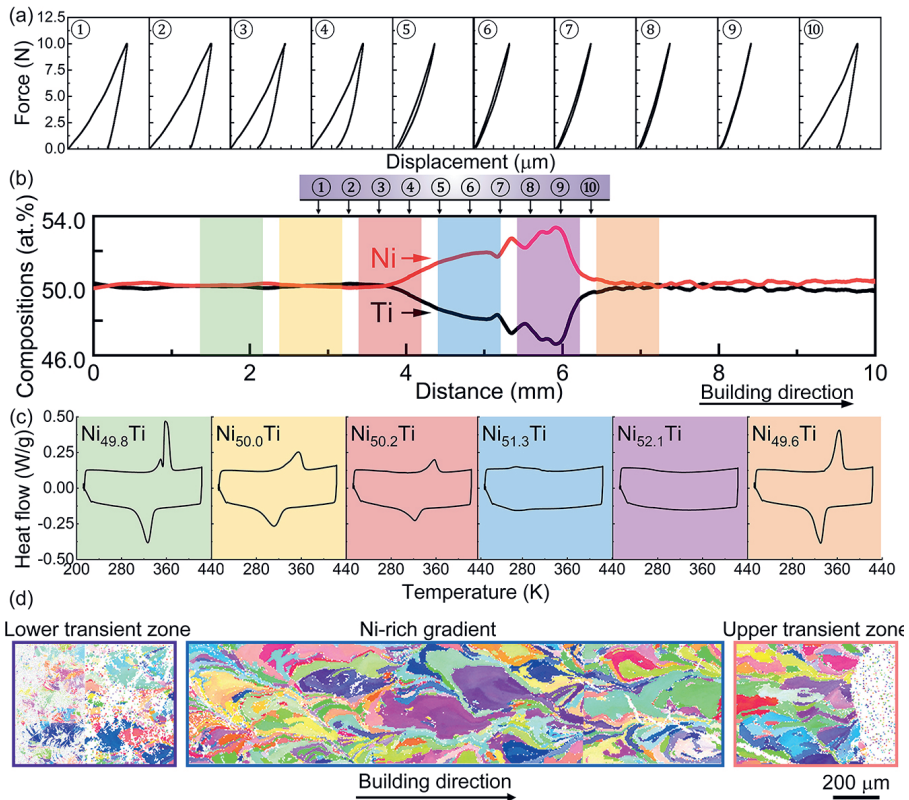
9

Figure 9.1. Functionally graded NiTi with various Ni/Ti ratios. (a) Force-displacement-curves at different locations in the L-PBF fabricated part. (b) EDS line scan along the building direction, showing Ni and Ti contents. (c) DSC curves showing different phase transformation behaviour in various locations of functionally graded NiTi. (d) Optical microstructures from various locations in functionally graded NiTi.
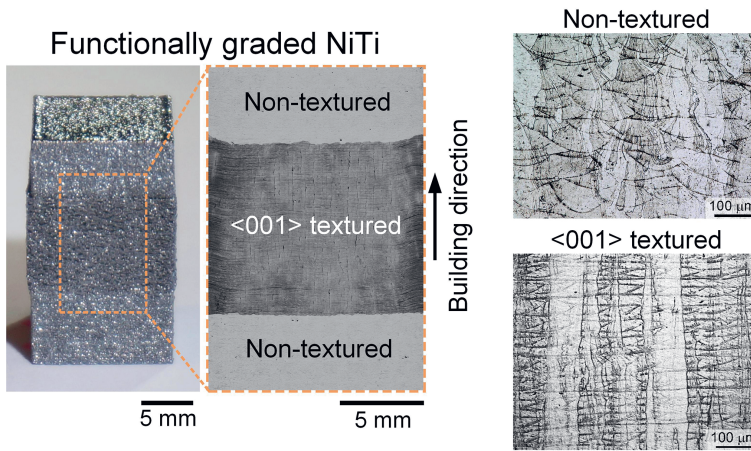
9

Figure 9.2. Functionally graded NiTi created by various L-PBF process parameters: (a) Macroscopic view and (b) microscopic images of corresponding zones.

4. One of the notable advantages of the L-PBF technique is its ability to fabricate complex geometries. Therefore, an intriguing avenue for future exploration would be to combine topological design with the unique functions of NiTi to create novel functionalities, such as high negative Poisson's ratio and superior damping properties. Moreover, gaining a deeper understanding of how NiTi functions within meta-structures is crucial for the development of new functional materials. Harvesting the synergistic effects between NiTi and the meta-structure will unlock further opportunities for designing innovative materials and components with enhanced truly unique characteristics.

9

9

Curriculum Vitae

Jianing Zhu

Born on 05 February 1993, Nei Mongol

Education

11. 2023 - Current	Postdoc. Department of Materials Science and Engineering
	Delft University of Technology, Delft, the Netherlands
06. 2019 - 10. 2023	Ph.D. Department of Materials Science and Engineering
	Delft University of Technology, Delft, the Netherlands
08. 2015 - 06. 2018	Master of Science in Material Processing Engineering
	Jilin University, Changchun, China
08. 2011 – 06. 2015	Bachelor of Science in Material Science and Engineering
	Jilin University, Changchun, China

List of Publications

Journal papers

1. **J.-N. Zhu**, Z. Ding, E. Borisov, X. Yao, J.C. Brouwer, A. Popovich, M. Hermans, V. Popovich, Healing cracks in additively manufactured NiTi shape memory alloys, *Virtual and Physical Prototyping* (2023) e2246437.

2. **J.-N. Zhu**, W. Zhu, E. Borisov, X. Yao, T. Riemslag, C. Goulas, A. Popovich, Z. Yan, F.D. Tichelaar, M. Hermans, V. Popovich, Effect of Heat Treatment on Microstructure and Functional Properties of Additively Manufactured NiTi Shape Memory Alloys, *Journal of Alloys and Compounds* (2023) 171740.

3. **J.-N. Zhu**, K. Liu, T. Riemslag, F.D. Tichelaar, E. Borisov, X. Yao, A. Popovich, R. Huizenga, M. Hermans, V. Popovich, Achieving superelasticity in additively manufactured Ni-lean NiTi by crystallographic design, *Materials & Design* 230 (2023) 111949.

4. **J.-N. Zhu**, E. Borisov, X. Liang, R. Huizenga, A. Popovich, V. Bliznuk, R. Petrov, M. Hermans, V. Popovich, Controlling microstructure evolution and phase transformation behavior in additive manufacturing of nitinol shape memory alloys by tuning hatch distance, *Journal of Materials Science* (2022) 1–19.

5. **J.-N. Zhu**, E. Borisov, X. Liang, E. Farber, M.J.M. Hermans, V.A. Popovich, Predictive analytical modelling and experimental validation of processing maps in additive manufacturing of nitinol alloys, *Additive Manufacturing* 38 (2021) 101802.

Other journal papers and conference proceedings

1. Z. Ding, , J. C. Brouwer, **J.-N. Zhu**, V.A. Popovich, M. J. M. Hermans, W. G. Sloof, Effects of boron addition on the high temperature oxidation of $MoSi_2$ alloys. *Scripta Materialia* 234 (2023): 115580.

2. M. Liu, **J.-N. Zhu**, V.A. Popovich, E. Borisov, J.M.C. Mol, Y. Gonzalez-Garcia, Passive film formation and corrosion resistance of laser-powder bed fusion fabricated NiTi shape memory alloys, *Journal of Materials Research and Technology* 23 (2023) 2991–3006.

3. Z. Ding, J.C. Brouwer, C. Kwakernaak, **J.-N. Zhu**, V. Popovich, M.J.M. Hermans, W.G. Sloof, $Mo(Al_xSi_{1-x})_2$ healing particles for high temperature ceramics and encapsulation by selective oxidation of aluminium, *Materials & Design* 225 (2023) 111577.

4. Z. Yan, **J.-N. Zhu**, E. Borisov, T. Riemslag, S.P. Scott, M. Hermans, J. Jovanova, V. Popovich, Superelastic response and damping behavior of additively manufactured Nitinol architectured materials, *Additive Manufacturing*. 68 (2023) 103505.

5. Ming Liu, **J.-N. Zhu**, V. Popovich, E. Borisov, J.M.C. Mol, Y. Gonzalez-Garcia, Corrosion and passive film characteristics of 3D-printed NiTi shape memory alloys in artificial saliva, *RARE Metals*. (2022): 1–16.

6. J. Rong, **J.-N. Zhu**, W. Xiao, X. Zhao, C. Ma, A high pressure die cast magnesium alloy with superior thermal conductivity and high strength, *Intermetallics* 139 (2021) 107350.

7. M. Laot, B. Rich, I. Cheibas, J. Fu, **J.-N. Zhu**, V.A. Popovich, Additive Manufacturing and Spark Plasma Sintering of Lunar Regolith for Functionally Graded Materials, *SPOOL* 8(2) (2021) 7–30.

8. I. Polozov, A. Kantyukov, I. Goncharov, N. Razumov, A. Silin, V. Popovich, **J.-N. Zhu**, A. Popovich, Additive Manufacturing of Ti-48Al-2Cr-2Nb Alloy Using Gas Atomized and Mechanically Alloyed Plasma Spheroidized Powders, *Materials*, 2020.

9. A. Kim, T. Makhmutov, N. Razumov, A. Silin, A. Popovich, **J.-N. Zhu**, V. Popovich, Synthesis of NiTi alloy powders for powder-based additive manufacturing, *Materials Today. Proceedings*. 30 (2020) 679–682.

10. E. Farber, **J.-N. Zhu**, A. Popovich, V. Popovich, A review of NiTi shape memory alloy as a smart material produced by additive manufacturing, *Materials Today Proceedings* 30 (2020) 761–767.

11. E.V. Borisov, V.A. Popovich, A.A. Popovich, V.S. Sufiiarov, **J.-N. Zhu**, K.A. Starikov, Selective laser melting of Inconel 718 under high laser power, *Materials Today Proceedings* 30 (2020) 784–788.

12. **J.-N. Zhu**, T.T. Zhou, M. Zha, C. Li, J.H. Li, C. Wang, C.L. Gao, H.Y. Wang, Q.C. Jiang, Microstructure and wear behaviour of $Al-20Mg_2Si$ alloy with combined Zr and Sb additions, *Journal of Alloys and Compounds*. 767 (2018) 1109–1116.

13. H.-Y. Wang, **J.-N. Zhu**, J.-H. Li, C. Li, M. Zha, C. Wang, Z.-Z. Yang, Q.-C. Jiang, Refinement and modification of primary Mg_2Si in an $Al–20Mg_2Si$ alloy by a combined addition of yttrium and antimony, *Crystal Engineering Communications* 19 (42) (2017) 6365–6372.

Acknowledgment

With finishing writing my dissertation, I am reflecting on my PhD journey with a profound sense of gratitude. I consider myself fortunate to have been a member of the MSE at TU Delft, where I had the opportunity to develop my PhD career. I would like to express my heartfelt appreciation to all those who have played a significant role in my PhD journey.

Firstly, I am deeply indebted to my promotor and daily supervisor Dr. Vera Popovich, for her unwavering guidance, patience, and mentorship throughout my Ph.D project. I am truly appreciative of her trust and the freedom she provided, enabling me to embark on explorations with confidence. It is through her unwavering support that I was able to fully immerse myself in research and find enjoyment in the field of materials science. I am also profoundly grateful to my co-promoter, Dr. Marcel Hermans, for his valuable and inspiring discussions. His encouragement and sense of humor have been a source of great motivation and enjoyment for me.

I extend my appreciation to the members of my thesis committee: Prof. Jilt Sietsma, Prof. Leo Kestens, Prof. Maurizio Vedani, Prof. Ian Gibson, and Prof. Erik Schlangen, for their valuable insights and constructive feedback, which greatly improved the quality of this thesis.

I would like to express my gratitude to Evgenii Borisov for preparing and printing the test samples. I would like to sincerely thank Richard Huizinga for facilitating my experimental work and valuable discussion. My heartfelt thanks go to Ton Riemslag, Elise Reinton, Sean Scott, and Raymond Dekker for their support in mechanical tests and the design of experimental setups. Your contributions and dedication ensured the smooth execution of complex thermo-mechanical tests. Additionally, I would like to express my gratitude to Hans Brouwer for his assistance with SPS tests and training.

I would also like to thank Kees Kwakernaak, Sander van Asperen, Durga Mainali Sharma, Roy Awater, Wiel Evers for help in providing training and troubleshooting. Thanks Frans D Tichelaar for helping me with TEM and valuable discussion.

I am also thankful to my colleagues and friends who offered companionship and support during my Ph.D life. I owe gratitude to our group members, present and past, Virgínia, José, Quanxin, Tim, Jaji, Vitoria, Wei, Kaveh, Jia, Jhon, Jithin, Jan, Soroush, Fei, Yucheng, Meng, Yang, Yuliu, Qiang, Zhiyuan, Aravind, Jiahui, Ajun, Amin and Mengmeng for being really nice and helpful to me in my PhD daily life. I would like to thank my collaborators, at the same time my good friends. Thank Zhaoying, Xiaohui, Kai (Liu), Xiyu, Yi-Chieh and Feiyu. I really benefit a lot from your expertise. My office-mates, Zhaorui, Gaojie, and Dongil, deserve my gratitude for our daily conversations and shared moments of laughter.

I extend my thanks to Dingshan, Jingwei, Jiaxiang, Maolong, Dongdong, Hanqing, Rui, and Jian for the enjoyable times we spent playing basketball. I am grateful to Zhaoying (once again), Rui (once again), and Yuxuan for appointing me as the "Godfather" of your cats (Julie, Felix, Ginger, and Juzi). Their companionship and playful antics have added vibrancy to my life.

I would like to acknowledge the financial support provided by the China Scholarship Council and the RSF Grant, which made this research possible. Although my Ph.D. career is coming to an end, my journey at TU Delft continues as I embark on a postdoc position starting on November 15th. In this regard, I would like to express my appreciation to Dr. Sid, Dr. Vera, and Dr. Jovana for their assistance in preparing and reviewing project proposals and funding applications.

My family—my parents and brother—deserve special recognition for their unwavering love, encouragement, and belief in me. Their steadfast support has been the pillar of strength that sustained me throughout this journey.

Finally, I am grateful to all the participants and individuals who contributed to this research. Their willingness to share their knowledge and experiences was instrumental in the success of this project.

Thank you all!

Jia-Ning in Delft

01-10-2023